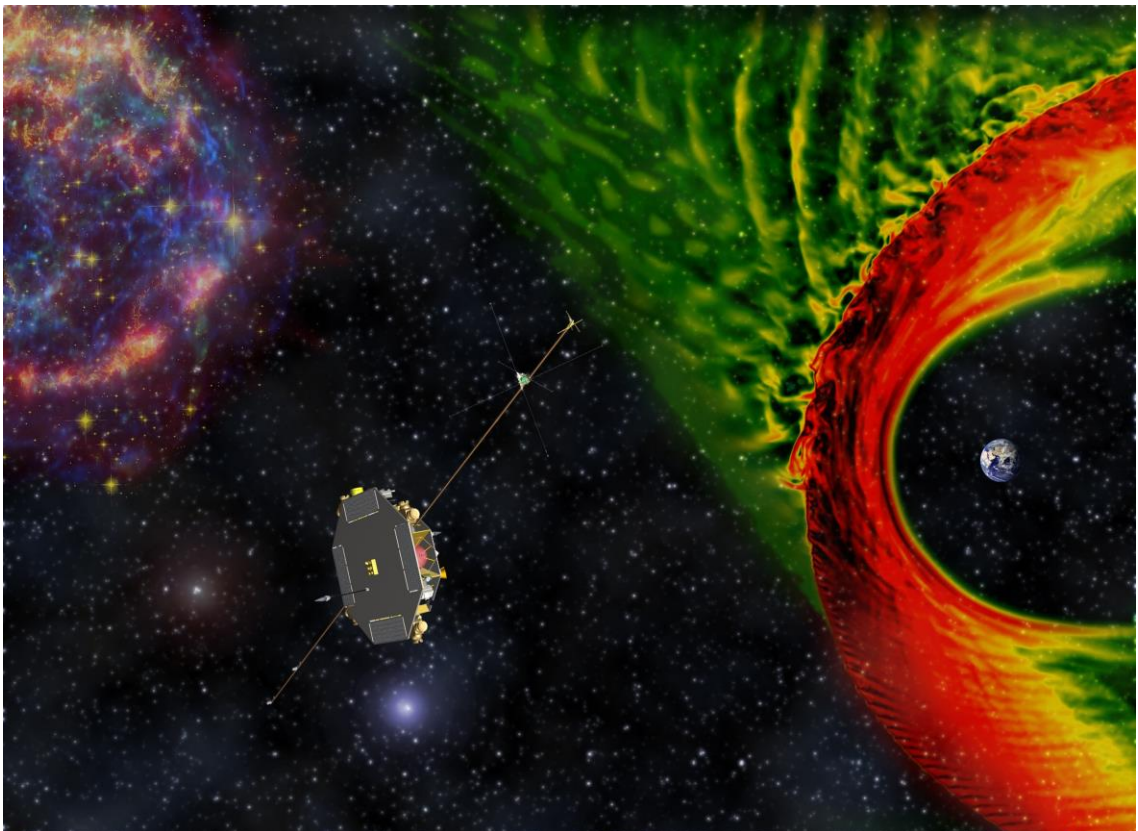


THOR

Exploring plasma energization in space turbulence



Assessment Study Report

Material used in the title page image: plasma turbulence surrounding the bow shock in a Vlasator simulation (M. Palmroth), CAD drawing of THOR from the proposal (OHB-Sweden), a false colour image of Cassiopeia A using observations from the Hubble and Spitzer telescopes as well as the Chandra X-ray Observatory (NASA).

Cover design by Walter Puccio.

THOR Assessment Study – Mission Summary																															
Key scientific objectives	<p>THOR will investigate the fundamental science theme “turbulent energy dissipation and particle energization” which addresses the ESA Cosmic Vision question “How does the Solar System work?” In particular, THOR will answer the following specific science questions:</p> <p style="padding-left: 40px;">Q1: How are plasmas heated and particles accelerated? Q2: How is the dissipated energy partitioned? Q3: How does dissipation operate in different regimes of turbulence?</p>																														
Spacecraft	<p>Sun-pointing, to allow high quality electric field and particle measurements. Slow spinner (2 rpm), to achieve high angular resolution particle data. Payload mass 170 kg, total dry mass 1250 kg, total wet mass 2400 kg. Bipropellant propulsion system.</p>																														
Payload	<table border="0" style="width: 100%; border-collapse: collapse;"> <tr> <td style="padding-right: 10px;">MAG</td> <td>fluxgate magnetometer</td> <td>B field, DC–64 Hz</td> </tr> <tr> <td>SCM</td> <td>search coil magnetometer</td> <td>B field, 1 Hz–100 kHz</td> </tr> <tr> <td>EFI</td> <td>electric field instrument</td> <td>E field, 2D DC–100 kHz, 3D 0.1–100 kHz</td> </tr> <tr> <td>FWP</td> <td>fields and waves processor</td> <td>E, B time series and spectral products</td> </tr> <tr> <td>TEA</td> <td>electron spectrometer</td> <td>3D distr. function of electrons (5ms)</td> </tr> <tr> <td>CSW</td> <td>cold solar wind analyser</td> <td>3D distr. function of H⁺(50ms), He⁺⁺(300ms)</td> </tr> <tr> <td>IMS</td> <td>ion mass spectrum analyser</td> <td>3D distr. function of H⁺(150ms), He⁺⁺(300ms), O⁺</td> </tr> <tr> <td>PPU</td> <td>particle processing unit</td> <td>TEA, CSW, IMS, EPE data products</td> </tr> <tr> <td>FAR</td> <td>Faraday cup</td> <td>cold solar wind ion moments, 32 Hz</td> </tr> <tr> <td>EPE</td> <td>energetic particle analyser</td> <td>3D distr. function energetic e⁻ and ions (15s)</td> </tr> </table> <p>Active spacecraft potential control to improve plasma and field measurements.</p> <p>In comparison to earlier/upcoming missions, required key major improvements include:</p> <ul style="list-style-type: none"> • accuracy/sensitivity of electric and magnetic field measurements, • temporal resolution of mass resolved ions (H⁺, He⁺⁺), • temporal/angular resolution of pristine solar wind ions, • temporal resolution of electrons, • wave and electron correlation up to electron plasma frequency. 	MAG	fluxgate magnetometer	B field, DC–64 Hz	SCM	search coil magnetometer	B field, 1 Hz–100 kHz	EFI	electric field instrument	E field, 2D DC–100 kHz, 3D 0.1–100 kHz	FWP	fields and waves processor	E, B time series and spectral products	TEA	electron spectrometer	3D distr. function of electrons (5ms)	CSW	cold solar wind analyser	3D distr. function of H ⁺ (50ms), He ⁺⁺ (300ms)	IMS	ion mass spectrum analyser	3D distr. function of H ⁺ (150ms), He ⁺⁺ (300ms), O ⁺	PPU	particle processing unit	TEA, CSW, IMS, EPE data products	FAR	Faraday cup	cold solar wind ion moments, 32 Hz	EPE	energetic particle analyser	3D distr. function energetic e ⁻ and ions (15s)
MAG	fluxgate magnetometer	B field, DC–64 Hz																													
SCM	search coil magnetometer	B field, 1 Hz–100 kHz																													
EFI	electric field instrument	E field, 2D DC–100 kHz, 3D 0.1–100 kHz																													
FWP	fields and waves processor	E, B time series and spectral products																													
TEA	electron spectrometer	3D distr. function of electrons (5ms)																													
CSW	cold solar wind analyser	3D distr. function of H ⁺ (50ms), He ⁺⁺ (300ms)																													
IMS	ion mass spectrum analyser	3D distr. function of H ⁺ (150ms), He ⁺⁺ (300ms), O ⁺																													
PPU	particle processing unit	TEA, CSW, IMS, EPE data products																													
FAR	Faraday cup	cold solar wind ion moments, 32 Hz																													
EPE	energetic particle analyser	3D distr. function energetic e ⁻ and ions (15s)																													
Mission	<p>3 year nominal mission, extended mission possible:</p> <p style="padding-left: 40px;">1st year, 6×15 R_E (geocentric), focus on bow shock and magnetosheath. 2nd year, 6×26 R_E (geocentric), focus on pristine solar wind and foreshock. 3rd year, 6×45 R_E (geocentric), focus on pristine solar wind and interplanetary shocks.</p> <p>Survey data downloaded for the whole period while burst data downloaded for short high science value intervals through selective downlink.</p> <p>Open data policy from 6 months into the nominal operations.</p>																														

Foreword

During the past century of exploration of the Universe, we have learned that the vast majority of ordinary matter that it contains is in the plasma state. It is this hot dilute plasma (ionized gas) between galaxies and galaxy clusters that dominates baryonic matter. Hot dilute plasma can also be found within galaxies, for example in the interstellar medium, outer atmospheres and stellar winds of stars, and coronas of accretion disks. Astrophysical plasmas are generally turbulent, and dissipation of turbulent fluctuations leads to continuous plasma heating and acceleration of charged particles. Understanding the basic plasma processes of heating and energization in turbulent magnetized plasmas is of fundamental importance if we are to fully understand the evolution of the Universe. This is one of the main motivations of the Turbulence Heating ObserveR (THOR) mission.

Choosing the mission name was not a difficult task. In Norse mythology, Thor is a hammer-wielding god associated with thunder and lightning, storms and strength, as well as the protection of mankind. Most importantly, Thor brings order out of chaos.

The THOR mission has grown from a seed which was the Call for Ideas for an "Innovative low-cost research satellite mission" by the Swedish National Space Board in January 2012. At that time, the mission was called Tor and it was intended to be a small national satellite, although it already involved a fully international payload. The evaluation showed clearly that, while the science case was compelling, the mission did not fit the "low-cost" concept.

In June 2012, Tor was submitted as a candidate for the ESA S1 mission. The outcome was very similar: the mission was ranked highly scientifically, but despite different advanced cost-saving suggestions, the mission cost was still not within the S-class envelope.

At that time, the team decided to extend the scientific topics addressed by Tor and submit a proposal for the upgraded THOR mission to the ESA M4 call. The payload capabilities were increased: instead of focusing the observations on electromagnetic fields, it was expanded to include kinetic scale observations of the plasma particles, which are required to study heating and acceleration processes. This major upgrade allowed an important new set of science questions to be addressed, as described in this report.

THOR is a fundamental plasma physics mission, which uses near-Earth space as its laboratory. This focus has not only attracted large support for the mission from the laboratory, solar and astrophysical plasma communities, but it has also already initiated many synergetic studies between them. The answers to important unsolved questions, such as those that THOR will address, require strong collaboration among scientists from very different fields and one goal of the THOR project is to continue bringing these communities closer together.

The work on the THOR mission has been a major international team effort. On the payload side, THOR has ten instruments, each of which are designed and built by a consortium of several laboratories. On the mission side, THOR has involved tens of ESA scientists and engineers from different offices. On the industry side, industries from almost all ESA countries have contributed to the mission design. Last but not least, more than one hundred scientists have actively contributed to the mission. There have been two THOR workshops, many sessions and presentations at international conferences, national workshops, and several studies leading to refereed papers addressing different aspects of the THOR mission. The excellent team spirit provides a strong foundation for the future of the THOR mission.

The THOR Science Study Team

Authorship and acknowledgements

This report is the result of work by the THOR team; the full list is given in Annex A.

This report is prepared by:

ESA Science Study Team (SST)		
<i>Name</i>	<i>Affiliation</i>	<i>City, Country</i>
Christopher Chen	ICL	London, UK
Andrew Fazakerley (PI TEA)	MSSL	Dorking, UK
Yuri Khotyaintsev (PI EFI)	IRF	Uppsala, Sweden
Benoit Lavraud (PI CSW)	IRAP	Toulouse, France
Maria Federica Marcucci (PI PPU)	INAF	Rome, Italy
Yasuhito Narita	IWF	Graz, Austria
Alessandro Retinò (PI IMS)	LPP	Paris, France
Jan Soucek (PI FWP)	IAP	Prague, Czech Republic
Rami Vainio (Co-PI EPE)	UTU	Turku, Finland
Andris Vaivads (Lead Scientist)	IRF	Uppsala, Sweden
Francesco Valentini	UNICAL	Rende, Italy
Additional Instrument Principal Investigators		
Rumi Nakamura (PI MAG)	IWF	Graz, Austria
Zdeněk Němeček (PI FAR)	Charles University	Prague, Czech Republic
Fouad Sahraoui (PI SCM)	LPP	Paris, France
Robert Wimmer-Schweingruber (PI EPE)	University of Kiel	Kiel, Germany

The ESA Team supporting the activities is composed by:

ESA Study Team		
C. Philippe Escoubet (Study Scientist)	ESA/ESTEC	Noordwijk, The Netherlands
Thomas Voirin (Study Manager from June 2016)	ESA/ESTEC	Noordwijk, The Netherlands
Martin Gehler (Study Manager until June 2016)	ESA/ESTEC	Noordwijk, The Netherlands
Arno Wielders (Payload Manager)	ESA/ESTEC	Noordwijk, The Netherlands
Nathalie Boudin (Payload Engineer)	ESA/ESTEC	Noordwijk, The Netherlands
Jens Romstedt (Payload Engineer)	ESA/ESTEC	Noordwijk, The Netherlands
Ana Piris Niño (Mission Operations Study Manager)	ESA/ESOC	Darmstadt, Germany
Pedro Osuna (Science Operation Study Manager)	ESA/ESAC	Madrid, Spain
Axel Junge (EMC Study Manager)	ESA/ESTEC	Noordwijk, The Netherlands
ESA Coordinators		
Luigi Colangeli	ESA/ESTEC	Noordwijk, The Netherlands
Arvind Parmar	ESA/ESTEC	Noordwijk, The Netherlands
Fabio Favata	ESA/ESTEC	Noordwijk, The Netherlands

Additional subsection responsibilities: Stein Haaland (MPS, Germany), Alexis Rouillard (IRAP, France), Robert Wicks (MSSL, UK).

National agencies contributing to the study phase: ALR/FFG, ASI, BELSPO, CNES, DLR, JAXA, NASA, PRODEX/MEYS-CR, PRODEX (Poland), SNSB, UKSA.

Important contributions to the mission design: Airbus Defence & Space, OHB System AG & Consortium.

Table of contents

1	Executive summary	6
2	Scientific objectives.....	9
2.1	Introduction.....	9
2.2	Science question Q1: how are plasmas heated and particles accelerated?.....	12
2.2.1	Uniform dissipation.....	12
2.2.2	Localized dissipation.....	17
2.3	Science question Q2: how is the dissipated energy partitioned?	19
2.3.1	Partition among species.....	20
2.3.2	Partition between heating and acceleration	22
2.4	Science question Q3: how does dissipation operate in different regimes of turbulence? ...	25
2.4.1	The pristine solar wind.....	25
2.4.2	Interaction regions between flows.....	27
2.4.3	Shocks and associated sheath regions	28
2.5	Additional science.....	31
2.5.1	Additional science in the key science regions	31
2.5.2	Additional science outside the key science regions	33
3	Scientific requirements	35
3.1	Instrument requirements	35
3.2	Mission requirements	45
4	Payload	48
4.1	Introduction.....	48
4.2	Instruments.....	52
4.2.1	MAG – Fluxgate Magnetometer	52
4.2.2	SCM – Search Coil Magnetometer	53
4.2.3	EFI – Electric Field Instrument	54
4.2.4	FWP – Fields and Waves Processor.....	55
4.2.5	FAR – Faraday Cup instrument.....	57
4.2.6	CSW – Cold Solar Wind instrument	58
4.2.7	TEA – Turbulence Electron Analyser	59
4.2.8	IMS – Ion Mass Spectrometer.....	61
4.2.9	EPE – Energetic Particle Experiment.....	62
4.2.10	PPU – Particle Processing Unit.....	63
4.2.11	ASP - Active Spacecraft Potential control unit	64
4.3	Payload operations	65
4.3.1	Payload modes.....	65
4.3.2	Science data.....	65
4.3.3	Instrument settings	67
4.4	Electromagnetic cleanliness.....	67
4.4.1	DC and low frequency magnetic field.....	67
4.4.2	Electrostatic requirements	68
4.4.3	AC electric and magnetic field requirements	68
4.4.4	Requirement verification.....	69
5	Mission design.....	70
5.1	Mission requirements.....	70
5.2	Mission design drivers	70
5.2.1	Key Science Regions crossings.....	70
5.2.2	Specific constraints for orbital manoeuvres	71
5.2.3	Radiation environment	71
5.2.4	Selective downlink	72
5.2.5	EMC	73
5.2.6	Payload accommodation.....	74
5.3	Mission phases	74
5.3.1	Launch and transfer to NSP1.....	75
5.3.2	Nominal science phases.....	75

5.3.3	Incursions in the GEO protected region	76
5.3.4	Safe mode.....	76
5.3.5	Spacecraft disposal	77
5.4	Spacecraft design	77
5.4.1	Spacecraft design – solution 1.....	77
5.4.2	Spacecraft design – solution 2.....	79
5.5	System budgets	82
5.6	Critical elements and risks mitigation.....	82
5.7	Conclusions.....	83
6	Ground segment.....	84
6.1	Operations concept.....	84
6.1.1	Mission operations centre.....	84
6.1.2	Science operations centre	84
6.1.3	Principal investigator teams	84
6.2	Operations ground segment	85
6.3	Science ground segment.....	86
6.3.1	Overview	86
6.3.2	Uplink.....	87
6.3.3	Downlink.....	87
6.3.4	Data types and data processing	88
6.3.5	Data distribution and archiving	88
6.4	Scientific data analysis.....	89
6.4.1	Waves and turbulent fields	89
6.4.2	Structures and discontinuities.....	90
6.5	Wave-particle correlation capabilities.....	91
6.6	Numerical simulation support.....	92
7	Management	95
7.1	Procurement scheme	95
7.2	Programme participation.....	95
7.3	Science management.....	96
7.4	Schedule.....	96
8	Communication and outreach	97
9	Bibliography	99
10	List of acronyms	105
11	Annex A: Assessment study contributors.....	106
12	Annex B: L1 and L2 requirements	109

1 Executive summary

Science objectives of THOR

Turbulence Heating ObserveR (THOR) will be the first mission ever flown in space to investigate the ubiquitous and fundamental process of plasma turbulence. Plasma is the dominant state of (baryonic) matter in the Universe and is mostly in a turbulent state. We can *see* the plasma Universe because plasma is heated to extremely high temperatures and emits electromagnetic radiation, but we still do not fully understand why and how this happens. THOR will take a major step forward in solving this fundamental problem.

The prime science questions of the THOR mission are:

Q1: How are plasmas heated and particles accelerated?

Q2: How is the dissipated energy partitioned?

Q3: How does dissipation operate in different regimes of turbulence?

THOR science directly addresses the Cosmic Vision theme "How does the Solar System work?" by studying the basic processes occurring "From the Sun to the edge of the Solar System". By quantifying the fundamental processes involved, the advances made by the THOR mission will extend beyond the Solar System to plasmas elsewhere in the Universe.

THOR will lead to an understanding of the basic plasma heating and particle energization processes, of their efficiency for different plasma species and of their relative importance in different turbulent regimes. THOR will provide closure on these fundamental questions by making detailed *in situ* measurements of the closest available collisionless and turbulent magnetized plasmas at unprecedented temporal, spatial and energy resolution.

THOR will explore both the ion and, for the first time, electron kinetic range of turbulence where most of the energization occurs, and reveal the dominant energization mechanisms. This will allow the key question of whether energization occurs mainly at specific localized structures, or is distributed more uniformly over large volumes in space, to be solved. Furthermore, THOR will perform accurate measurements of different particle species in both the thermal and non-thermal ranges, allowing the partition of the energy dissipated by turbulent fluctuations between the heating and acceleration of electrons, protons and heavier ions to be quantified. This is a fundamental problem for plasma physics and a major puzzle in astrophysical plasmas when resolving the physical conditions lying behind the emission from distant astrophysical objects.

Studying how energy dissipation and particle energization depend on different regimes of turbulence is required to assess which energization mechanisms dominate under specific plasma conditions. By providing measurements in several near-Earth turbulent regions, THOR will reveal how plasma energization works in different Solar System plasmas and will also help understand how energization operates in many laboratory and astrophysical plasmas, which often have conditions similar to those in near-Earth space.

Mission design

While expanding supernova shocks and other spectacular manifestations of plasma heating will forever remain beyond our capability for *in situ* measurements, the Earth's plasma environment serves as the laboratory that is needed to further our understanding. THOR, therefore, focuses on several specific regions of near-Earth space: the pristine solar wind, Earth's bow shock and interplanetary shocks, and the compressed solar wind regions downstream of shocks (e.g., the magnetosheath). These regions have been selected because of their differing plasma regimes and turbulent fluctuation characteristics, which also reflect the relevant variety of other astrophysical environments. In addition, characteristic plasma scales in the key science regions are sufficiently large for the particle instruments to resolve the kinetic scale turbulence.

The mission baseline is planned to start in June 2026 with a launch on an Ariane 62 rocket from Kourou, placing the spacecraft in a transfer orbit of $250 \text{ km} \times 15 \text{ Earth radii (R}_E\text{)}$. Then, using the onboard propulsion system, the spacecraft will raise its perigee to reach the orbit of $6 \times 15 \text{ R}_E$. After a commissioning period of 3 months, the first phase of the mission will start and focus on the bow shock and magnetosheath regions.

After approximately 1.5 years, the apogee will be increased to 26 R_E and a new turbulence regime will be observed in the foreshock during phase 2. Finally, one year later, the apogee will be raised again to 45 R_E and long intervals of time will be dedicated to understanding the turbulence in the pristine solar wind during phase 3. The nominal mission duration is 3.5 years, including 0.5 years for commissioning and de-commissioning of the spacecraft. A mission extension of two years after phase 3 is possible, which would lead to a total mission duration of 5.5 years.

Scientific payload

To answer the science questions, the THOR spacecraft will carry, for the first time, a comprehensive payload tailored to explore plasma energization in turbulence, with both fields and particle instrumentation that will allow simultaneous resolution of both turbulent fluctuations and signatures of the resultant plasma energization. The payload consists of state-of-the-art experiments with the highest temporal and spatial resolutions ever flown in space. The instruments on THOR all have relevant heritage from recent missions and most of the subsystems of the instruments have the required maturity for this phase. The ten PI-led hardware investigations are:

The Fluxgate Magnetometer (MAG) experiment providing measurements of the DC and low frequency magnetic field with high accuracy.

The Search Coil Magnetometer (SCM) experiment providing sensitive measurements of the magnetic field in the frequency range 0.1 Hz to 100 kHz.

The Electric Field Instrument (EFI) providing measurements of the electric field and waves in the range 0-100 kHz and the spacecraft potential with high accuracy and sensitivity.

The Fields and Waves Processor (FWP) experiment providing measurements of electromagnetic waves, including snapshots up to 524 sps, the plasma sounder and triggers for electron superburst data. FWP will control the other field instruments.

The Faraday Cup instrument (FAR) providing solar wind parameters (density, three velocity components, and thermal speed) at 32 sps.

The Cold Solar Wind instrument (CSW) providing 3D velocity distribution functions of the cold solar wind ions with high energy (7%) and angular (1.5°) resolution at a resolution up to 50 ms.

The Turbulent Electron Analyser (TEA) providing 3D velocity distribution functions of electrons between 10 eV and 30 keV with a time resolution up to 5 ms and pitch-angle distributions up to 1.25 ms. It also provides timed electron detection events for wave-particle interaction studies.

The Ion Mass Spectrometer (IMS) experiment providing 3D velocity distribution functions of ions between 10 and 30 keV with mass distinction between 1 and 32 amu at time resolution of 150 ms for H^+ and 300 ms for He^{++} .

The Energetic Particle Experiment (EPE) providing the energy spectra and angular distributions of energetic electrons (20-700 keV) and ions (20-8000 keV/n) at 15 s resolution and pitch-angle snapshots at 7.5 s.

The Particle Processing Unit (PPU) performing moment calculations on 3D particle velocity distribution functions, providing magnetic field for pitch-angle distribution measurements and solar wind direction for ion beam tracking mode, and compression of 3D distribution functions. PPU controls the other particle instruments (except FAR).

Spacecraft

THOR is a low risk mission with a spacecraft design relying on mature, high TRL technologies for all subsystems. The preliminary design solutions studied in phase A demonstrated two feasible solutions, technically and programmatically, fulfilling the mission and science requirements. The two solutions studied present good margins with respect to the launch performance requirements.

THOR is a spin stabilized spacecraft spinning at 2 rpm, with a Sun-oriented spin axis. The shape of the spacecraft structure is octagonal, with a total diameter around 4 m and a total height of 2 m. Spacecraft wet mass is 2400 kg, leaving a 14% launch margin on Ariane 62. A bi-propellant propulsion subsystem will be used for orbital and attitude maneuvers. The mechanisms are limited to the two two-segment rigid booms, which have a total length of at least 6.5 m each. The solar array is body-mounted and represents a total area of at least 5 m^2 , the size of which is driven by the power requirement of nominal science mode when communicating with the ground. The spacecraft external surfaces are conductive, including the solar array coated with indium tin oxide, to comply with spacecraft charging requirements. A large capacity Flash Memory of 12 Tbits End Of Life is used for data storage and high time resolution data selection. X-band is used for communication.

Operations

The THOR ground segment consists of the Mission Operations Centre (MOC), the Science Operations Centre (SOC), and the ground station network with 3 ESTRACK deep space stations in New Norcia, Cebreros, and Malargüe. The THOR payload is operated as a single virtual instrument – all instruments operate at the same time and target common payload-wide science objectives. The SOC and MOC payload operation is simplified by the fact that all instruments except FAR interface with the spacecraft via FWP and PPU. The payload generates two parallel science data streams transferred to the spacecraft mass memory:

Burst data covering almost the full time at high bitrate. Only a small fraction of the burst data is downlinked using a selective downlink approach, data downlink is at perigee.

Survey data covering the full time at low bitrate. All of the survey data is downlinked to the ground.

An archive for the THOR data will be built at ESAC based on experience from existing archives such as the Cluster Science Archive. THOR will employ the open data policy starting from 6 months into the nominal mission. Refinement of the calibrations, using inflight experience and cross-calibration activities, is the responsibility of the PI teams.

THOR data will be analysed using a variety of methods available for studying waves and coherent structures in turbulence. Numerical modelling support is crucial, both from the science and mission design points of view. The support is provided by the synergistic activities of the Numerical Simulation Support Team, which includes scientists developing, running and supplying results from different plasma simulation codes, and the Virtual Instrument Team, which aids the definition of the THOR payload.

THOR in the wider context

Plasma in the Universe is often so hot and dilute that collisions between charged particles are very rare, making most of the baryonic matter in the Universe detectable only through high-energy radiation, e.g., X-rays, generated by heated particles. This is the case for a variety of environments, such as galaxy clusters, the interstellar medium, outer atmospheres and stellar winds of stars, and coronas of accretions disks. These plasmas are frequently highly turbulent due to large scale shear motions, shock waves, jets, and other large-scale processes, and they may well be energized by the dissipation of turbulence. Understanding the basic processes of plasma energization in turbulence is of fundamental importance for understanding the evolution of the Universe. THOR will provide an understanding of fundamental plasma processes from *in situ* measurements in near-Earth space. This will help us to understand many aspects of laboratory and astrophysical plasmas and will drive new synergies between space, astrophysical and laboratory communities, to advance these fundamental science topics.

A number of space missions, including Cluster, THEMIS and MMS (and future missions such as Solar Orbiter and Solar Probe Plus) provide data on many aspects of plasma turbulence, such as its 3D properties, from multi-spacecraft observations. However, how the turbulence dissipates and heats the surrounding medium and energizes particles is not at all well understood. None of these missions were designed to reach the resolution required to understand the dominating wave-particle interactions that heat and accelerate plasma. The goal of THOR is to employ innovative instruments that significantly increase the time resolution of particle measurements (5 ms for electrons, 50 ms for solar wind protons and 300 ms for alpha particles), and increase the spatial resolution of solar wind ions (1.5°). The sensitivity and accuracy of electromagnetic field measurements are also significantly enhanced with long magnetometer booms (>6.5 m) and with the spacecraft spin axis pointing towards the Sun. Furthermore, the high time resolution of electron counts and wave measurements will allow, for the first time, advanced wave-particle correlation studies up to the electron plasma frequency. THOR will provide measurements that go beyond our current expectations, thus allowing the exploration of new physics and challenging our current theories.

Conclusion

THOR is an innovative mission that will revolutionize space plasma physics. Its powerful instrumentation, in terms of resolution and sensitivity, will address the science objectives directly relevant to the Cosmic Vision science programme. THOR represents a crucial step forward after the Cluster, THEMIS and MMS missions. It will capitalize on the strong European expertise in the field of plasma turbulence and particle energization. THOR will therefore achieve major breakthroughs in our understanding of turbulence and particle energization in the Solar System and will be a major step forward in understanding these fundamental processes in other astrophysical systems.

2 Scientific objectives

2.1 Introduction

The turbulent plasma universe

Plasma processes are at work everywhere, from radio galaxy jets and supernova explosions (Figure 1) to the solar corona and interplanetary space. It is for this reason that H. Alfvén coined the term "Plasma Universe" [1]. The information we have on distant astrophysical plasmas is obtained from the radiation they emit and that we remotely observe. Therefore, it is of crucial importance to understand plasma energization mechanisms that are behind such emissions. Astrophysical plasmas are generally in a turbulent state [2] and significant plasma energization is thought to be related to the dissipation of the turbulent fluctuations.

Examples of turbulent dissipation can be found in galaxies [3,4], stellar interiors [5], interstellar [6,7] and interplanetary [8–10] media and planetary magnetospheres [11–13]. Indeed, turbulence is a fundamental plasma processes occurring in the vast majority of natural and laboratory plasmas. Shocks are some of the most spectacular, visually-striking phenomena in the Plasma Universe and are responsible for the acceleration of copious amounts of charged particles up to energies 10^{18} eV and maybe even as high as 10^{20} eV. Turbulence plays a major role in particle acceleration at shocks [14]. Turbulent energy dissipation is also important in laboratory plasmas, e.g., in fusion devices, where turbulence has detrimental effects on the confinement of the plasma.

Despite their importance, remote observations of turbulence and plasma energization in astrophysical plasmas lack spatial resolution and can only provide integrated, often model-dependent results. Solar observations have considerably increased in resolution in the last decade owing to data from Soho, Hinode and SDO missions. However, they are still not adequate for the detailed study of energy dissipation mechanisms. Measurements in laboratory plasmas have also improved recently in terms of diagnostics, see for example the LAPD [16] or TORPEX [17] experiments, but the boundary conditions imposed by a laboratory setup and the difficulty of resolving multiple scales simultaneously are often severe limiting factors. Due to the inherent complexity of the underlying physics, understanding such mechanisms in depth from an experimental point of view requires direct measurements of plasma and electromagnetic fields. THOR will make such measurements *in situ* in the near-Earth space environment (see Figure 2) at higher resolution than ever before, with a payload tailored to study the turbulent energization processes. The synergy between such *in situ* and remote observations will significantly advance our understanding of the Plasma Universe.

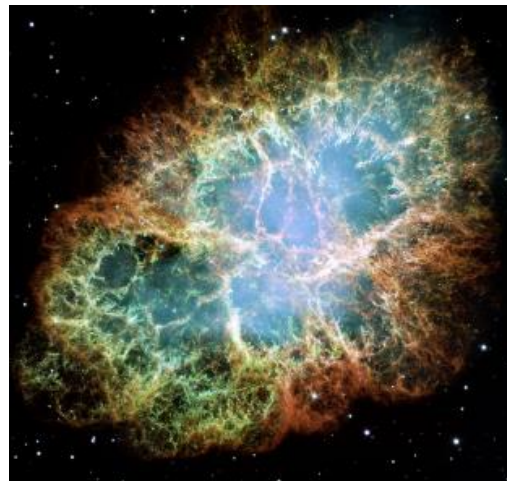


Figure 1: A classic example of turbulence in an astrophysical object: the highly turbulent supernova remnant Crab nebula. By using the near-Earth environment as a laboratory to study turbulent heating and acceleration, THOR makes the connection to this astrophysical object. Credit: NASA, ESA, J. Hester, A. Loll (ASU), D. De Martin (Skyfactory).

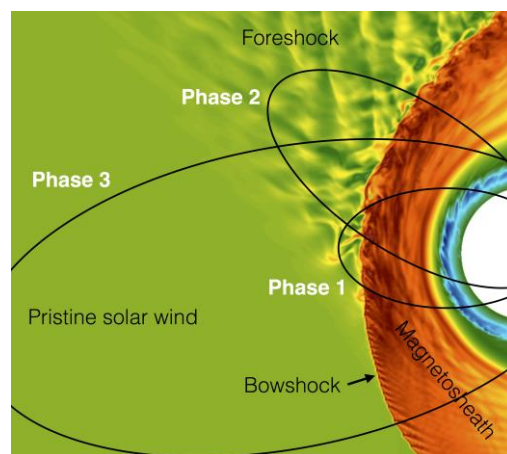


Figure 2: Illustration of near-Earth space based on Vlasiator numerical simulations [15]. The colouring shows plasma density. Key turbulent regions are shown: pristine solar wind, shock, foreshock and magnetosheath. The THOR targets these key science regions during the three mission phases.

Turbulent dissipation at kinetic scales

In space plasma turbulence, energy is injected into the system at large scales, and then transferred to smaller and smaller scales by non-linear interactions which generate a variety of different turbulent fluctuations. This process is known as the *turbulent energy cascade* (see Figure 3). Energy dissipation is negligible at fluid scales but becomes important in the *kinetic range*, where the scales of turbulent fluctuations become comparable to those of the particles, e.g., their gyroradii. Kinetic scales are very small compared to the typical size of many astrophysical systems; for example, ion and electron gyroradii in near-Earth space are about a few hundred kilometres or few kilometres, respectively. In the kinetic range, the energy of the turbulent fluctuations is thought to be transferred to heating and acceleration of charged particles, which modifies the shape of the particle distribution functions. At lower particle energies, dissipation corresponds to heating, namely the increase in the temperature of the thermal (core) population. At higher energies (up to several times the thermal energy), a suprathermal tail is typically formed, while at even higher energies (up to many tens of thermal energies), an energetic population is found. These populations are shown in Figure 4. THOR is designed to investigate the turbulence at kinetic scales and how this leads to energization of the different particle populations.

The near-Earth space

Most astrophysical plasmas are collisionless at kinetic scales, so that in many ways the plasma processes are comparable to Solar System plasmas. Yet remote observations of kinetic scales, even for the case of high-resolution imaging of the Sun, are not accessible. In laboratory plasmas, kinetic scales are typically of the order of a few centimetres or less. Manufacturing advanced plasma sensors capable of resolving such small scales is technically very challenging. The near-Earth space (see Figure 2) is a privileged laboratory for studying turbulent energy dissipation at kinetic scales because high resolution *in situ* measurements can be performed there and transmitted to ground with high cadence. Furthermore, near-Earth turbulent regions offer the possibility of studying many different types of turbulent fluctuations under different conditions over an extremely broad range of scales. Due to similarities with other solar, astrophysical and laboratory plasma regimes, see Figure 5, many of the results obtained in near-Earth space are helpful for understanding other plasma environments. One important example of a turbulent environment in near-Earth space is the solar wind, where the complex dynamics of the Sun's atmosphere provides the initial energy at large scales that drives the turbulence in interplanetary space, followed by dissipation at kinetic scales. Another important example are turbulent shock regions, e.g., the terrestrial bow shock, where locally generated turbulent fluctuations play a major role for particle acceleration.

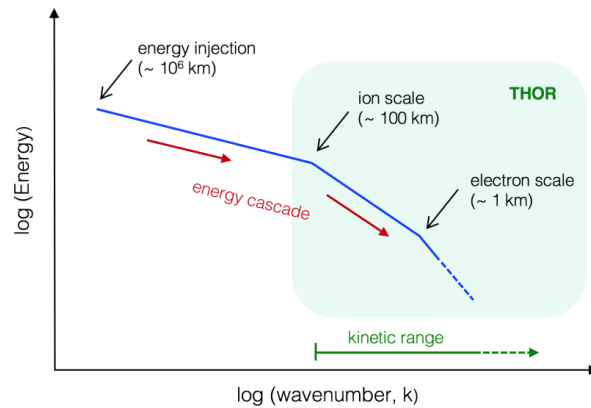


Figure 3: Schematic of turbulence energy spectrum. Energy injected at large (fluid) scales cascades to small (kinetic) scales where it is dissipated. THOR will explore kinetic plasma processes that determine how the turbulent electromagnetic fluctuations dissipate.

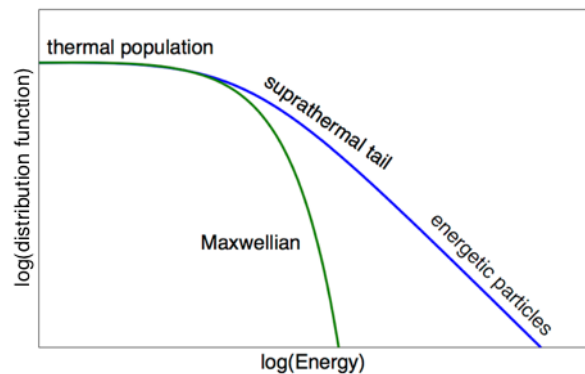


Figure 4: Turbulent dissipation leads to plasma heating and/or acceleration of particles to high energies, forming suprathermal and energetic tails in their distribution function. THOR will measure these particle populations to understand the heating and acceleration processes.

Previous and current space missions in near-Earth space provide a large number of *in situ* measurements, that have allowed impressive advances in characterizing turbulence at large scales. It was found for the pristine solar wind that a fluid description captures most aspects of the large scale (low frequency) turbulent cascade [8,18]. On the other hand, most of energy dissipation and particle energization is expected to occur at kinetic scales [19–22]. Yet the dissipation mechanisms at such scales are still poorly understood. Understanding such mechanisms requires *in situ* high-resolution and high-sensitivity measurements at kinetic scales in different near-Earth turbulent regions. THOR would be the first spacecraft tailored to perform such measurements.

Comparison to other missions

Many past and current spacecraft missions have studied near-Earth space plasmas. None of these missions, however, have been, or will be capable of, reaching the sensitivity and accuracy of electric and magnetic field measurements and the high temporal, angular and energy resolutions of particle distribution functions that THOR will provide. Such measurements are required to study and fully understand turbulent energy dissipation and plasma energization at kinetic scales. A more detailed comparison with current and upcoming missions, in terms of fulfilling the THOR science requirements, is discussed in Section 3. For example, the NASA Magnetospheric Multiscale (MMS) mission was designed to study the magnetic reconnection process at large scale boundaries, such as the terrestrial magnetopause and magnetotail. However, its instrumentation and orbit is not tailored to study turbulent heating and acceleration processes, meaning it cannot fully address the THOR science questions. The future missions ESA Solar Orbiter (SO) and NASA Solar Probe Plus (SPP) will make measurements in the pristine solar wind and address turbulence as one of their many goals. Yet the *in situ* instrumentation on board such spacecraft is not tailored for studying kinetic scales, and their orbits do not cover the range of near-Earth environments needed to address the THOR science questions. Furthermore, due to their large distance from Earth, the volume of high resolution data that both SO and SPP can transmit is limited compared to THOR. Such a large data volume is required to provide a complete statistical description of turbulent energy dissipation processes. On the other hand, due to the different orbits of THOR and both SO and SPP, the synergy between these missions will allow other questions, such as turbulence evolution with distance from the Sun, to be studied.

Finally, Table 1 gives the main science questions and summarizes the basic approach by which they will be addressed. The following subsections explain each of the science questions in more detail.

Table 1: Summary of THOR science questions and how they will be addressed.

Science question	Closure
Q1: How are plasmas heated and particles accelerated?	Identify wave modes and coherent structures. Characterize the effects of the different heating/acceleration mechanisms on the plasma.
Q2: How is the dissipated energy partitioned?	Quantify the energy partition among electrons, protons and heavier ions. Quantify the energy partition between heating and particle acceleration.
Q3: How does dissipation operate in different regimes of turbulence?	Explore the different parameter ranges of turbulence by measuring in pristine solar wind, flow interaction regions, shocks and sheaths behind shocks.

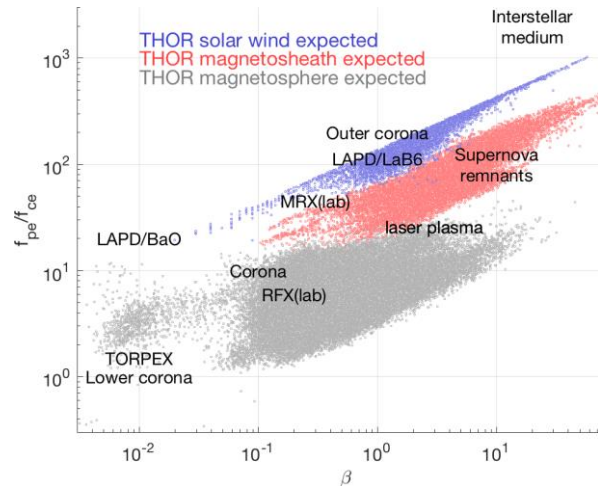


Figure 5: Typical parameters of different plasma environments based on real observations by Cluster, ACE and MMS spacecraft. Many of the astrophysical and laboratory environments are similar to the near-Earth space that THOR will measure when compared in non-dimensional parameter space (ratio of plasma and cyclotron frequencies, and $\beta =$ ratio of thermal and magnetic pressures).

2.2 Science question Q1: how are plasmas heated and particles accelerated?

Most of the plasma energization (plasma heating and particle acceleration) occurring in turbulent collisionless plasmas, such as those permeating the Solar System and many astrophysical environments, is expected to occur at kinetic scales, that is, at scales comparable to particle gyroradii and below. Figure 6 shows a simulation of turbulence driven by velocity shear, with a cascade of turbulent fluctuations down to kinetic scales, where electrons are energized. Different kinds of turbulent fluctuations, of which Figure 6 shows one example, do exist in plasmas; yet the exact mechanisms through which they dissipate their energy and particles are energized are basically unknown. The identification of the dominant dissipation and particle energization mechanisms is the first main question that THOR will address:

Q1: How are plasmas heated and particles accelerated?

The key issue is whether turbulent energization occurs only at localized structures, or whether it is distributed more uniformly throughout the volume by other processes. Both of these possibilities are associated with a number of different proposed physical mechanisms through which the energization may occur, which may be linear or nonlinear in nature (see Figure 7). Different numerical simulations show that a variety of these possibilities can be in operation in a turbulent plasma [23–28].

Due to the lack of dedicated measurements so far, it is not known which of these mechanisms are in operation in space and astrophysical environments, and how the plasma energization varies under different conditions. THOR will explore these mechanisms, and with its advanced instrumentation, will be able to distinguish between them.

2.2.1 Uniform dissipation

The first class of dissipation mechanisms that may be operating are those that are more uniform in nature, i.e., they operate throughout the volume of the plasma. Several such collisionless mechanisms have been proposed, e.g., linear Landau and cyclotron damping [21,29–31], stochastic heating [25], trapping and heating in large amplitude waves [32–34] and nonlinear Landau damping resulting in the generation of phase-space holes [35,36]. These are associated with different types of waves and turbulence, so to investigate them requires first determining the type of fluctuations present, then looking for their effects on the plasma particles.

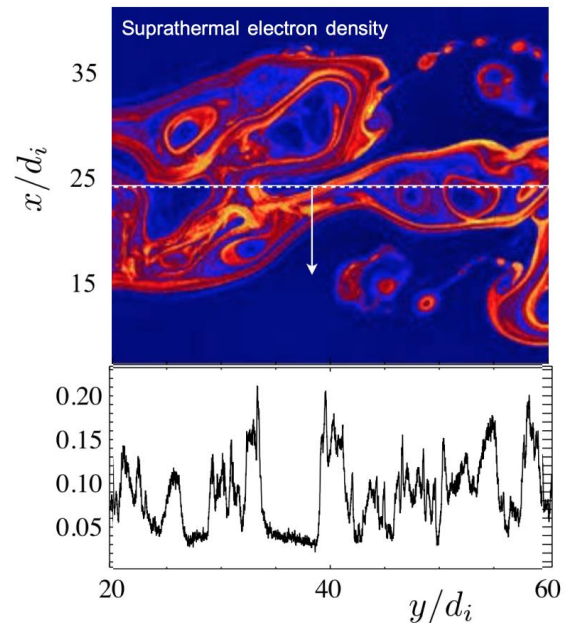


Figure 6: Top: Electron energization within kinetic-scale fluctuations as seen in particle-in-cell simulations of turbulence driven by flow shear. The density of suprathermal electrons is colour coded. Bottom: cut at $X=24$ showing the density of suprathermal electrons as would be seen by a spacecraft [23]. THOR high time resolution measurements will allow to resolve such structures in space and identify particle energization mechanisms.

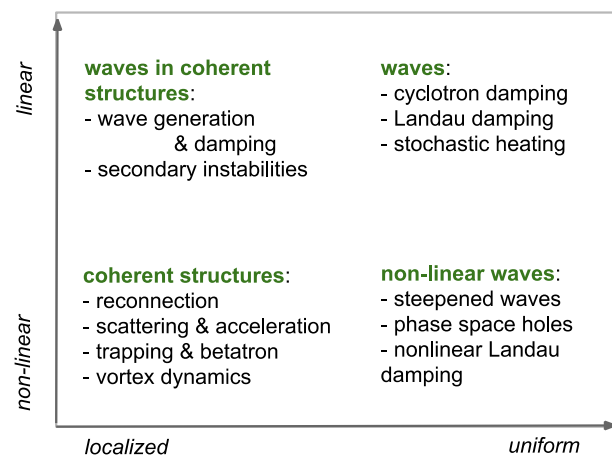


Figure 7: Possible dissipation mechanisms organised according to their spatial uniformity and degree of non-linearity. THOR will distinguish which mechanisms are taking place.

Turbulent fluctuations and wavemode identification

The different dissipation mechanisms are associated with different types of turbulence, which can be present at different times, or locations in the near-Earth space environment. Many different types of turbulent fluctuations can exist at kinetic scales, e.g., whistler turbulence [29,38–41], kinetic Alfvén turbulence [31,37,42,43], mirror mode waves [44–46], and cyclotron waves [47–49]. Figure 8 shows the magnetic field in a kinetic Alfvén turbulence simulation. It is important to distinguish under what conditions these different types of waves and turbulence occur.

One way to distinguish the different types of turbulence and waves is by comparing the fluctuations of different measured fields. For example, kinetic Alfvén turbulence has been identified by the ratio of electric to magnetic fluctuations $\delta E/\delta B$ [21,50,51] and density to magnetic fluctuations $\delta n/\delta B$ [52,53]. The magnetic compressibility $\delta B_{\parallel}/\delta B_{\perp}$ has also been used [54–56], and is good for identifying mirror modes [44,45,57]. Other measures, such as magnetic helicity and polarisation are possible [20,58], and have been used to identify parallel-propagating cyclotron or whistler waves [59–61], see Figure 9. However, these measurements are limited by instrument noise and resolution, meaning that we currently do not know the nature of turbulence at electron scales, or how the type of turbulence in general varies under different plasma conditions.

Another important diagnostic is the power spectrum; its properties and shape reveal a lot about the cascade and dissipation processes. Figure 10 shows example spectra from the solar wind. The magnetic spectrum steepens at the ion scale (~ 0.5 Hz) and again at the electron scale (~ 50 Hz), showing changes in the turbulence, associated with dispersive and dissipative effects. The electric spectrum flattens at the ion scale, although this is due to instrumental noise. The density spectrum steepens at the ion scale, but due to the limited resolution, we do not know its behaviour at the electron scale. The precise shape of the magnetic spectrum at electron scales, and the implications for dissipation, however, are debated [62,63] and we do not have good quality electric, density, or particle spectra here. Knowing the anisotropy of the spectrum, i.e., whether kinetic turbulence is made up of perpendicular ($k_{\perp} \gg k_{\parallel}$), parallel ($k_{\perp} \ll k_{\parallel}$), isotropic ($k_{\perp} \sim k_{\parallel}$) fluctuations, or some combination, is also important, since these can heat the plasma and accelerate particles in different ways. While such measurements have been possible to some extent with magnetic fluctuations in the solar wind [64–66] and magnetosheath [67,68], they are close to instrumental noise levels, and not possible with current electric field or particle instruments. Measurements of spectra and anisotropy down to electron scales and below are needed to understand turbulent heating. Long periods of high resolution data are needed for statistical techniques [e.g. ,69] to be used to measure the anisotropy.

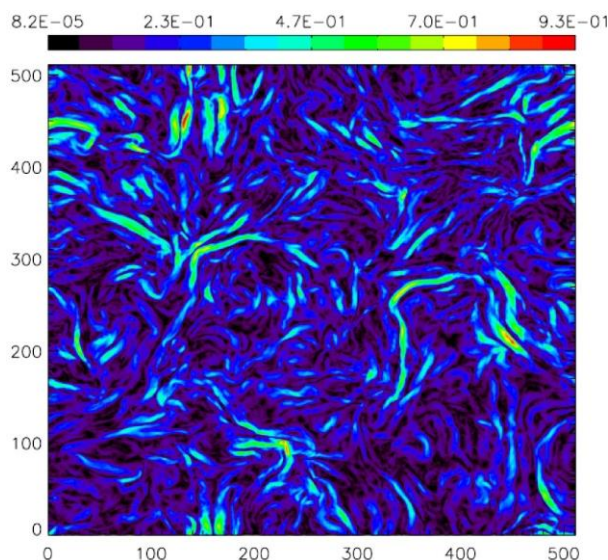


Figure 8: Strength of magnetic field fluctuations (colour) in a simulation of kinetic Alfvén turbulence, showing elongated structures that will be measured with THOR [37].

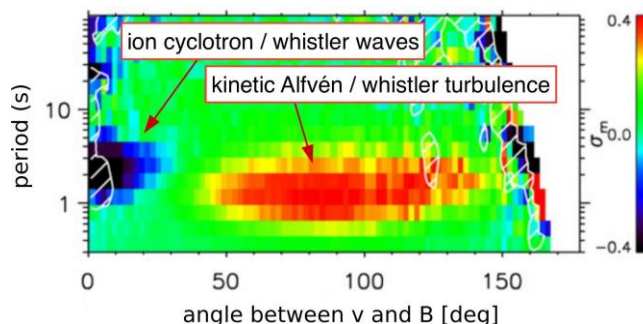


Figure 9: Magnetic helicity (colour) at ion kinetic scales. The red area at large angles to the magnetic field suggests kinetic Alfvén or whistler turbulence and the blue area at small angles suggests ion cyclotron or whistler waves [59]. THOR will allow to distinguish these different kinds of fluctuations.

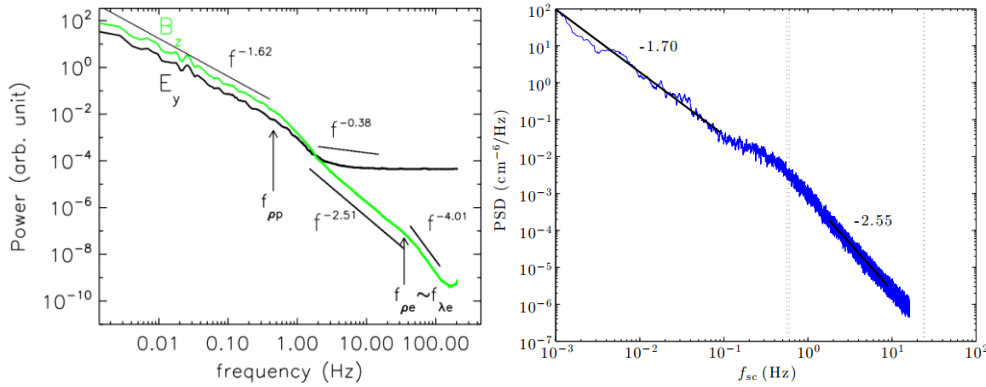


Figure 10: Energy spectra of electromagnetic fields and plasma density in pristine solar wind. Left: energy spectra of electric (black) and magnetic (green) fields measured by Cluster spacecraft [21]. The noise level of magnetic field is reached at electron scales, while the electric field below proton scales is unresolved due to noise (flat part of the curve). Right: energy spectrum of density measured by Spektr-R [70] almost reaching the electron scale. THOR will measure electromagnetic fields and density with sufficient sensitivity to resolve turbulence fluctuations down to sub-electron scales.

The high accuracy and resolution measurements of THOR will allow the nature of the fluctuations at kinetic scales to be fully identified. Magnetic fluctuations will be measured with high sensitivity and with a time resolution to allow the typical turbulence spectrum and anisotropy to be measured down to electron scales (Science Requirements **R1**, **R2** in Table 3). The electric field measurements will also have a high sensitivity, and due to the Sun-pointing spacecraft spin axis, there will be two good components, with minimal spin-tone interference, allowing accurate spectrum / polarisation anisotropy and phase velocity measurements down to electron scales (**R1**, **R2**, **R3**, **R4**). The time resolution of the particle moments will be higher, with increased sensitivity, to probe kinetic scales (**R6**). These will allow the nature of the turbulence and waves to be comprehensively diagnosed in the range of near-Earth environments (**R10**) at kinetic scales (**R11**).

Signatures of heating mechanisms

To determine which of the possible uniform dissipation mechanisms may be acting (Figure 7) also requires searching for their effects on the plasma particles. The uniform dissipation mechanisms can be broadly classed into two categories: resonant wave-particle interactions, and non-resonant wave-particle interactions. Resonant mechanisms include cyclotron, Landau and transit-time damping. Cyclotron damping has been invoked to explain the high temperatures in the solar corona [71] and solar wind at 1 AU [72,73], and is expected to lead mainly to perpendicular temperature increase. Landau damping has also been invoked [28,30,31,42] since it can act on low-frequency perpendicular turbulence, and is expected to lead to parallel temperature increase. How such mechanisms operate in a nonlinear setting is a topic of current investigation [74,75]. It has been suggested [31] that Landau-damped energy will nonlinearly cascade in velocity space to reach small enough scales for weak collisions to enable irreversible heating. One of the main types of non-resonant heating mechanism proposed is stochastic heating [25,76,77]. This is thought to occur when turbulent amplitudes are sufficiently large to cause particle orbits to become chaotic, leading to a spread in velocity space (see Figure 11), and can lead to perpendicular heating in low-frequency turbulence.

One of the most effective ways to distinguish between these mechanisms is through examining the velocity-space structure of the particle distributions, and how this correlates to the turbulent fluctuations. For example, cyclotron resonances lead to diffusion plateaus [72,78], Landau damping leads to parallel structure at the thermal speed [79,80], an entropy cascade generates small-scale velocity-space structure

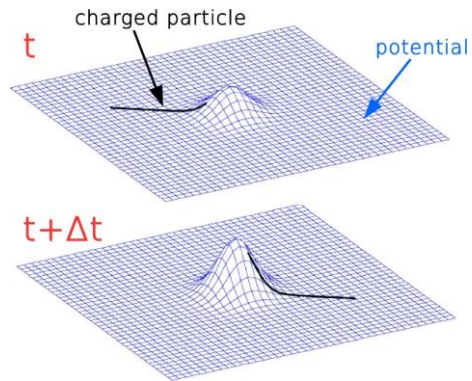


Figure 11: The mechanism of stochastic heating: particles gain energy as the electric potential (mesh-grid) varies in time during the particle motion (black line) [25].

[31,81], and stochastic heating creates flat-top distributions [82]. Particle acceleration mechanisms lead to high energy tails on the distributions [83].

Recent Hybrid Vlasov-Maxwell numerical simulations [24,27,84,85] have shown the behaviour of ion distribution functions around the ion scales. When the turbulent activity reaches its maximum, the shape of the 3D velocity distribution shows non-Maxwellian features, such as temperature anisotropy along or across the local magnetic field and particle beams mainly aligned to the local magnetic field (Figure 12). Such features are the smoking gun of wave-particle interactions and dissipation processes. Particle-in-cell simulations have also shown the development of large electron parallel temperature anisotropy, and, possibly, the formation of electron beams [24,86]. Such large anisotropy is localized within regions that extend less than ~ 0.1 ion gyroradii, and is smoothed out when averages of particle measurements are done over larger regions. These simulations indicate that measuring both ion and electron distributions with high temporal, angular and energy resolution is crucial to understand particle heating and acceleration. Moreover, resolving the sharp velocity gradients of both ion and electron distribution functions is essential for establishing whether or not plasma collisionality can be locally enhanced in presence of fine velocity structures, to enable true irreversible heating to take place [31,82,87].

While some aspects of these features have been identified in observations [72,90], current measurements lack the velocity space resolution to definitively distinguish between the different mechanisms. To address this, THOR will have an advanced suite of particle instrumentation, with high time resolution, and in particular high velocity space resolution (**R6, R7**). Both ion and electron instruments will sample at sub-ion and sub-electron scales respectively and both will sample velocity space at a fraction of the thermal speed to enable the different mechanisms to be distinguished. Together with the synchronized high time resolution electromagnetic field measurements (**R1**), this will enable field-particle correlation techniques to be applied to identify the signatures of each mechanism. Figure 13 shows a field-particle correlation technique [88,89] applied to three different types of heating mechanism in turbulence simulations; the different correlation signatures allow these to be distinguished, and the resolution of the THOR instrumentation will allow this to be used to determine the turbulent heating mechanisms in the near-Earth space environments. The TEA electron instrument will also have a “superburst” mode, in which individual electron counts are telemetered, allowing direct wave-particle correlation measures to be applied (see Section 6.5 for more information on the correlation data analysis techniques).

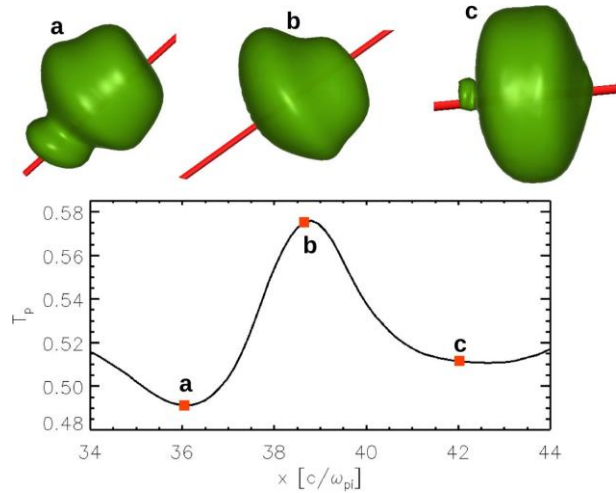


Figure 12: Iso-surface plots (upper) of the proton velocity distribution at three locations in a turbulence simulation, corresponding to different temperatures (lower). The distributions are strongly non-Maxwellian, displaying characteristic dissipation signatures (anisotropies, resonances, beams, etc.) that THOR will be able to resolve.

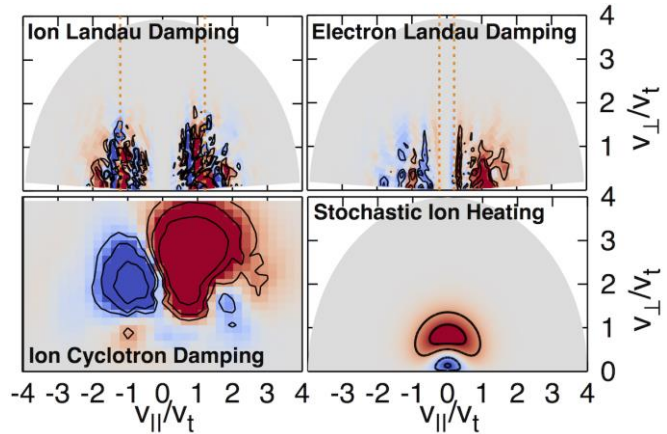
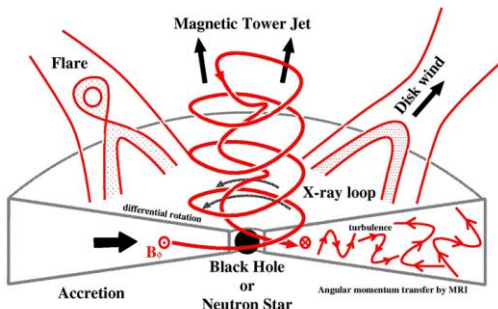


Figure 13: Field-particle correlation technique applied to simulations to obtain energy transfer in velocity space (colour) for different heating mechanisms [88,89]. Different structures can be seen for the different mechanisms, which can be resolved with sufficient velocity space resolution.

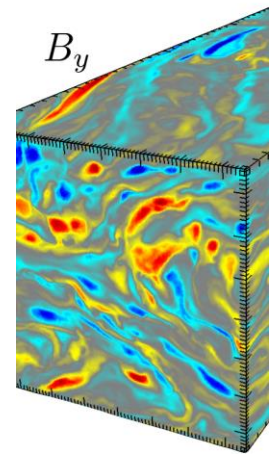
Astrophysical example: kinetic instabilities in accretion disks



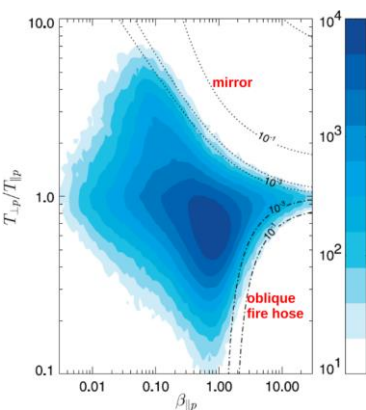
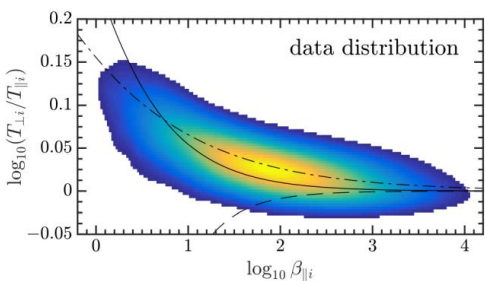
Accretion disks play a key role in many astrophysical environments, ranging from forming planets to supermassive black holes in the centre of galaxies and gamma ray bursts. In accretion disks, plasma is continuously moving inward and therefore angular momentum must be transported outwards in the disk. The magnetorotational instability (MRI) is a fluid instability that is widely accepted to account for such transport and it has been studied through many MHD simulations [91]. In some cases, plasma in accretion disks can be considered as collisionless, e.g., near the black hole at galactic centre, and

therefore similar to solar wind plasma. In such conditions, the plasma within the disk cannot be represented anymore as a fluid and kinetic physics, e.g., kinetic instabilities and turbulence, become crucial. In addition to their effect on large-scale plasma transport, kinetic instabilities and turbulence can also play an important role for plasma heating and particle acceleration within the disk (e.g., disk heating, flares, etc.) since it is at kinetic scales that particle energization is the strongest.

An important example of a kinetic instability in accretion disks, receiving growing attention, is the kinetic magnetorotational instability (KMRI) [92–96]. An example in the figure shows the formation of kinetic-scale structures in a portion of the collisionless disk. The KMRI generates enhanced outward angular momentum transport with respect to the fluid case [96]. It also generates turbulence, whose energy spectrum shows an Alfvén-wave cascade at large scales and a kinetic Alfvén-wave cascade at small scales similarly to the solar wind. Particle distribution functions become non-Maxwellian and show anisotropy with respect to the magnetic field direction. This anisotropy drives kinetic instabilities such as firehose and mirror, as shown in the figure, which can enhance particle scattering as well as affect



the topology of the magnetic field producing small-scale reconnection regions. Eventually, non-thermal particle acceleration is observed in the disk through dissipation of turbulent fluctuations and/or reconnection. This particle acceleration may explain the origin of high-energy particles observed around massive black holes.



Conditions observed in simulation of KMRI can be very similar to those found in the solar wind [97]. The figure shows the distribution of temperature anisotropy and plasma β obtained from the Wind spacecraft in the pristine solar wind, compared with the mirror and firehose instability thresholds in a similar fashion to the simulation. Instability thresholds are computed with the assumption of bi-Maxwellian proton distributions. Yet actual distribution functions in solar wind turbulence are often far from bi-Maxwellian, as also observed in recent simulations [98]. This could lead to incorrect thresholds and affect the identification of the instabilities at work. **THOR high-resolution measurements of both electron and mass-resolved ion distribution functions at kinetic scales will help to identify realistic conditions for simulations of both KMRI of other kinetic instabilities that are important for the dynamics of large-scale astrophysical objects.** As an example, the KMRI simulations assumed an electron/proton plasma with equal initial temperatures. Yet electrons and different ion species are expected to be heated differently, as often observed in the solar wind and in planetary magnetospheres. The value of T_e/T_i plays an important role in several theories of black-hole accretion [99]. The use of accurate distribution functions and anisotropies in simulations of KMRI can also be important to interpret the radiation emitted by accretion disks, such as the one around the supermassive black hole Sgr A, from the radio to the gamma-ray ranges. Over-simplified assumptions in the simulations, e.g., assuming Maxwellian and isothermal electrons, can make comparison with observations difficult since electrons dominate the emission.

As an example, the KMRI simulations assumed an electron/proton plasma with equal initial temperatures. Yet electrons and different ion species are expected to be heated differently, as often observed in the solar wind and in planetary magnetospheres. The value of T_e/T_i plays an important role in several theories of black-hole accretion [99]. The use of accurate distribution functions and anisotropies in simulations of KMRI can also be important to interpret the radiation emitted by accretion disks, such as the one around the supermassive black hole Sgr A, from the radio to the gamma-ray ranges. Over-simplified assumptions in the simulations, e.g., assuming Maxwellian and isothermal electrons, can make comparison with observations difficult since electrons dominate the emission.

2.2.2 Localized dissipation

It is also possible that the plasma energization occurs within highly localized structures generated by the turbulence, rather than occurring throughout the whole volume. These are small kinetic scale structures, at scales comparable to the particle gyroradii, and include current sheets, magnetic islands, isolated flux tubes and small-scale vortices [100–102]. Different types of particle energization are associated with these structures. Turbulent structure generation and localized dissipation are closely related to the phenomenon of intermittency, the non-uniform distribution of energy within a turbulent medium. Figure 6 shows the intermittent acceleration of energetic electrons in a shear-driven turbulence simulation.

Intermittency

The focussing of turbulent fluctuation energy and dissipation into particular regions is known as intermittency, and is important for determining how turbulent heating operates. However, it is not well understood, especially at kinetic scales. Previous studies, based on field fluctuations, have found differing degrees of intermittency in the solar wind kinetic range [70,103,104], and significant intermittency was found in magnetopause Kelvin-Helmholtz kinetic turbulence [105]. Numerical simulations (e.g., Figure 8) generally show kinetic scale turbulence to be quite intermittent [23,37,106] and scaling models have been developed to incorporate this [37]. The high resolution field and particle (**R1**, **R2**, **R6**, **R7**, **R8**) instrumentation on THOR will allow the intermittency of the dissipation itself to be probed at kinetic scales to reveal how it is distributed, how this corresponds to the intermittent turbulent structures, and which models provide the best description. Previous work, based on dissipation proxies, e.g., localized field-particle energy transfer ($\mathbf{E} \cdot \mathbf{j}$) [22,107], temperature enhancements [107,108] and field fluctuations [109,110] has shown high degree of intermittency. These measurements, however, were not adequate to quantitatively probe the dissipation, which requires more comprehensive high-resolution instruments and diagnostic techniques. THOR will provide long periods of high resolution data in different plasma conditions (**R10**) to resolve the nature of intermittent turbulence and dissipation at kinetic scales.

Current sheets

It is thought that plasma turbulence can generate current sheets at small scales [2,111] and it has been proposed that many of these undergo magnetic reconnection (see Figure 14) [26,86,101,112,113] as part of the dissipation process [114,115]. Plasma heating and particle acceleration at scales comparable to the kinetic scales of reconnecting current sheets have been suggested from [29,116–118]. Turbulent reconnection events have been reported in the magnetosheath [22,107], in the pristine solar wind [119–121] and at coronal mass ejections [122]. Despite some observations of these structures, however, we do not have a clear understanding of the role they play in turbulent heating and acceleration.

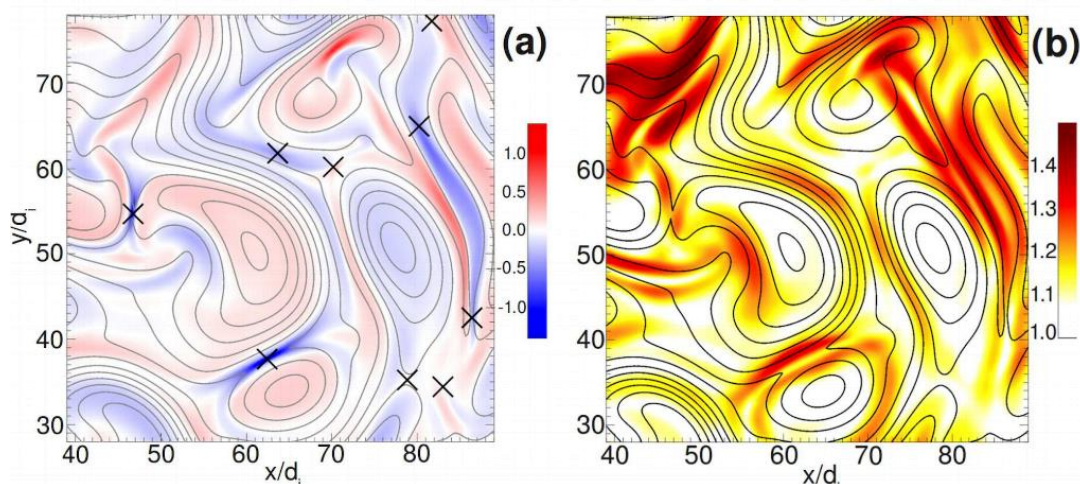


Figure 14: Generation of small-scale reconnection current sheets in turbulence. (a) Shaded contours of current density and magnetic potential (isolines) in a turbulence simulation; possible reconnection sites are indicated by crosses. (b) Shaded contour of the ion temperature anisotropy together with magnetic field lines (black). Deformations of the particle velocity distributions are concentrated around coherent structures that are located near the peaks of current density. THOR measurements will allow resolving thin current sheets and small-scale reconnection down to electron scales.

These current sheets can energize the plasma particles in different ways. For example, at sites of magnetic reconnection, parallel electric fields can lead to electron heating [123] and ions can be heated by pickup processes as they enter the exhaust regions [124]. It has also been proposed [125] that intense current structures can lead to double layers, which can accelerate particles or generate electrostatic waves leading to eventual dissipation. Figure 15 shows recent measurements of an ion-scale current sheet in the magnetosheath observed by MMS, which has the highest temporal resolution currently available. The electron measurements have sufficient cadence to resolve heating in the parallel direction at current sheet edges. The ion measurements show a drop in parallel temperature in the centre of the current sheet, suggesting ion parallel cooling, but ion composition is not resolved at ion scales. The cadence of the electron measurements onboard MMS is not sufficient to resolve electron-scale current sheets in the fast streaming magnetosheath and the pristine solar wind. The same field-particle correlation techniques described in Section 6.5 can also be applied to current sheets to determine the energization processes occurring within them. This will allow the role of current sheet structures in turbulent heating and acceleration to be determined.

THOR will allow the role of current sheets to be determined in several ways. Due to the spacecraft spin-axis orientation, a high quality electric field measurement (**R2**) will be obtained; this, together with high resolution measurements of particle moments (**R6**) will enable energy transfer measures such as $\mathbf{E} \cdot \mathbf{j}$ to be calculated at the site of plasma structures. The higher time resolution of the particle moments (**R6**) will also allow quantitative measures of local heating at sub-ion and sub-electron scale structures. The high velocity space resolution (**R7**, **R8**) will also allow the nature and amount of heating to be determined within these structures for the first time, by resolving non-Maxwellian features of particle distribution functions associated with energization.

Shocklets and vortices

Important intermittent dissipation and acceleration at kinetic scales can also occur in other structures, such as shock-like structures (often referred to as shocklets) and vortex-like structures via non-linear processes. One example, where shocklet formation at kinetic scales is of key importance for plasma heating and particle acceleration, is the quasi-parallel shock [32,127,128], see Figure 16. Understanding the intricate feedback of ion dynamics within shocklets on the resulting variability in the shock structure is required to find a definitive solution to the injection problem, the formation of a seed population of suprathermal ions on which Fermi acceleration can act to accelerate particles to very high energies [129]. Another example, vortex formation, is very pronounced in plasma environments exhibiting a velocity shear. Numerical simulations show that, as shear-flow instabilities set in, turbulent vortex

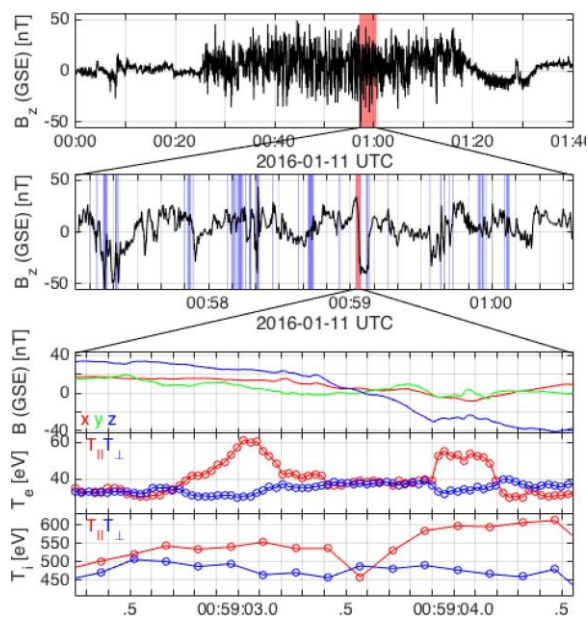


Figure 15: MMS spacecraft measurements of magnetic field, electron and ion temperatures in an ion-scale current sheet within magnetosheath turbulence. The ion data suggests parallel cooling in the current sheet but composition cannot be measured at ion scales. THOR will measure both protons and alphas within such current sheets, as well as resolve electron-scale current sheets in the magnetosheath and pristine solar wind.

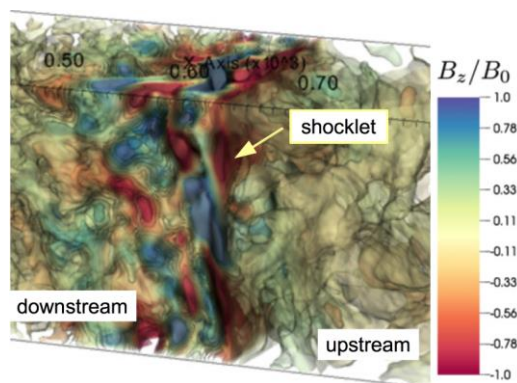


Figure 16: Three-dimensional particle-in-cell simulation showing the complex behaviour of quasi-parallel shock turbulence showing the presence of shocklets at kinetic scales [126]. THOR will resolve such structures and the particle energization within them.

formation and secondary instabilities develop down to the smallest kinetic scales [23], see Figure 6. Such simulations show that plasma heating and particle acceleration occur at those scales [23,130]. A few in-situ observations of vortex structures exist [131–133], however, plasma measurement resolution has not been sufficient to study plasma heating and particle acceleration within those vortices at kinetic scales. THOR high resolution measurements of both fields and particles will allow the role of shocklets and vortices to be understood for dissipation at kinetic scales. Accurate determination of the phase speed of structures (**R4**) will allow proper identification of shocklets (fast, slow) and vortices. High accuracy THOR electric field measurements will enable the shock electric fields which energize particles to be determined (**R2**) together with high resolution measurements of particle distribution functions and moments (**R6, R7, R8**) both in thermal and suprathermal ranges. Discrimination of ion species at high resolution (**R5, R7**) will allow to understand differential energization between protons and heavier ions.

2.3 Science question Q2: how is the dissipated energy partitioned?

A key issue for collisionless plasma turbulence is energy partition among particle species and among energy ranges. Despite its importance, experimental measurements of how turbulent energy is partitioned in space plasmas is very scarce, in particular at kinetic scales. The partition of the energy dissipated by turbulence at kinetic scales is the second question that THOR will answer.

Assessing energy partition is of pivotal importance for understanding the behaviour of many astrophysical plasmas. As an example, equipartition between high-energy cosmic rays and thermal gas in clusters of galaxies is invoked to explain observations of non-thermal radiation in a wide range of wavelengths [135]. Remote observations in the solar corona suggest that the magnetic energy dissipated during flares into the acceleration of high-energy particles is higher than that going into plasma heating [136,137]. On the other hand, an important fraction of magnetic energy dissipated in the corona is expected to go into thermal plasma and account for coronal heating. Remote observations also indicate that the energy spectrum of cosmic rays is dominated by ions, 99% of which are protons and alpha particles. Assessing energy partition between energy ranges and species from *in situ* measurements is crucial to understand how Solar System plasma energization works and can help to understand the energization mechanisms lying behind the electromagnetic radiation measured from distant astrophysical objects during key phenomena.

Q2: How is the dissipated energy partitioned between heating and acceleration of electrons, protons and heavier ions?

Many signatures exist in the turbulent solar wind and shock regions indicating that plasma is continuously being energized. For example, solar wind observations of ion temperature over many astronomical units are not consistent with an adiabatic behaviour [134,138] indicating that solar wind plasma is being continuously locally heated, see Figure 17. Yet, solar wind electrons and protons show different temperatures, e.g., electrons are cooler than protons in the fast wind while hotter in the slow wind [139] suggesting that different heating mechanisms are at work for electrons and ions respectively. Furthermore, heavier ions (alpha particles in particular) seem to be preferentially heated with respect to protons, the temperature ratio being more than mass proportional [140].

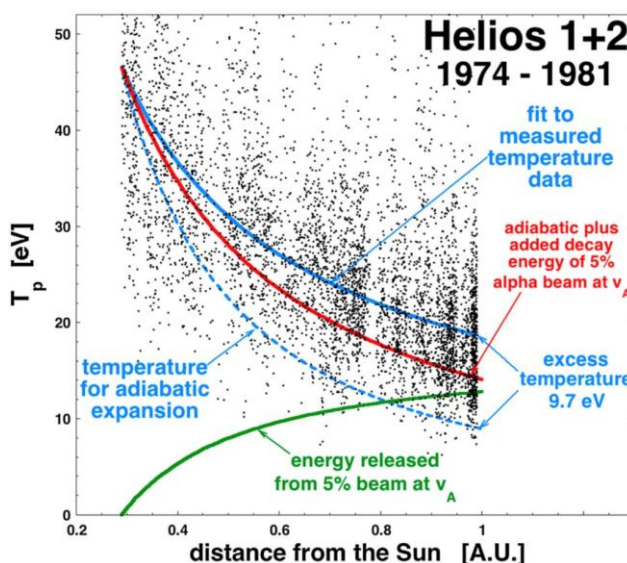


Figure 17: Evidence of local heating in fast solar wind. The proton temperature profile over distance from the Sun (black: measurements; blue curve: power law fit) is not consistent with the temperature expected from adiabatic expansion (dashed blue line). The proton temperature (red line) after including the decay of the alpha-proton relative drift (green line) indicates the importance of instabilities between protons and alphas. THOR will provide measurements of ion composition that are necessary to study such processes at kinetic scales [134].

Non-Maxwellian features of distribution functions such as beams and energetic tails are also found both in the solar wind and in planetary, interplanetary and termination shock regions [139,141–144], indicating that both heating and acceleration are at work. Most of these signatures have been provided by large-scale observations of turbulent fluctuations and particle distribution functions, while major turbulent dissipation is expected at kinetic scales. This is due to the fact that high-resolution coordinated field and particle measurements in solar wind and shock regions resolving kinetic scales are at present very scarce. THOR will provide such measurements and allow the energy partition problem in turbulent plasma dissipation to be solved.

2.3.1 Partition among species

There are very few *in situ* measurements at kinetic scales in the solar wind and shock regions providing information on how energy is distributed among plasma species for different turbulent dissipation mechanisms. Available observations are basically based on magnetic and electric field measurements in combination with expectations from theory and simulations [21,25,120] while observations of particle distributions are scarce [107]. Most of the information comes from numerical simulations, e.g., gyrokinetic [42], hybrid [145], particle-in-cell [24,146,147] and Vlasov codes [148,149]. Yet such simulations are only able to reproduce specific scales and particle species at a time, while understanding dissipation at kinetic scales requires resolving simultaneously electrons, protons and heavy ions each at their own kinetic scales. At present, simulations are not capable of reproducing such physics in detail. However, it is expected that the development in the next decade will allow simulations to open new pathways to investigate turbulence and dissipation, thus providing invaluable tools for studying the observations provided by THOR.

Important electron and ion heating and acceleration at kinetic scales can occur through damping of a number of wave modes such as kinetic Alfvén, fast and slow magnetosonic, whistler and electrostatic waves [31,139], as discussed in Section 1. How the dissipated energy is distributed between electrons and different species of ions depends on the specific dissipation mechanisms as well as on plasma conditions such as the amplitude of turbulent fluctuations, plasma β , plasma composition, etc. Different mechanisms also produce different features in the distribution functions, e.g., parallel or perpendicular anisotropies with respect to the magnetic field, that can be used as evidence for a specific mechanism.

As an important example, kinetic Alfvén waves (KAWs) can be dissipated at proton scales either into proton heating (via Landau damping or

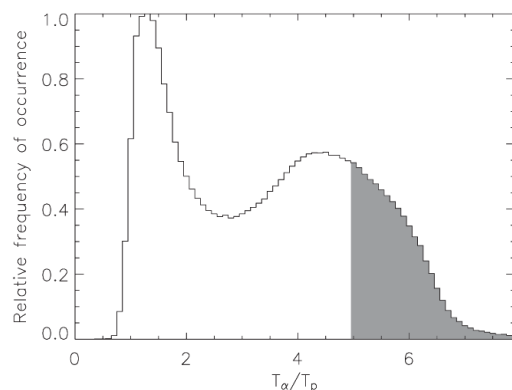


Figure 18: Observation of the relative occurrence of T_α/T_p in the solar wind by the Wind spacecraft, showing peaks near equal temperature ($T_\alpha/T_p=1$) and equal thermal speed ($T_\alpha/T_p=4$). 23% of the observations (highlighted in grey), have $T_\alpha/T_p > 5$ indicating anomalous heating. The observations were made by the Faraday Cup instrument with low temporal resolution. THOR high-resolution measurements will allow exploration of the ion kinetic scales that are required to understand preferential ion heating.

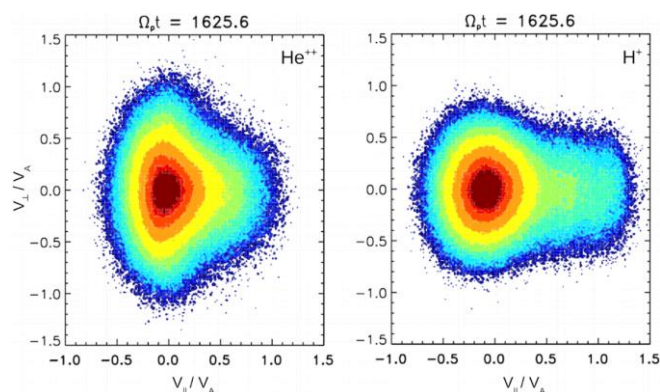


Figure 19: Snapshots of the ion velocity distributions of He^{++} ions and protons when the system was initialized with a broadband spectrum of Alfvén-cyclotron waves [151]. He^{++} ions are preferentially heated with respect to protons, which in turn develop a stronger suprathermal beam. THOR high-resolution measurements of mass-resolved distribution functions will allow the preferential ion heating mechanisms to be studied and understood.

stochastic heating) or into electron heating [25,150]. Proton Landau damping and stochastic heating would result in heating in the parallel and perpendicular directions respectively. On the other hand, solar wind observations seem to suggest that KAW turbulence is only slightly damped at proton scales and that most of energy is dissipated below proton scales [21]. Numerical simulations of dissipation of turbulent fluctuations at electron scales suggest that heating is directed mainly to electrons and that electrons are heated in parallel direction via electron Landau damping. Heated electrons are 20% hotter than the protons [24]. In order to study and understand thermal energy partition between protons and electrons resulting from dissipation of KAWs, high resolution particle measurements in typical thermal ranges of solar wind and magnetosheath are required. THOR will allow such studies by resolving moments (density, velocity, temperature and temperature anisotropy) and by measuring full 3D distribution functions in the thermal range of electrons at electron scales and of protons at sub-proton scales in the pristine solar wind, foreshock, shock and magnetosheath (**R6**, **R7**, **R10** and **R11** in Table 3). In particular, the high energy and angular resolution measurements of THOR particle distribution functions will be crucial to verify conditions for Landau damping and to identify particle anisotropies and narrow beams.

As another example, solar wind observations indicate that heavier ions (alpha particles in particular) are preferentially heated with respect to protons, the temperature ratio between the two species being more than mass proportional [140], as shown in Figure 18. Dissipation of KAWs via stochastic heating seems to have a greater efficiency for heavier ions, pointing out the privileged channel for alpha particle heating and energy dissipation in the solar wind [152].

Preferential turbulent heating and acceleration of alpha particles can also be produced by dissipation of cyclotron waves [151], see Figure 19. Such waves are also efficient to energize heavier ions such as oxygen ions and to produce highly complex velocity distribution functions and temperature anisotropies [153,154]. Wave damping also plays an important role for mass-dependent heating and acceleration of heavier ions in shock regions. An example is the observation of oxygen ions around quasi-parallel shocks. Such ions can be in many cases explained as escaping from the magnetosphere, yet it is not understood if they can also be related to local acceleration by quasi-parallel shock fluctuations [155]. Understanding the energy partition between different ion species due to dissipation of fluctuations such as KAWs or Alfvén-cyclotron waves requires high resolution measurements of mass-resolved ions. THOR will allow such studies by providing measurements of ion composition (**R5**) that will be able to resolve temperature anisotropy (**R6**) and non-Maxwellian features of distribution functions (**R7**) at kinetic scales in the pristine solar wind and magnetosheath (**R10**, **R11**).

Important heating and acceleration of electrons and ions is also expected within coherent structures such as reconnecting current sheets, magnetic islands, vortex-like structures, etc. As for other kinds of turbulent fluctuations, the energy partition between electrons and ions in such

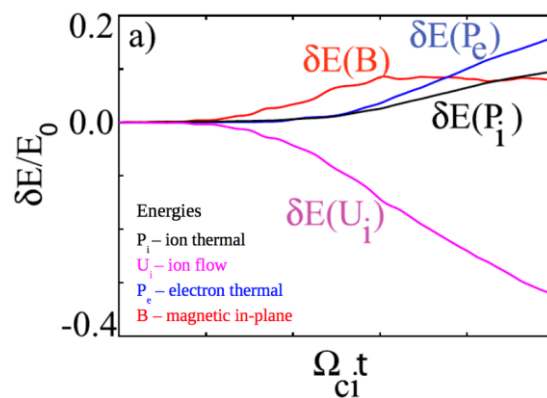


Figure 20: Turbulence simulation showing the time evolution of δE for the electron thermal energy, ion thermal energy, in-plane magnetic field energy, and ion flow energy. δE is defined to be the change in the energy for each component from its initial value [23]. THOR measurements of electromagnetic fields and particle moments will allow determination of the energy partition during coherent structure formation and interaction.

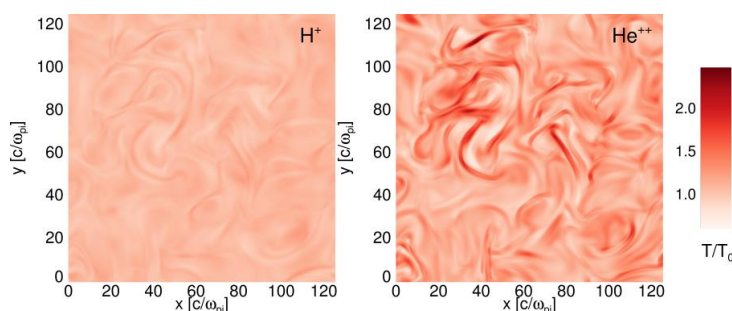


Figure 21: Contour plot of proton (left) and alpha particle (right) temperature normalized to the initial value in Vlasov turbulence [98,156]. Particle heating occurs in thin filaments with a typical width of a few ion inertial lengths; preferential heating of alphas with respect to protons is observed.

localized dissipation is not fully understood. Figure 20 shows the time history of the changes in the energy budget for a kinetic simulation of shear-flow turbulence where a large number of dissipating small-scale coherent structures is formed. About 30% of the initial energy in the flow has been converted into other forms, with about 25% of such energy going into ion heating and 50% into electron heating. The simulation also shows that electrons are mainly heated in the direction parallel to the magnetic field, consistent with the expected heating due to parallel electric fields generated in the reconnection process [23].

Pioneering *in situ* observations of such dissipation was provided by the Cluster spacecraft in ion-scale reconnecting current sheets [107]. Cluster observations could show evidence of electron heating [157] but the time resolution was not sufficient to resolve temperature anisotropies as well as to resolve ions. More recent MMS spacecraft measurements in similar ion-scale current sheets have allowed electron anisotropies to be resolved and have shown that electrons are mainly heated in parallel direction within ion-scale current sheets [158]. MMS observations can also resolve ions, see Figure 15, but are not able to distinguish ion species at kinetic scales. On the other hand, kinetic simulations strongly suggest that heating in ion-scale coherent structures is more efficient for alphas than for protons, see Figure 21 [98,156]. At present, no measurements of both protons and heavy ions are available with a cadence sufficient to resolve heating in ion-scale current sheets. Furthermore, no electron measurements are available to resolve electron heating in electron-scale coherent structures in the solar wind and magnetosheath. These measurements are required to assess energy partition between electrons, protons and heavier ions during localized dissipation at kinetic scales. THOR will allow such studies by providing high-resolution measurements of electrons, protons and alpha particles at their respective kinetic scales in the magnetosheath and pristine solar wind (**R10, R11**), in particular high-time resolution measurements of temperature anisotropies (**R6**).

2.3.2 Partition between heating and acceleration

Understanding energy dissipation at kinetic scales requires also assessing how energy is distributed between thermal and non-thermal components. Figure 22 shows typical components of particle distribution functions for collisionless plasmas. The thermal component is represented by a Maxwellian distribution; particle heating typically corresponds to an increase of the temperature of such a distribution. The suprathermal component refers to energies several times larger than the thermal energy while the energetic component to energies many times larger. Both suprathermal and energetic components are typically approximated by power-law distributions.

It is poorly understood from *in situ* measurements how the energy dissipated by turbulent fluctuations is distributed between these different energy ranges, and most of the knowledge currently comes from numerical simulations. Mechanisms of uniform dissipation such as linear Landau and cyclotron damping and stochastic heating produce heating and suprathermal acceleration (e.g., beams at suprathermal energies) [139] but in some cases they can also lead to the formation of power-law tails of highly energetic particles [159,160].

Localized dissipation within coherent structures at kinetic scales, such as thin reconnecting current sheets and small-scale magnetic islands, seem on the other hand to be efficient to both heat plasma and create energetic particles [116,117,162–164]. Thermal, suprathermal and energetic particles can be found at different spatial locations within the turbulence, suggesting different heating and acceleration mechanisms at work [117], as shown in Figure 22. Energetic particles typically constitute a small fraction

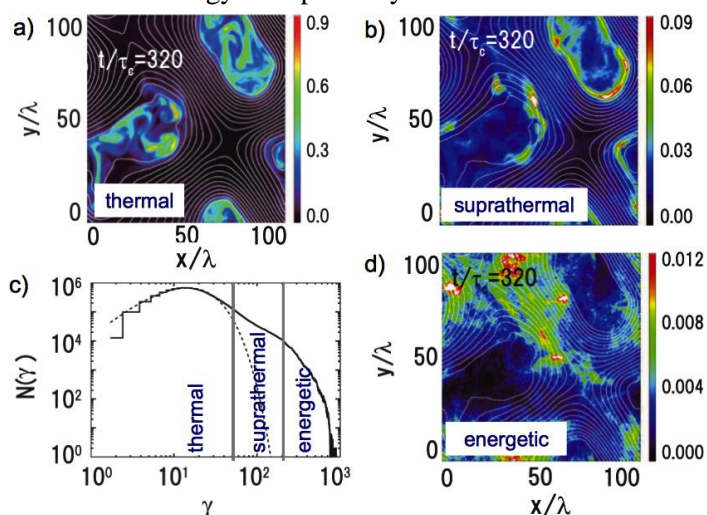


Figure 22: Particle-in-cell simulations of thermal, suprathermal and energetic particle acceleration in turbulent plasma [117]. Plasma heating and particle acceleration occurs at kinetic scales but at different locations. THOR high-resolution measurements of ions, thermal and non-thermal electrons will allow the partition of dissipated energy between the components and its spatial distribution to be assessed.

of the energy partition (a few %) during dissipation within coherent structures [23], although in some cases the total energy density of the energetic particles can be comparable with the remaining magnetic energy suggesting that, at least in some cases, equipartition between energetic particles and magnetic field is energetically accessible [163]. In order to study and understand energy partition between thermal, suprathermal and energetic components in kinetic turbulence, simultaneous high resolution particle measurements in different energy ranges are required. THOR will allow such studies by measuring full 3D distribution functions of electrons, protons and heavy ions in the thermal (**R5**, **R7**), suprathermal (**R8**) and energetic (**R9**) energy ranges at their corresponding kinetic scales both in the pristine solar wind and in the magnetosheath (**R10**, **R11**).

Partition between the thermal and non-thermal ranges is also very important at shocks, where kinetic turbulence plays a key role. An important example is diffusive shock acceleration (DSA) at quasi-parallel shock [165,166] such as the Earth's bow shock. Such a mechanism is responsible for the formation of power-law spectra of energetic particles; however thermal particles must be pre-accelerated to suprathermal energies first for the DSA acceleration to take place. How this pre-acceleration, the so-called injection, occurs is far from being understood. Numerical simulations strongly suggest that dissipation of electromagnetic fluctuations at kinetic scales is responsible for it [166], although how much turbulent fluctuations dissipate into heating or suprathermal acceleration is not clear. Another important example is the acceleration of energetic particles at strong interplanetary shocks. Figure 23 shows STEREO spacecraft measurements of pressure from different components (magnetic, thermal and energetic) around an interplanetary shock [161]. The region just upstream of the shock is dominated by energetic particle pressure, indicating the importance of resolving kinetic scales for both thermal and energetic components in order to assess their relative role. In order to understand energy partition between thermal, suprathermal and energetic components at turbulent shocks, high resolution particle observations are needed in shock regions. THOR will allow such studies by measuring full 3D distribution functions of electrons, protons and heavy ions in different energy ranges (**R5**, **R7**, **R8** and **R9**) both at interplanetary shocks and at the bow shock (**R10**). In particular, the high energy and angular resolution will allow the suprathermal proton and alpha beams (**R8**) and energetic tails (**R9**) to be resolved.

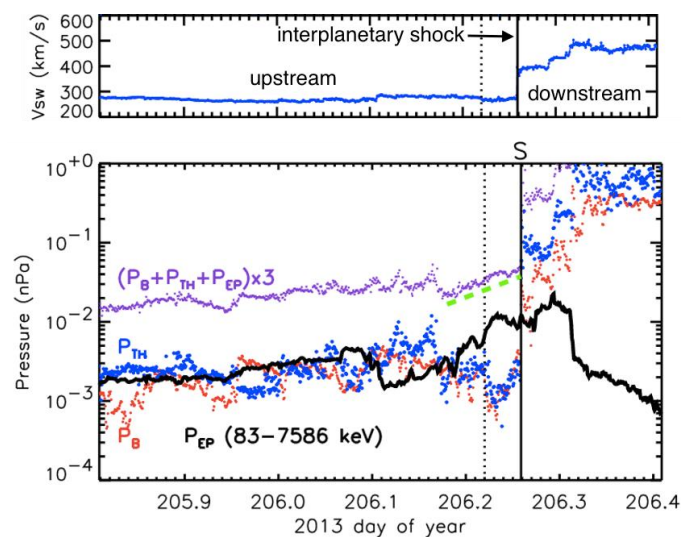
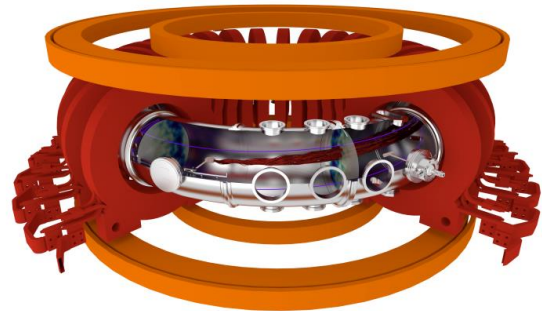


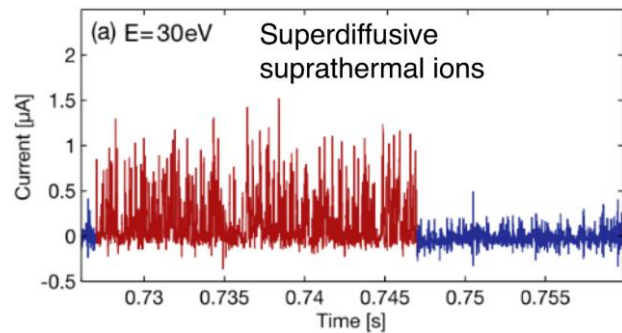
Figure 23: Solar wind speed and different pressure components (due to the magnetic field in red, thermal in blue and energetic particles in black) during the passage of a strong interplanetary shock observed by STEREO [161]. Different pressures dominate in different regions with energetic particles dominating upstream of the shock. THOR high-resolution measurements of particles at kinetic scales corresponding to their energy will allow the partition of energy at turbulent shocks to be assessed.

Laboratory plasmas

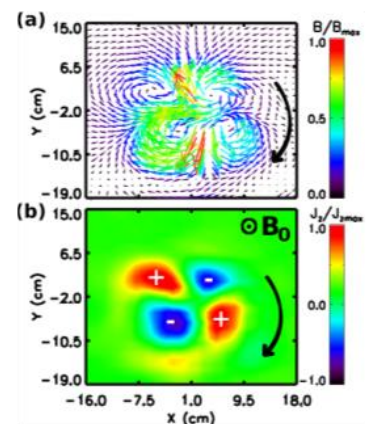
Understanding basic plasma processes requires the combination of theory and experiments in both laboratory and natural plasmas. Synergy between *in situ* spacecraft observations and laboratory measurements is of utmost importance since, while laboratory setups provide full control over the experimental conditions allowing for highly repeatable plasma scenarios, plasma diagnostics are still limited, especially for accessing plasma kinetic scales. As an example, full 3D particle distribution functions cannot currently be measured in laboratory experiments. Therefore, kinetic-scale measurements, such as those that will be performed by THOR, may strongly benefit the plasma laboratory science community. One example is the TORPEX basic plasma physics device in Europe, shown in the figure to the right (http://spc.epfl.ch/research_basic_plasmas_torpeX), which is devoted to the investigation of turbulence and its interaction with different plasma species [167,168].



A key question for plasmas is how ion transport is affected by small-scale turbulence, in particular for suprathermal ions with energies significantly exceeding the temperature of the background plasma [169–171]. Such ions are ubiquitous in fusion devices and astrophysical environments and their dynamics is largely unexplored. The figure shows the temporal evolution of the suprathermal ion current in the TORPEX plasma as the suprathermal ion source is turned on (red) and off (blue) periodically [172]. The interaction of plasma turbulence with ions is energy dependent. Lower energy suprathermal ions show superdiffusive transport across the field lines, while higher energy ions show sub-diffusive transport. In the superdiffusive case, the suprathermal ion signals exhibit a high level of intermittency suggesting that this is due to their higher sensitivity to intermittent turbulent structures. A deeper understanding would require measurements at the kinetic scales, which are not of easy access in laboratory plasmas. **THOR high resolution measurements of mass-resolved ion distribution functions and electromagnetic fields will help to understand the interaction between intermittent structures, also observed in space, and ion transport.**



Another example that provides a platform for studying processes relevant to THOR, such as waves, turbulence, dissipation, and particle energization, is the Basic Plasma Science Facility in the USA (<http://plasma.physics.ucla.edu/>). In particular, recent experiments using the LArge Plasma Device (LAPD) shown in the figure are being devoted to investigate problems such as excitation of whistler waves by energetic electrons [173], laser-driven magnetized collisionless shocks [174] and Alfvén wave parametric instabilities [175]. The figure shows results of a recent experiment in a low β plasma that is relevant for THOR science. Here an energetic ion beam excites Alfvén waves via the Doppler-shifted ion-cyclotron resonance [176]. In turn, **THOR high resolution measurements of ion anisotropies for different species will help to understand the generation of turbulence through ion-driven instabilities in laboratory devices.**



Here an energetic ion beam excites Alfvén waves via the Doppler-shifted ion-cyclotron resonance [176]. In turn, **THOR high resolution measurements of ion anisotropies for different species will help to understand the generation of turbulence through ion-driven instabilities in laboratory devices.**

2.4 Science question Q3: how does dissipation operate in different regimes of turbulence?

The third science question that THOR will answer is how dissipation operates at kinetic scales in different turbulent regimes. This will allow an understanding of which turbulent fluctuations and dissipation mechanisms are dominant under specific plasma conditions and how plasma energization works in Solar System plasmas. The near-Earth space provides an excellent laboratory to test this, thanks to the different regions sampled by THOR along its orbit, see Figure 2. These regions are characterized by different values of typical plasma parameters, e.g., amplitude of turbulent

Q3: How does dissipation operate in different regimes of turbulence?

fluctuations, plasma β , plasma composition, homogeneity, collisionality, Mach number, system size, etc. Key regions are the pristine fast and slow solar wind, interaction regions between flows, shocks and associated sheath regions. Such near-Earth regions are representative of a number of astrophysical turbulent environments, so that the identification of dominant dissipation mechanisms by THOR would help understanding dissipation in distant objects where *in situ* measurements are not available.

2.4.1 The pristine solar wind

The pristine solar wind is the region upstream of the Earth’s bow shock and foreshock, which has not yet encountered any effects of the Earth’s magnetosphere. It represents a plasma which is well evolved during its journey from the Sun, and contains a well-developed turbulent cascade. It provides an opportunity to study turbulent heating and acceleration in its purest form, without the additional effects generated by the bow shock, such as reflected particles, unstable distributions, boundaries, wave bursts, etc. The plasma here is also in a particular parameter regime, which, together with the other regimes nearer the Earth, can be used to study the variability of turbulent heating and acceleration.

The pristine solar wind is variable in many ways, and this can be used to probe the different heating and acceleration mechanisms. The two main types of solar wind are fast and slow. These have different speeds, but originate from different regions of the Sun, so vary significantly in their physical properties. It is possible that the turbulence in fast and slow wind may be driven in different ways. This can be seen from the magnetic spectrum at large scales: the fast wind contains an f^{-1} spectrum of Alfvén waves, but the slow wind contains an $f^{-5/3}$ inertial range to very large scales (Figure 24). THOR will be able to determine how heating and acceleration vary under these different large-scale plasma conditions.

There is also variability in the relative turbulent energy fluxes propagating in either direction along the magnetic field, a property known as imbalance. At large scales, the solar wind can have balanced fluxes or can be very imbalanced, usually with a higher flux in the anti-sunward direction [8]. It has been found that the turbulence properties can depend on the degree of imbalance [177–179]. However, the imbalance in the kinetic range and its effect on turbulent heating and acceleration has not been well-measured due to the limited resolution and quality of previous measurements. The increased sensitivity of the electromagnetic measurements on THOR will allow turbulent heating and acceleration in different regimes of imbalance to be understood. Similarly, the solar wind has a varying degree of particle collisionality, which affects various features of the particle distributions [140,180,181]. THOR will also

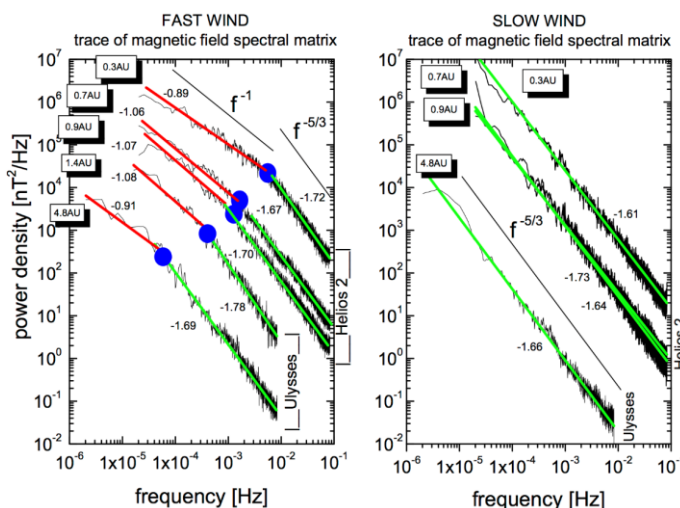


Figure 24: Difference between fast and slow pristine solar wind at large scales at different distances from the Sun [8]. The spectrum of magnetic fluctuations in the slow wind contains a long $f^{-5/3}$ cascade but the fast wind has a f^{-1} injection range at large scales. THOR will determine how heating and acceleration at kinetic scales depend on different large-scale turbulent conditions.

be able to test how turbulent heating depends on the degree of collisionality of the plasma, allowing the understanding to be applied to a wide range of astrophysical plasmas.

The plasma beta β (ratio of thermal and magnetic pressures) is an important parameter determining much of the plasma behaviour, and is expected to affect the nature of the heating. In the solar wind, the beta is on average around 1, but there is significant variability allowing the dependence to be studied. For example, it has been proposed that stochastic heating can be important in low beta plasmas ($\beta \ll 1$), where the efficiency of the heating is greater for a given turbulent spectrum [25]. Landau and transit-time damping, however, are expected to be more efficient at higher beta, since there are then more particles to satisfy the wave-particle resonance condition. The ability of current sheets to undergo reconnection (and therefore heat via this mechanism) also depends on the beta in addition to the magnetic shear angle [182]. The pristine solar wind will allow turbulent heating in different β regimes to be studied.

In the last decade, small-scale reconnection events have been found to occur in the solar wind [119]. It is debated, however, how common these are, and whether they are able to dissipate a significant fraction of the turbulent energy [121,183]. This understanding is limited by the time resolution of solar wind particle instruments, which limit the ability to detect such events, and also by the lack of quantitative measures of dissipation. THOR will address this with its high time resolution particle measurements and the ability to probe the nature of the turbulent heating within the reconnection events at high resolution.

The pristine solar wind is important for understanding energy dissipation in other distant turbulent environments where *in situ* measurements are not available, e.g., weakly collisional plasmas such as galaxy clusters, accretion disks and the interstellar medium [31,185–187]. The interstellar medium has a plasma composition similar to that of solar wind (mainly hydrogen and helium) [188] and is suggested to be turbulent by remote observations [184]. Turbulent dissipation occurs there, with intermittent heating in vortex-like structures as one key mechanism invoked for the star formation process [189]. Turbulent dissipation is also important for the amplification of magnetic fields and for the re-acceleration and diffusion of cosmic rays. Remote observations in the interstellar medium show a typical Kolmogorov-like spectrum in the inertial range as in the solar wind, see Figure 25, yet no remote measurements can unambiguously resolve the kinetic scales, although some measurements seem to suggest a -2 spectral exponent below the ion gyroscale [190]. The resolution of such remote measurements is expected to improve thanks to new observatories, e.g., LOFAR and SKA. THOR *in situ* measurements in the pristine solar wind at kinetic scales will be very important to support and complement such new remote measurements.

THOR will repeatedly sample the pristine solar wind (R10), performing high sensitivity and accuracy measurements of both the electromagnetic fields and plasma particles (R1...R7). This will allow the connection between the turbulent fluctuations and plasma energization to be understood in this plasma regime.

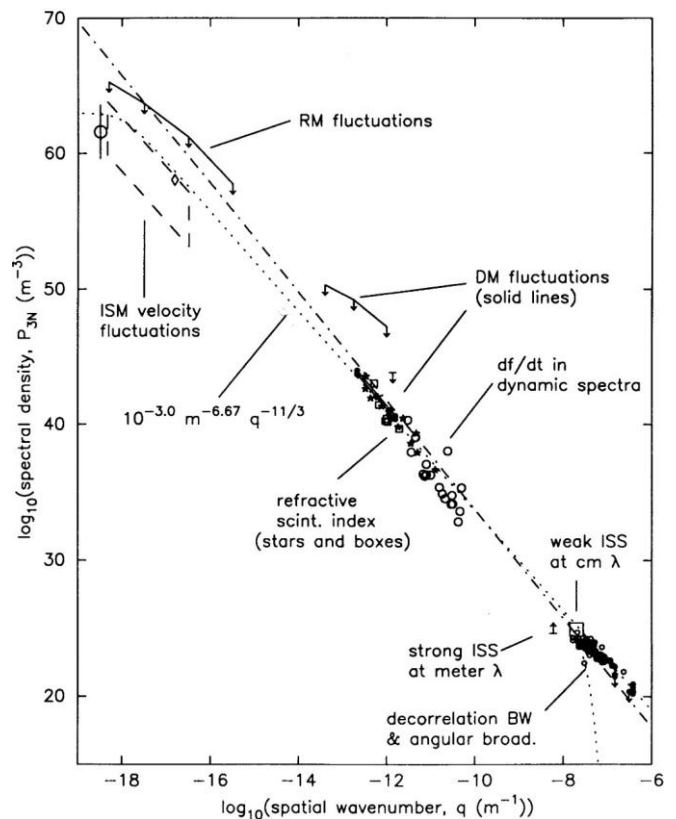


Figure 25: Inferred electron density power spectrum in the interstellar medium, suggesting that a turbulent cascade is operating at fluid scales [184]. THOR *in situ* measurements in the kinetic range will help understand how dissipation operates at small scales in the interstellar medium since remote measurements cannot access kinetic scales.

2.4.2 Interaction regions between flows

Interaction regions between flows are regions of strong turbulence in astrophysical plasmas and are associated with important plasma transfer, mixing, and energization. One example of such flow interaction regions is shear-flow boundaries, where the Kelvin-Helmholtz (KH) instability develops. This large scale instability can drive turbulence at small scales and has been observed *in situ* within planetary magnetospheres [131,192,193] and at the heliopause [194]. The KH instability is also expected to occur in the pristine solar wind due to the interaction of strongly twisted magnetic flux tubes that originate in the solar corona and get carried away by the solar wind [195,196]. Energy dissipation associated with Kelvin-Helmholtz turbulence plays an important role in plasma heating and particle acceleration in the solar wind, as well as in the interaction between the Sun and the planets, so-called space weather. Other examples of flow interaction regions are the boundaries between fast and slow wind streams, known as corotating interaction regions (CIRs), where turbulent fluctuations can be important for several energization mechanisms, e.g., scattering of energetic particles [87]. Recent results, on the other hand, indicate that typical signatures of large-scale turbulence, such as spectral slopes and entropy changes, are not evident within CIRs suggesting that driving of turbulence by shear could be less important than expected [197]. More observations of CIRs, particularly at kinetic scales, are needed to clarify this issue and assess the importance of turbulence and associated energy dissipation within CIRs.

Recent large-scale kinetic simulations of shear-flow turbulence [23,130] suggest that localized dissipation in small-scale current sheets and magnetic islands may be dominant with respect to dissipation by wave damping. The major electron heating mechanism is parallel heating by the parallel electric field produced by small-scale reconnection events. Thin current sheets at ion scales have been observed around KH vortices [198]. Yet, the lack of high temporal and energy resolution particle measurements means it is currently not possible to measure the expected particle anisotropies. It is not yet established from an observational point of view if localized dissipation within coherent structures is indeed the dominant dissipation mechanisms within flow interaction regions and more detailed measurements are needed to solve this problem (**R6**, **R7**, **R8**). Simulations also indicate that the properties of shear-flow turbulence at kinetic scales can be different between 2D and 3D turbulence. Accurate measurements of turbulence anisotropies at kinetic scales for the case of shear-flow turbulence are needed to understand how dissipation depends on the properties of such turbulence (**R3**, **R6**). THOR will explore plasma interaction regions both at interplanetary boundaries, such as CIRs, and at the magnetopause boundary between the solar wind and the Earth's magnetosphere (**R10**) and will allow the energy dissipation within such regions to be understood.

Observations of interaction regions in near-Earth space can be important to understand energy dissipation mechanisms in distant environments. One such example is energy dissipation in the solar corona in the presence of shear flows. KH vortices have been observed through remote measurements in the solar corona at the surface of a fast coronal mass ejection [191,199], see Figure 26, but no assessment of energy dissipation is possible from such measurements. 3D simulations of the incompressible MHD equations reveal that the growth rate of the KH instability on the boundary of erupting CMEs should be strongly attenuated by turbulence [200]. Such an energy dissipation scenario is also important for other astrophysical environments where shear flows are expected, such as astrophysical jets and accretion disks. In accretion disks, the large-scale magnetorotational instability [91] is thought to generate MHD turbulence that is eventually dissipated at kinetic scales,

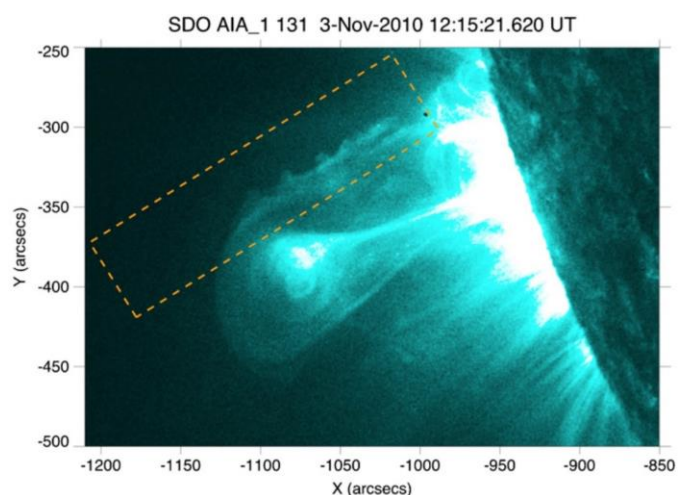


Figure 26: Evidence of Kelvin-Helmholtz turbulence close to the Sun [191]. The image from the AIA instrument onboard SDO spacecraft shows a fast coronal mass ejection erupting from the Sun and the formation of Kelvin-Helmholtz waves. THOR will observe *in situ* the microphysics of Kelvin-Helmholtz turbulence in interplanetary space at high resolution and help understand the dissipation and energization processes at small scales close to the Sun.

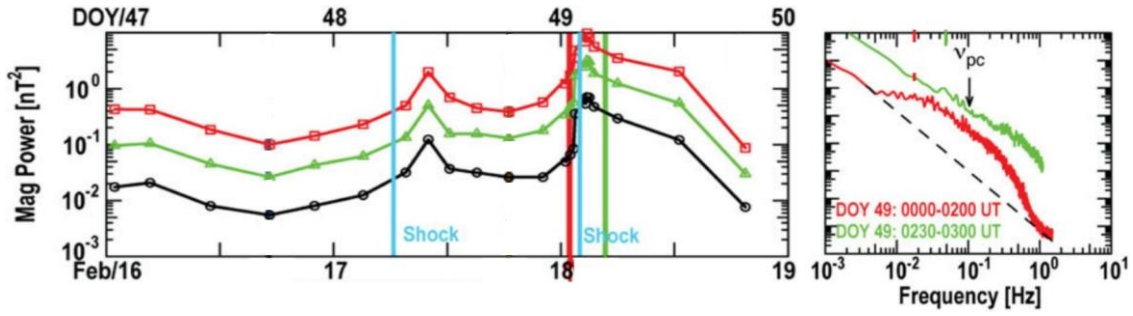


Figure 27: Turbulence spectra for two consecutive interplanetary shocks shown as a function of time (left panel) and frequency (right panel). The spectrum just upstream of the second shock (red curve in the right panel) is modified by instabilities driven by suprathermal ions [202]. THOR accurate measurements of magnetic field fluctuations and mass-resolved ion distribution functions at interplanetary shocks will allow an understanding of how turbulence is modified by instabilities.

producing plasma heating and particle acceleration in the disk. Remote measurements of the radiation coming from such distant objects are even less detailed than in the solar corona, and the exact energization mechanisms are unknown.

2.4.3 Shocks and associated sheath regions

Shocks are very important regions of particle heating and acceleration in many astrophysical plasmas and are sources of strong turbulence [201]. The interplay between shocks and turbulence is very complex and it is crucial to study and understand it since turbulent shocks are sites of major energy dissipation. Also, heated and accelerated particles produced at shocks generate waves that can modify the properties of the background turbulence, as shown in Figure 27 where the spectrum of magnetic fluctuations upstream of an interplanetary shock is strongly modified in the inertial range by wave generated by resonance of suprathermal ions [202].

Three major regions are associated to shocks and are important for energy dissipation: the upstream region (foreshock), the shock itself and the downstream region of shocked plasma (sheath region). Turbulence in all these regions strongly depends on the large-scale properties of the shock, such as the angle between the upstream magnetic field and the normal to the shock surface θ_{Bn} , the system size and the Mach number. Figure 28 shows a large-scale kinetic simulation of the terrestrial bow shock. This shock is the most studied due to the availability of many *in situ* observations, such as those by Cluster and more recently by MMS, which provide important information on kinetic physics. Yet a deeper understanding of energy dissipation and plasma energization mechanisms related to shock turbulence is currently not possible due to the lack of high-resolution measurements of electron and mass-resolved ions that are able to resolve at the same time kinetic scales in the incoming pristine solar wind and in the foreshock, shock and magnetosheath regions.

Quasi-parallel shocks

The quasi-parallel shock, $\theta_{Bn} < 45^\circ$, is the shock region where the strongest turbulence is observed, as indicated by Figure 28, top-

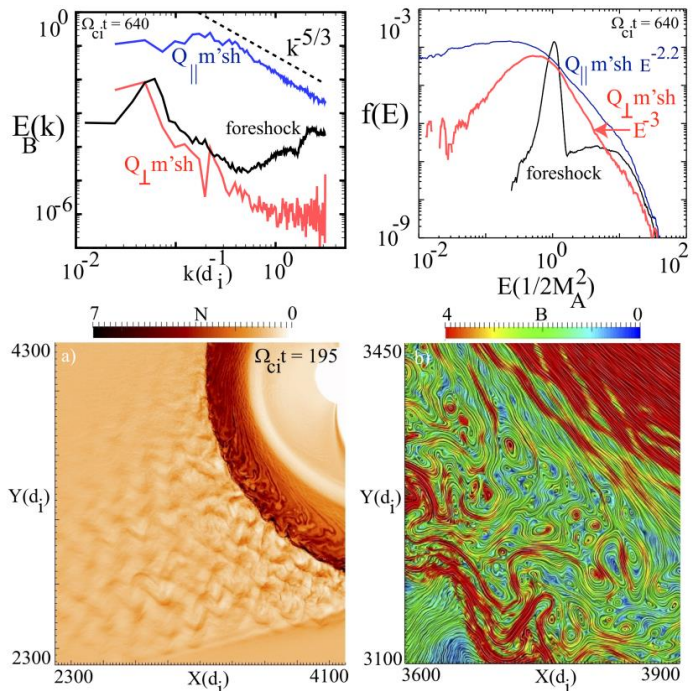


Figure 28: Large-scale particle-in-cell numerical simulation of the terrestrial bow shock [203]. Top, left: spectra of magnetic fluctuations. Top, right: proton distribution functions. Bottom, left: map of plasma density. Bottom, right: map of magnetic field.

left panel where amplitude of magnetic fluctuations is shown. Strong energy dissipation and particle energization due to turbulence is expected there.

In the foreshock of quasi-parallel shocks, an important source of turbulence is represented by low-frequency waves generated by reflected ions [126,142,203]. Earlier observations indicated that the basic wave generation mechanism is related to the cyclotron resonance of such ions with the waves themselves, yet many important details of the wave and ion beam generation processes remain unexplained [142,204]. Observations in the quasi-parallel foreshock show high amplitude fluctuations having $|\delta B|/B \approx 1$, often referred to as SLAMS [127,205], and other kinds of coherent structures such as shock-like kinetic structures (shocklets), vortices and magnetic islands and non-gyrotropic particle distributions, most likely involving specular reflection of ions at the shock and/or nonlinear trapping of ions in the wave fields. Understanding the generation mechanisms of these waves and coherent structures and their interaction with different ion species requires accurate high resolution measurements electromagnetic fields and of ion distribution functions at kinetic scales. Accurate THOR measurements of electric and magnetic fields at high cadence (**R1**, **R3**), as well as phase velocities of structures/waves (**R4**), will be combined with high temporal and angular resolution measurements of mass-resolved ion distributions in the thermal (**R7**) and suprathermal (**R8**) ranges at the Earth's bow shock (**R10**). This will allow a full characterisation of ion-scale turbulence in quasi-parallel foreshocks.

Large-amplitude foreshock disturbances affect not only ions but can also accelerate electrons to near-relativistic energies, as recently observed by the THEMIS spacecraft at the Earth's bow shock [206]. Figure 29 shows the evolution of the electron distribution functions as electrons interact with large-amplitude ion scale magnetic structures in the foreshock. The formation of an energetic tail of the distribution function up to relativistic energies is observed together with foreshock fluctuations suggesting that electron energization is produced by kinetic-scale turbulence in the foreshock. Yet understanding the energization mechanism of energetic electrons requires also measuring the thermal source electrons at their kinetic scales, as well as mass-resolved ions to understand the generation mechanism of turbulent fluctuations in the foreshock. None of these measurements are currently available in the foreshock region. THOR's high temporal resolution measurements of mass-resolved ion and electron distribution functions in the thermal (**R7**), suprathermal (**R8**) and energetic ranges up to relativistic energies (**R9**) in foreshocks (**R10**) will allow us understand in detail the generation of relativistic electrons around quasi-parallel shocks.

In the downstream sheath regions, the compression of the flow affects the spectrum of the turbulent fluctuations transmitted through the shock, e.g., SLAMS, by increasing the amplitude of the fluctuations perpendicular to the shock normal and compressing the wavenumber in the direction parallel to it [207,208]. This will lead to enhanced dissipation as wave energy from the inertial range is abruptly amplified and transported to the dissipation range, leading to additional heating of the downstream plasma. Other coherent structures, like current sheets, magnetic islands, vortices, etc., can be, on the other hand, generated locally as found in kinetic simulations [126,203], see Figure 28, bottom right panel. Turbulent fluctuations at kinetic scales in quasi-parallel shock regions lead to strong plasma heating and particle acceleration to high energies. One important example is small-scale reconnection occurring in thin current sheets in the terrestrial magnetosheath [22,107]. The efficiency of such small-scale reconnection seems to depend on shock boundary conditions and parameters such as θ_{Bn} and system size. Current sheets and magnetic islands are much

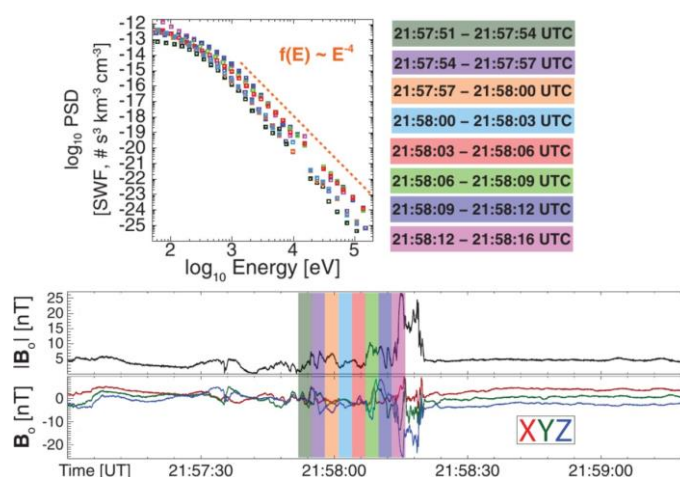


Figure 29: Acceleration of relativistic electrons by foreshock fluctuations observed by THEMIS at the Earth's bow shock. The distribution function of electrons up to relativistic energies is shown at different times corresponding to the spacecraft crossing large-amplitude foreshock fluctuations. THOR's high resolution measurements of thermal, suprathermal and energetic electrons at their kinetic scales will allow us to understand in detail the electron energization mechanisms in foreshock turbulence.

more frequent in the quasi-parallel magnetosheath than in the quasi-perpendicular [107,203]. However, the exact dependence of this dissipation mechanism on θ_{Bn} is not known. Furthermore, the number of current sheets and islands and their interactions is expected to increase with the size of the magnetosheath [203], suggesting that dissipation due to turbulent reconnection could be stronger in the larger sheath regions associated with interplanetary shocks. THOR's high temporal resolution measurements of moments and anisotropies of electrons at electron scales and mass-resolved ions at ion scales (**R6**), together with accurate and fast measurements of electric and magnetic fields (**R1**, **R3**), will allow us to establish the importance of small-scale reconnection for dissipation and heating in the magnetosheath depending on shock boundary conditions, both at the bow shock and at interplanetary shocks (**R10**).

Another important example where shock turbulence plays a key role is diffusive shock acceleration (DSA), which is one of the most important mechanisms invoked for particle acceleration in astrophysical plasmas and is efficient at quasi-parallel shocks [166]. This mechanism is the prime candidate to explain the acceleration of galactic cosmic rays in supernova remnants to energies of $\sim 10^{15}$ eV and beyond. In the DSA mechanism, particles are scattered in pitch angle by turbulent fluctuations so that they cross back and forth the shock and gain energy at each shock crossing [165]. As this process takes time, shocks driven by interplanetary coronal mass ejections, with propagation times of days from the Sun to the observer, offer the best possibility to study DSA *in situ* [e.g. 202]. However, thermal particles must attain a threshold energy through an "injection" mechanism in order to get efficiently accelerated by DSA. Despite this importance, the mechanism of particle injection is not fully understood. Kinetic scale turbulent fluctuations in shock regions, e.g., SLAMS or foreshock cavities, are important candidates for particle injection by reflecting and scattering ions. Whatever the mechanism, injection is likely to occur much more quickly than the DSA itself, and thus it can be studied well even in the Earth's bow shock, which has a limited size to accelerate particles via DSA to the highest energies. THOR's high energy and angular resolution measurements of both electron and mass-resolved ion distribution functions at kinetic scales in both thermal (**R7**) and suprathermal (**R8**) ranges, together with accurate measurements of electric and magnetic fields (**R3**), will allow us to study and understand the role of kinetic-scale turbulent fluctuations for particle injection at the Earth's bow shock and interplanetary shocks (**R10**).

Quasi-perpendicular shocks. The quasi-perpendicular shock, $\theta_{Bn} > 45^\circ$, is typically associated with a lower amplitude of turbulent fluctuations, as indicated by Figure 28, top left panel. Yet such fluctuations can play a significant role for particle energization at kinetic scales. Geometry and dispersion relations of downstream wave modes are important to determine the acceleration characteristics [160]. Field-aligned beams observed upstream of the quasi-perpendicular terrestrial bow shock have distributions showing high-energy tails that are produced by intermittent turbulence [209]. On the downstream side, different fluctuations (e.g., mirror modes) grow because of free energy in the anisotropic $T_\perp > T_\parallel$ ion distributions [210]. THOR's accurate measurements of anisotropies (**R3**) and phase velocities (**R4**) of kinetic fluctuations, both upstream and downstream of the bow shock and interplanetary shocks (**R10**), together with particle anisotropies at kinetic scales (**R6**), will allow us to understand kinetic-scale turbulence and particle energization around quasi-perpendicular shocks.

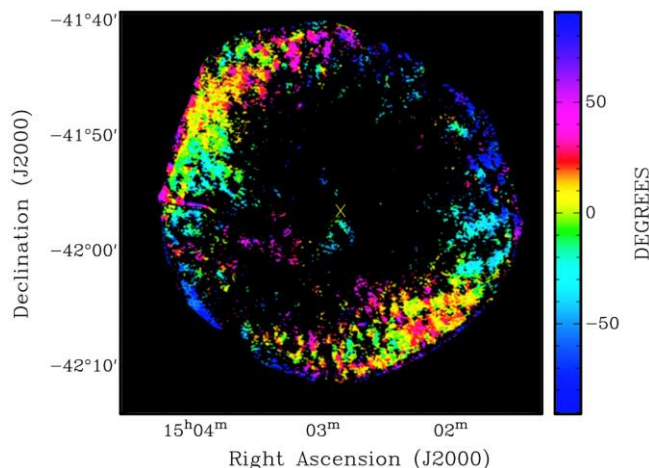


Figure 30: Evidence of strong turbulence and particle acceleration at quasi-parallel supernova remnant shock SN 1006. The magnetic field is radial in yellow regions (quasi-parallel) and perpendicular to radial direction in blue regions (quasi-perpendicular). The most efficient particle acceleration and generation of magnetic turbulence is attained at the quasi-parallel portion of the shock [14]. THOR measurements of both interplanetary shocks and bow shock will allow us to understand turbulence generation and particle acceleration under different Mach numbers and shock inclinations.

By making measurements of particle energization at both interplanetary shocks and at the bow shock with different parameters (Mach numbers, obliquity, size), THOR will identify properties that could be scaled to understand distant shocks such as coronal shocks, the solar-wind termination shock or astrophysical shocks.

One such astrophysical example is supernova remnant shocks that are site of major acceleration of galactic cosmic rays and are thought to be efficient for particle acceleration when the shock is quasi-parallel [14], as shown in Figure 30. *In situ* observations of strong particle acceleration and turbulence at quasi-parallel shock having relatively large Mach number (up to ~ 100) have been reported at Saturn's bow shock [212], however particle instrumentation was not sufficient to resolve the detailed processes responsible for the particle acceleration, see Figure 31. Higher resolution observations, e.g., by the Cluster spacecraft, have been reported for the case of the Earth's bow shock [32], which on the other hand has a much smaller size and lower Mach number (typically below 10) than some other planetary shocks and the strongest interplanetary shocks. THOR observations in different quasi-parallel shock regions will contribute to advancing our understanding of particle acceleration therein.

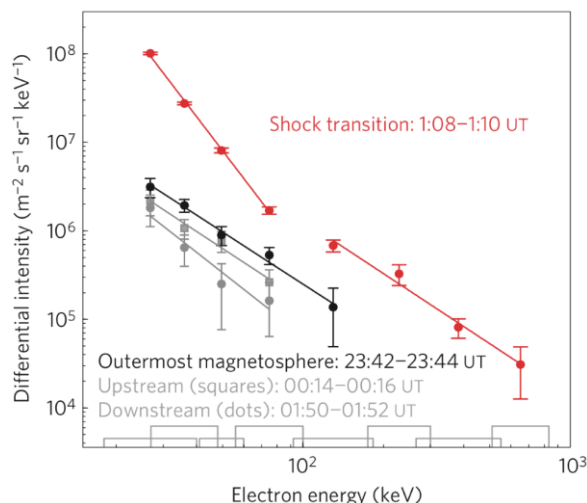


Figure 31: *Electron acceleration to relativistic energies at a high-Mach number quasi-parallel shock wave at Saturn [212]. THOR measurements have much higher time resolution than those at planetary bow shocks, allowing to properly address electron acceleration when the Mach number at Earth's bow shock is sufficiently high.*

2.5 Additional science

In addition to the prime mission goals there are quite a few additional important science questions that can be addressed with THOR but which do not drive the mission requirements. Here we concisely review a few such examples. The topics are split into those that are possible to study in the Key Science Regions (KSRs) but do not fall under the core science goals of the mission, and those that the THOR mission will be able to address in regions that are not in the KSRs.

2.5.1 Additional science in the key science regions

Turbulence at fluid scales in the pristine solar wind. The survey data will provide long-duration time series data with higher time cadence and accuracy than any other mission in pristine solar wind. This allows higher accuracy and higher quality investigations of turbulence at fluid scales than in the past. The turbulent cascade at such scales is observed ubiquitously in the solar wind and is thought to progress primarily through the nonlinear interaction of counter-propagating Alfvénic fluctuations. Being Sun-pointing, THOR will allow the most precise test of this process by performing very accurate Poynting flux measurements of waves and measuring the magnetic and velocity fields for computation of Elsasser variables [178,213]. The high accuracy with which THOR will measure particle moments will enable the correlations between fields and particles at fluid scales to be measured with unprecedented precision, allowing a better understanding of the anisotropic and non-linear processes that drive fluid plasma turbulence [69,214–216]. Survey mode data will provide many days of continuous solar wind measurements, long enough to observe the largest scales of the turbulent cascade, the outer-scale [217].

Reconnection in the pristine solar wind. The solar wind is a unique laboratory for studying plasma heating and particle acceleration in very large-scale reconnecting current sheets [218] which may reflect the conditions observed in extended astrophysical systems. Magnetic field measurements from earlier spacecraft (e.g., Cluster, Wind, ACE) were able to identify such current sheets and a number of important features therein, such as rotational discontinuities / slow shocks far downstream from the X-line. However, the time resolution of particle measurements was too coarse, see example in Figure 32, to quantitatively study the

heating and acceleration processes [183,218–221]. Higher time resolution is currently available from MMS spacecraft, but the MMS plasma instruments are not designed for measuring solar wind plasma. THOR will allow us to study, with high accuracy reconnecting current sheets in the solar wind by, e.g., estimating the exact inflow speeds into current sheets and separatrices through high accuracy $\mathbf{E} \times \mathbf{B}$ measurements as well as particle moments measurements. This will allow an accurate measurement of the reconnection rate and the energy dissipation rate $\mathbf{E} \cdot \mathbf{j}$, as well as plasma heating. THOR will also allow accurate studies of the breaking of the condition of frozen-in magnetic fields and related Hall physics, due to its high-quality electric field measurements in solar wind.

Reconnection-generated turbulence in the solar wind. The identification of small-scale fluctuations in reconnection regions is very important for understanding energy dissipation during reconnection. Large gradients and anisotropies are observed around such regions supporting a variety of wave generation mechanisms. One important example is the reconnection outflow region, where waves and turbulence have been observed [222]. Reconnection outflows can generate local turbulence with different characteristic wavenumbers implying the occurrence of different dissipation mechanisms near ion scales. THOR's accurate measurements of electric and magnetic fields as well as accurate phase velocity determinations will allow the study of such turbulence.

Electromagnetic emission generation in the solar wind. Another important additional science question which can be studied using THOR is how electromagnetic waves are produced in Type II solar radio bursts. Only a small number of Type II source regions have been observed directly by past missions, e.g., Wind and Stereo [223,224]. Although these missions have electric field instruments capable of resolving the Langmuir waves, they lack magnetic field instruments which can resolve waves at the plasma frequency and its harmonics. As a result, the mechanisms responsible for radio wave emission are still a matter of debate. It is expected that THOR will encounter a number of Type II source regions in the solar wind. THOR's improved wave measurements of both electric and magnetic fields at the plasma frequency and its harmonics will allow us to understand in detail the generation mechanisms.

Transport of energetic particles in plasmas around shocks. The standard mechanism to explain particle acceleration at shocks is diffusive shock acceleration (DSA). This mechanism predicts energetic particle fluxes that decay exponentially in space in the presence of a spatially constant diffusion coefficient [225]. However, recent analyses of time profiles of energetic particles far upstream of interplanetary shocks have revealed power law decays indicating superdiffusive transport [226,227], implying that DSA should be extended to include non-diffusive, anomalous transport regimes. In addition, superdiffusion predicts steeper-than-exponential particle profiles in the close upstream region of the shock. This technique has further been applied to relativistic electrons accelerated at supernova remnants, in order to reproduce the spatial profile of X-ray emission [228]. THOR's high energy and angular resolution particle data will be crucial to obtain accurate particle energy profiles close to the shock, and therefore to better assess particle transport in space plasmas.

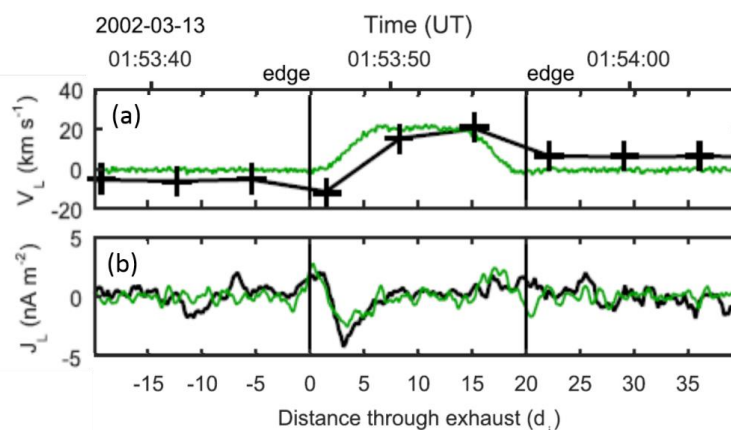


Figure 32: A solar wind reconnection exhaust observed by Wind (black) and a comparative PIC simulation (green) [221]. (a) Exhaust outflow speed (the solar wind background flow is subtracted). The Wind measurement cadence of 3s is sufficient only to capture two data points in the exhaust. (b) Current density along the outflow, derived from magnetic field measurements. The simulation predicts that the signature on the left-hand side of the exhaust is caused by kinetic physics and that is important for heating. High resolution THOR measurements will allow us to quantify heating in such solar wind reconnection exhausts.

2.5.2 Additional science outside the key science regions

Magnetospheric regions. During a substantial part of the orbit, THOR will be in the Earth's magnetosphere, see Figure 33, where several important additional science questions can be addressed such as the structure of the magnetopause and magnetotail current sheet at kinetic scales, the microphysics of the Kelvin-Helmholtz instability at the magnetopause and the microphysics of plasma jet fronts in the magnetotail.

Locally generated turbulence in the magnetosphere. Fluid and kinetic turbulence is found throughout the magnetosphere, in the polar cusp, magnetotail, and current sheet. Much of this turbulence is locally generated by the high temperature anisotropy of the ions and electrons in these regions [229]. THOR will provide the detailed and high-cadence distribution functions necessary to investigate these phenomena which provide a unique opportunity to study the generation of inverse cascade processes thought to be generated by temperature anisotropy instabilities.

Plasma jet fronts in the magnetotail. The interaction of fast jets with ambient plasma results in the formation of jet fronts [230–232]. Jet fronts are important for energy dissipation and particle energization at kinetic scales, the front itself having a thickness ranging from few ion to electron scales [233,234]. One important question is whether such thin jet fronts are shock-like structures, as expected in solar corona and other astrophysical environments and suggested by Cluster observations [232], or tangential discontinuities with no plasma flow across [230,231]. It was not possible to solve this problem with the available data, due to the insufficient accuracy of electric field measurements and the low time resolution of particle measurements that are required to quantify plasma inflow across the front and evaluate energy dissipation through $\mathbf{E} \cdot \mathbf{j}$. THOR will provide such measurements.

Geomagnetic storms and current sheet disruptions. During geomagnetic storms, reconnection in the magnetotail current sheet is thought to drive sub-storm events, accelerating plasma towards the Earth at high energies. THOR will join any spacecraft remaining from the THEMIS, Cluster, MMS and Van Allen Probes missions enabling extensive investigation of the whole magnetosphere system, or offer an opportunity to continue the science of these missions after these spacecraft stop operations. THOR will offer higher resolution and cadence measurements, which is particularly useful for investigating reconnection and turbulence in the current sheet, thought to be responsible for the triggering and onset phase of substorms, producing distinctive patterns and shapes in aurora structure and the geomagnetic response of the Earth to space weather [235].

Space weather. In combination with other missions in near-Earth space, THOR can address science that is important for space weather. The recent COSPAR Roadmap on Space Weather [236] spells out several key requirements to make progress in such science. In the nearest term, it will be crucial to improve our understanding of which solar wind structures, seen at L1 by monitoring missions, can actually reach the Earth's magnetosphere and become "geo-effective". THOR will provide such observations by acting as near-Earth monitor. This science is very important for both the space plasma and space weather communities and can be investigated by THOR already during its nominal lifetime. THOR observations, together with those from still existing and/or newly arriving L1 missions, will lay the foundation for the planning of a later optimized long-term space weather monitoring program. In the longer term, the roadmap spells out the need for a coordinated fleet of solar wind monitoring spacecraft. Some of the instruments that will be developed for THOR are excellent space weather monitors, e.g., FAR and CSW, and could be used on such future L1/L4/L5 missions. In addition, depending on the results of the initial and extended science phase, it may be envisaged to move THOR to L1 after its extended phase.

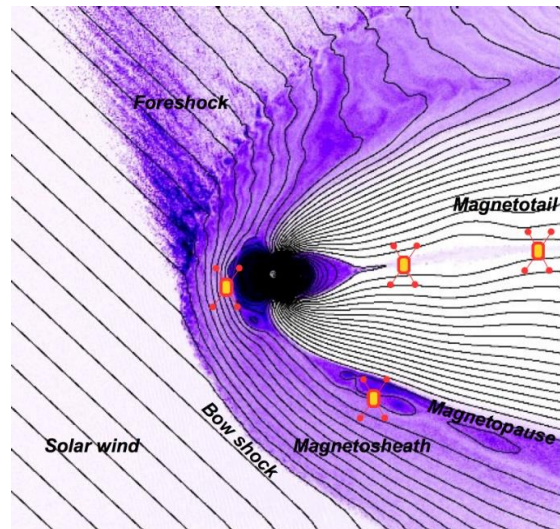
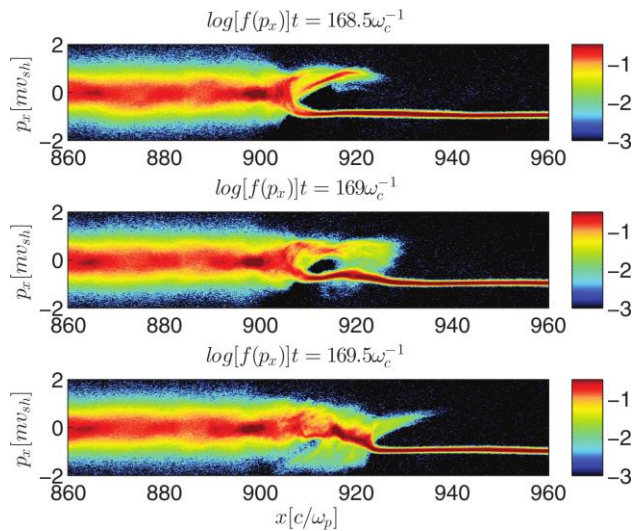


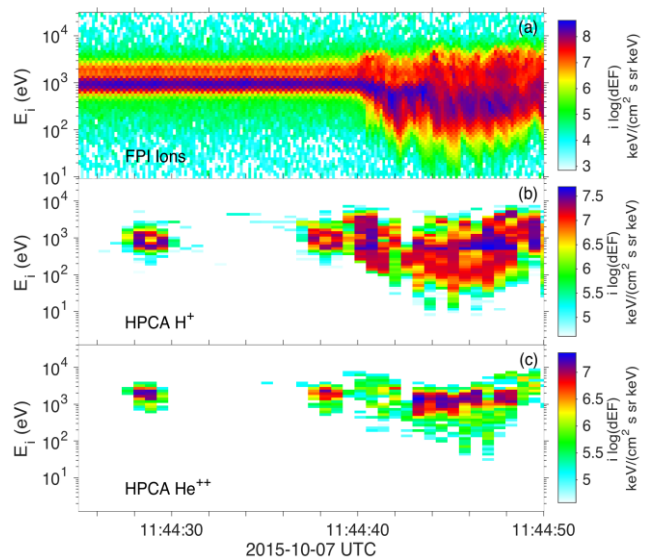
Figure 33: Different regions encountered by THOR in near-Earth space illustrated with the help of a hybrid simulation (Courtesy: D. Krauss-Varban). The key science regions are the solar wind, shock and magnetosheath. THOR will also make observations at the magnetopause boundary and in the magnetotail (marked with spacecraft positions).

Astrophysical example: particle injection at collisionless shocks

The mechanism of Galactic Cosmic Ray (GCR) acceleration is a fundamental problem of plasma astrophysics. Acceleration by Diffusive Shock Acceleration (DSA) [165] occurring at non-relativistic collisionless shock waves, e.g., supernova remnant blast waves, is a well-established mechanism to produce GCRs. In order for DSA to proceed efficiently, however, a fraction of the seed population particles needs first to be pre-accelerated to suprathermal energies. This process is usually referred to as injection. Determining without free parameters the exact fraction of particles that need to be injected and their spectra as function of shock strength and inclination, as well as composition (electrons, protons, alpha particles, heavier nuclei), is a key open question for cosmic ray physics. Such an injection model requires a self-consistent calculation of the shock structure on microphysical scales, which can be achieved only with kinetic plasma simulations. The figure above shows an example of kinetic simulations of particle injection at a quasi-parallel shock with relatively high Mach number $\mathcal{M}=20$ [166]. The shock discontinuity evolves on kinetic timescales (a few proton gyrotimes) and becomes more and more turbulent. Ion reflection and scattering is due to the interaction with fluctuations at kinetic scales and depends on ion masses and energies. Therefore, accurate measurements of particle distribution functions and electromagnetic fields in shock regions are crucial to validate injection models, which, in turn, are very important to understand DSA.



High-resolution *in situ* spacecraft measurements that are able to resolve kinetic physics are scarce. The top panel of the figure to the right shows high time resolution measurements of ions at the Earth's bow shock from the Fast Plasma Instrument onboard the MMS mission [211]. These measurements are currently those with highest possible cadence and are sufficient to resolve ion kinetic scales. Yet, the energy resolution is not adequate to resolve the details of the incoming pristine solar wind distribution function since MMS instruments were not designed to study the solar wind. Furthermore, the Fast Plasma Instrument does not discriminate ion species. The two bottom panels show measurements from the Hot Plasma Composition Analyzer which can separate protons from heavier ions (e.g., alpha particles) but whose cadence is not sufficient to resolve proton and alpha particle kinetic scales.



THOR *in situ* measurements of proton and alpha particle distribution functions at kinetic scales and of electric and magnetic field fluctuations will allow accurate measurement of both the cold incoming ions and the hot reflected ions in turbulent shock regions and the determination of how such ions interact with kinetic-scale turbulent fluctuations. Due to the size of the terrestrial shock and its typical Mach number (normally $\mathcal{M} < 10$, but sometimes up to $\mathcal{M} \sim 20$), THOR measurements can only partially help in studying DSA such as that operating in supernova remnants. **Yet THOR measurements may help obtaining realistic injection models to be used to study Diffuse Shock Acceleration and cosmic ray acceleration, considering that most of cosmic rays are composed of protons and alpha particles which will be very accurately measured by THOR.**

3 Scientific requirements

This section lists the major scientific measurement and mission/spacecraft requirements, and provides a short motivation for each of these.

3.1 Instrument requirements

Table 2 gives a summary of the traceability from the science questions (Level 0) to the scientific measurement requirements (Level 1) which was discussed in detail in the previous section. Addressing each of the science objectives requires several of the measurement requirements to be fulfilled simultaneously. The detailed science measurement requirements and their traceability to the instrument performance requirements (Level 2) are given in Table 3.

Table 2: Traceability matrix from science questions (Level 0) to the scientific measurement requirements (Level 1).

Cosmic Vision		2. How does the Solar System work?								
THOR Science Theme		2.1 From the Sun to the edge of the Solar System								
THOR Science Theme		Turbulent energy dissipation and particle energization								
Science Questions		L1 Requirements								
		Fields				Particles				
		R1	R2	R3	R4	R5	R6	R7	R8	R9
Q1. How are plasmas heated and particles accelerated?	Wave mode identification	•	•		•	•	•	•		
	Effects of waves on plasma					•	•	•	•	•
	Coherent structure identification	•	•	•	•	•	•	•		
	Effects of coherent structures on plasma					•	•	•	•	•
Q2. How is the dissipated energy partitioned?	Among electrons, protons and heavier ions					•	•	•	•	
	Between heating and particle acceleration					•		•	•	•
Q3. How does dissipation operate in different regimes of turbulence?	Pristine solar wind	•	•	•	•	•	•	•	•	•
	Flow interaction regions	•		•	•	•	•	•	•	•
	Shocks and sheath behind shocks	•		•	•	•	•	•	•	•
	(goal) Magnetotail turbulence	•		•	•	•	•	•	•	•

Table 3: The scientific measurement requirements (Level 1) and their traceability to the payload performance requirements (Level 2). Only the main requirements are described, grouped according to type (R1,R2,..). The correspondence of these requirements to the detailed requirements in the Science Requirement Document is given in Appendix B.

Scientific Measurement Requirement Level 1	Instrument Performance Requirement Level 2
R1 EM field cadence Measure electric E and magnetic B field vectors with sufficient temporal resolution to resolve plasma frequency.	RP1 Measure E and B in frequency range from DC to 100 kHz.
R2 EM field sensitivity Measure at least two components of E and full vector B down to electron kinetic scales with high enough sensitivity to resolve fluctuations with power below the typical solar wind fluctuation levels.	RP2 Measure at least two components of E with sensitivity better than $[2 \cdot 10^{-12}, 10^{-14}, 10^{-15}, 10^{-16}, 10^{-16}] \text{ (V/m)}^2/\text{Hz}$ @ $[10, 10^2, 10^3, 10^4, 10^5] \text{ Hz}$, full E $[10^{-11}, 10^{-12}, 3 \cdot 10^{-13}] \text{ (V/m)}^2/\text{Hz}$ @ $[10^3, 10^4, 10^5] \text{ Hz}$, B $[10, 5 \cdot 10^{-3}, 3 \cdot 10^{-5}, 10^{-7}, 3 \cdot 10^{-10}, 5 \cdot 10^{-11}] \text{ nT}^2/\text{Hz}$ @ $[10^{-3}, 0.1, 1, 10, 10^2, 10^3] \text{ Hz}$.
R3 EM field accuracy Measure background B with sufficient accuracy to construct a reference system for anisotropy in field fluctuations, pitch-angle and gyro-phase of particles for typical solar wind and magnetosheath plasma conditions. Measure E with sufficient accuracy to resolve E \times B -drift velocities down to a fraction of the Alfvén velocity.	RP3 Measure background B with accuracy better than 0.2 nT in pristine solar wind and 0.5 nT in magnetosheath. Measure at least two components of E with absolute accuracy better than 0.1 mV/m for $ E < 1 \text{ mV/m}$, and with relative accuracy better than 10% for $ E > 1 \text{ mV/m}$.
Measure B and E with amplitudes covering the largest DC and fluctuation levels expected inside key science regions (KSR)	Measure DC E with amplitudes up to 1V/m and B with amplitudes up to 1000 nT.
Measure satellite potential in the range covering the expected satellite potential values inside KSR.	Measure satellite potential in the range from -10V to +30V.
R4 Phase velocity Measure the phase velocities of structures/waves having electric field, magnetic field and/or plasma density signal moving with speeds up to a few times electron thermal speed.	RP4 Measure phase velocities of at least up to 10,000 km/s.
R5 Ion composition Distinguish at least H^+ , He^{++} and O^+ ions.	RP5 Measure at least H^+ , He^{++} with $m/\Delta m > 8$, and O^+ with $m/\Delta m \geq 3$.
R6 Particle moments Resolve moments - density, velocity, temperature and temperature anisotropy - of electrons at electron scales, H^+ at sub- H^+ scales and He^{++} at He^{++} scales. Characteristic scale values are given in R11 .	RP6 Measure moments with temporal resolution for e- of at least 5 ms, for H^+ down to 50 ms (solar wind) and 150 ms (magnetosheath), for He^{++} down to 300 ms.

<p>R7 Particle distribution functions in thermal range</p> <p>Measure full 3D distribution functions in the thermal range with resolved non-Maxwellian features – for electrons at electron scales, for H⁺ at sub H⁺ scales, and for He⁺⁺ at He⁺⁺ scales.</p> <p>Measure reduced distribution functions of electrons over selected angles and energies to resolve sub-electron spatial and temporal scales.</p>	<p>RP7</p> <p>Measure the 3D distribution function of ions and electrons in energy range up to E_{max}, with maximum resolutions in: energy ΔE/E, time ΔT, angle Δα. These maximum resolutions are not required simultaneously.</p> <p><i>Pristine solar wind:</i> H⁺:E_{max}<20keV,Δt=50ms,ΔE/E=7%,Δα=1.5° He⁺⁺:E_{max}<20keV,Δt=300ms,ΔE/E=7%,Δα=1.5° e⁻:E_{max}<100eV,Δt=5ms,ΔE/E=17%,Δα=11.25°</p> <p><i>Magnetosheath:</i> H⁺:E_{max}<5keV,Δt=150ms,ΔE/E=15%,Δα=11.25° He⁺⁺:E_{max}<5keV,Δt=0.3ms,ΔE/E=15%,Δα=11.25° e⁻:E_{max}<500eV,Δt=5ms,ΔE/E=17%,Δα=11.25°</p> <p>Measure 2D pitch-angle distribution functions of electrons with maximum time resolution Δt=1.25 ms.</p> <p>Record time tags of individual electron counts in up to 32 directions for correlation with wave measurements up to 100 kHz.</p>
<p>R8 Particle distribution functions in suprathermal range</p> <p>Measure 3D distribution functions in the suprathermal energy range with resolved non-Maxwellian features – for electrons, H⁺ and He⁺⁺ at a few times the characteristic scale of the respective species.</p>	<p>RP8</p> <p><i>e⁻ in pristine solar wind:</i> E_{max}<500eV, Δt=20ms, ΔE/E=17%, Δα=11.25°</p> <p><i>e⁻ in magnetosheath:</i> E_{max}<3keV, Δt=20ms, ΔE/E=17%, Δα=11.25°</p> <p><i>e⁻ in solar wind transient events:</i> E_{max}<10keV, Δt=20ms, ΔE/E=17%, Δα=11.25°</p> <p><i>Ions:</i> E_{max}<30keV, Δt=0.3s, ΔE/E=15%, Δα=12°</p>
<p>R9 Energetic particles</p> <p>Measure 3D distribution function of ions and electrons up to sub-relativistic and relativistic energies respectively at about hundred times ion characteristic scale and reduced distribution at about ten times ion characteristic scale.</p>	<p>RP9</p> <p>Measure the 3D distribution function of ions with energies up to 8MeV/nuc and electrons with energies up to 600 keV with temporal resolution down to 15 s and energy resolution ΔE/E down to 20%. Measure reduced distributions with time resolution higher than 2 s.</p>
<p>R10 Key Science Regions (KSRs)</p> <p>The science measurement requirements shall apply to at least the key science regions (KSRs): pristine solar wind, foreshock, bow-shock and magnetosheath. An additional goal is to collect data also from other regions of scientific interest, such as plasma sheet and outer radiation belts.</p>	
<p>R11 Characteristic scales</p> <p>For measurement at e-/H⁺/He⁺⁺ scale it is required that the measurement cadence is at least equal to e-/H⁺/He⁺⁺ scales Doppler shifted by typical plasma speed values in the corresponding KSR.</p>	

Characteristic scales (R11). Most of the scientific measurement requirements for THOR in Table 3 are formulated with respect to kinetic scales. We need to know the expected values of kinetic scales to derive the instrument performance requirements in Table 3 from the scientific requirements. Figure 34 shows the expected statistical distribution of plasma temperature and density in pristine solar wind and magnetosheath, together with characteristic length scales of proton inertial length (corresponding to proton kinetic scales) and Debye length. Electron kinetic scales are roughly 40 times smaller than proton kinetic scales. The properties of shock and foreshock lie between the properties of pristine solar wind and the magnetosheath. Figure 35 summarizes all the expected temporal scales in solar wind (coloured blue) and magnetosheath (red). On top of that are marked the required resolutions from payload performance requirements. It demonstrates that THOR requirements are clearly optimized for particle instruments to resolve Doppler shifted kinetic scales and for electromagnetic field instruments to resolve plasma frequency and Doppler shifted Debye length scales.

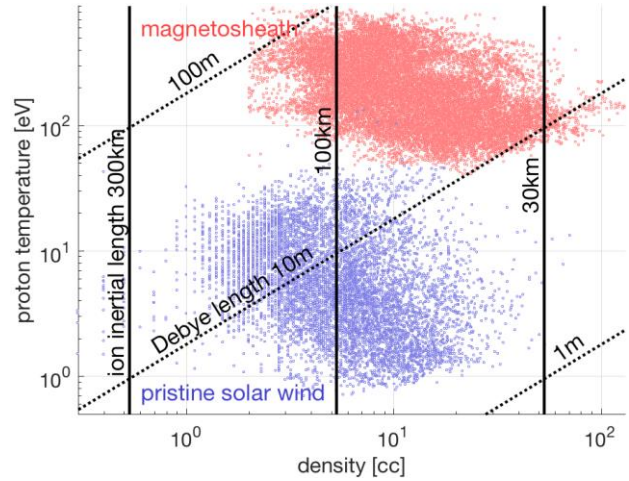


Figure 34: Expected plasma parameters encountered by THOR based on real data (OMNI and Cluster). Electron temperatures are comparable to proton temperatures in solar wind but factor 3-5 smaller than proton temperatures in magnetosheath. Proton kinetic scales are defined by proton inertial length which is comparable to proton gyroradius.

E and B fields temporal resolution (R1).

To characterize electric and magnetic fields in turbulent plasma down to the smallest in space and shortest in time dissipation scales, **E** and **B** fields shall be measured with temporal resolution which is sufficient to resolve the electron plasma frequency (**R1**), see Figure 35. All three components of **E** and **B** must be measured for high frequency waves in order to characterize polarisation of waves and structures. The existing or upcoming missions, such as Cluster and MMS can resolve E but not B with such a high temporal resolution, while measurements of both E and B are needed to identify important energy dissipation processes at the smallest scales. This will allow us to achieve full wave and structure polarization identification, and therefore to distinguish electrostatic and electromagnetic waves, to resolve parallel and perpendicular wave components, or to use the magnetic component of fast moving electric solitary waves to estimate the speed of the waves.

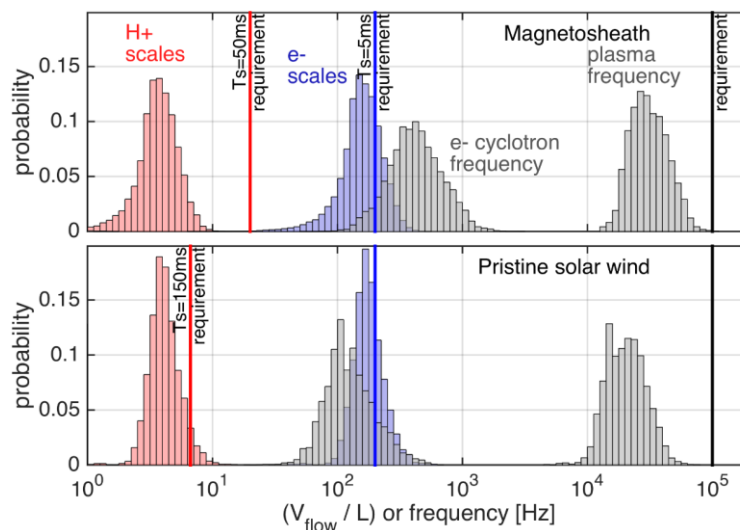


Figure 35: Typical temporal (grey) and Doppler shifted spatial scales (red for H+ and blue for e-) characteristic of physical processes in the solar wind. Coloured vertical lines show the payload requirements for H+(red), e- (blue) and fields (black), meaning the payload can resolve the frequencies to the left of the corresponding requirement.

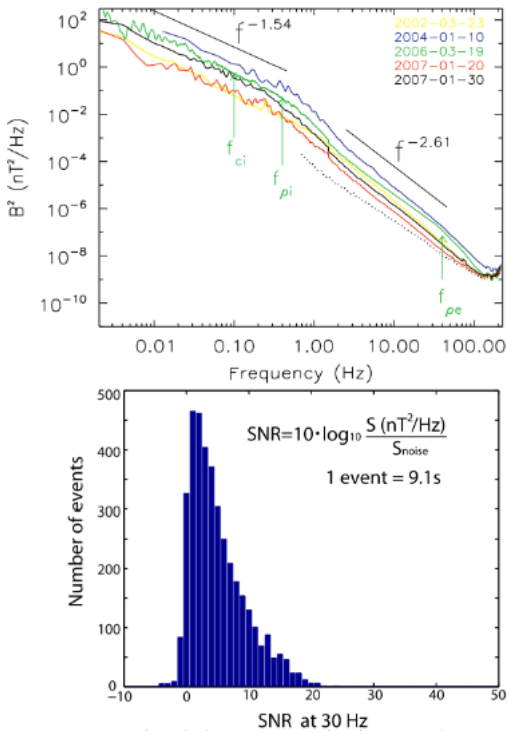


Figure 36: (top) Examples of solar wind B field spectra from Cluster data [65], (bottom) statistics of signal to noise ratio at 30 Hz, roughly electron kinetic scale [62].

EM field accuracy (R3). The background B should be measured with sufficient accuracy to construct a reference system for anisotropy in field fluctuations, pitch-angle and gyro-phase of particles for typical solar wind and magnetosheath plasma conditions. This requires that the background B is measured with accuracy better than 0.2 nT in pristine solar wind and 0.5 nT in magnetosheath (RP3). In addition, E should be measured with sufficient accuracy to distinguish kinetic/inertial Alfvén waves, to resolve reconnection inflows into reconnecting current sheets, to resolve tangential discontinuities from shocklets moving in the plasma frame; this requires accuracy of the $\mathbf{E} \times \mathbf{B} / B^2$ velocity estimate comparable to a fraction of the Alfvén speed. The solar wind is the driving region for this requirement, and E makes the dominant contribution to the convection velocity estimate error. For typical solar wind plasma parameters (velocity of 350 km/s and IMF along the Parker spiral, $\mathbf{E} \times \mathbf{B} / B^2 \sim 250$ km/s), the required 10% relative accuracy of the E measurement (RP3) translates into 25 km/s convection accuracy, which is below the typical Alfvén speed in the solar wind of about 50 km/s. The required E measurement accuracy is not satisfied by current missions, such as Cluster or MMS, which have spin axes perpendicular to the sun-pointing direction. The major limitations are in the accuracy of the DC measurement of the Sun-pointing component

EM field sensitivity (R2). To resolve waves and coherent structures in turbulent plasma both E and B measurements must have sufficient sensitivity in comparison to expected levels. The required levels are given in RP2. So far, the most sensitive B measurements in the solar wind at kinetic scales have been carried out by Cluster, Figure 36(top) shows several examples of such measurements. Often, as in these cases, the amplitude of fluctuations is comparable to the instrument noise level (shown by the dashed line). This is confirmed by a statistical study of signal to noise ratio at electron scales over all Cluster observations of solar wind shown in Figure 36(bottom). To satisfy R2, the sensitivity of the B measurement should be increased in comparison to Cluster. The requirements on the sensitivity levels for E measurements are comparable to earlier missions (RP2) and in particular it is important that at least two components of E are measured with the required sensitivity levels (R2). The sensitivity of electric field is discussed in the payload section, see Figure 65.

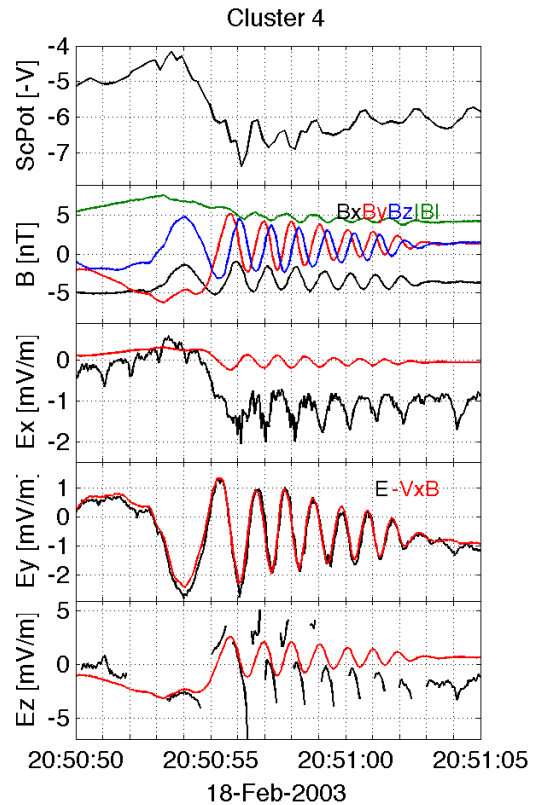


Figure 37: Cluster observations of an Alfvén wave in the solar wind. The last three panels show E measurements which are expected to match $-\mathbf{v} \times \mathbf{B}$ values. While E_y (perpendicular to the Sun direction) is reliably estimated, the Sun-pointing E_x is not. Thus, also E_z , obtained using assumption $\mathbf{E} \cdot \mathbf{B} = 0$, is inaccurate. Having two accurate electric field components on THOR will allow accurate measurements of full E vector.

(measured by long wire booms) and the spin axis component (measured by axial booms on MMS). The most accurate measurement is done by the wire booms in the spin plane perpendicular to the Sun line. This is demonstrated in Figure 37 which shows observations of an Alfvén wave in the solar wind by Cluster. The Sun-pointing measurement of E_x clearly shows low accuracy by differing significantly from the expected $(-\mathbf{v} \times \mathbf{B})_x$ value. This disagreement in addition depends on the plasma environment, being different at the beginning and at the end of the interval. Apart from the asymmetric photoelectron cloud, the E_x measurement is also strongly affected by the spacecraft wake showing up as a spike in the field every second. Only the component perpendicular to the Sun direction E_y shows acceptable accuracy. The total electric field constructed from the assumption $\mathbf{E} \cdot \mathbf{B} = 0$ is not accurate because of the low accuracy of E_x . Adding an axial probe in this case would not help to improve the accuracy. As discussed later, THOR will achieve the accuracy requirement by having the spin plane perpendicular to the spacecraft-sun line and thus being able to make high accuracy measurements in two directions.

Phase velocity (R4). To identify spatial scales of waves and coherent structures, as well as their electric potential (which decides the efficiency of energy transfer in interaction with particles), it is important to resolve their phase velocity. Direct phase velocity measurement involves measuring the signal difference between probes separated by significant distance, such as Langmuir probes at the end of the wire booms in the spin plane. In such cases, the full phase velocity vector can be reconstructed, if the orientation of the boundary or wave vector is known from other methods, e.g., minimum variance analysis. The highest phase velocities that need to be resolved are comparable to the electron thermal speed that normally is higher than whistler phase velocity or electron Alfvén speed. For typical solar wind plasma parameters, this translates into the requirement to resolve phase velocities up to about 10,000 km/s. Existing and upcoming missions do not have sufficiently high temporal resolution, as well as sufficient sensitivity of individual probe signals to achieve this. Complementary indirect methods can also be used. For example, for planar structures the phase velocity can be estimated based on Faraday’s Law as the tangential component of \mathbf{E} should be constant in the structure reference frame. Some other methods are given in Table 27.

Ion composition (R5). Most of the physical processes driving ion heating and ion acceleration are dependent on the ion mass. Therefore, it is important to resolve this mass dependence. The dominant solar wind ion species are H^+ and He^{++} . Therefore, at least these two species should be measured separately by the particle instruments. In addition, it is important also to resolve also other species, such as O^+ . For example, significant O^+ ion fluxes of terrestrial origin may be observed the magnetosheath when spacecraft is close to the magnetosphere.

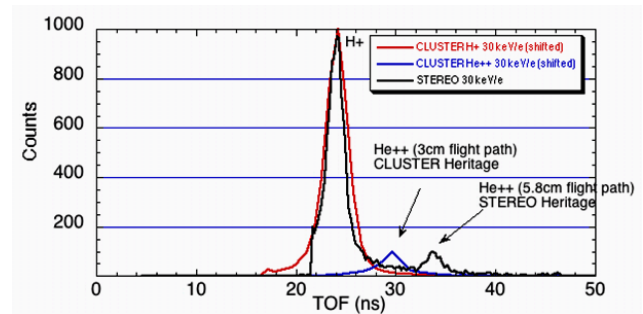


Figure 38: A distribution of counts for H^+ and He^{++} of Cluster/CODIF and STEREO/PLASTIC instruments. To resolve He^{++} a mass separation comparable to STEREO/PLASTIC is required.

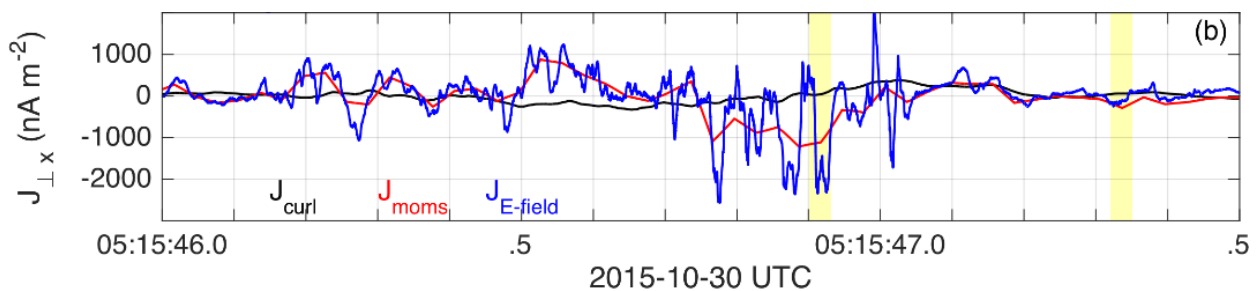


Figure 39: MMS observations of drift lower hybrid wave turbulence. MMS single spacecraft current measurements based on particle instrument data (red line) are significantly better than multi-s/c curlometer estimates (black line) but even higher cadence is required to resolve the expected current on electron scales (blue line) [237].

Particle moments (R6). To understand the physics of plasma heating at kinetic scales it is essential to measure particle moments of electrons and mass resolved ions (density, velocity, temperature and temperature anisotropy) at their characteristic scales (**R6**). Plasma moments can provide local current estimates as shown by MMS, see Figure 39. Plasma density measurements are particularly critical for the identification of wave modes, the construction of wave dispersion relations and the identification of density gradients. Plasma density can be measured by different methods, with their applicability depending on the plasma environment and temporal scale. It is important that THOR can use these methods, such as plasma frequency tracking, integration of particle velocity distributions and (as a proxy) the satellite potential, to cover all required temporal scales and expected plasma parameters. Satellite potential measurements have provided the highest time resolution plasma density information so far, down to electron scales. A spacecraft oriented with its spin plane close to the ecliptic exhibits large variations in satellite potential during each rotation, see Figure 40 (Cluster). These prevent the use of satellite potential for accurate estimates of density and density fluctuations. THOR will use a Sun-pointing spacecraft spin axis to avoid this problem, and can meet the science requirement.

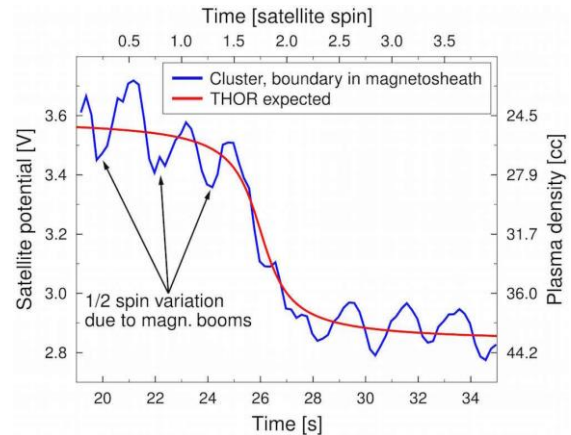


Figure 40: Boundary observed in satellite potential. Cluster shows strong variations due to spin dependent changes in total illuminated area created by solid magnetometer booms. All spacecraft with a large angle between the spin axis and the Sun direction (Cluster, THEMIS, MMS) show such variations. No such variations will be seen in THOR data, due to its Sun-pointing spacecraft spin axis.

The accuracy of plasma moments derived from 3D velocity distributions depends on counting statistics. The number of counts in a 3D distribution are higher when longer accumulation times are used by the particle sensors. On the other hand, short accumulation times are necessary to obtain high time resolution and thus to resolve kinetic scales. Figure 41 shows that, despite the high time resolution of the TEA, CSW and IMS instruments (dashed horizontal lines), their measurements will usually have sufficient count statistics in the KSRs that the moments can be accurately computed. The low peak counts number for TEA is a consequence of the very high time resolution, but nonetheless corresponds to a sufficiently large total counts value as electron fluxes are seen from all directions. In contrast, the CSW instrument samples a narrow cold solar wind ion beam with higher peak fluxes concentrated within a smaller solid angle range. Events having sufficient count statistics correspond to a broad range of density values (shown in Figure 41) as well as temperature and flow speed values (not shown), so that good measurements will be available for a broad range of turbulence conditions. Measurements from a representative set of conditions will be collected as the mission progresses by using the selective downlink approach described in Section 6.3.3.

Particle distribution functions summary. THOR shall characterize electron and mass resolved ion populations in order to resolve the thermal and suprathermal parts of the distribution functions (**R5, R7, R8**), to understand, e.g., what determines the observed ion/electron temperature ratio in a collisionless plasma turbulence [8] and the role of different wave damping mechanisms for the acceleration of suprathermal particles [83].

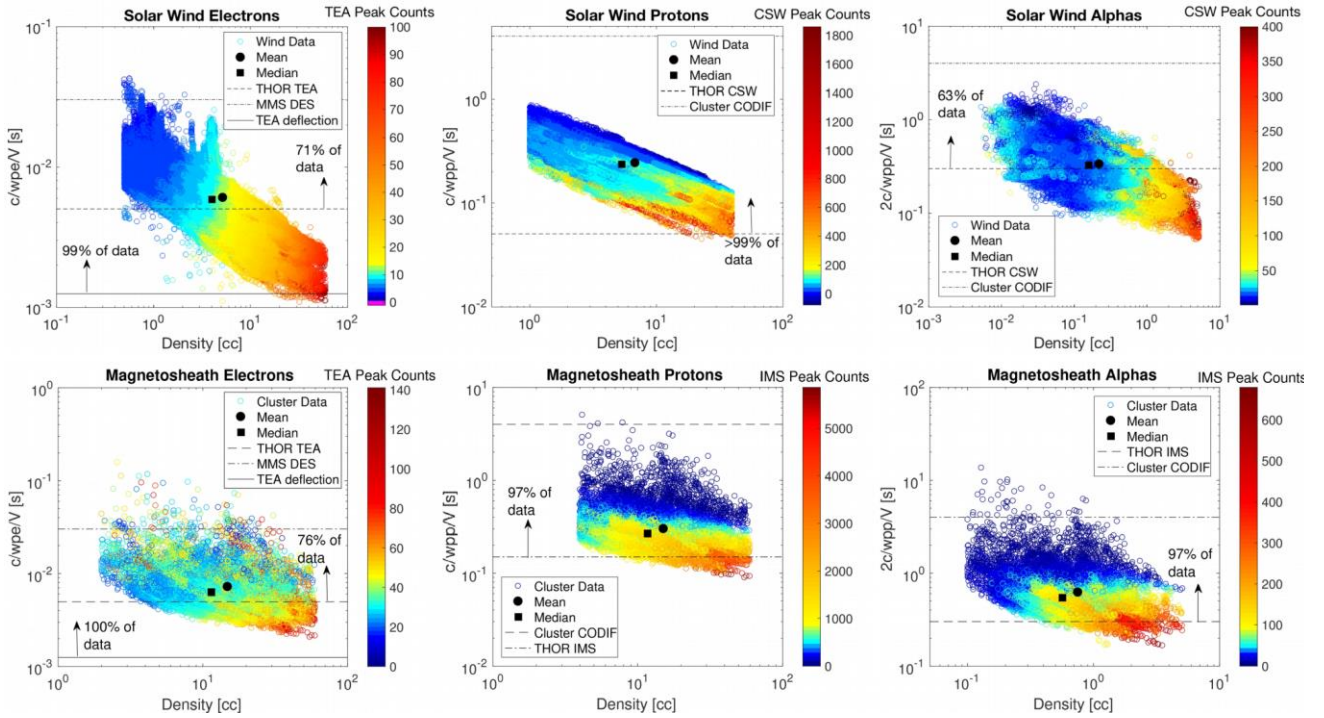


Figure 41: Example distributions of solar wind and magnetosheath parameters based on a large dataset from previous missions (Wind, Cluster). The figure shows that the THOR instruments are able to resolve electron and proton structures in the solar wind with sufficient count rates to measure energy spectra. The X-axis shows the plasma density. The Y-axis shows temporal scales corresponding to Doppler shifted kinetic scales of electrons and ions. The scales of alpha particles are assumed to be twice the scales of protons. The cadence of CSW, IMS and TEA 3D VDF measurements are marked, and also that for an individual TEA energy sweep/deflection state used to collect very fast 2D pitch angle distributions. The coloured points show particle counts per pixel in the peak count rate pixel of a 3D VDF. The figure identifies parameter ranges where particle statistics are good and demonstrates that the instruments can measure the mean and median of the populations. For reference, cadences of state-of-art-instruments onboard currently operating spacecraft are shown. The MMS/FPI-DIS instrument has the same cadence as THOR/IMS (150 ms) but cannot distinguish ion species. The MMS/HPCA can distinguish ion species but its cadence (10s) is lower than Cluster/CODIF (4s) and neither can resolve kinetic scales in pristine solar wind and magnetosheath.

Non-Maxwellianity (R7). The departure of a particle velocity distribution function from a Maxwellian (or bi-Maxwellian) distribution can be described by the ϵ parameter, $\epsilon = (1/2n) \int |f - f_{biMaxw}| d^3v$ (adapted from [238]), where, f is the measured distribution and f_{biMaxw} is the corresponding bi-Maxwellian distribution. The latter is calculated from the moments of f (density n , temperatures parallel and perpendicular to magnetic field and bulk speed). The ϵ parameter is an important proxy to study particle energization. It is expected to be large around turbulent structures, such as e.g., current sheets; the higher the value of ϵ , the stronger is the non-Maxwellianity. Figure 42 shows an example of ϵ peaking in a Hybrid-Vlasov-Maxwell kinetic simulation of turbulence close to a localized current sheet for protons (red) and alpha particles (blue). Virtual CSW instrument simulations show that the CSW is able to resolve properly such ϵ peaks. In order to have meaningful measurements of the ϵ parameter, it is important that the geometric factor of the particle instruments is large

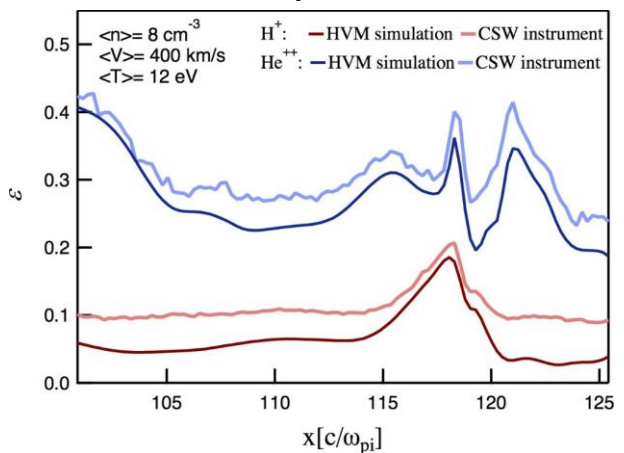


Figure 42: Virtual CSW instrument flying through a turbulence simulation representing pristine solar wind. The counting statistics are sufficient to resolve significant non-Maxwellianity at kinetic scales.

enough so that the counts statistics are sufficient. THOR virtual instrument simulations have been performed with CSW parameters to reproduce Cluster/CIS actual measurements in pristine solar wind, see Section 6.6, and such simulations have confirmed that the expected count statistics for CSW are sufficient to resolve the peaks in ε . Similar tests using data from different numerical simulations have been done for the IMS and TEA instruments both in pristine solar wind and in the magnetosheath, with satisfactory outcomes.

Particle distribution functions examples.

We give a few examples motivating the THOR requirements on particle distribution function measurements. As an example of temporal resolution, Figure 43 shows results from a numerical simulation of electron scale turbulence. The electron distribution function looks like a heated bi-Maxwellian when measured at ion scale, while at electron scales beams and a non-isotropic core are revealed, indicating the importance of resolving distribution functions at electron scales (**R7**). In another example, recent studies comparing simulations with Helios observations of alpha particle temperature anisotropy in the solar wind revealed how the low time resolution of velocity distribution measurements can generate an unphysical apparent increase in perpendicular temperature, due to procedures of data sampling and averaging [239]. Both examples illustrate the need for the requirements on the high cadence of particle distribution function measurements (**R7**, **R8**). The requirements on energy/angular resolution of measurements of ion distribution functions are more severe in the case of drifting plasmas, such as fast drifting pristine solar wind (**RP7**). For drifting plasmas the energy resolution $\Delta E/E$ required to resolve the distribution function scales roughly as the ratio of thermal velocity versus drift velocity and therefore two different ion energy resolution requirements apply for the pristine solar wind and the magnetosheath, while the same resolution can be used for electrons in those two regions (**RP7**). For the case of shock regions, it is required to simultaneously resolve the distribution function of both the fast drifting pristine solar wind and the thermalized sheath ions, including reflected and accelerated ions in the foreshock (**RP8**). Finally, acceleration and heating mechanisms work differently for different ion mass species, as discussed in Section 2.3, translating into the requirement to resolve ions of different mass (**RP5**). Figure 38 illustrates that to resolve He^{++} well, THOR has to achieve mass separation comparable to STEREO/PLASTIC instrument (**RP5**).

Energetic particles (R9). Particle spectra need to be measured over several orders of magnitude in energy to be able to recognize the fingerprints of different acceleration processes occurring in different turbulent plasmas. In order to be able to characterize the shape of the energy spectra at energies well above the thermal and suprathermal range, the energetic particle spectrum needs to be measured at least three orders of magnitude above the most probable particle energy, which for ions has its highest value of about several keV/nucleon upstream of the bow shock while for electrons the highest value is about hundred eV in the magnetosheath. These requirements translate into resolving scales of the order of one hundred ion thermal scales for 3D distribution functions, while smaller scales of the order of ten times ion thermal scale can be resolved by reduced distributions (**R9**). In the case of THOR this means that 3D VDFs shall be measured at least once per half spin (15s) while it should be possible to measure pitch-angle distributions at sub-spin time resolution (cadence higher than 2s, **RP9**).

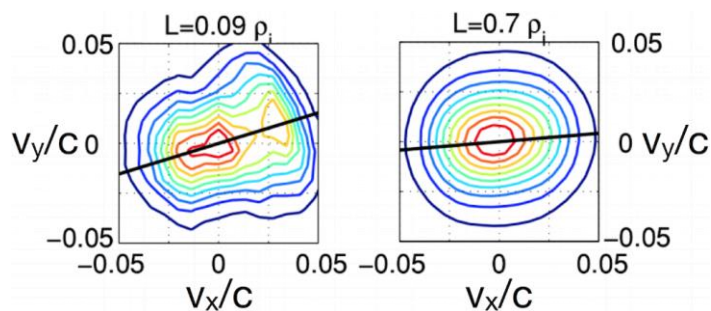


Figure 43: Electron velocity distribution function in turbulence when averaged over electron scales (left) and ion scales (right). Physics of electron energization can be only resolved at electron scales[24].

Comparison to other missions

Table 4 shows the comparison of THOR with existing and upcoming missions (which have been designed to address different science goals and requirements). The table shows which science requirements of THOR are satisfied by the different missions. Only missions that have been or will be able to cover at least some of the plasma regions targeted by THOR are included. It can be seen that only a few of the requirements can be satisfied by other missions. In particular, it is clear that no other mission has satisfied all the science measurement requirements as required by the THOR science questions. To be more specific, Table 5 compares the performance of some current and upcoming missions relevant to THOR science in terms of their temporal, angular, energy resolution of 3D particle distribution functions. The performance of current missions Cluster and Wind do not satisfy most of the THOR requirements. Solar Orbiter satisfies most energy/angular resolution requirements for pristine solar wind, but has inadequate temporal resolution. MMS improves on temporal resolution relative to Cluster and Wind, but does not meet THOR requirements for electrons and He⁺⁺, while it has insufficient angular/energy resolution to resolve pristine solar wind ions. Summarizing, the combination of all THOR requirements on measuring particle distribution functions of thermal and suprathermal electrons and ions is not satisfied by any existing or upcoming mission.

Table 4: Mission compliance with the THOR scientific measurement requirements (●-compliant, ○-partially compliant). Other missions compliant with two or less requirements are not shown. These include: ACE, THEMIS, Helios-1,2, Spektr-R.

Mission	Scientific Measurement Requirements								
	Fields					Particles			
	R1	R2	R3	R4	R5	R6	R7	R8	R9
THOR	●	●	●	●	●	●	●	●	●
Cluster	○			○	○				○
MMS	○		○	○	●	○			●
Solar Orbiter	○	●			○				○
SPP	○	●			○				○
Wind	○								●

Table 5: Resolution of 3D distribution functions in comparison to other spacecraft. "*" indicates that the resolution differs in the two angular coordinates, the given value is the finer resolution case. Green marks values that are compliant with the THOR instrument performance requirements.

	Electrons			Ions (solar wind)			Ions (m/sheath & bow shock)			
	Δt (ms)	$\Delta E/E$	$d\theta$	Δt (ms)	$\Delta E/E$	$d\theta$	Δt (ms)	$\Delta\alpha$	$\Delta E/E$	$d\theta$
THOR	5	17%	11.25°	50	7%	1.5°	150	300	10%	11.25°
Solar Orbiter	1000	10%	* 3°	1000	5.7%	5°	-	-	-	-
Solar Probe Plus	437	20%	* 6°	3500	20%	* 11.25°	-	-	-	-
MMS	30	17%	11.25°	150	12%	11.25°	150	10000	10%	11.25°
THEMIS	3000	17%	22.5°	3000	18%	* 5.6°	3000	-	18%	22.5°
Cluster	4000	13%	15°	4000	18%	* 5.6°	4000	4000	18%	22.5°
Wind	3000	20%	* 5.6°	3000	20%	5.6°	3000	-	20%	11.25°

3.2 Mission requirements

Table 6 summarizes major requirements at the mission level. Appendix B describes in more detail the relationship between these summary requirements and the complete list in the SciRD and the MRD.

Table 6: Mission and spacecraft level requirements.

Mission Requirements
<p>R12 Science data return</p> <p>The Burst telemetry downlinked shall be at least 100h in the magnetosheath, 35h in the bow shock, 50h in the foreshock, 150h in the pristine solar wind. Based on payload telemetry rates this requires that 6.4 Tbit in the magnetosheath, 2.9 Tbit in the bow shock, 2.8 Tbit in the foreshock and 3.2 Tbit in the pristine solar wind shall be returned.</p>
<p>R13 Orbit requirements</p> <p>The orbit shall be optimized for the spacecraft to spend long time intervals in the top priority regions (TPR). During the nominal science phase the spacecraft shall spend altogether within TPRs: at least 60 days in pristine solar wind, 47 days in foreshock, 21 days in bow shock and 14 days in magnetosheath.</p>
<p>R14 Spacecraft and payload operation requirements</p> <p>The science payload shall continuously operate when the spacecraft is within the KSRs. The payload shall operate in a way to maximize the data return from all KSRs. It shall be possible to save on-board high resolution data from which scientifically interesting time intervals can be selected and transmitted to the ground.</p> <p>When the science payload is operated during the nominal mission: The spin axis should always point toward the Sun within the interval $[-5.5^\circ, +1.5^\circ]$ XY GSE plane (+ defined anti-clockwise) and $[-1.5^\circ, +1.5^\circ]$ XZ GSE plane. The spin rate shall be of two (2) full rotations per minute.</p>
<p>R15 Ground Segment requirements</p> <p>Calibrated science data shall be available under the open data policy starting 6 months from the time of data acquisition. Science parameters which can be measured by more than one instrument shall be cross-calibrated between the different instruments prior to public release of the calibrated science data.</p>

Mission success criteria (R12). To achieve the goals of the mission and get closure on the three main science questions, sufficient high-resolution (burst) data needs to be returned from THOR’s key science regions (pristine solar wind, foreshock, shock and magnetosheath). Each of these regions needs to be sampled under a variety of conditions to study the variability of the different forms of plasma energization and understand their physics. The mission success criteria, both scientific and experimental, are given in Table 7. To study acceleration and heating at quasi-perpendicular shocks, different possible combinations of Mach numbers, shock angles and alpha to proton ratios shall be sampled. To cover each combination in this parameter space about 30 min of data are required to make statistically significant analysis, since one shock crossing typically lasts few minutes. In total this requires at least 10 h data at quasi-perpendicular shock crossings to be returned. For the quasi-parallel shock a similar number of different shock parameter combinations are required. Quasi-parallel shock crossings last typically longer than quasi-perpendicular ones and therefore at least 25 h of data shall be returned. For the foreshock there are additional parameters that have to be covered such as ion vs electron foreshock, distance from the shock, different populations of shock-reflected particles. Therefore, 50 h of data shall be returned. For the magnetosheath, typical parameters to be covered are plasma beta, distance from the bow shock, level of fluctuations, alpha to proton ratio. For each combination in this parameter space about 1 h of

Table 7: Mission success criteria.

THOR mission success criteria
<p>THOR will be scientifically successful when its data analysis has resulted in significant, qualitative and quantitative progress in understanding plasma heating and particle acceleration mechanisms in different turbulent plasma environments.</p>
<p>THOR will be experimentally successful when high quality Burst mode data have been returned from at least:</p> <ul style="list-style-type: none"> • 10 h quasi-perpendicular shock crossings, • 25 h quasi-parallel shock crossings, • 50 h foreshock, • 20 h magnetosheath behind quasi-perpendicular shock, • 100 h magnetosheath behind quasi-parallel shock, • 50 h fast solar wind, • 100 h slow solar wind.

continuous data shall be returned to properly characterize intermittency. Thus at least 20 h of data from magnetosheath behind the quasi-perpendicular shock shall be returned. The magnetosheath behind the quasi-parallel shock is much more complex and includes larger number of different turbulent structures. Therefore, at least 100 h of data shall be returned. Finally, in the pristine fast solar wind, different plasma conditions, such as plasma beta, ion-to-electron temperature ratio, collisionality, etc., need to be sampled. To cover several turbulence correlation lengths for each combination in this parameter space, a few hours of continuous data are required. In total this requires at least 50 h of data to be returned. The pristine slow solar wind is much more variable, with compressible structures and interaction regions, so 100 h of data are required.

Key Science Regions and Top Priority Regions (R10, R13). Figure 44 shows the THOR reference orbit coloured per key science region (KSR), and on top are marked numbered top priority regions (TPR). KSR locations are derived from nominal solar wind conditions assuming the Parker spiral model for the magnetic field. In practice, day to day variations in the solar wind parameters will lead to variation in the KSR location. Orbital analysis of the KSR crossings has been done both using nominal solar wind conditions and using real solar wind parameters. THOR has to spend long time periods within the KSRs so that a sufficient amount of high quality data can be returned. Conditions within the KSR regions themselves are not uniform. For example, the bow shock at its nose has higher Mach numbers than on the flanks. Thus, to observe shocks with wide range of Mach numbers it is important that orbits cross the relatively small nose region to sample the shocks there. Therefore, to simplify and optimize the assessment of KSR coverage, it has been decided to introduce Top Priority Regions (TPRs) which are a subset of KSRs, and to formulate the requirements of orbit dwell times **R13** using the TPRs. The TPRs are defined as conic volumes where the cone angle is 30° for bow shock and 45° for other TPRs. In addition, the TPRs have outer and inner boundaries in the radial direction which are defined using magnetopause and bow shock models.

Orbit requirements (R13). The large difference between turbulent plasma states in an undisturbed solar wind in comparison to those in close proximity to the shock, and the astrophysical importance of understanding these differences, requires that THOR spends long time intervals in the undisturbed solar wind (away from the foreshock), in the foreshock, at the bow shock, as well as in the magnetosheath (**R10**). There are no strict requirements on the orbital plane orientation, inclination or perigee values, except that the bow shock region at the nose of the magnetosphere shall be covered during some part of the mission. This requires the line of apsides to be typically within 10° from the ecliptic plane. The perigee should be above 2,000 km altitude, to avoid stability problems of lunar interactions and sensor contamination (observed on Cluster when the perigee fell below about 800 km altitude).

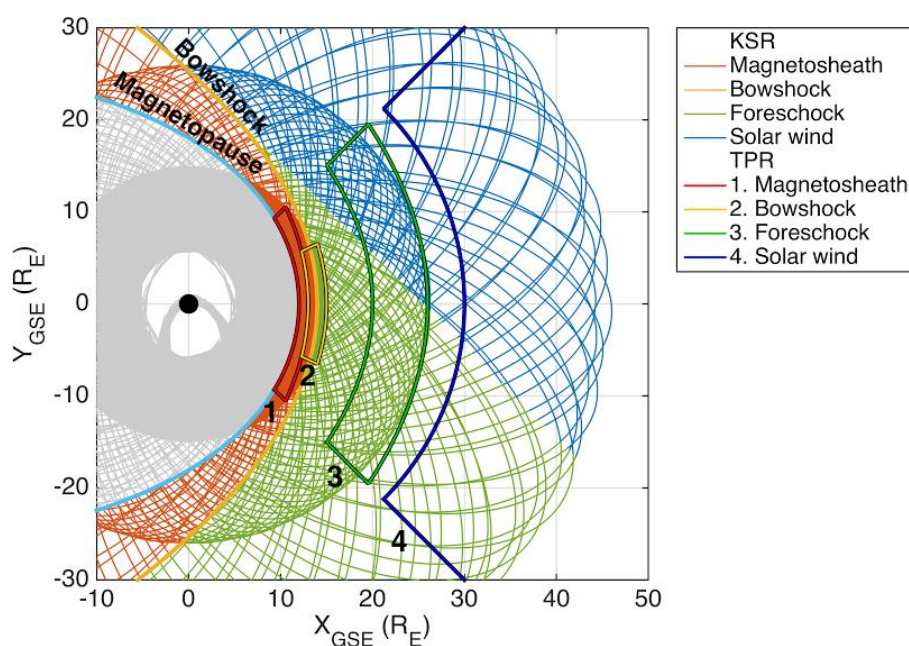


Figure 44: THOR orbit coloured by the Key Science Regions and Top Priority Regions.

Science operations (R14). The science payload can generate much more data than can be downlinked to ground. Therefore, THOR has a capability to save the high-resolution data on-board, and to regularly downlink low-resolution survey data to ground, which is then used to select a subset of the intervals of high-resolution data for downlink to ground. This ensures that the data intervals of highest science interest, such as shock crossings, solar wind intervals with particular parameters and large scale boundaries are collected. To make selection process in a reasonable time there shall be capability to save high resolution data from payload from at least 6 days of operations. This technique is currently in routine use on the MMS mission.

Science Ground Segment (R15). To achieve the scientific objectives of the THOR mission, calibrated high-resolution data should be available on short time scales (6 months after data acquisition). Cross-calibration of the instruments with each other is an essential activity. For instance, the density from TEA, IMS and CSW will be compared to the absolute density measured by the plasma wave instruments to enable correction of any evolution of the sensitivity of the particle analysers. The cross-calibration activity will also allow provision of advanced data products which combine data from several instruments, for example magnetic field covering the entire frequency range accessible by THOR based on MAG and SCM data, plasma moments covering the entire energy range accessible by THOR based on data from TEA and EPE (electrons), and CSW, IMS and EPE (ions).

The cross-calibration will be done with the support from each PI team involved and ESA will coordinate the activity. Two annual workshops will be necessary to exchange information and improve calibrations on short time scales. This cross-calibration effort required from PI teams will be partly supported by ESA, similarly to the successful approach of the Cluster Science Active archive, also adopted by the Rosetta mission.

4 Payload

4.1 Introduction

The THOR spacecraft has a payload suite consisting of 10 different science instruments.

The THOR instruments' main characteristics are summarized in Table 8 and are designed to fulfil the instrument performance requirements in Table 3.

The total mass of the instruments is around 170 kg and the average nominal power consumed is ~200 W. These values include design margin, but do not include any system margin. The harness mass is a separate mass item as the detailed accommodation of the instruments inside the spacecraft is very preliminary.

Technology readiness of instruments

The instruments on THOR all have relevant heritage from recent missions and most of the subsystems of the instruments have the required maturity for this phase.

Table 8: Summary of the THOR payload (* power incorporated inside the FWP)

Instrument	Description	Measured quantity	Number of Units	Nominal mass [kg]	Nominal power [W]
MAG	Fluxgate Magnetometer	Magnetic field	2 units on a boom	0.8	0*
SCM	Search Coil Magnetometer	Magnetic field	1 unit on a boom	2.4	0*
EFI	Electric Field Instrument 2x double probes, 3x dipoles	Electric field	4 SDP and 1 HFA on a boom	10.7	0*
FWP	Fields and Waves Processor	E, B time series and spectral products	1 unit	8.9	26.8
FAR	Faraday cup	Fast ion moments	1 unit	4.6	3.5
CSW	Cold Solar Wind instrument	Cold solar wind ion distributions (H ⁺ , He ⁺⁺)	1 unit	12.4	19.2
TEA	Turbulence Electron Analyser	Electron distributions	6 units	45.8	58.8
IMS	Ion Mass Spectrometer	Ion distributions (H ⁺ , He ⁺⁺ , O ⁺)	4 units	39.1	41.2
EPE	Energetic Particle Experiment	Energetic particles	2 units	4.9	10.0
PPU	Particle Processing Unit	Particle data products	1 unit	16.0	42.0
Harness				24	
Total				169.6	201.6

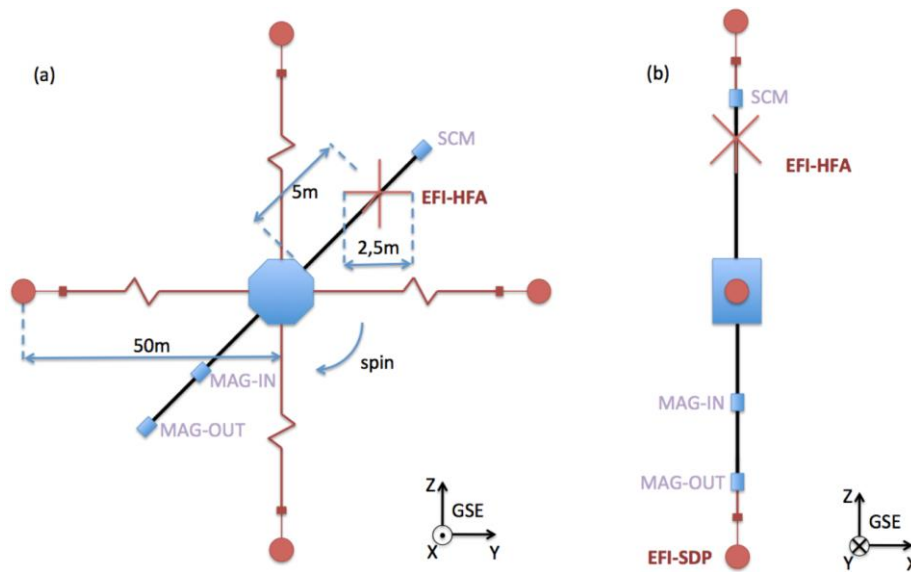


Figure 45: THOR configuration, showing the location of the MAG and SCM sensors, as well as EFI-SDP wire booms and EFI-HFA dipole antennas.

Fields

To satisfy the payload performance requirements **RP1** to **RP3**, the THOR payload includes AC and DC magnetometers (respectively SCM and MAG), four wire probe antennas each of 50 m length and three orthogonal dipole antennas to measure DC and AC electric fields in three dimensions, see Figure 45 and Table 9. All measurements from these electromagnetic field sensors will be processed by dedicated electronic modules embedded inside the FWP instrument box, one of the payload data processors. The MAG instrument will measure AC and DC magnetic fields from DC up to 64 Hz with an accuracy of better than 10 pT/ $\sqrt{\text{Hz}}$. The MAG uses two fluxgate magnetometers placed on a long (> 6 m) boom. They can be used in a gradiometer mode to correct for the spacecraft generated magnetic field. The SCM measures the AC magnetic field in the frequency range from 1 Hz to 200 kHz and is placed at the tip of a second boom (> 6 m) in order to stay away from the spacecraft generated disturbances.

Table 9: Traceability of measurement capabilities of field instruments towards payload requirements derived from THOR science requirements.

Measurement	Instrument	Amplitude Range	Frequency range	Performance Requirement
DC Magnetic field (B)	MAG	± 500 nT, low range ± 8000 nT, high range	DC-64 Hz	RP1, RP3
AC Magnetic Field (B)	SCM	LF: ± 1 nT HF: ± 4 nT	LF:0.1 Hz - 4 kHz HF:(1-200) kHz	RP1, RP2, RP3, RP4
Electric Field (E)	EFI-SDP EFI-HFA	± 1 V/m ± 3 V/m	DC-100kHz ~(1–100)kHz	RP2, RP3, RP4

Ions

THOR will carry advanced particle instrumentation designed to enable very high time resolution measurements of particle distributions. Ion 3D distribution functions are measured using electrostatic analysers (CSW and IMS), a Faraday cup (FAR) and a solid state detector (EPE). The Ion Mass Spectrometer (IMS) instrument will allow the separation of individual ion species (RP5) at very high time resolution (RP6, RP7). A dedicated Cold Solar Wind (CSW) instrument will be included to provide high resolution measurements of the drifting cold solar wind ion beam (RP7). High-energy ions are measured with the Energetic Particle Experiment (EPE) instrument at a lower time resolution (RP9). All data measured by the IMS, EPE and CSW instruments will be processed by a common digital processor unit (PPU) to reconstruct the particle distribution functions and compute moments (RP6). As a complement to these, a Faraday cup (FAR) measures the ion density, temperature and flow velocity to satisfy payload performance requirements (RP5, RP6), while the electron temperature and density can be derived from electric field data produced by FWP.

Table 10: Traceability of measurement capabilities of the ion instruments to the instrument performance requirements in Table 3.

Measurement	Instrument	Energy resolution / range	Time resolution / Angular resolution	Requirement
3D H ⁺	IMS	10 eV – 30 keV	150 ms / 11.25°	RP5
	CSW	20 eV/q – 20 keV/q	50 ms / 1.5°	RP6
	EPE	20 keV/nuc – 8 MeV/nuc	15 s / 45°	RP9
3D He ⁺⁺	IMS	10 eV – 30 keV	300 ms / 11.25°	RP5
	EPE	20 keV/nuc – 8 MeV/nuc	15 s / 45°	RP9
3D O ⁺	IMS	10 eV – 30 keV	≥1.5s / 11.25°	RP5
	EPE	20 keV/nuc – 8 MeV/nuc	15 s / 45°	RP9
Moments H ⁺	IMS	10 eV – 30 keV	150 ms / 11.25°	RP6
	CSW	20 eV/q – 20 keV/q	50 ms / 1.5°	RP6
	FAR		31.25 ms	RP6
Moments He ⁺⁺	IMS	10 eV – 30 keV	300 ms / 11.25°	RP6
	FAR		1.5 – 3 s	RP6
Moments O ⁺	IMS	10 eV – 30 keV	≥1.5 s / 11.25°	RP6

Electrons

Electron 3D distribution functions are measured using the TEA electrostatic analysers and the EPE solid state detectors. The Turbulent Electron Analyser (TEA) instrument will sample the thermal electron distribution at a cadence down to 5 ms (RP6, RP7) and suprathermal electrons down to 20 ms (RP8), while energetic electrons are measured by EPE at 15 s cadence (RP9). From these measurements, 3D velocity distributions will be created by the PPU data processor. TEA can also actively collect 2D pitch angle distributions (PADs) in a magnetic field tracking mode with higher cadence than full 3D distribution functions (RP7). Additionally, the TEA superburst mode periodically collects 125 ms duration samples containing time tags for every detected electron (RP7). These form part of the burst telemetry; for example, one sample can be transmitted every 60 s for magnetosheath science (Table 22).

Table 11: Traceability of measurement capabilities of the electron instruments to the instrument performance requirements in Table 3. Full energy range coverages and maximum temporal and angular resolution are not required simultaneously.

Measurement	Instrument	Energy range	Time / angular resolution	Requirement
Electron 3D	TEA	10 eV – 30 keV	5 ms / 11.25°	RP6, RP7, RP8
Electron PAD	TEA	10 eV – 30 keV	1.25 ms / 11.25°	RP7, RP8
Electron 3D	EPE	20 keV – 700 keV	15 s / 45°	RP9
Electron PAD	EPE	20 keV – 700 keV	7.5 s / 45°	RP9
Superburst	TEA	10 eV – 30 keV	125 ms (every 60 s)	RP7

Count statistics of particle instruments

The geometrical factors of the particle instruments have been chosen such that sufficient count statistics will usually be available in the Key Science Regions (KSRs) to satisfy the science requirements. In addition, the SITL is able to select burst data based on high-quality count statistics criteria. The count statistics have been simulated in a virtual instrument for each particle sensor and the results have confirmed the choice of geometrical factor (see Section 3.1 and 6.6).

Wave-particle correlation

A special mode enables THOR to synchronously sample the high resolution electromagnetic field waveform snapshots by the FWP instrument and to operate the superburst mode of the TEA instrument (Figure 46). The data are separately put into the burst data stream and only on ground are the wave snapshots and the superburst data put together and analysed. This allows the science question of energy transfer between electromagnetic field fluctuations and particles to be directly addressed (**RP1**, **RP7**).

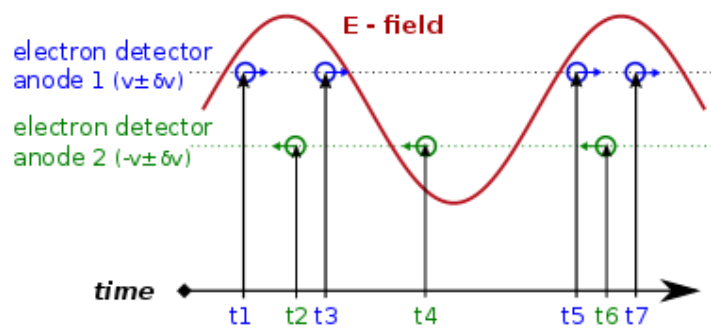


Figure 46: The THOR "superburst" product combines high resolution electromagnetic field waveforms with time tags of individual electrons registered by up to 32 anodes of the TEA instrument. Individual anodes sample different azimuthal directions, covering the full range of pitch angles (in the plot, data from two anodes with opposite look directions are shown). The accuracy of time synchronization between wave measurements and superburst data (better than $1 \mu\text{s}$) will be sufficient for matching the phase of the wave and variations in particle flux up to the electron plasma frequency.

4.2 Instruments

4.2.1 MAG – Fluxgate Magnetometer

The fluxgate magnetometer (MAG) is required to measure the DC and low frequency magnetic field vectors in order to determine the background plasma and field conditions throughout the THOR key science regions and to resolve the magnetic field fluctuations in the solar wind.

The MAG instrument is a dual-sensor fluxgate magnetometer which measures the ambient magnetic field below 64 Hz. The two sensors are placed along a solid boom, one at the end of the boom and the second at an intermediate distance along the boom, in order to enable a reliable detection of any residual spacecraft magnetic field.

Each of the two fluxgate sensors shown in Figure 47 uses only two ring-cores to measure the magnetic field along the three required directions which enables proper sensor miniaturization. The magnetic field is sensed in the X and Y directions via separate ring-cores, while the Z direction is picked-up over both ring-cores. The design of the outboard and inboard sensors is based on THEMIS and Solar Orbiter heritage, respectively. Both THOR sensors will have the same mounting interface to simplify the boom design.

MAG will return magnetic field vectors at up to 128 samples per second (sps), with a noise floor less than 0.01 nT/ $\sqrt{\text{Hz}}$ at 1 Hz. THOR MAG provides high quality data with sufficient overlap (1-64 Hz) with the SCM sensor to allow for an accurate synchronization and alignment of the two data sets.

Critical for the achievement of the MAG related science requirements is the magnetic cleanliness of the spacecraft.

Table 12: MAG key characteristics.

Data products	B field vectors
Range	± 500 nT & ± 8000 nT
Sensitivity	< 10 pT / $\sqrt{\text{Hz}}$
Sampling rate	128 vector / s
Highest datarate	16 kbps

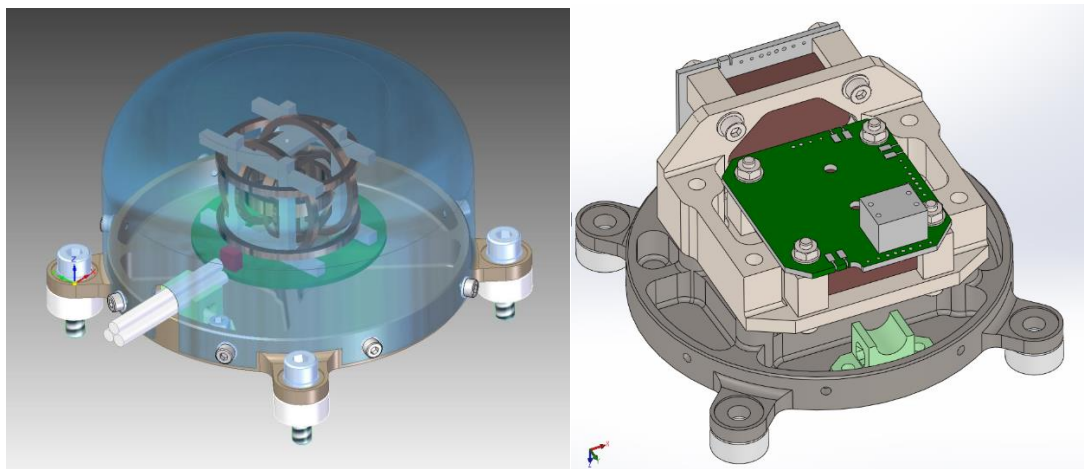


Figure 47: CAD drawings of the outboard sensor (THEMIS heritage) with transparent lid (left) and the inboard sensor without housing (right).

Heritage

THOR MAG sensors and electronics bear direct heritage from Cassini MAG, Double Star FGM, THEMIS FGM, VEX MAG, and MMS DFG successfully flown in space and from Solar Orbiter MAG accepted for flight. The design effort to ensure synchronization between fluxgate and search coil sensors, with the lower noise floors, will considerably improve the quality of the merged dataset compared to previous missions. These synchronization efforts are proven to be successful based on experience from MMS DFG and SCM, which will be an advantage to meet the mission science goals. The two THOR MAG sensors are mounted on the same booms so that they can work as a gradiometer, which was shown to work successfully for the VEX MAG and the Double Star FGM. For THOR MAG this capability will provide redundancy and allows further improvement of the inflight calibration, in particular to reduce unforeseen noise from the spacecraft and other instruments.

4.2.2 SCM – Search Coil Magnetometer

The Search Coil Magnetometer (SCM) will measure magnetic field fluctuations in the frequency range corresponding to the Doppler-shifted plasma kinetic scales, where the dissipation is thought to be taking place, with high sensitivity, to allow the turbulence and dissipation processes to be identified in the range of different near-Earth environments.

Table 13: SCM key characteristics.

Data products	AC B-field LF	AC B-field HF
Range	0.1 Hz - 4 kHz	1 kHz - 200 kHz
Sensitivity	0.1 pT/ $\sqrt{\text{Hz}}$ @ 10 Hz	
	0.01 pT/ $\sqrt{\text{Hz}}$ @ 100 Hz	6 fT/ $\sqrt{\text{Hz}}$ @ 30 kHz
	0.008 pT/ $\sqrt{\text{Hz}}$ @ 1 kHz.	
TM rate	(part of FWP)	(part of FWP)

The dual-band SCM is a tri-axial inductive magnetic sensor, see Figure 48. It is intended to measure three components of the magnetic field in the frequency range between 0.1 Hz and 100 kHz (with sensor bandwidth reaching up to 200 kHz).

Connected (analogue) to the Fields and Waves Processor (FWP), SCM provides spectral information over that range and in addition delivers waveform measurements sampled up to 524 sps.

SCM is composed of three dual-band magnetic antennas. Each antenna is made of a ferrite core with two coils: one for measurements in the Low Frequency range [0.1 Hz, 4 kHz], and the second coil sensitive in High Frequency range [1, 200] kHz. A mutual reducer is inserted to decouple the two windings. The mutual reducer is a cylinder made of a high permeability material. Secondary coils are used as a flux feedback, to create a flat frequency response on a bandwidth centred on the resonance frequencies of the two main coils. The magnetic sensors are assembled orthogonally in a compact configuration.

EMC is an important issue for SCM. The intensity of magnetic fields generated by the spacecraft and by other instruments at the location of SCM should be below the sensitivity level of SCM.

Heritage and evolution

THOR SCM has a long heritage from earlier space missions such as Cluster (STAFF), THEMIS (SCM), MMS (SCM), BepiColombo (PWI/DBSC), Taranis (IMM), Solar Orbiter (RPW/SCM), Solar Probe Plus (FIELDS/SCM) and JUICE (RPWI/SCM). In comparison, the SCM of THOR has a higher sensitivity level than the instruments of all the previous missions. Typically, its noise floor is three times lower than that of Cluster SCM. This makes the THOR SCM capable of measuring very low amplitude magnetic fluctuations, in particular in the pristine solar wind, which is one of the major science goals of THOR. In addition, the THOR SCM will be the first instrument to measure all the three components of the magnetic field fluctuations in the high frequency range up to 100 kHz thanks to its three HF sensors.

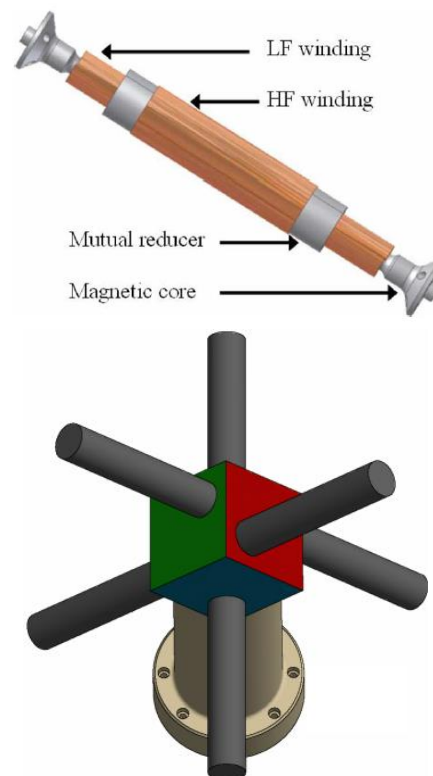


Figure 48: Scheme of the dual band (LF and HF) SCM instrument and of the SCM instrument mechanical concept (tri-axial antennae).

4.2.3 EFI – Electric Field Instrument

EFI will provide measurements of the electric field with unprecedented accuracy and sensitivity in a frequency range extending from DC up to the electron plasma frequency in the solar wind and magnetosheath. EFI will provide very low-noise AC electric field measurements, making it possible to characterize electric field variations associated with kinetic scale plasma processes down to electron scales and plasma thermal noise. EFI

consists of a novel combination of four spherical probes located on the tips of 50-m-long wire booms (EFI-SDP) and three crossed 2.5-m-long dipoles mounted on a rigid boom (EFI-HFA), see Figure 45. As the THOR spacecraft has a Sun-pointing spin axis, the EFI-SDP measurement plane is approximately orthogonal to the Sun direction. This provides in a highly symmetric configuration of the SDP sensors with respect to the Sun (see Figure 63), which does not change with the spin phase, unlike the case for missions having the spin axis perpendicular to the ecliptic plane, e.g., Cluster and MMS. This greatly reduces errors due to asymmetries of the photoelectron cloud, as well as due to wakes caused by the supersonic solar wind flow (see Figure 49), as well as generally reducing the artefacts caused by the spacecraft spin.

Interferometry using the electric field probes can be used to infer wavelengths and scale sizes at the smallest scales in the plasma. EFI is optimized for interferometry measurements, which will make it possible to reliably estimate the phase velocities of electric structures up to 20,000 km/s, i.e., moving with velocities in a range up to the typical electron thermal velocity. This is achieved by having the possibility of sampling sensitive AC-coupled differential and single-ended waveform signals for frequencies up to 100 kHz.

The combination of SDP and HFA makes EFI less susceptible to finite antenna length effects, which is crucial to characterize the electric field structures and the smallest plasma scales, which can be as small as 100 m and below for the plasma regions encountered by THOR.

Table 14: EFI key characteristics.

Science measurements	2D DC E-field, 3D AC E-field spacecraft potential, interferometry
Frequency range	SDP: DC - 100 kHz HFA: 0.1 – 100 kHz
Accuracy	± 0.1 mV/m, $E < 1$ mV/m 10%, $E \geq 1$ mV/m
TM rate	(part of FWP)

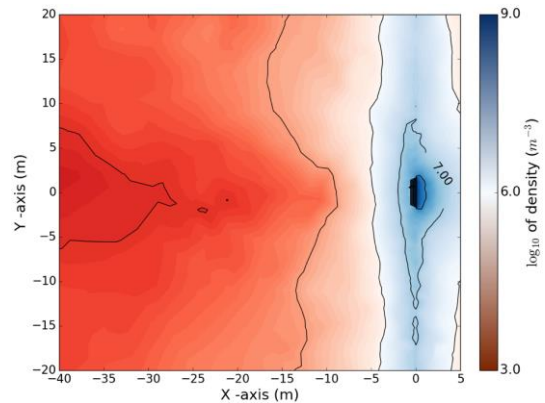


Figure 49: THOR modelling using the SPIS code in GSE XY plane. Wake forms behind the spacecraft (red colour), but electric field wire booms (located at X=0) are outside the wake and can make a high-quality measurement.

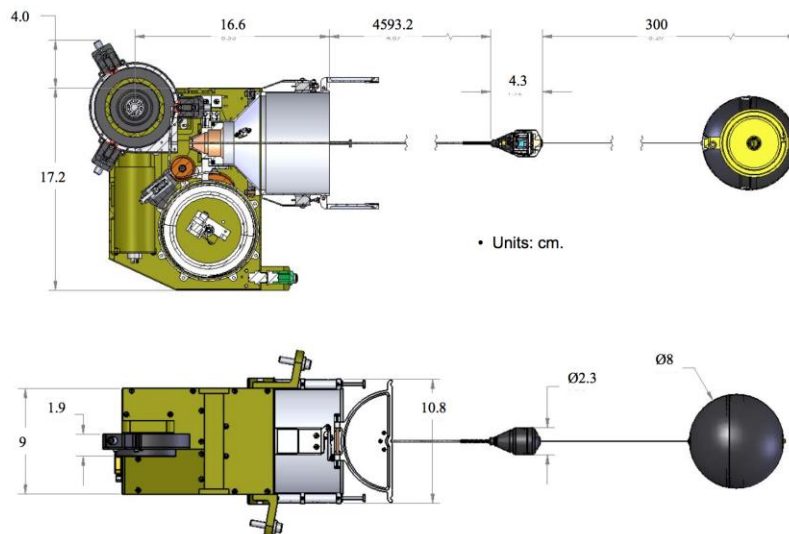


Figure 50: Schematic of EFI-SDP (units: cm).

EFI also measures the floating potential of the satellite, which can be used to estimate the plasma density at very high time resolution. The Sun-pointing attitude greatly reduces spin-related changes in the illuminated area, and hence the associated spin-dependent errors. In combination with densities derived from the observed plasma frequency emission line, EFI monitors the plasma density from DC to a few hundred Hz.

EFI measures components of the electric field vector in space as the potential difference between two probes. In order to bring the probe-plasma voltage closer to the plasma potential, and to decrease the interface impedance to improve the signal to noise conditions, a bias current is applied to the probes. The design goal of the EFI instrument is to measure the electric field vector in the frequency range 0-100 kHz. EFI consists of two sets of sensors as shown in Figure 45: the Spin-plane Double Probes (EFI-SDP) providing high sensitivity DC electric field in the spacecraft spin plane (2D), and the High-Frequency Antenna (EFI-HFA) providing 3D AC electric field at frequencies above ~1 kHz.

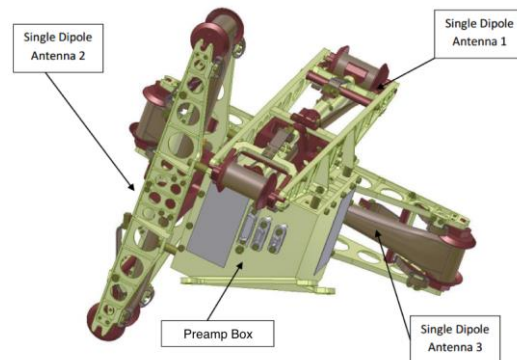


Figure 51: CAD model of the EFI-HFA subassemblies configuration.

In order to achieve the required high input impedance and sensitivity the HFA preamplifier is located at the root of the antenna (Figure 51), and for SDP at the end of the long wire boom, close to the spherical sensor (Figure 50). Both EFI-SDP and EFI-HFA sensors interface with two Boom Electronics Boards (BEBs) hosted in the Fields and Waves Processor (FWP) electronics box. FWP supplies operational and deployment power, and samples and processes the analogue signals from the EFI BEBs.

The four EFI-SDP units are mounted at the side of the spacecraft so that the deployed booms form two orthogonal boom pairs. A schematic of one probe and boom is shown in Figure 50.

EFI-HFA consists of 6 cylindrical probes forming 3 orthogonal pairs having 2.5 m length tip-to-tip. EFI-HFA is mounted on a boom (provided by the spacecraft and shared with the SCM instrument), in such a way that all of the sensors have the same area facing the Sun as well as the spacecraft. A model of the stowed antenna configuration is shown in Figure 51.

Heritage and evolution

The EFI-SDP has direct heritage from the Van Allen Probes EFW wire boom units, which are based on the UC Berkeley design used for 100+ boom units flown on many missions, including multi-spacecraft missions THEMIS and Cluster. EFI-HFA is a relatively new instrument currently in development for the RPWI instrument on the JUICE mission. The HFA antennas on THOR will be identical to the JUICE unit except for some optimisations with respect to mass. EFI electronics (BEBs) have heritage from Solar Orbiter RPW, MMS FIELDS/SDP and Cluster EFW.

4.2.4 FWP – Fields and Waves Processor

The FWP instrument will provide unprecedented measurements of electromagnetic fields from very low frequencies up to 100 kHz. FWP does not include any sensors and the objective is achieved by digitization and digital processing of data from all THOR electromagnetic field sensors, i.e. EFI, SCM and MAG. The waveform and spectral data combine measurements from all field sensors, necessary to resolve the energy transfer associated with the turbulent cascade as well as the polarization and dynamics of coherent plasma waves. Measurements of electron density and temperature from electric field oscillations at the plasma frequency provide an absolute measurement, complementing TEA measurements.

<i>Table 15: FWP key characteristics.</i>	
Data products	Electric and magnetic field waveforms, spectra and cross-spectra, plasma parameters estimated from thermal noise analysis and plasma sounding.
Cadence	Up to 524 ksps
TM rate	Maximum: 1600 kbps (includes EFI, SCM and MAG data)

FWP is an electronic box housing 11 circuit boards with different functionalities, see Figure 52. The boards are interconnected via a backplane. Individual subunits of the FWP box also interface to the spacecraft (power and communication interface) and to EFI, MAG and SCM sensors via external connectors and harnesses.

The instrument represents the single power and communication interface between all electromagnetic field instruments and the spacecraft, and all data from those instruments are transmitted to the spacecraft through FWP.

The individual subsystems of FWP, realized as circuit board cards are listed below:

MAG-IBS and MAG-OBS electronics boards: The FWP box will house the electronics boards responsible for driving and data acquisition from the MAG sensors.

EFI Boom Electronics Boards (BEB): The BEB is a set of two boards in the FWP main electronics box (EFI-SDP, EFI-HFA), one for each set of the sensors.

The **Low Frequency Receiver (LFR)** is a wave analyser board responsible for digitization and processing of multicomponent signals from the EFI antennas and SCM in the frequency range up to 20 kHz. A continuous waveform, waveform snapshots and cross spectral matrices of up to 12 field components can be provided.

The **Thermal noise High frequency Receiver (THR)** is a wave analyser board responsible for digitization and spectral analysis of signals from the EFI antennas and SCM at higher frequencies up to 200 kHz (the 200 kHz bandwidth is necessary to properly resolve a time series of oscillations up to 100 kHz). THR also provides measurements of plasma density through analysis of plasma thermal noise spectra.

Electron Density Sounder (EDS) is an active experiment injecting an oscillating signal on the shield of the EFI/SDP wire booms and measuring the response of the plasma electric field. Analysis of plasma resonances then allows a precise absolute measurement of electron density, which is invaluable for particle instrument cross-calibration.

The **Data Processing Unit (DPU)** is a central computer dedicated to controlling the units within the FWP box, receiving raw telemetry data from all FWP units, formatting and compressing the science data and transmitting them to the spacecraft.

A direct low latency digital link to PPU will be implemented, using the SpaceWire interface. This link will allow FWP to send MAG data to the PPU for the purpose of pitch angle calculation, and spacecraft potential measurements to optimize TEA energy sweeps. FWP will use this link to inform PPU about the selection of high resolution waveform snapshots. This information is used by PPU to store collected high resolution electron data (TEA superbust data) to ensure that both high resolution data products are collected for the same interval.

The FWP instrument provides a common power interface between the spacecraft and SCM, MAG and EFI instruments. The power required from the spacecraft is 28 V power (regulated between 26 V – 30 V). The low voltage power supply unit in the FWP box will convert the primary power to lower regulated voltages used by the subsystems, but also by the preamplifiers of SCM and EFI, therefore their power requirements are included in FWP power budget. Two power supply units and two DPUs in cold redundancy are included for increased reliability.

Consistent with the THOR operations concept, FWP will produce survey and burst data streams in parallel. The survey data will include electromagnetic waveform measurements at a low time resolution, averaged spectra and plasma density estimates. The burst data stream will include waveform data at a significantly

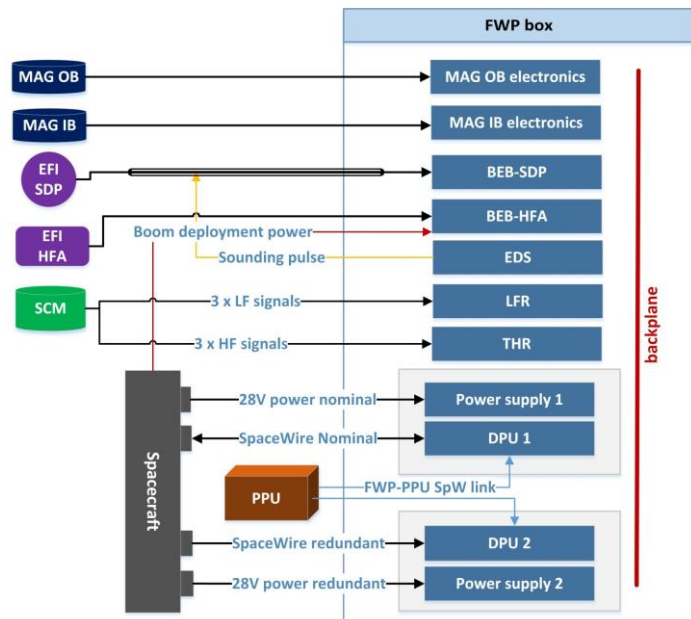


Figure 52: Top level block diagram of FWP showing all external connections.

higher resolution (up to 8192 sps), waveform snapshots sampled up to 524 ksp/s, as well as high frequency spectral data.

Heritage and evolution

All spacecraft dedicated to magnetospheric, solar or planetary physics carried instruments for electromagnetic field and wave measurements. Older spacecraft carried multiple field instruments, each with its own dedicated electronic unit, but more recently, such as on NASA MMS or Van Allen Probes, the electronics for field measurements was integrated in one unit to improve coherency between datasets and to reduce the total mass, power and number of spacecraft interfaces. This approach is used on THOR as well, with FWP serving as the common fields electronic unit.

The strength of FWP compared to previous mission lies in the large number of components to be sampled simultaneously (up to 12 field components as a continuous time series and up to 8 components in high resolution snapshots). The integrated design of the FWP will allow for excellent synchronization between waveform measurements. All sampling clocks of FWP will be derived from a single clock distributed to all FWP sub-units ensuring full phase coherence and zero drift among all FWP signals and also easier removal of spacecraft interference from scientific data by ground post-processing. The FWP real time clock will also be synchronized with the particle instruments (PPU) enabling exact matching of the data, in particular the TEA superburst data overlapping with FWP high resolution waveform snapshots.

FWP design is based on the heritage of the teams in the consortium from previous missions, in particular the recently developed JUICE RPWI and Solar Orbiter RPW, but also from Cluster WHISPER and EFW, MMS DFB, TARANIS and BepiColombo SORBET.

4.2.5 FAR – Faraday Cup instrument

The Faraday cup instrument (FAR) is designed as a fast monitor of solar wind parameters (density, three velocity components, and thermal speed) based on simultaneous measurements of the total ion flux and ion integral energy spectrum by six identical Faraday cups (FCs), see Figure 53, with collectors split

Table 16: FAR key characteristics.

Data products	Ion density, velocity, temperature
Instantaneous Field-of-View	View angle of each FC as well as the whole instrument is 50°.
Time resolution	20-30 ms for H ⁺ , 1.5 – 3 s for He ⁺⁺
Cadence	H ⁺ : 32 ms, He ⁺⁺ : ~ 1.5 - 3 s
Telemetry data rate	Maximum 13 kbps

into two halves. In this configuration, two FCs will be used for a determination of two flux direction angles, one FC will monitor the full ion distribution function within 1-3 s, and one FC will measure the alpha particle distribution with the same cadence as protons. Collector currents of the last two FCs will serve as a proxy of the moments of the proton energy distribution for adjustment of the CSW sweeping ranges (via PPU). The moments will be determined (under a Maxwellian approximation) on the ground with the time resolution determined by the FC geometrical factor and telemetry rate. A sampling rate of 32 Hz is proposed to satisfy the scientific requirements with a sufficient margin. All FAR FCs are oriented approximately along the Sun-Earth line and their entry window diameter is 34 mm, thus the angular characteristics cover large entry angles and the instrument noise will be lower compared to previous designs of the instrument. The location of the FAR instrument on the sunward side of the spacecraft ensures an optimum orientation for the solar wind and foreshock and flank magnetosheath regions.

Heritage and evolution

FAR follows and enhances basic ideas applied in the BMSW instrument that has been operating successfully since 2011 onboard the Spektr-R mission, with a number of improvements to reduce the pre-amplifier noise and to increase overall SNR.

Like BMSW, FAR is designed with six FCs but the split collectors effectively enhance their number. It facilitates in-flight calibration and allows simultaneous measurements of proton moments

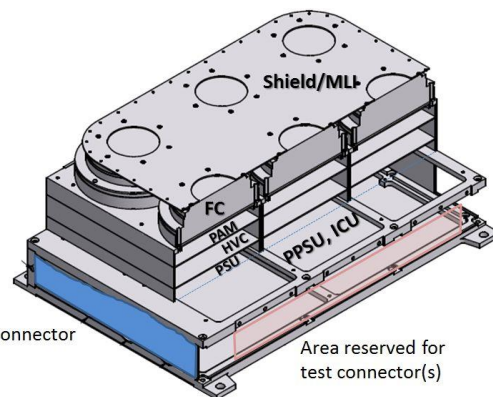


Figure 53: Design of the FAR unit.

and proton and helium energy distributions. The larger voltage on the FC control grids extends the velocity range to 750 km/s. Furthermore, the larger entry windows of the FCs together with the new preamplifiers under development will increase the signal-to-noise ratio by an order of magnitude compared to the previous instrument.

4.2.6 CSW – Cold Solar Wind instrument

The Cold Solar Wind (CSW) instrument is primarily devoted to the study of solar wind turbulence at the ion scale. It will provide measurements complementary to the FAR, which does not provide full 3D velocity distribution functions (VDFs). CSW will measure the 3D VDFs of the cold solar wind ions with high energy (7%) and angular (1.5°) resolutions at a cadence down to 50 ms. To achieve such fast cadences, the fastest modes have reduced energy and angular coverage focussed on the solar wind beam using a well-defined beam-tracking strategy. The He⁺⁺ solar wind population will be measured using specific modes with broader energy range, using the factor 2 separation in energy naturally resulting from the electrostatic analyser energy-per-charge (E/Q) selection.

Table 17: CSW key characteristics.

Data products	3D ion distribution functions
Energy range	20 eV/q - 20 keV/q
Energy resolution ($\Delta E/E$)	7 %
Field-of-View	$\pm 24^\circ$ (elevation and azimuth)
Angular resolution	1.5° (elevation and azimuth)
Time resolution	50 ms
Geometrical factor	$2.2 \times 10^{-5} \text{ cm}^2 \text{ sr eV/eV}$ (for 1.5° anode)
Highest datarate	2627 kbps (w/o compression)

The CSW basic elements and detailed block diagram are respectively displayed in Figure 54 and Figure 55. CSW can be divided into two main units: the detector unit and the electronics unit. The detector unit comprises entrance deflectors which allow it to sweep over look angles $\pm 24^\circ$ in elevation out of the main detection plane, with 1.5° angular binning. A collimator is used to provide the required angular resolution in elevation angles. Deflected and collimated ions are then subject to E/Q selection through a classic top-hat electrostatic analyser. Through this analyser, the E/Q selected ions are focused onto the main detection plane, which consists of 32 channel electron multipliers (CEMs). These perform a $\sim 10^7$ gain in charge collection (due to electron avalanching following the impact of ions on the entrance of CEMs) on anodes with a 1.5° resolution in azimuth over an angular range of $\pm 24^\circ$ as well. More details on the electrostatic design and its measurements capabilities can be found in [240,241], where the operation scheme, resolutions, expected count rates and measurements are demonstrated to achieve significant advancements compared to past missions.

The CEMs and collecting anodes are mounted on a front-end board which contains two 16-way ASICs for signal discrimination. The detector unit also comprises a high-voltage board to supply the entrance deflectors, the analyser plates, and the CEMs with the required voltages and with appropriate high-cadence voltage sweeping properties. The counting and data acquisition (output from the two ASICs) will be performed in a Control Unit board, which will control functions such as the electrostatic analyser voltage sweeps and the entrance detector sweeps.

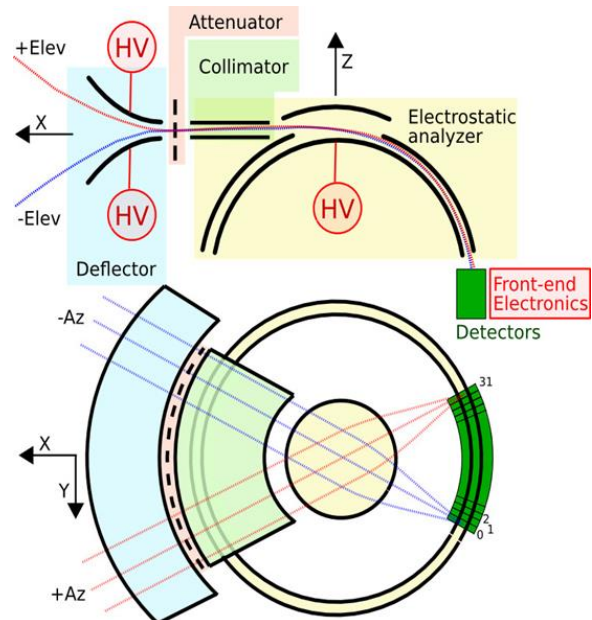


Figure 54: (Top) Vertical view cut of the top-hat analyser, showing the two hemispheres for energy-per-charge selection, as well as the collimator and deflectors at the sunward entrance. (Below) Horizontal view cut illustrating the basic electrostatic optics focalisation of ambient particles (parallel trajectories) on the detector plane when using such a top-hat design.

The electrostatic analyser voltage sweeps will be faster than previous instruments. To achieve the measurement goals, CSW will have an overall geometric factor nearly 10 times higher than earlier instruments. The volume (owing to the high geometric factor) and power consumption (owing to the fast sweeps, 32 CEMs and computing needs) of the instrument are thus also larger. In some modes of operation, CSW will use solar wind peak energy and angular information to optimize the tracking of the solar wind beam, using either the previous CSW measurement or data received from the FAR instrument.

Heritage and evolution

Current space missions such as Wind, Cluster, or THEMIS typically perform *in situ* ion measurements in space with rather low temporal (a few seconds at best), energy (e.g., 15-20%), and angular resolutions (typically 5°-6°, e.g., Cluster or Solar Orbiter). On the one hand, there are instruments like SWEPAM-I on ACE with a high energy resolution of 5% and a reasonable angular resolution (3 - 4.5°), but with a poorer time resolution of 64 s. On the other hand, the ion instruments on the recent MMS mission provide fast measurements of the full distribution function, every 150 ms, but with limited resolution in energy (15%) and angle (11.25°).

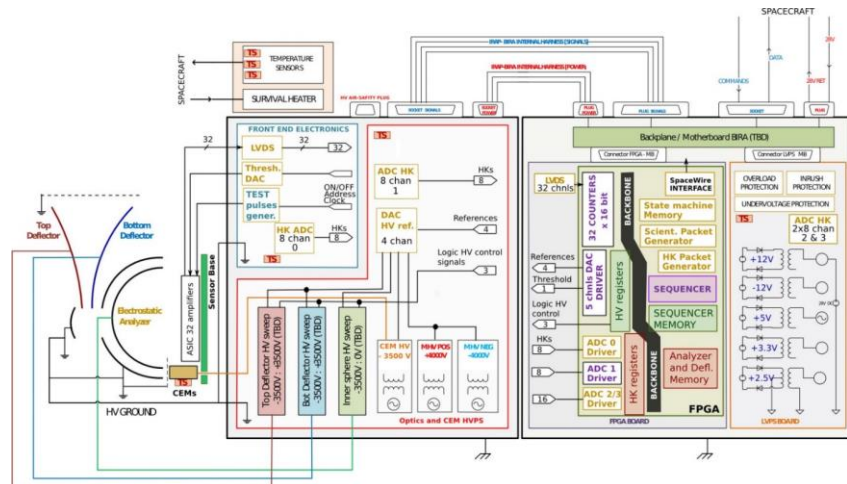


Figure 55: Preliminary block diagram of CSW main units, electronics boards and functionalities.

CSW is designed to obtain high quality measurements in all respects, as required to tackle the small scales involved in solar wind turbulence. The design builds on significant heritage for the key subsystems: the electrostatic optics, detectors, high voltages and control unit. These subsystems all have heritage from projects such as Cluster CIS, STEREO SWEA, MAVEN SWEA, BepiColombo MEA, Solar Orbiter PAS HIS, Venus Express SOIR, Mars Express SPICAM, ExoMars NOMAD and others.

4.2.7 TEA – Turbulence Electron Analyser

The Turbulence Electron Analyser (TEA) will be the first instrument that can provide solar wind and magnetosheath electron moments data at 5 ms cadence and hence provide power spectra of electron parameters such as density or temperature at frequencies up to 100 Hz. The TEA instrument consists of a set of 6 Dual Electron Analyser (DEA) units. The energy range coverage capability is designed to be between 10 eV to 30 keV in order to be able to observe the solar wind core population, the magnetosheath and the magnetotail plasma sheet (the spacecraft potential is expected to typically be +10V or more positive, in which case the least energetic plasma electrons will still be measured with energies of at least 10 eV).

Table 18: TEA key characteristics.

Data Products	3D electron distribution functions
Energy Range	10 eV to 30 keV
Energy Resolution ($\Delta E/E$)	17%
Instantaneous Field-of-View	180° x 5° per EA
Angular resolution	A 3D VDF at 11.25° spacing (polar and azimuth)
Time resolution	A 3D VDF during 5 ms
Geometric Factor	5 x 10 ⁻⁴ cm ² sr eV/eV (per 11.25° anode) 79,872 kbps
Highest datarate	optional additional superburst contribution 2,560 kbps

A 17% $\Delta E/E$ step will give a good balance of resolution and sampling time for the solar wind and magnetosheath. An angular resolution of 11.25° will resolve fine-scale structures in the electron VDF.

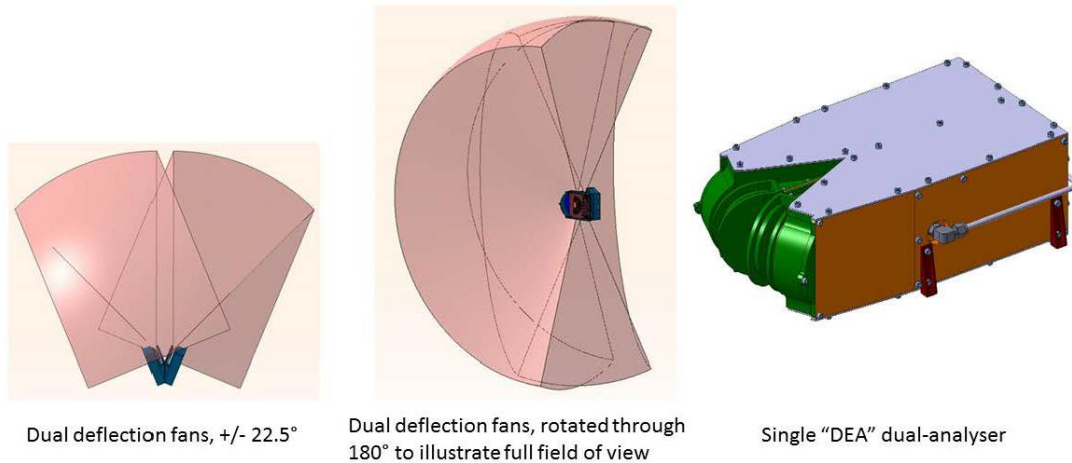


Figure 56: A complete DEEA unit with two analysers and the electronics box. The combined field of view of the pair of analysers is also illustrated.

Each DEEA unit consists of two Electron Analysers (EAs) mounted on an Analyser Electronics Unit (AEU). The instrument commanding, power and telemetry interfaces to the spacecraft will be via the Particle Processing Unit (PPU). The AEU houses the Analyser Electronics and provides the mechanical structure to which the EAs are mounted. The AEU provides the mechanical interface to the spacecraft and the electronic interface to the PPU.

The mechanical structure of a complete DEEA unit with two analysers and the electronics box, and the fields of view of the two analysers are shown in Figure 56.

Each EA consist of a mechanical structure containing the electron optics, a microchannel plate detector assembly and anode boards with pre-amplifiers.

Due to the Sun-pointing spacecraft configuration, an accommodation scenario is proposed (Figure 57), in which the DEEAs are grouped in threes on opposite sides of the spacecraft, and each DEEA is individually oriented as indicated, to provide complementary field of view coverage without any DEEA “looking” directly at the Sun. This could be achieved by mounting each set of 3 DEEA units in a shared “cradle”, however other arrangements are also possible provided the indicated field of view coverage is supported.

Heritage and evolution

The TEA instrument has direct heritage in terms of the analyser head subsystem which is currently in use on the MMS mission, and the sensor electronics sub-systems which will be very similar to those that have been developed for the Solar Orbiter SWA-EAS instrument. The TEA instrument will measure the solar wind and magnetosheath electron plasmas at thermal and suprathermal energies, by collecting 3D velocity distributions, which will be used to calculate moments but which also carry detailed information relevant to testing competing models of energy conversion and dissipation. The cadence is more than 100 times faster than for previous solar wind electron instruments (e.g., Wind), and a factor 6 faster than for electron instruments of the MMS mission. A novel capability of the TEA instrument is a magnetic field tracking mode able to produce 2D pitch-angle resolved measurements either at 5 ms (with improved counting statistics compared to 3D data) or at 1.25 ms for maximum time resolution (for use in studying electron scales in the fast solar wind). TEA will be the first instrument that can supply individually timed electron detection events. These “superburst” data will be acquired periodically alongside high time resolution wave data during intervals of 125 ms duration, to support wave-particle interaction studies (see Section 6.5).

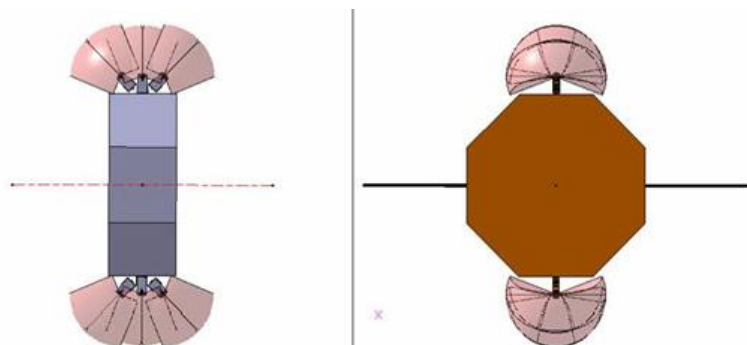


Figure 57: Proposed accommodation of the TEA DEEA units onboard the spacecraft.

4.2.8 IMS – Ion Mass Spectrometer

IMS will provide for the first time very high temporal resolution measurements of mass-resolved ions (H^+ , He^{++} , O^+) in near-Earth space. The time resolution of the 3D velocity distribution functions will be 150 ms for H^+ and 300 ms for He^{++} in the foreshock, shock and magnetosheath turbulent regions. Oxygen is measured with lower time resolution. IMS measurements are required to study how ion-scale turbulent fluctuations heat and accelerate different ion species, e.g., how He^{++} particles are preferentially heated with respect to H^+ within ion-scale coherent structures in the magnetosheath. IMS measurements are also crucial to properly distinguish H^+ and He^{++} particles in the foreshock/shock turbulent region, since they cannot be simply separated by energy as done for cold ions in the pristine solar wind due to their higher temperature produced by shock heating.

The IMS instrument is composed of three main subsystems, as shown in Figure 58: the entrance optics, the TOF chamber and the electronics box. The instrument combines energy (E) per charge (q) selection by an electrostatic analyser (ESA) and azimuthal direction selection by electrostatic deflectors together with a time-of-flight (TOF) measurement, to determine 3D distribution functions of ions with given mass per charge M/q . Four IMS sensors are mounted on the spacecraft and are phased by 90° in the spacecraft spin plane, Figure 59. Each sensor covers a $45^\circ \times 360^\circ$ Field-Of-View (FOV) so that the total FOV of IMS is 4π . The energy range is 10 eV/ q to 30 keV/ q and the mass range is 1-32 amu. Ions entering the deflection system are selected in E/q by the ESA. At the exit of the electrostatic analyser, ions are accelerated by 15 keV/ q (nominal post-acceleration) and then hit a thin carbon foil located at the entrance of the TOF section. Electrons knocked off the foil are steered to the inner micro-channel plate (MCP) and a sectored anode (Anode Board), providing the “start” signal and the ion entrance position. Ions pass through the foil and hit the outer MCP to generate a “stop” signal. Within the TOF chamber, the ion velocity is obtained from the difference of the start and the stop signal, the so-called "time of flight", and from the length of the TOF chamber (5.8 cm). The mass per charge M/q is then derived from the ion velocity and the E/q earlier determined by the ESA. The high flux in the pristine solar wind will be reduced in the sunward direction through an electrostatic flux reducer by an adjustable factor of up to 100. IMS detection electronics (Analog Board) combines two 16-channels ASIC Charge Pulse Discriminators, which perform charge amplification and discrimination and generate start and stop signals, together with one discrete Time-to-Amplitude-Converter associated to an FPGA, which compute the time of flight. The electronics box includes both fast sweep and static High Voltage Power Supplies, Low Voltage Power Supplies, and Digital and Processor (CPU) boards assuring instrument control and data formatting.

Table 19: IMS key characteristics.

Data products	3D ion distribution functions (H^+ , He^{++} , O^+)
Energy range	10 eV – 30 keV
Energy resolution ($\Delta E/E$)	10 %
Instantaneous field-of-View	$4 \times 6^\circ$ (azimuth) $\times 360^\circ$ (polar)
Angular resolution	11.25° (azimuth) $\times 11.25^\circ$ (polar)
Mass-per-charge resolution	≥ 8 for He^{++} , ≥ 3 for O^+
Time resolution	150 ms for H^+ , 300 ms for He^{++}
Estimated Geometrical factor	$5.74 \times 10^{-4} \text{ cm}^2 \text{ sr eV/eV}$ (per 11.25° pixel)
Highest datarate	5927 kbps (w/o compression)

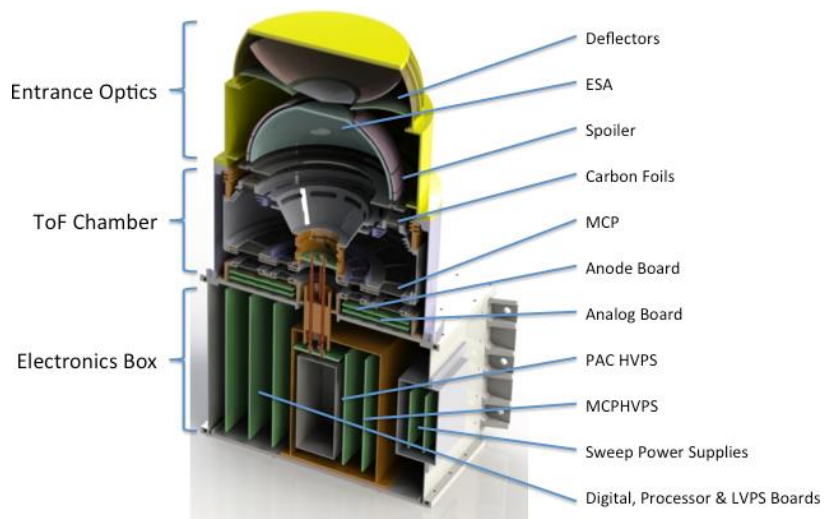


Figure 58: CAD model of the IMS instrument

Heritage and evolution

The IMS has significant heritage for all the three sub-systems from previous and ongoing missions including Cassini CAPS, Cluster CODIF, STEREO PLASTIC, MMS HPCA, Solar Orbiter SWA and BepiColombo MPPE. IMS can perform the fast composition measurements due to the use of 4 units, even though the units are individually similar to heritage designs. The IMS high time resolution measurements are not possible with composition instruments on earlier and current missions like HPCA on MMS (10 s resolution) and CODIF (4 s resolution) on Cluster. In addition, the combination of a sufficiently long time-of-flight chamber (6 cm) and modern detection electronics allows for adequate discrimination of H^+ and He^{++} and reduction of dead time.

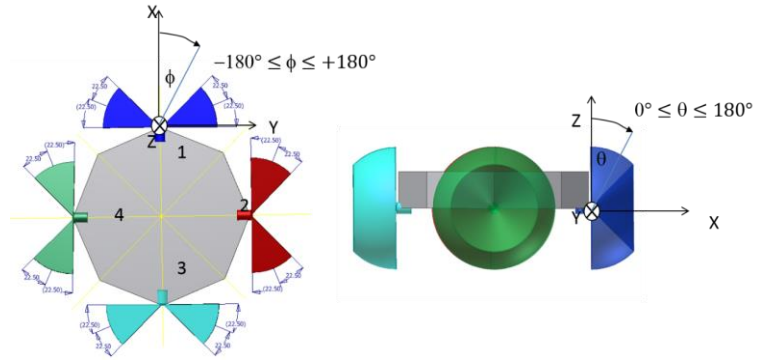


Figure 59: Accommodation of the four IMS sensors and IMS coordinate system.

4.2.9 EPE – Energetic Particle Experiment

EPE is a particle instrument that will measure the energy spectra and angular distributions of energetic electrons (20-700 keV) and ions (20-8000 keV/n). The instrument has two sensor units, each one measuring with two double-ended telescope pairs in four view cones. Utilizing the spin of the spacecraft, EPE observations cover the full sky, see Figure 60.

The two ends of the telescopes observe electrons and ions, respectively. Each telescope consists of a stack of three solid-state detectors. On one end, the stack is covered by a thin polyimide layer, stopping ions below a few hundred keV/n but letting electrons pass almost unaffected. The uppermost detector (500 μm thick Si) on this side is operated in anticoincidence with the second and, thus, observes the energy spectrum of electrons stopping in the detector. The other end of the telescope has no foil but a broom magnet instead that deflects electrons below several hundred keV. This side of the telescope has a 20 μm thick Si detector followed by a 500 μm Si detector, which thus form an ion telescope observing at energies from 20 keV to 8 MeV/n. Ions passing the first detector can be identified using the ΔE vs. E technique, which enables full elemental and even isotopic resolution at MeV/n energies. Ions stopping in the thin detector and depositing more than 1.2 MeV are heavier than H (mainly He at >300 keV/n) and more than 4.8 MeV are heavier than He (mainly CNO above

Table 20: EPE key characteristics.

Data products	Particle VDF
Energy range	e ⁻ : 20-600 keV i ⁺ : 20-8000 keV/nuc
Energy resolution (ΔE/E)	20%
Instantaneous Field-of-View	45° per view cone (4 cones per unit)
Time resolution	< 15 s
Geometrical factor (per telescope)	e ⁻ : 0.5 cm ² sr i ⁺ : 0.1 cm ² sr ion
Cadence	15s for 3D VDF 7.5s for pitch angle VDF
Highest datarate	13 kbps

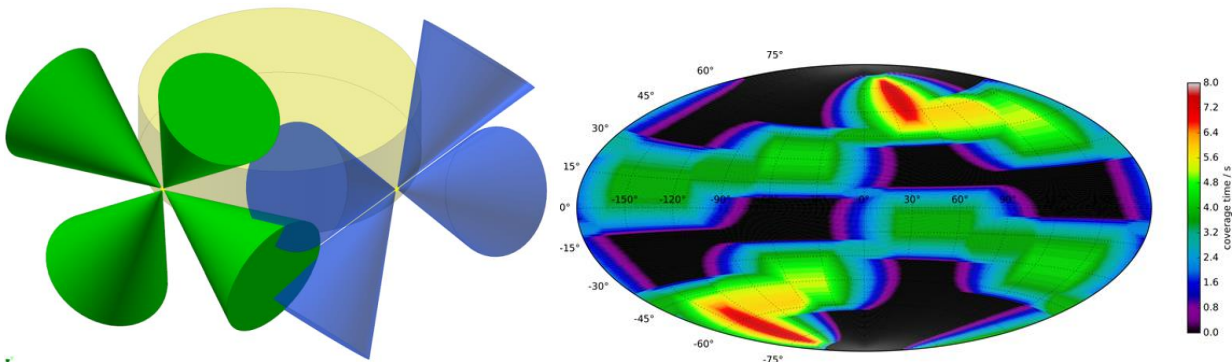


Figure 60: (Left) Example of a possible accommodation of the two sensors of EPE. (Right) Sky coverage of the EPE detectors.

300-400 keV/n). Thus, partial elemental resolution is achieved already from ~ 300 keV/n.

Each of the two identical EPE units, see *Figure 61*, integrates the sensors and electronics in a single package. Each unit has an independent data and power interface to the PPU, providing partial redundancy.

The EPE instrument collects almost the full 3D distribution of all particles in one half of the spacecraft spin period (every ~ 15 s). The relative orientation of the 8 independent telescopes was conceived to enable good quality sub-spin measurements for most magnetic field configurations. The instrument will be able to generate energy-resolved VDF snapshots in 8 directions every ~ 2 s and, on average, it will be possible to recover a full pitch angle distribution of energetic ions and electrons every 7.5 s.

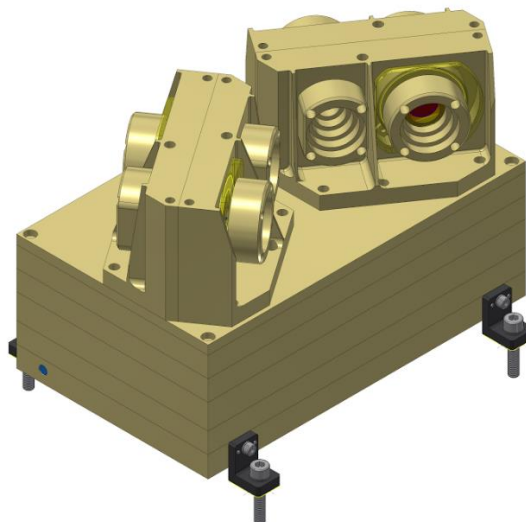


Figure 61: CAD model of the EPE unit.

Heritage and evolution

EPE has heritage from the Solar Orbiter instrument EPT. The improvement compared to EPT consists of the addition of a third detector in each sensor, which increases the capability of compositional measurements. This detector design has heritage from SOHO ERNE LED and STEREO IMPACT LET.

4.2.10 PPU – Particle Processing Unit

PPU is a central electronics unit for all the particle instruments: IMS, CSW, TEA and EPE. The approach of a common processing unit allows an efficient management for correlative plasma measurements, also facilitating interoperation with the other instruments on the spacecraft.

The PPU has to provide the particle instruments with adequate data management and processing capability to assist the instruments in the fulfilment of their performance requirements.

The three basic data processing operations of the PPU are:

Moments computation: PPU performs moment calculations on particle instrument 3D distribution functions. The resulting data on density, velocity vector, pressure tensor and heat flux vector are included in the telemetry stream toward the spacecraft memory.

Assistance to particle instruments in the measurement of pitch angle distributions (PADs): In this case PPU drives the particle instrument sensors in order to record 2D PADs with respect to the magnetic field vector received from MAG through FWP.

Data compression: The PPU compresses the 3D and 2D PADs with a lossless compression algorithm.

Moreover, the PPU assists CSW in the solar wind beam tracking operation.

The PPU provides a single power, telemetry, and control interface to the spacecraft as well as power switching, commanding and data handling for IMS, CSW, TEA and EPE, as shown in *Figure 62*.

The PPU performs the following tasks:

- Receive/Transmit commands from spacecraft;
- Distribute primary power to sensors;
- Drive instrument operations (at different levels according to instrument);
- Acquire and process data from the instruments;
- Download science and telemetry data through the spacecraft interface

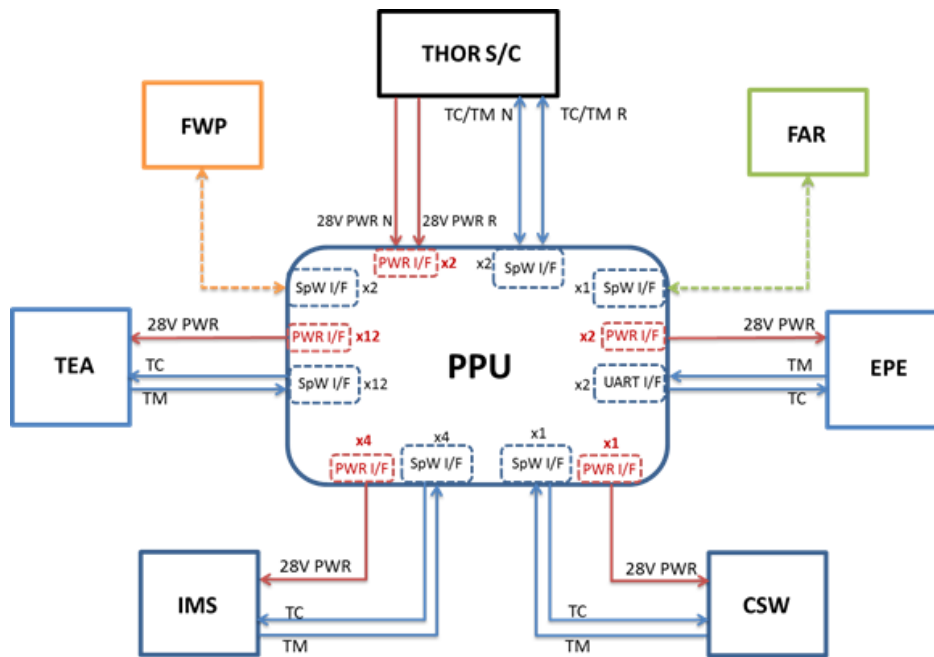


Figure 62: THOR PPU Interface Block Diagram.

The PPU architecture is based on the jointly use of a GR712RC Dual-Core LEON3-FT SPARC V8 processor and several FPGA operating as hardware accelerators, communication manager, or communication router.

The PPU has a fully redundant configuration, with two Central Processing Unit boards (CPU), based on the dual-core LEON3-FT processor and two groups of two Compression and Scientific Processing boards (CSP) based on FPGAs. Each CSP is provided with three FPGAs (Actel RTAX family) and dedicated input (raw scientific data) and output (data resulting from processing) buffers for each sensor.

The PPU delivers two data streams to the spacecraft memory; the survey data (e.g., moments of the distribution functions) and burst data (high resolution distribution functions and TEA superbust data).

Heritage and evolution

The proposed design for PPU is based on experience and designs from the Solar Wind Analyser Data Processing Unit (SWA-DPU) of Solar Orbiter, developed under INAF-IAPS responsibility by a consortium of Italian Industries led by Technosystem Development (TSD) - Pozzuoli, Naples. SWA is a suite of instruments, composed of 2 Electron Analyser Systems, the Proton-Alpha Sensor and the Heavy Ion Sensor (HIS), which provide the solar wind ion and electron bulk properties and ion composition. All of these sensors are connected to the DPU, which is in charge of supporting the overall instruments functions related to power, control, temporary storage, communication and computational capability (e.g., moments computation and 3D compression).

With respect to SWA-DPU, whose Central Processing Unit board is based on Leon2FT Sparc V8 Processor, PPU is characterized by enhanced controlling and data handling/processing capabilities, necessary for managing the increased number of the suite instruments and the high temporal and phase space resolution of the particle measurements. This is achieved by means of the optimized use of the dual-core LEON3-FT together with an adequate number of FPGA based HW accelerators.

4.2.11 ASP - Active Spacecraft Potential control unit

ASP will be under Prime Contractor procurement and is not part of the scientific payload of THOR.

The ASP unit reduces the positive spacecraft potential by emitting indium ions of 4 to 10 keV energy. Reducing the spacecraft potential to lower values, 10 V and below, allows for more accurate plasma measurements at low energies, i.e., energies comparable to the spacecraft potential. On the other hand, too low spacecraft potential may lead to an increased photoelectron cloud and less accurate electric field measurements. Therefore, the capability to control the spacecraft potential is very valuable for finding the optimal spacecraft potential to obtain the highest quality measurements.

The ASP units will shoot the beam into the spacecraft wake (anti-sunward) direction to ensure that the emitted ions do not disturb the symmetry in the spacecraft potential within the spin plane, see Figure 63. This ensures that accurate electric field measurements can be made with ASP being activated. THOR accommodates two ASP units to ensure a proper control of the spacecraft potential.

The main constituent of the ASP instrument is a pair of ion emitter units (4 emitters in total), each connected to a dedicated high voltage supply. The four emitters are present due to lifetime and redundancy reasons. The emitters currently flying on the NASA mission MMS have demonstrated a capability to achieve 9350 h of operational time at a current level of 20 μA , which is the nominal operational value for MMS. In the pristine solar wind and magnetosheath THOR is expected to be a few volts more positive than MMS due to THOR having larger fraction of Sunlit area.

4.3 Payload operations

The THOR payload is operated as a single virtual instrument with the intention to simplify the operations planning by the SOC/MOC and to minimize the interaction between the SOC and the instrument teams. From an operations point of view, SOC and MOC interface with only three instruments, FWP, PPU and FAR.

4.3.1 Payload modes

The THOR instruments will implement a simple set of operation modes which can be commanded by a single telecommand: OFF, INIT, STANDBY, SAFE, CALIBRATION, SCIENCE, with clearly defined rules for transition between the modes. This allows planning of the payload operations by SOC based on a set of well-defined flight rules, e.g., switching off and on some of the instruments during manoeuvres, radiation belt crossings or long eclipses, without the need to interact with the instrument teams.

4.3.2 Science data

In the SCIENCE mode the payload generates two parallel science data streams transferred to the spacecraft mass memory:

Survey data covering the full time at low bitrate, intended for immediate downlink. All the survey data is downlinked to the ground.

Burst data covering the full time in the Burst Collection Regions (BCRs) at high bitrate. Only a small fraction of the burst data is downlinked to the ground.

The primary way to select the burst intervals is based on ground analysis of the downlinked survey data by the SITL, see Section 6.3.3. This payload operations strategy is similar to the one used in the NASA MMS mission. A simple burst prioritization algorithm, based on the variation of the electromagnetic field in several frequency bands, will be also implemented in FWP, assigning a numerical priority parameter to each interval of burst data. In case the ground selection is not available, the spacecraft uses the priority parameter to determine the order in which the old data is overwritten.

Example of science data contained in the survey and burst streams planned to be used during NSP1 (primary focus on the magnetosheath science, TM driver) are given in Table 21 and Table 22.

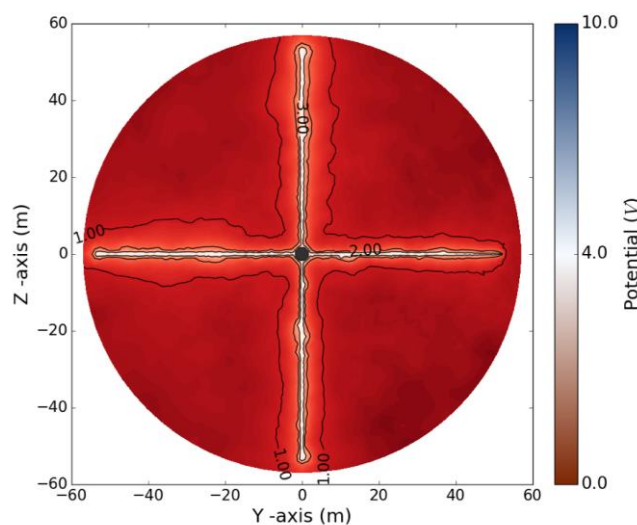


Figure 63: The potential distribution around the THOR spacecraft simulated using the SPIS code with ASP ion beam being on. The simulation confirms that the ASP ion beam is not affecting the symmetric potential distribution in the spin plane that is critical for sensitive electric field measurements.

Table 21: Survey telemetry targeting magnetosheath science

Instrument	Description	Time resolution [ms]	Compr. TM rate [kbps]
MAG	3D DC B-field waveform, 32 sps	31.25	2.0
SCM	3D AC B-field waveform, 32 sps	31.25	0.9
EFI	2D DC E-field waveform, 2xDCV SDP, 32 sps	31.25	1.4
FWP	HF spectral matrices, 10 components, 100 frequencies	7500	2.2
FWP	HF spectra, 6 components, 400 frequencies	7500	3.7
FAR	Ni, Ti, Vi derived from 8 currents + 4 voltages	32	3.7
TEA	3D distribution e-, 32 energies, 12x16 angles	500	53.2
TEA	e- moments, n, V, Tpar, Tperp1, Tperp2	100	8.3
CSW	3D distribution SW H+, 24 energies, 32x32 angles	5000	27
CSW	SW H+ moments (N,3V,6P,3Q)	150	0.6
IMS	3D distribution H+, 36 energies, 32x16 angles	7550	13.1
IMS	H+ moments: N, 3xV, 6xPij	150	0.4
IMS	3D distribution He ⁺⁺ , 36 energies, 32x16 angles	15000	6.6
IMS	He ⁺⁺ moments: N, 3xV, 6xPij	300	0.2
IMS	3D distribution O+, 36 energies, 32x16 angles	15000	6.6
IMS	O+ moments: N, 3xV, 6xPij	1500	.1
EPE	3D distribution of energetic e- and H+, He ⁺⁺ , O+, 16 energies, 3x8 angles	30000	0.9
Total			131

Table 22: Burst telemetry targeting magnetosheath science

Instrument	Description	Time resolution [ms]	Compr. TM rate [kbps]
MAG	3D DC B-field waveform, 128 sps	7.81	9
SCM	3D AC B-field waveform, 4096 sps	0.24	100
EFI	3D AC E-field waveform, 4096 sps	0.24	100
EFI	2D DC E-field waveform, 2xDCV SDP, 4096 sps	0.24	132
FWP	10D snapshot 32 ksps 3x SCM-HF, 3x HFA, 2x ACE SDP, 2x ACV SDP, 131072 samples	15000	709
FWP	10D snapshot 256 ksps 3x SCM-HF, 3x HFA, 2x ACE SDP, 2x ACV SDP, 32768 samples	15000	180
FWP	HF cross spectra, 24 components, 200 frequencies	2000	29
FWP	HF spectra, 8 components, 400 frequencies	500	74
FWP	QTN Ne, Te values, 128 sps	7.81	1
FAR	Ni, Ti, Vi derived from 12 currents + 6 voltages	16	15
TEA	3D distribution e-, 32 energies, 32x16 angles	5	19661
TEA	Electron Superburst snapshot, 125 ms duration, timestamps of e- impacts from 32 anodes	60000	640
CSW	3D distribution SW H+, 24 energies, 32x32 angles	150	870
IMS	3D distribution H+, 36 energies, 32x16 angles	150	659
IMS	3D distribution He ⁺⁺ , 36 energies, 32x16 angles	300	334
IMS	3D distribution O+, 36 energies, 32x16 angles	1500	66
EPE	3D distribution of energetic e- and H+, He ⁺⁺ , O+, 32 energies, 6x8 angles	15000	7
Total			23585

4.3.3 Instrument settings

In SCIENCE mode, the instrument settings (e.g., energy range, angular resolution, sampling frequency) are changed by using pre-defined sequences (macros) stored in the instruments flash memory. A similar macro approach exists on, e.g., the Rosetta LAP instrument. Uploading new macros is considered a routine operation, which can be part of standard operations. The execution of a macro is tested on a ground reference unit by the instrument team before uploading, and its telemetry output and power consumption is verified. Tests on any integrated unit at ESA will not be needed for post-launch macro uploads. During prelaunch integrated tests, several macros will be used for on-ground calibration and verification purposes.

SOC and MOC payload operation is simplified by the fact that all instruments except FAR interface with the spacecraft via FWP and PPU. Therefore, a single macro can be used to control instrument settings, further decreasing the telecommand volume. A library of macros with corresponding power and telemetry parameters is provided by instrument teams to the SOC. The SOC will use them for planning and commanding.

4.4 Electromagnetic cleanliness

The THOR payload is designed to provide very sensitive measurements of electromagnetic fields and charged plasma particles. Electromagnetic fields generated by the spacecraft itself can impact such measurements by introducing artificial signals interfering with the weak natural electromagnetic fields measured by the sensors. The spacecraft electrostatic field and magnetic dipole field can deflect low energy charged particles, distorting the measurements of plasma distribution functions. The ambitious science objectives of THOR can thus only be achieved if the electromagnetic field generated by the spacecraft platform and payload is controlled and maintained within limits compatible with the payload sensitivity.

The requirements on electromagnetic cleanliness (EMC) of the spacecraft have been studied and formulated by the EMC working group during phase A and are included in the THOR SciRD [242]. The EMC aspects of THOR have also been presented at a topical conference and summarized in an article [243]. The EMC requirements discussed below are only applicable in regions of interest during nominal science operation. Outside of those intervals, in particular during manoeuvres and close to perigee, deviations from the required limits are acceptable.

4.4.1 DC and low frequency magnetic field

Requirements on the spacecraft magnetic field are imposed to ensure that proper in-flight calibration of MAG sensor can be performed and that the target accuracy in absolute magnetic field measurements can be reached by the MAG instrument. The total spacecraft magnetic field magnitude is limited to 2 nT at the position of the outboard MAG sensor, mounted on a boom at least 6.3 m away from the spacecraft body and slow variations of the spacecraft field on the timescales of minutes to hours are also limited. Spacecraft magnetic field compliant to these limitations can be subtracted from science data using the dual magnetometer technique, combined with offset calibration based on the known properties of rotational discontinuities in the solar wind [244]. This method shall allow reaching the accuracy specified by the THOR requirement **RP3**. The 2 nT limit on spacecraft magnetic field is less strict than the corresponding requirement for Cluster spacecraft (0.25 nT), but stricter than for Solar Orbiter (20 nT). In comparison to Solar Orbiter, reaching better magnetic cleanliness shall be facilitated by THOR being a spin stabilized spacecraft, eliminating the field perturbations from reaction wheels, and the significantly longer magnetometer boom.

Finally, the EMC requirements limit the effect of the spacecraft magnetic field on the trajectory of low energy electrons registered by the TEA instrument and is thus expressed as the integrated magnetic field along radial particle trajectory. The imposed limit corresponds to the magnetic field introducing a deviation of 20% of TEA angular resolution on an electron of 5 eV (very low energy electrons are assumed to be accelerated by spacecraft potential to energies above 5 eV).

4.4.2 Electrostatic requirements

Charging of the spacecraft due to photoelectron fluxes impacts measurements of both low frequency electric field and particle distributions. In particular, electric fields associated with any differential charging of the spacecraft surface difference on the spacecraft surface would strongly degrade low frequency electric field measurements. The voltage between two points on the surface is thus limited to a maximum of 1 V, which effectively requires the spacecraft surface to be sufficiently conductive. An analogous requirement was applied to many previous missions performing electric field measurements, including Cluster, Solar Orbiter, JUICE or MMS.

Positive charging of the spacecraft will also prevent low energy positively charged ions to reach the detectors and the electrostatic field will bend the trajectories of electrons, potentially introducing errors in particle measurements. Estimates performed in phase A indicate that a spacecraft potential not exceeding 10 V is acceptable for the science measurements and THOR will carry an active spacecraft potential control device, allowing reduction of the spacecraft potential below this limit. Similar potential control instruments have been successfully used on several previous spacecraft (including Cluster, Double Star or MMS) and the technology is thus considered mature and reliable.

4.4.3 AC electric and magnetic field requirements

A significant aspect of the THOR EMC program is the requirements imposed on AC electric and magnetic field emissions from the spacecraft in the frequency range from 1 Hz to 200 kHz applied at the location of the SCM sensor and EFI electric antennas. Requirements are formulated in the spectral domain, for broadband noise and narrowband emissions separately. While broadband emissions cannot be removed from scientific data efficiently and must thus be eliminated, stable narrowband spectral spikes can be removed from the data by post-processing and higher amplitudes are thus acceptable. The THOR science objectives require that plasma waves are resolved through high quality time series measurements up to 100 kHz. To ensure sufficient quality of waveform measurements, the data will be sampled at frequencies up to 524 kHz and EMC requirements impose limits on interference up to the frequency of 200 kHz. Higher frequency interference can be eliminated by electronic filters in the FWP instrument, but the margin between 100 kHz and 200 kHz is required to implement filters offering sufficient attenuation and at the same time low distortion below 100 kHz.

The red line in Figure 64 shows the limit imposed by THOR EMC requirement on spacecraft magnetic emissions. This curve follows the expected performance of the THOR search coil magnetometer (green line) which improves on the heritage instrument STAFF from the Cluster spacecraft [3] (magenta line). While the EMC requirements are stricter than in the case of Cluster at the location of the sensor, when the longer booms of THOR are taken into account and the magnetic field is re-scaled appropriately, the limit imposed on the spacecraft magnetic emissions at their source is not much stricter than that of Cluster. The black dashed line shows the THOR requirement level re-scaled to the Cluster boom length for easy comparison with the analogous Cluster EID-A requirement (blue) and performance obtained in space (magenta). This assumes a boom length of 6.3 m for THOR.

Figure 65 shows analogous requirements for spacecraft generated electric fields required for unperturbed measurements of electric fields associated with turbulence at lower frequencies and plasma thermal noise at higher frequencies. The limit is imposed on the radiated electric field as seen by the

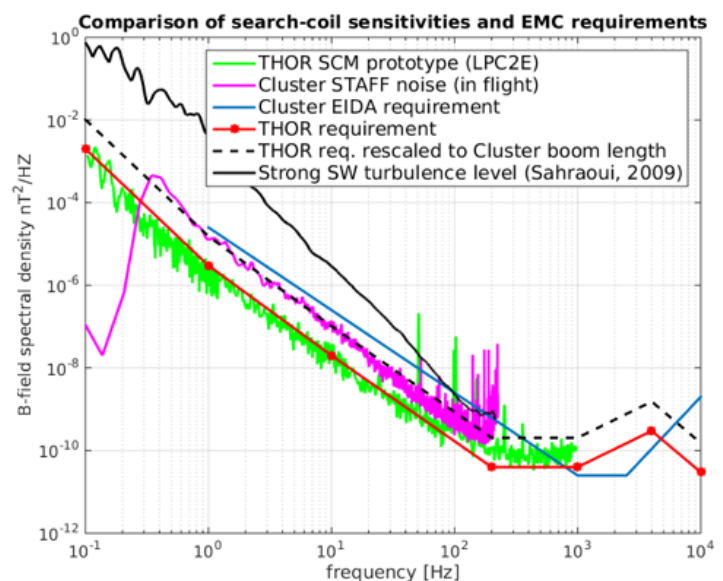


Figure 64: Comparison of THOR AC magnetic field requirement (red line) and performance of existing search coil magnetometers. Black line shows a typical turbulence level in the solar wind.

THOR double probe antennas (SDP) in the spin plane and 2.5m tip-to-tip tri-axial dipole antennas (HFA) mounted on a boom. The black lines show the expected instrument noise for the double probe antennas (SDP) and dipole antennas (HFA). The red and orange lines show the expected observed noise floor in the solar wind, including shot noise and effect of the plasma environment. Green lines show the actual EMC requirements. Over-plotted in grey are also actual solar wind spectra from the Cluster and THEMIS double probe experiments, showing the improved performance of THOR over the heritage instruments.

The curves in Figure 64 and Figure 65 set the limit for broadband spacecraft emissions. Narrowband spectral spikes, such DC-DC converter interference, can be allowed to exceed this level by 30 to 45 dB (depending on frequency). However, it must be ensured that these spikes can be effectively removed from the data by digital post-processing. For this reason, the spikes exceeding the requirement must be sufficiently stable in frequency that they remain within the same bin of (2048-point) discrete Fourier transform (DFT). The spikes also need to be limited to at most 2% of each frequency decade. The EMC requirements suggest an implementation of a stable master spacecraft clock at a frequency of 524 kHz distributed to platform devices and payload elements, such as FWP. This master clock would be used to synchronize all DC-DC converters likely to produce interference as well as the sampling clock of the FWP instrument. This phase synchronization of sampling clock and major sources of interference allows for very efficient removal of interference from the data, as shown for example on the STEREO spacecraft which used a similar concept.

4.4.4 Requirement verification

An important part of the THOR EMC program will be the verification of the requirement through ground tests and modelling. AC electromagnetic field emissions above several Hertz can be relatively easily characterized by direct measurements in an electromagnetically shielded chamber. Requirements on low frequency fields must be verified by a combination of direct measurements (remnant spacecraft magnetic dipole can be characterized in a dedicated facility) and modelling of induced magnetic field and spacecraft charging. In particular, a detailed spacecraft electrostatic charging model based on SPIS software (see Figure 49 and Figure 63 for initial results) shall be developed during mission preparation.

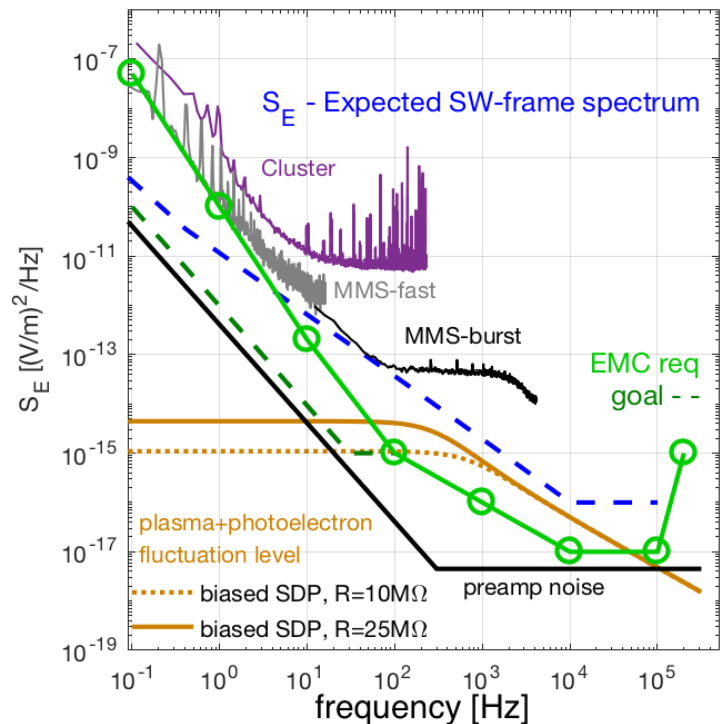


Figure 65: THOR AC electric field requirements compared with solar wind E-field levels expected for THOR and those measured by heritage instruments. Expected electric field spectra in the solar wind $S_E = V_A^2 S_B$ (inertial range), $V_A = 58$ km/s, $S_E \sim k^2 S_B$ (kinetic range), S_B is based on [21].

5 Mission design

5.1 Mission requirements

The main mission requirements are summarized below. The complete set of applicable requirements can be found in the Mission Requirement Document [245] and Science Requirements Document [242].

- THOR shall meet the following residence times in the Top Priority Regions (TPR) of each Key Science Region (KSR):
 - 60 days in the pristine solar wind
 - 47 days in the foreshock
 - 21 days in the bowshock
 - 14 days in the magnetosheath
- THOR shall be able to operate its payload:
 - 90% of the time spent in the TPR
 - 70% of the time spent in the nominal science phase
- THOR shall return 15.7 Tbits of high quality burst data, with a breakdown per phase as described in Table 23.

Table 23: Total KSR burst data volume science requirement and its breakdown per NSP.

	NSP1	NSP2	NSP3	TOTAL(Gbits)
Magnetosheath	5155.0	1289.0	0.0	6444.0
Bow shock 70*30min	2377.0	595.0	0.0	2972.0
Foreshock	0.0	2449.0	433.0	2882.0
Pristine solar wind	0.0	984.0	2296.0	3280.0
TOTAL (GBITS)	7532.0	5317.0	2729.0	15578.0

- THOR shall be spinning at 2 rpm, with a spin-axis oriented towards the Sun when performing science measurements.
- THOR shall comply with EMC requirements described in Section 4.4 to achieve the required science measurement performance.

5.2 Mission design drivers

THOR mission drivers are summarized below:

- The orbit and phases duration are driven by the science need to cross the key science regions, by the radiation environment, and by the specific manoeuvrability constraints of a Sun-pointed spinning satellite.
- The burst data return requirements drive the concept of operations of the mission, and the spacecraft on-board memory sizing.
- The payload-derived requirements, including EMC requirements, drive the whole spacecraft design to a large extent.

5.2.1 Key Science Regions crossings

As per the science requirements, THOR has to cross each Key Science Region (KSR) - magnetosheath, bow shock, foreshock, and pristine solar wind - and spend sufficient time in the Top Priority Regions (TPR). KSR and TPR are defined in the science requirements **R10** and **R13** and can be seen also in Figure 44.

All four KSR are best visited by spreading the nominal mission into 3 nominal science phases (NSP), corresponding to three highly elliptical orbits with a perigee at 6 Earth Radius (R_E), and an increasing apogee of 15, 26 and 45 R_E , with one year spent by the spacecraft in each NSP. The line of apsides of the orbit is chosen to coincide with the intersection of the Earth's equator and the ecliptic plane, the vernal equinox direction, to ensure a sufficiently small Sun-Earth-THOR angle at apogee to maximize science return.

5.2.2 Specific constraints for orbital manoeuvres

Since THOR is a spinning spacecraft with a Sun-oriented spin axis, orbit change manoeuvres require preferably at the same time the spin axis to be 1) tangential to the orbital velocity at perigee (for apogee raising manoeuvre) or apogee (for perigee raising manoeuvre) and 2) Sun-pointing to ensure the body-mounted solar arrays are illuminated with a large-enough Sun Aspect Angle (usually around 45°) to guarantee enough power for the propulsion system. Large slews of the spacecraft are time consuming due to the spin rate and the presence of four 50 m wired booms, making it difficult in practice to do tangential apogee or perigee manoeuvres outside a narrow window of a few weeks per year around solstices. Consequently, the duration spent in a given orbit is a multiple of one year.

In addition, THOR is injected into a [250-89000] km orbit. From a mission analysis point of view, THOR could be launched any day of the year (with some exceptions corresponding to the highest lunar perturbations, leading to poor orbit stability), but the spacecraft could not be transferred to the first NSP before the next solstice, for the reasons explained above. Meanwhile, the spacecraft would suffer an unnecessary build-up of the radiation dose and an increased probability of SEE on the spacecraft components, in an orbit with limited stability after one month. Therefore, it was decided to limit the duration in this very first orbit to the minimum possible, which is around 2 weeks considering a worst case of a safe mode occurring in that phase. This calls for a preferred launch date a few weeks before solstice, leading to two launch periods of 2 months per year.

Although both launch periods comply with science requirements, the June opportunity allows an orbit with lower ecliptic inclination, Kourou being in the Northern hemisphere, and is therefore the baseline. However, the achieved spacecraft designs presented in Section 5.4 are compatible with both launch periods, offering programmatic flexibility.

The use of an Ariane 62 re-ignitable upper stage to perform the initial Perigee Raising Manoeuvre (PRM) has not been studied further, due to the current uncertainty on launcher design and performance – in particular the capacity for a cryogenic upper stage to perform the required PRM several hours after the first burn was not confirmed. A conservative approach has been preferred, assuming the spacecraft needs to perform the initial PRM by its own means, which limits de facto the possible launch periods as detailed above. This assumption could be re-visited in a later stage of the project, as soon as the Ariane 62 design maturity improves. A direct injection in NSP1 by the launcher would for example allow launching any day of the year, simplifying the overall mission design.

5.2.3 Radiation environment

The radiation environment is a significant driver for the mission profile, with a direct impact on orbit chosen, instrument and equipment operations and shielding. As a consequence, the total radiation dose has been one of the important weighting factors when performing the trade-offs selecting the baseline orbit for THOR. A perigee at $6 R_E$ instead of $4 R_E$ was preferred for this reason, although it implied significantly higher delta V.

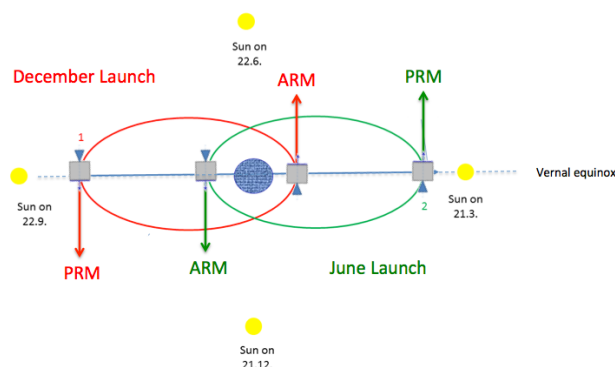


Figure 66: Illustration of the two launch periods per year around solstice with a line of apsides aligned with vernal equinox. ARM - Apogee Raising Manoeuvre, PRM - Perigee Raising Manoeuvre. For a June launch, ARM is possible only around winter solstice.

THOR will experience a changing radiation environment along the mission. The crossing of the inner Van Allen belt will be limited to the initial injection orbit, where THOR will remain for a maximum of 2 weeks. In the first two NSPs, while THOR will be passing above the inner Van Allen belt, it will still go through the electron belt twice per orbit. The dose accumulation in NSP3 (and potentially the whole extended phase) will be much more benign. The total ionizing dose is shown in Figure 67 and is about 100 kRad behind 3 mm of Al over a 3.5 year duration, including a factor of 2 margin on the environment. It is significantly below the dose for a geostationary satellite, though significantly higher than the dose for a typical LEO satellite. The shielding strategy consists of using a closed spacecraft structure to naturally shield the most sensitive equipment, and additional local and spot shielding of critical components such as instrument front-end electronics.

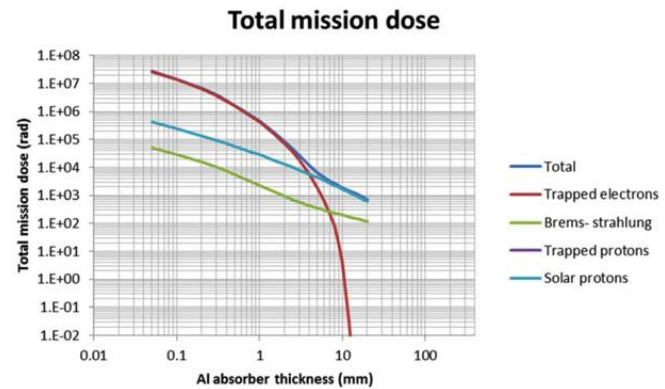


Figure 67: Total Ionizing Dose for the THOR nominal mission (excluding margin).

5.2.4 Selective downlink

A specific driver of the THOR mission is the return of the burst science data. It is required to return about 15 Tbits of burst data over the mission duration. While significant, this represents a very small fraction of the burst data the payload is actually generating on-board. Typically, only about 1% of the generated data is to be returned. There are therefore two possible strategies to retrieve this data: either downlink all the payload generated data (*non-selective* downlink strategy), or downlink only the relevant science data (a priori burst selection, known as *selective* downlink strategy). The non-selective downlink strategy requires a complex and costly TT&C system based on Ka-band to allow downlinking the data. The selective downlink strategy requires a ground-based data selection process based on the analysis of survey data to establish which of the generated burst data is relevant for downlink. This second approach allows a simpler X-band TT&C system and has been selected for THOR. The selective downlink strategy implementation benefits from the lessons learned from the ESA JUICE and Solar Orbiter missions, and is based on Scientist In The Loop scheme as successfully used by the NASA MMS mission, see Section 6.3.3 for details.

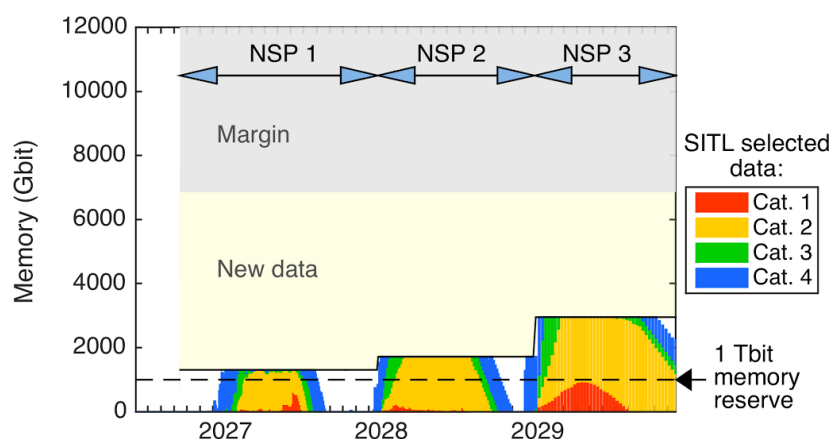


Figure 68: Simulation of the on-board memory usage assuming historic solar wind parameters from 2004-2007 as an input. A 12 Tbit EOL mass memory is sufficient with significant margin for storing the continuously generated burst data with the foreseen selective downlink scheme and allows in addition storage of more than the required 1 Tbit of SITL selected data in all mission phases. Cat. 1 data are the highest quality data which have to be returned to satisfy the mission requirements. Cat.2-4 are lower quality but scientifically interesting data. The first few months (white space) are the commissioning phase.

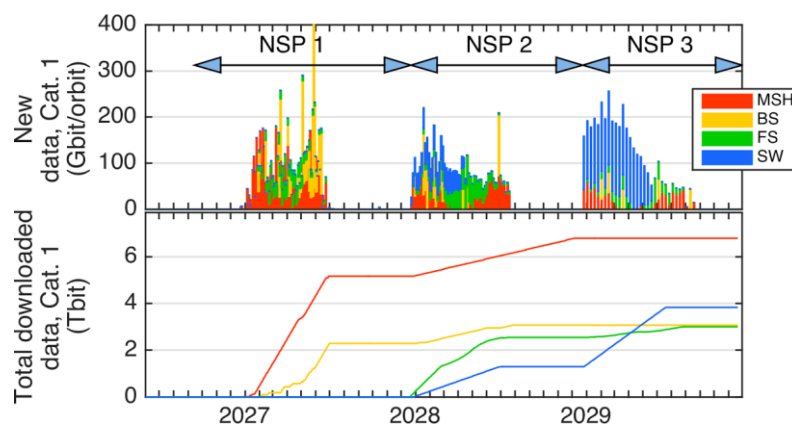


Figure 69: Simulation of minimum required data (Cat.1) acquisition (top) and downlink (bottom) based on real solar wind parameters, see also Figure 68.

The main consequence on the spacecraft of using the selective downlink is the need to have an on-board memory sized to store all the generated payload data while the SITL performs a selection. This decision time includes not only the SITL decision itself, but all the intermediate steps required for the data processing and transmission from (and back to) the ground station to the SITL, via the MOC and SOC. The process has been streamlined in the course of the study to minimize the overall ground loop duration, now established to be 3 days, including ad-hoc margins. With a survey data downlink every 3 days maximum, this means the on-board memory needs to store the equivalent of 6 days of burst data on-board. This translates into the required on-board memory size of around 12 Tbits EOL, including margins. The adequacy of the memory sizing has been verified by carrying out a simulation of data acquisition, on-board storing, SITL selection and downlink, using historic solar wind parameters from 2004-2007 as input, see Figure 68 and Figure 69.

5.2.5 EMC

The THOR science requirements specify accurate magnetic field, electric field and particle measurements, at unprecedented resolution, leading to stringent requirements on the electro-magnetic cleanliness (EMC) of the spacecraft. A comprehensive set of justified, traceable and verifiable EMC requirements have been established for THOR by a dedicated EMC Working Group. They are described in detail in Section 4.4. These requirements drive, to a major extent, the design of the spacecraft.

- AC/DC magnetic requirements for MAG and SCM require the mounting of these instruments on semi-rigid booms, of at least 6.5 m length, from the platform.
- AC/DC electric requirements at EFI require the implementation of the EFI-SDP instrument on 50 m long wired booms, and of EFI-HFA on a rigid boom at least four meters away from the spacecraft. This in-turn requires the spacecraft to spin at a sufficient rate of 2 rpm to ensure the wire booms remain under sufficient radial tension at all times.
- The integrated magnetic field requirement leads to a careful selection and accommodation of equipment and components on the spacecraft. For instance, solar cells and battery cells require a careful symmetric configuration to allow self-compensation of magnetic moments.
- The quasi “frequency stay-out” imposed to the spacecraft in the range [0.1mHz-200kHz] to comply with AC/DC magnetic and electric field requirements (with exceptions allowed over limited duration and at known frequencies) leads to careful selection and/or accommodation of electronics components, with consequences on all electrical subsystems: power, AOCS, DHS, TT&C but also the instruments themselves. It imposes, in particular, the need for a master clock at the spacecraft level, providing a stable and accurate synchronization signal to the payload instruments.
- Finally, the requirement on the differential voltage of maximum 1 V between any point of the spacecraft implies that all the spacecraft surfaces shall be conductive, requiring the use of specific conductive coatings for the solar arrays, MLI and radiative surfaces. The need for having a positive spacecraft potential lower than 10 V requires also active charging control of the spacecraft, which is achieved thanks to the ASPOC equipment.

5.2.6 Payload accommodation

The payload accommodation is another major driver for the design of the THOR spacecraft. The most EMC sensitive instruments need to be accommodated on sufficiently long booms to comply with their sensitivity requirements (four 50 m wired booms for EFI-SDP, and two longer than 6.5 m rigid booms for MAG, SCM, and EFI-HFA). The four 50 m long flexible booms (carrying the EFI-SDP probes) positioned radially on the spacecraft present a challenge for the spacecraft dynamics control and operations, making large slews very time consuming. In particular, a 2 rpm spin needs to be ensured at all times of the mission once the booms are deployed to sustain the tension in the cables, and the coupled booms-spacecraft dynamics need to be controlled to avoid in particular large angular deviations of the booms with respect to their attachment points. Deviations of the wired booms above 10° are avoided for spacecraft safety reasons. In addition, the impact of boom settling time on the science needs to be minimized: deviations higher than about 0.6° would impact the quality of some measurements, e.g., for the EFI.

As a consequence, the spacecraft attitude control system needs to ensure the booms remain in their domain of operation at all times, and needs to minimize the overall slew duration including booms tranquillization and propellant dissipation to mitigate the impact on science availability. This is achieved via a slow slew strategy with very short pulse, phased with spacecraft spin phase, requiring thrusters with very low Minimum Impulse Bit (MIB). This drives the choice of the RCS thrusters for THOR to 10 N bi-propellant with MIB around 10 ms. This strategy allows to complete a slew in typically 8 h around perigee, this duration being driven by the propellant settling time, without exceeding 0.6° deviation for the booms, therefore with a negligible impact on science availability.

The other instruments are located on the spacecraft panels and need to be accommodated carefully to limit the FOV obstruction from the various appendages, to avoid any local perturbations to other instruments, e.g., electron or ion deflection due to integral magnetic field along a sensor line of sight, and to respect their individual pointing requirements. In particular, FAR needs to be accommodated on the Sun-facing panel, while TEA, IMS, EPE and CSW need to be accommodated on the side panels. Each of the 4 IMS units need to be separated by 90° and the 2 EPE units need to have a separation of 90° . This poses a configuration challenge and minor obstructions, e.g., by wire booms are unavoidable.

The data processing units PPU and FWP need to be accommodated inside the spacecraft platform.

5.3 Mission phases

The following mission phases are identified for THOR:

- Launch and injection into initial orbit, LEOP (2 weeks)
- Perigee Raising Manoeuvre, Insertion into first Science Orbit and commissioning (3 months)
- First nominal science phase NSP1 (1 year)
- Transfer to NSP2 and NSP2 (1 year)
- Transfer to NSP3 and NSP3 (1 year)
- Decommissioning and spacecraft disposal (3 months)

The nominal mission duration is 3.5 years, including 0.5 years for commissioning and de-commissioning of the spacecraft. A mission extension of two years after NSP3 is possible, which would lead to a total mission duration of 5.5 years.

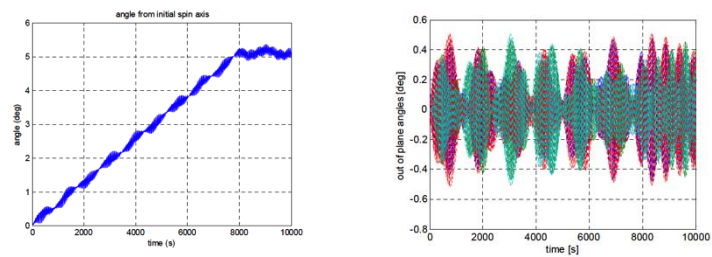


Figure 70: Slew angle evolution (left) and wire boom latitudinal deviation (right) during a 5° slew manoeuvre, assuming 0.06 s thruster pulse per spin cycle. The targeted slew is achieved in less than 3 h, the deflection of the booms remains below 0.5° at all times. (Credit: ESA)

5.3.1 Launch and transfer to NSP1

The baseline is that THOR is launched by an Ariane 62 rocket from Kourou in French Guyana in June 2026. The launch strategy assumes a trajectory very similar to a standard Geostationary Transfer Orbit, with a 7° inclination, a 180° argument of perigee, a 250 km altitude perigee, but a higher apogee (15 R_E radius, compared to 6 R_E for GTO). The launch window is chosen to be of three weeks duration, within the 2 months launch period around solstice discussed in Section 5.2.2. The exact time of launch is chosen such that the line of apsides coincides with the intersection of Earth equator and the ecliptic plane, the vernal equinox direction, as required. There is one instantaneous launch window per day which satisfies this constraint.

Ariane 62 will deliver the spacecraft in a Sun-pointed spin-stabilized mode, spinning at 8°/s, with dispersions of several °/s and a maximum nutation angle of up to 5°. The THOR attitude control system will correct for such dispersions right after launcher separation, thanks to de-nutation manoeuvres involving the use of the RCS thrusters which are pulsed in phase with the spinning motion of the spacecraft. Once the correct attitude and angular rate state is reached, the perigee raising manoeuvre will be performed by the spacecraft at apogee to reach NSP1 by raising the perigee from 250 km altitude to 6 R_E.

After reaching the first science orbit, deployment of the rigid and wired booms will occur as part of the commissioning activities. For this purpose, the nominal spin rate of the spacecraft needs to be increased to meet the required range of angular rates (2-3rpm) to deploy the wire booms. The deployment of the booms will occur pair-wise, deploying opposite wired booms in a step-wise approach, with typically 3 deployment steps of around 10 to 20 m each, as was successfully implemented on the NASA MMS mission. The whole deployment sequence will last up to two weeks. The attitude control will be done in open loop during the deployment, but each deployment step will be preceded by a spin-up manoeuvre to ensure the spin rate of the spacecraft remains higher than 2 rpm, even at the end of the deployment step, in order to maintain sufficient tension in the wires to ensure their rigidity.

5.3.2 Nominal science phases

There are three nominal science phases, each one year long:

- NSP1 with a perigee at 6 R_E and apogee at 15 R_E and a period of 2 days
- NSP2 with a perigee at 6 R_E and apogee at 26 R_E and a period of 3.75 days
- NSP3 with a perigee at 6 R_E and apogee at 45 R_E and a period of 7.5 days

For each NSP, the core science measurements are performed in the Key Science Regions (KSR), which are crossed during about 6 months per year around equinox, when apogee is on the day side of the Earth. When apogee is on the night side, for the remaining months of the year, THOR will be performing complementary science, e.g., magnetotail crossings, increasing the overall science data return of the mission.

As illustrated in Figure 71, most of the magnetosheath and bow shock data are accumulated during NSP1, while foreshock data is mostly accumulated during NSP2 and pristine solar wind is mostly accumulated during NSP3. The chosen orbits allow the TPR residence time requirements to be met.

In the nominal science phase, the spacecraft attitude is passively controlled thanks to its spin at 2 rpm, with the spin axis pointed towards the Sun. The spacecraft spin axis needs to remain Sun-pointed within -5.5° to +1.5° range with respect to the GSE xy-plane as per the science requirements. Since the THOR orbit is rotating in the GSE frame by around 1°/day, as illustrated in Figure 44, this means THOR will need to slew its spin axis by 7° roughly once per week.

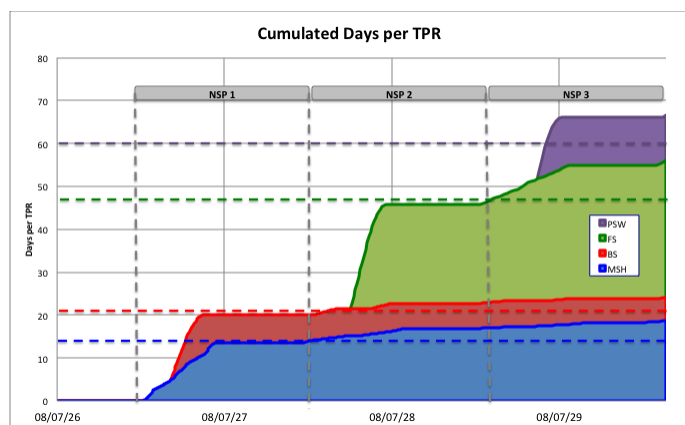


Figure 71 Accumulated days within TPR over mission duration compared with residence time requirements (dotted lines).

In NSPs, the payload is always switched ON, except during long eclipses (occurring only in NSP3), and for some of the instruments except during slew maneuvers. Survey data is acquired by the payload all along the orbit, while burst data is acquired all along the orbit excluding an 8 hours long region around the perigee where downlink occurs.

The burst data is downlinked at each perigee pass to an ESA 35m deep space antenna. A perigee pass is required for burst data downlink to allow for maximum data rate with a simple X-band TT&C system (close to 10 Mbit/s). The survey data, together with spacecraft housekeeping, has to be downlinked at least every 3 days to an ESA 35m deep space antenna to ensure frequent enough contacts with ground. The data can be transmitted from any point in the orbit up to apogee, allowing the data return scenario to be optimized based on ground segment constraints in those phases, resulting in one survey pass per orbit in NSP1, two in NSP2 and three in NSP3.

The transition from one NSP to the following NSP is achieved via apogee raising manoeuvres with the orbit control thrusters. The transition takes place at perigee around each winter solstice for the June launch opportunity, within a manoeuvre window of several weeks.

The THOR orbit, due to its high eccentricity and high apogee (especially in NSP3) will be subject to Luni-Solar perturbation, leading to significant perigee excursions, as well as angular changes of up to 20° of the line of apsides with respect to ecliptic at some points during NSP3, as can be observed in Figure 72. These excursions have no impact on the science performance.

5.3.3 Incursions in the GEO protected region

The protected region for the geostationary orbit extends from 200 km below to 200 km above the geostationary radius ($42164.2 \text{ km} = 6.61 R_E$) and to latitudes of $\pm 15^\circ$ from the equator as illustrated in Figure 72. The THOR orbit will cross the protected region during all mission phases.

The actual risk of collision with an object in such an orbit is expected to be very small, in the order of 10^{-6} over mission duration. Though the risk is very low, the THOR mission needs to have the capability to analyse the risk of collision on a routine basis, and the spacecraft is designed to be able to perform Collision Avoidance Manoeuvres (CAM), should an unacceptable collision risk event be triggered. At mission level, the ground segment will therefore perform a collision risk assessment, based on Two-Line-Elements tracking provided by the US Joint Strategic Operations Command centre, as was successfully implemented for instance on the ESA XMM and Cluster missions. At spacecraft level, a delta V of few m/s is allocated to perform CAMs, and sufficient control authority is provided by the thrusters to perform such a CAM in due time. These CAMs are optimally performed at perigee or apogee and consist of changing the orbital period sufficiently to ensure sufficient distance (10 to 20 km) at closest approach to the identified object; less efficient CAMs can be performed post apogee in the event that the collision warning time is smaller than half of the orbital period, which could happen only in NSP3 (7.5 days period). The spacecraft is sized to perform several of these non-efficient CAMs along its mission, which is well above the likelihood of such an event and therefore very conservative.

5.3.4 Safe mode

Since the spacecraft will be naturally spin-stabilized and always Sun-pointed as from Launcher separation, the safe mode strategy is very simple and consists of the spacecraft to remaining mostly passive, while waiting for the ground segment to understand the contingency case and uplink the recovery commands. The Solar Array sizing allows the spacecraft, in the worst case, to remain passive for more than 2 weeks without changing its orientation, which is sufficient, with margin, for a ground-based recovery. The communication

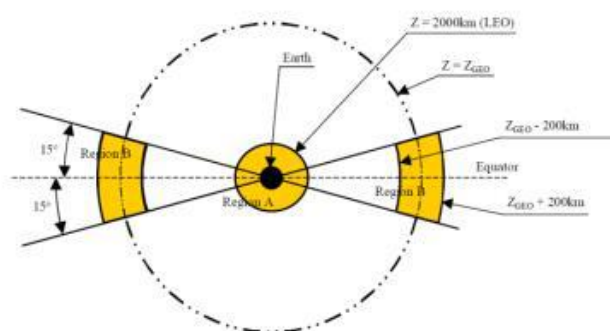


Figure 72 GEO protected region (left) and geocentric latitude evolution of the THOR orbit for a June launch, with all NSP represented. The geo-protected region, represented in orange, is crossed in all phases of the mission around perigee.

to and from the spacecraft is possible all year long thanks to the set of Low Gain Antennas on the spacecraft which provide full angular coverage.

5.3.5 Spacecraft disposal

At the end of NSP3 or ESP if granted, two disposal strategies are identified: disposal into a graveyard orbit above GEO, or disposal into a heliocentric orbit after a transfer to L1 which allows the disposal delta V to be minimized, while ensuring non-interference with the Geo Protected Region within 100 years, as per debris-mitigation requirements applicable to ESA projects. The respective delta V cost of each solution is in the order of 200 to 300 m/s.

5.4 Spacecraft design

Two design solutions have been studied in the THOR Phase A, both meeting the applicable requirements.

5.4.1 Spacecraft design – solution 1

Configuration and structure

The mechanical design consists of an octagonal Aluminium Honeycomb structure, with a maximal diameter of 4.3 m and a maximal height of 2.56 m, around a CFRP central cylinder. The octagonal shape allows the accommodation of 8 spherical tanks, being rigidly attached to the central cylinder via 16 struts.

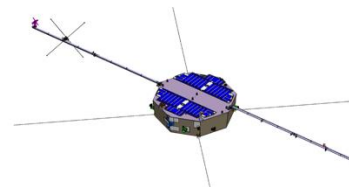


Figure 73: Solution 1. Stowed and deployed configuration.

The pressurant tank would be accommodated within the central tube. A 400 N main engine would protrude from the lower part of the central cylinder in the centre of the spacecraft. Two rigid booms of at least 6.5 m are attached to and deployed from the upper panel of the spacecraft.

AOCS

The attitude and orbit control system relies on a gyroless design, with a triple optical head APS Star Tracker as the main attitude sensor to measure its attitude and spin rate. The STR is able to operate autonomously in the THOR orbit environment in acquisition and tracking modes at more than 30°/s (5 rpm) which is well above the maximum spin rate encountered during the mission (3 rpm during the wire boom deployment). This sensor is supplemented by a set of fine Sun sensors the Sun aspect angle to be monitored in all phases for the FDIR purpose. The only AOCS actuators are the 10 N RCS thrusters. The RCS configuration consists of 4 (+4) thrusters located on the bottom panel of the spacecraft, with a small tilt angle allowing for high efficiency axial delta V manoeuvres, while providing enough torque authority on three axes for performing slew manoeuvres, spin rate adjustment and de-nutation manoeuvres.

THOR will spend most of its time passively spinning at 2 rpm. AOCS will be solicited mostly for the initial launcher dispersion correction, the wire booms deployment, the periodic slew and nutation control manoeuvres to maintain the spin axis Sun-oriented, and the orbit change manoeuvres. The initial perigee raising manoeuvre is performed with a large apogee engine, while all subsequent orbital changes, including disposal and collision avoidance manoeuvres, would be performed by the simultaneous use of four 10 N thrusters.

Propulsion

The propulsion subsystem relies on a regulated blow-down bi-propellant MON/MMH system. It is composed of a 400 N Large Apogee Engine (Isp of 321 s), and 8 redundant RCS thrusters of 10 N (Isp of 290 s). There are 8 PMD tanks selected to ensure the correct flow-down of the propellant into the tank outlets even under the expected spin conditions. The maximum total Δv required from the system is 1800 m/s. The tanks store more than 1 ton of propellant for the needs of orbital changes, slew manoeuvres, collision manoeuvres and the disposal manoeuvre for the extended mission duration.

Electric and power

The solar array is body-mounted and represents a total area of 6 m², driven by the nominal science mode when communicating with ground at the same time. This surface includes an Optical Surface Reflector as required for thermal reasons on the Sun-pointing face of the spacecraft. Solar cells are ITO-coated to comply with spacecraft charging requirements. The cells are arranged in a self-compensating symmetrical configuration to minimize the residual magnetic moment and comply with DC magnetic requirements.

The power system provides 28 V regulated to the spacecraft. The power bus is directly switched to the solar arrays in a so-called Direct Energy Transfer (DET) architecture. The Li-Ion battery consists of four modules, sized by the long eclipse duration occurring in NSP3, which lasts for up to 8 h. The four modules are placed symmetrically on the spacecraft to ease the spacecraft mass balancing.

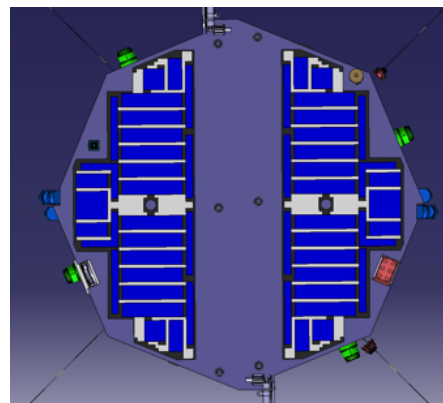


Figure 74: Body-mounted solar array.

Data handling subsystem

The data handling system consists mainly of a Central Data Management Unit (CDMU) including the On Board Processor and a flash memory, a Remote Interface Unit (RIU), and an external large capacity Flash Memory of 12 Tbits End Of Life. The burst data selected for downlink is transferred to the CDMU memory. The CDMU interfaces with the instruments via SpaceWire interface. The CDMU also implements a reference master clock providing a stable synchronization signal for DC/DC converters within instruments. The spacecraft uses file-based protocols for all its operations, simplifying the management of science data and overall spacecraft operations.

Communications

The communication subsystem relies on a set of 2 X-band Low Gain Antennas, providing almost full instantaneous visibility from Earth, complemented by two Solid State Power Amplifiers (SSPA) and two X-band deep space transponders. The TT&C implements two different coding schemes: TurboCode 1/2 and Reed-Solomon 223/225. Reed-Solomon 223/225 is used at perigee to maximize the usage of the ITU-allowed bandwidth in X-band (10 MHz for this class of mission), which is then close to 10 Mbit/s. For survey passes, which could occur at different orbital positions, TurboCode 1/2 is preferred to minimize the duration of the passes. Only one ESA Deep Space Antenna station of 35 m diameter is used at each downlink pass. This strategy allows the burst data return science requirement of 15 Tbits to be met, with an average use of ESA 35 m antennas of less than 2 h per day over mission duration, with peaks of up to 4 contiguous hours for burst perigee sessions.

Thermal design

The thermal design is driven by the attitude of the spacecraft, spinning at 2 rpm, nominally Sun-pointed, with periods of several hours with off-Sun pointing angles up to 45 degrees. Most of the instruments are on the side and lower part of the spacecraft.

The thermal design is based on simple and reliable technology, relying mostly on passive control with radiators, Optical Surface Reflectors and Multiple-Layer Insulation, and active control through heaters only. The thermal system is also designed to ensure external surface conductivity and proper grounding to meet spacecraft requirements – this means all MLI and radiators have a conductive coating to allow proper grounding at any point of the surface.

Payload accommodation

The overall payload configuration is illustrated in Figure 75.

MAG inboard and outboard sensors are accommodated on the rigid boom, with 2 m distance between the two instruments. SCM and EFI-HFA are accommodated on a similar boom located on the opposite side of the spacecraft, SCM being at the tip of the boom and HFA 2 m away.

TEA accommodation is driven by its 4π FOV requirement. TEA has therefore to be accommodated as far as possible from the rigid booms. The 3 heads would be located at opposite corners, 90° away from the rigid booms.

Two IMS units are accommodated at two opposite corners of the octagonal shape, and the two other units in the middle of two side panels, so that the four units are separated by 90° .

The EPE units cannot be accommodated on the TEA shear walls, due to the presence of a permanent magnet within EPE which would perturb the TEA measurements. The two EPE units are therefore located at two corners of the octagonal shape on the side of the spacecraft, allowing 90° between both units' observation planes.

CSW is accommodated inside one of the spacecraft panels, which allows to avoid obstruction to the other instruments' FOV.

To allow for simpler thermal control, FAR is positioned at the edge of the Sun-facing panel rather than at the centre, allowing for passive cooling via the radiator which is on the side panel, while still meeting the pointing requirement for FAR, which needs to be Sun-pointed.

The two ASPOC units are located on the lower panel, as far as possible from the TEA and IMS instruments to avoid perturbations, and look away from the spacecraft, out of thrusters' Line of Sight.

With this solution, FOV obstructions of all instruments are minimized.

Mechanisms

The mechanisms are limited to the two two-segment rigid booms, and include two hold-down and release mechanisms per boom. The rigid booms have a total length of at least 6.5 m each. Both boom segments are deployed at the same time, controlled by a pulley cable system, adopting a similar technology as the rigid booms being developed for JUICE.

5.4.2 Spacecraft design – solution 2

Configuration and structure

The shape of the spacecraft structure is octagonal, with a total diameter of 4 m and a total height of 1.9 m. The primary structure is organized around a 1194 mm diameter central tube. The 6 propellant tanks are accommodated in 6 compartments separated by 6 shear walls. The pressurant tank is accommodated within the central tube. Four 22 N thrusters are oriented longitudinally and located on the anti-Sun panel of the spacecraft and are used for orbit control manoeuvres. Eight 10 N thrusters are also accommodated on the lower panel of the spacecraft but are tilted with respect to the longitudinal (spin) axis to provide some attitude control authority around all axes. Two rigid booms of at least 6.5 m are attached to and deployed from the upper panel of the spacecraft.

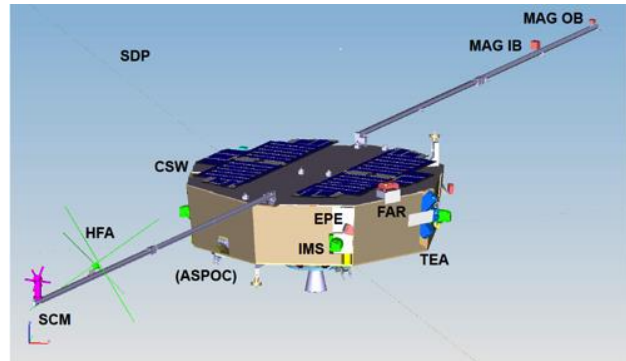


Figure 75: Overview of instrument accommodation.

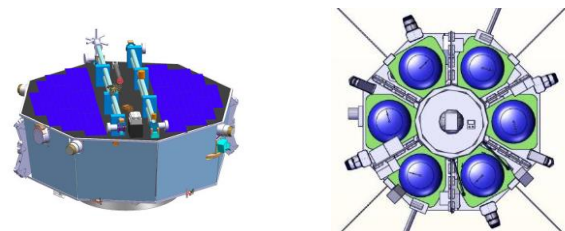


Figure 76: spacecraft configuration highlighting in particular the accommodation of the 6 tanks.

AOCS

The attitude and orbit control system relies on a triple optical head APS Star Tracker to measure its attitude and spin rate, complemented by two redundant fibre optic gyroscopes. The triple head STR is able to operate autonomously in acquisition and tracking at more than 30 degrees per second (5 rpm) which is more than the maximum spin rate encountered during the mission during the wired booms deployment. The fibre optic gyroscopes provide robustness to the attitude and rate estimation functions in case of the unavailability of STR measurements (e.g., occultation, or radiation-related events), and also aid the acquisition function of the STR by providing the rate information to the STR and guaranteeing at all times an accurate attitude state measurement availability to the payload. In addition, there is a set of fine Sun sensors allowing the Sun aspect angle to be monitored in all phases for FDIR purpose.

The only attitude control actuators are a set of 8 redundant 10 N RCS thrusters, tilted with respect to the spin axis. The spacecraft spends most of its time passively spinning at 2 rpm. The AOCS will be solicited mostly for the initial launcher dispersion correction, the wire booms deployment, the periodic slew and nutation control manoeuvres to maintain the spin axis Sun-oriented and the orbit change manoeuvres.

All orbit change manoeuvres, including the initial perigee raising manoeuvre, are performed thanks to the use of two 22 N thrusters (plus 2 redundant), aligned with the spin axis direction.

Propulsion

The propulsion subsystem relies on a regulated pressurized bi-propellant MON/MMH system. It is composed of a set of four redundant 22 N thrusters (Isp of 300s), aligned with the spin axis direction, and 8 redundant RCS thrusters of 10 N (Isp of 290s), tilted with respect to the spin axis. There are 6 PMD tanks selected and one Helium pressurant tank. The maximum total Δv required from the system is 1800 m/s. The tanks store a total of 1 ton of propellant for the purpose of orbital changes, slew manoeuvres, collision manoeuvres and disposal manoeuvres for the extended mission duration.

Electric and power

The solar array is body-mounted and represents a total area of 5 m², driven by the nominal science mode when communicating with the ground. It is composed of 3G30C triple junction GaA cells which are ITO-coated to comply with spacecraft charging requirements and ensure conductivity of all spacecraft external surfaces. The cells' arrangement is self-compensating the residual magnetic moment to comply with the DC magnetic field requirements. The battery is sized by the longest eclipse duration encountered in NSP3 (8 h) and consists of 2 modules, with strings internally arranged for self-compensating the residual magnetic moment.

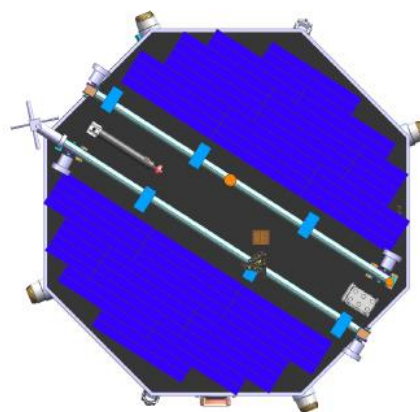


Figure 77: Body-mounted solar array configuration.

Data handling

The data handling system relies on an On-Board Computer (OBC), two Remote Terminal Units and a segregated NAND flash mass memory unit of 12 Tbits EOL in charge of platform and science data management. The DHS relies on MIL-BUS-1553B and implements SpaceWire interfaces with the payload. The OBC also implements a reference master clock providing a stable synchronization signal for DC/DC converters within instruments and within spacecraft units, as required. The spacecraft uses file-based CFDP protocols, simplifying the management of science data and overall spacecraft operations.

Communications

The communication system relies on a set of 3 low gain X-band antennas, which allow full coverage, two redundant Traveling Wave Tube Amplifiers (TWTA) and two X-band transponders. Two low gain antennas are accommodated on small booms to mitigate multipath effects, the third one being used only during LEOP.

The coding scheme used is concatenated code to cope with varying slant ranges all along the mission. The communication strategy allows a data rate close to 10 Mbps to be provided at perigee passes, exploiting the maximum bandwidth as allowed by ITU regulations. The required perigee passes are usually shorter than 2 h for burst data downlink. This strategy the burst data return science requirement of 15 Tbits to be met, with an average use of ESA 35 m antennas of 1.5 h per day over mission duration.

Thermal design

The thermal design relies on passive control with radiators, optical surface reflectors and multiple-layer insulation. The thermal control is driven by the highly eccentric orbits with long eclipse durations (up to 8 h), the spinning attitude with a Sun-pointing upper platform, and the off-Sun pointing during manoeuvres (up to $\sim 40^\circ$). Highly-dissipative units are located on the bottom platform with thermal radiators while low-dissipative units are radiatively controlled inside a thermal cavity below the upper panel. The spacecraft is equipped with additional radiators on the lateral side of the platform. All external surfaces are covered with an electrical conductive coating to cope with charging requirements.

Payload accommodation

The payload configuration is similar to Solution 1, see Figure 78.

Mechanisms

The mechanisms subsystem is composed of the two 2-segment rigid booms (at least 6.5 m long) carrying the magnetometers, as well as their associated three hold-down and release mechanisms per boom.

In addition, there are two additional small booms for LGA support, with their associated HDRM.

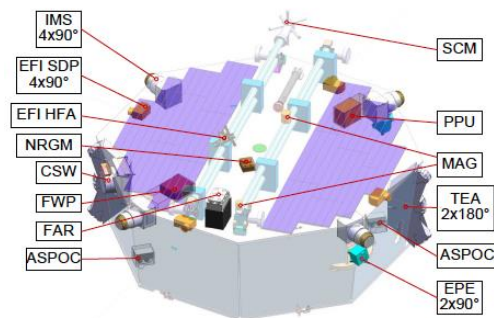


Figure 78: Payload instrument configuration for Solution 2 (stowed configuration).

5.5 System budgets

Table 24 summarizes the mass budget for the two solutions studied. On a subsystem level, mass margins have been applied according to Technology Readiness Level (TRL) status and in addition a 20% system margin has been applied. The capability of Ariane 62 for the specific THOR injection orbit (perigee of 250 km altitude, apogee at 15 Earth Radii) has been consolidated with the ESA/CNES Ariane 6 project team, and amounts to 3300 kg. However, a 500 kg margin has been considered as recommended by the Ariane 6 project team to account for the early level of definition of this launcher. As a consequence, a 2800 kg launch performance has been considered as applicable for the study. Still, both design solutions show compliance with the launch mass requirements with more than 10% additional margin.

Table 24: Mass budgets for the two spacecraft solutions studied. All values include maturity margins, and a 20% system margin on dry mass is also included.

Subsystem	Solution 1 mass [kg]	Solution 2 mass [kg]
Total dry mass	1264	1230
Communications	20	22
Power	136	72
Data Handling	34	44
Propulsion	145	168
Mechanisms	53	78
Structure	358	308
AOCS	9	18
Thermal	66	20
Payload	175	175
Harness	58	119
System Margin	211	205
Propellant including 2% Residuals	1064	1099
Launch Adapter	80	90
TOTAL Wet Mass including launch adapter, maturity margin and system margin	2408	2419
Ariane 62 performance	2800	2800
Launch margin	392 (14%)	381 (14%)

5.6 Critical elements and risks mitigation

At mission level, the uncertainty on the Ariane 62 performance and the capability of Ariane 62 to inject THOR directly in the science orbit was highlighted as a risk. As a consequence, as a mitigation approach, it has been considered as a mission requirement to have a launch profile similar to a standard GTO launch (for which Ariane 62 is primarily designed), with only one injection burn and no need for re-igniting the upper stage. This requires the spacecraft to perform the first perigee raising manoeuvre by its own propulsion, with significant impact on propellant mass, and at mission level restricting the launch opportunities to two periods per year, around the solstices. The mission and spacecraft designs studied in the phase A are fully compatible with this conservative approach, with good margins, demonstrating that the associated risk is properly mitigated.

A failure in performing on time the first perigee raising manoeuvre would leave the spacecraft on an orbit which intrinsic stability is limited to typically 1 month, after which perigee excursions due to Luni-solar perturbation would lead to a likely re-entry of the spacecraft. This risk is mitigated at mission level by ensuring the time window for performing such a manoeuvre is long enough (more than 1 month) and at spacecraft level by sizing the solar arrays for a worst case Sun aspect angle compatible with the window as established.

THOR would rely on significant heritage from the Solar Orbiter, JUICE and Lisa Pathfinder missions, with no new technology development identified, all subsystems being at a Technology Readiness Level higher than or equal to 6.

5.7 Conclusions

The preliminary design solutions studied in phase A demonstrated two feasible solutions, technically and programmatically, meeting the main mission and science requirements. The two solutions studied present good margins with respect to the launch performance requirements. In both design solutions, a suitable configuration has been found for all instruments, which minimizes, as much as possible, field of view obstructions. Further optimization of instrument accommodation will be pursued in a later phase of the project to try to minimize further any obstruction.

THOR is a low risk mission with a spacecraft design relying on mature, high TRL technologies for all subsystems. Mission-level risks are limited, understood and mitigation strategies have been put in place already in phase A.

6 Ground segment

ESA will be responsible for the launch and operations/checkout of the spacecraft. A THOR Ground Segment (GS) will be set up to provide the means and resources with which to manage and control the mission via telecommands, to receive and process the telemetry from the satellite, and to produce, disseminate and archive the generated products.

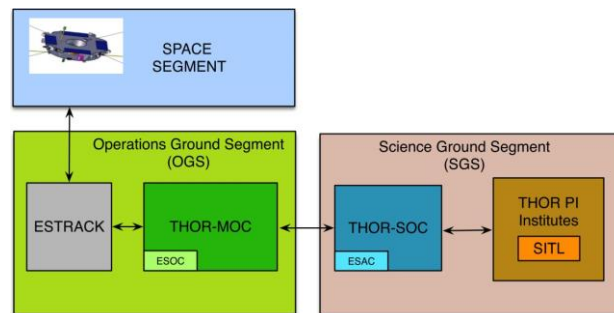


Figure 79: THOR Ground Segment and operational interfaces.

6.1 Operations concept

Responsibility for, and provision of, the THOR GS is split between ESA and the THOR instruments teams. ESA will be responsible for the following GS elements:

- ESA tracking station network
- Mission Operations Centre (MOC)
- Science Operations Centre (SOC)

A schematic drawing of the top level operational interfaces of the THOR mission is shown in Figure 79.

6.1.1 Mission operations centre

A Mission Operations Centre (MOC) will be established at ESOC (Germany). MOC is responsible for the operations of the THOR spacecraft, for ensuring the spacecraft safety and health, monitoring instrument safety and health, for provision of flight dynamics support including determination and control of the satellite's orbit and attitude, and intervention in case of anomalies.

MOC is responsible for handling telemetry/telecommands for both the THOR spacecraft and instruments. The telemetry, tracking and command subsystem of the THOR mission is to be compatible with the ESA GS and the ESA tracking station network.

MOC is responsible for collecting the THOR raw telemetry science and auxiliary data and for making it available to SOC for further processing.

The responsibility for the design, implementation, and operation of MOC rests with ESA/ESOC.

6.1.2 Science operations centre

A Science Operations Centre (SOC) will be established at ESAC (Spain). ESAC is also the host of all ESA Science Missions' data archives. SOC will design, coordinate and operate the ESA-funded part of the THOR Science Ground Segment (SGS).

SOC will be responsible for the scientific operations of the mission, contact with MOC for overall planning, the operation of the pipeline processing and archiving, and the interface with the user community.

6.1.3 Principal investigator teams

The PI teams will provide the elements of the THOR SGS required for the calibration processing of the science data and generation of data products.

The PI teams will be responsible for the monitoring and calibration of the instruments. They will also maintain the on-board S/W (OBSW), and raise anomaly reports as well as support the investigation and resolution of anomalies. The SOC supports these activities through Instrument Scientists.

The PI teams are distributed over a number of institutions, with activities that are to be performed under national funds.

6.2 Operations ground segment

The ground station network to be used consists of the 3 ESTRACK deep space stations in New Norcia, Cebreros, and Malargüe and the usage of smaller antennas is not discarded. Only NNO-2 ground station for initial acquisition is foreseen.

The burst data downlink will be dumped at the perigee during the KSR (and SRR) crossing season. It is assumed that the perigee duration is several hours under ground visibility and, as far as possible, during working hours. The survey data (and HK telemetry) can be dumped outside this region considering the possible spacecraft antenna angle constraints during the mission and, as far as possible, after the KSR region.

Due to the orbit evolution over the mission lifetime, the different orbit durations will impact the ground station visibilities and link budget. Table 25 represents an example of the ground station coverage and the number of downlinks per orbit.

Due to the very low ground station coverage per year, in case one pass is missed another ground station pass will have to be scheduled to downlink the data of the missed pass, a reallocation of the missed pass will have to be scheduled when there is station available to support.

The MOC is responsible for the commanding of the spacecraft and instruments, including overall mission planning, for ensuring the spacecraft

safety and health, for provision of Flight Dynamics support including determination and control of the satellite’s orbit and attitude, and intervention in case of anomalies. The MOC performs all communications with the satellite through the ground stations for the upload of the platform and payload telecommands and reception of the downloaded telemetry data. They are also responsible for collecting the science data and its transmission to the SOC, along with the raw telemetry, housekeeping and auxiliary data. Due to the non-continuous coverage, the spacecraft will be mainly controlled via off-line operations. Operations will be conducted by loading a master schedule of commands for later execution on the spacecraft. Anomalies will normally be detected with a delay.

Special mission phases follow the same basic concept, but with an adaptation of the timescales for planning and feedback.

Table 26: Mission phases.

Phase	Tasks
LEOP	Short feedback capability with on-site presence of experts and redundancy of services to enable accelerated reaction in case of problems. (The reaction time capability is matched to the duration of spacecraft autonomy during LEOP.)
SCP and NSP1 Transfer	Feedback capability to enable an accelerated replanning in case of needed adaptations or of problems.
NSP	Measurements (survey & burst data) in elliptical orbits, particularly within BCRs. Transfer manoeuvres to reach the various orbits required for entering the BCRs. Spin-axis and spin-rate corrections.
DCP	Several options are being considered: After the end of Phase 3, insertion to a Lissajous or Halo orbit around the L1 region can be envisaged, then transfer to heliocentric. Final orbit is a graveyard orbit.

The mission planning cycle will include the platform and payload activities, including burst data selection. It will be performed during office hours. Given that the mission only comprises *in situ* instruments, activation-deactivation and programming of data acquisition can be achieved automatically by the MOC using mission

Table 25: Example of ground contact usage.

Phase	Ground contact		
	Downloaded data	length [h]	# per orbit
NSP1	Survey, HK	0.4	1
	Burst, HK	3.1	1
NSP2	Survey, HK	1.8	1
	Burst, HK	3.9	1
NSP3	Survey, HK	2.1	2
	Burst, HK	4.1	1

planning based on planning rules. No dedicated pointing or observation schedule is required. The spacecraft will be able to continue nominal operations without ground contact for a period of up to 7 days.

On-board control procedures will allow autonomous execution of complex procedures, including decision loops which the GS cannot support due to the limited ground coverage. The MOC will provide telecommand history and other auxiliary data to the SOC.

Power usage needs to be modelled and payloads may need to be switched off if not enough energy is available from the batteries during the eclipse season.

The firing of thrusters may impact particle instrument payloads that will need to be switched off during Sun pointing and orbit control manoeuvres.

Throughout the mission duration and as long as the level of risk justifies, the Space Debris Office will closely monitor the orbit evolution and alert for potential encounters with objects in the GEO ring based on reception of JSpOC conjunction alerts. Such alerts shall be produced at least 7 days in advance of the predicted encounter. The Flight Control Team will coordinate the activities to analyse and decide upon the counter-measures for the particular encounter. Flight Dynamics will produce emergency manoeuvres only during normal working hours. All encounters are analysed and decided on a case-by-case basis and when appropriate, in coordination with the counterpart entity responsible for the object that is in collision course.

The orbit determination will be carried out using range/Doppler. The Flight Dynamics Team will also support trajectory and manoeuvre optimisation: the manoeuvre performed for LEOP, the orbit evolution manoeuvres and Sun pointing slews.

6.3 Science ground segment

6.3.1 Overview

An overview of the elements of the THOR SGS and the operational interfaces between them is presented in Figure 80.

Close links between the instrument teams and the SOC will be implemented in order to maximize the science return of the THOR mission. These links will be established in the early phases of the mission and will be maintained throughout the mission lifetime: interactions between the SOC, MOC and PI teams will already be set up during the development phase.

During commissioning phase, the MOC will make the spacecraft telemetry available both to the SOC and the PI teams.

After the commissioning phase, the SOC will get the telemetry from the MOC for all the payload. A direct interface between the MOC and the instrument teams will be available only in cases of necessity. During routine operations, the SOC will pass Planning Skeleton Files (PSFs) received from the MOC to the instrument teams to fill in the relevant instrument commanding sequences, that will be sent back to the SOC for checking and consolidation. These commanding files will then be sent to the MOC for uplink to the spacecraft.

Once telemetry with data is received from the MOC, the SOC will process the Level 0 (L0), Level 1(L1) and Level 1.5 (L1.5) data with pipelines provided by the PI teams. Level 1.5 data are necessary for the selective downlink procedure, see Section 6.3.3, which returns the FOM assignments to burst intervals that

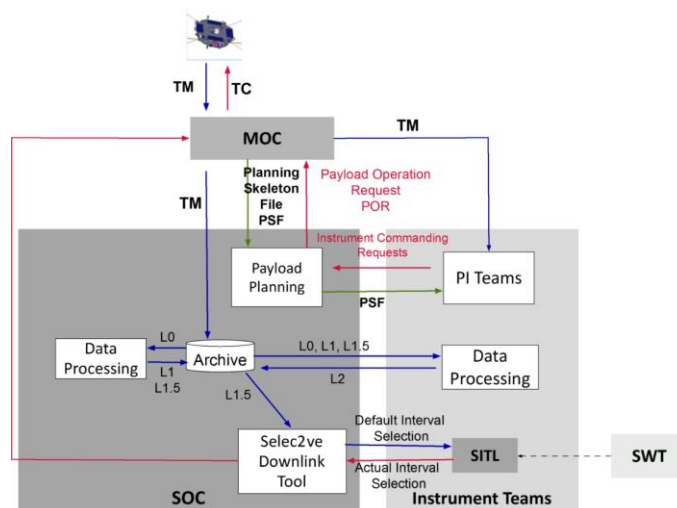


Figure 80: THOR Science Ground Segment scheme. TM (Blue arrows): Spacecraft Telemetry (including Housekeeping, Attitude information, auxiliary data and Science Raw TM); TC (red arrows): Telecommands to operate the spacecraft and instruments; L0,...,L2: Data Processing Levels; SITL: Scientist in the Loop; SWT: Science Working Team. Support Templates (Green Arrows): Planning Skeleton files prepared by MOC and completed by SOC with PI Team inputs.

can be later uplinked to the spacecraft via the MOC.

The PI teams will receive the L0, L1 and L1.5 telemetry from the SOC, and will run their pipelines at their respective sites, giving processed L2 products back to the SOC for archiving and further distribution.

6.3.2 Uplink

The THOR science instruments make *in situ* measurements, and all are intended to operate simultaneously. The SOC and MOC payload operation is simplified by the fact that all instruments, except FAR, are interfacing the spacecraft via FWP and PPU. Routine instrument operations are simple, consisting of a reduced number of commands (e.g., OFF, INIT, STANDBY, SAFE, CALIBRATION, SCIENCE), see Section 4.3.1. Planning of routine tasks as weekly maintenance manoeuvres and long eclipses is done by the MOC based on a set flight rules provided in the instrument operations manuals, and only requires minimal interaction between the MOC and SOC.

The payload instruments will also operate with different internal settings depending on which Key Science Region (KSR) is crossed. Change of the settings is performed via execution of macros stored in the instrument non-volatile memory, see Section 4.3.3. A library of macros with corresponding power and telemetry parameters is provided by instrument teams to SOC as part of the long-term planning. This library is then used by SOC and MOC for constraint checks with respect to resource envelope and to generate detailed commanding.

The SOC will therefore implement a Mission Planning System that will include the following:

- Mission Level Planning, led by the SWT, which plans activities for the whole mission according to the Science Requirements. This results in a Science Activity Plan over the whole mission and an Operations Plan modelled at the SOC.
- Long Term Planning, led by the SWT and SOC, resulting in a timeline of coordinated and individual Observation Plans, covering periods of approximately 6 months.
- Medium Term Planning, led by the Instruments Teams producing Instrument Operations Requests that the SOC converts into Payload Operational Requests, resulting in a 6-months-long medium-term-plan with fixed resource envelope that is fully constraint-checked by MOC
- Short Term Planning, during which science operations are updated within the fixed resources, resulting in approximately week-long command timelines to be sent to the spacecraft.

6.3.3 Downlink

The payload will generate two parallel science data streams (survey and burst) transferred to the spacecraft mass memory, see Section 4.3.1

During the ground contact, all of the survey data and, in addition, burst data from the previously selected intervals are transmitted, see Figure 81. The survey data will be pipeline processed by the SOC to produce Survey QuickLook products using software developed in cooperation with the PI teams and the best available calibrations at the moment the data are received.

A Scientist In The Loop (SITL) will be identified among members of the PI and Co-I teams to make a detailed selection of the most scientifically relevant intervals of burst data to download from the spacecraft. The SITL will be able to carry out his/her responsibilities remotely over the internet. A similar strategy involving a SITL is employed by the NASA MMS and Van Allen Probes missions.

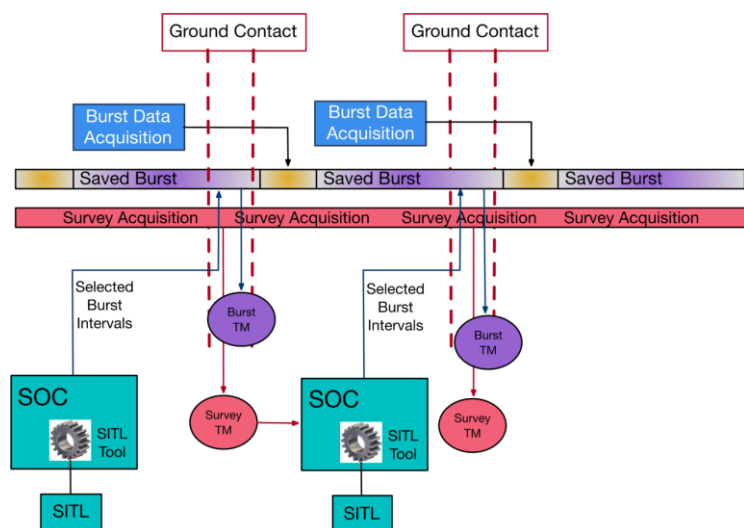


Figure 81: Selective downlink scheme.

The Survey QuickLook products will provide the Scientist In The Loop (SITL) with an overview of the data captured during the preceding period and will be used by the SITL to select the intervals of burst data to be downloaded.

Selection of intervals will be done by the SITL using the SOC provided SITL tool to help in the process. A fall-back automatic algorithm will be implemented in the tool, so that in case of SITL unavailability, default burst data can be downloaded. This kind of process has already been shown to work in MMS. The time duration of each of the intervals in the selective downlink scheme is composed of several contributors, some of them being

mission-design dependent (e.g., interval between survey passes), the other being driven by the incompressible duration for survey data downlink, transmission, processing and analysis. These contributions would add up to the overall time spent in the whole cycle, exemplified in Figure 82, and therefore affect the overall on-board memory sizing.

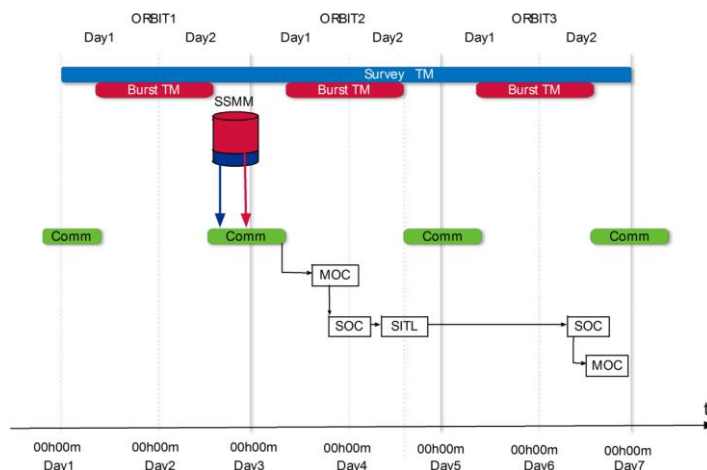


Figure 82: Details of selective downlink. The total ground loop duration for burst interval selection is up to 3 days. The on-board memory is sized for 6 days of burst data, assuming up to 3 days between ground passes.

6.3.4 Data types and data processing

Data types are defined as:

Survey data are a subset of scientific data that are continuously acquired and downlinked with highest priority. They are used both for science and SITL selection.

Burst data are the high-resolution data of the primary scientific interest for the mission. Only burst intervals selected by the SITL are downlinked.

Calibration data are data used typically to derive the Level 2 data from the Level 1 data. Preliminary calibration data are used to go from Level 1 to Level 1.5 data.

Ancillary data are any data that are provided to the scientific community as context for the scientific data. These are data products derived from spacecraft or payload HK TM that are useful for scientific analysis, and could include: instrument status for all payload, SPICE kernels for orbit and spacecraft attitude, time conversion files (OBT to UTC), time periods of burst modes, science operation plans, etc.

Data levels are defined as:

Level 0. Telemetry packets, that are decommutated and decompressed and made available in a well-documented format.

Level 1. Un-calibrated data expressed in engineering units (counts) and may contain extra engineering metadata from other sources.

Level 1.5. Calibrated data derived from the survey mode L1 measurements using preliminary calibrations. They are in physical units and in despun spacecraft coordinates. They are used as input to the SITL tool as well as the fallback automatic selection algorithm.

Level 2. Calibrated data, ready for scientific analysis.

Level 3. Calibrated data products combining data from several instruments.

6.3.5 Data distribution and archiving

Data distribution and archiving are essential parts of the mission. An archive for the THOR data will be built at ESAC under the auspices of the overall ESDC infrastructure. The ESDC holds data and access interfaces for all the ESA science missions, and ensures the long-term preservation of the data and the access.

A single archive will be built for the whole mission, based on the experience of the ESDC in building archives such as the existing CAA/CSA (interface and design). This will reduce archive implementation costs exploiting the experience and knowledge of the ESDC team.

Implementation of the system needs to start 2 years before launch, and archiving needs to continue 2 years after the end of the operations. Within one month of receipt, initial versions of the science data will be generated based on the latest calibrations and will be put online for use by the science community. All THOR data products will be open access from the time of delivery to the SOC by the PI teams. Refinement of the calibrations, using inflight experience and cross-calibration activities, is the responsibility of the PI teams. ESA will support cross-calibration activities through external contracts with the PIs. In case the calibration refinements affect old data products, these products will be reprocessed and redelivered to the SOC with the file versions incremented. After the end of the post-operations phase of the mission, the THOR archive will be maintained as a legacy archive within the ESAC/ESDC premises.

Data Rights and Policy. THOR will employ the Open Data policy starting from 6 months into the nominal operations (after the end of commissioning). This 6-month delay is needed for the PI teams to establish the data processing and calibration pipelines. The PI/Co-I must approve publication of data during the nominal mission. After the end of the nominal mission, PI/Co-I approval is no longer needed, but consulting the PI team for data quality issues is still recommended.

6.4 Scientific data analysis

There is an extensive list of data analysis methods available for studying waves and turbulence (Table 27) and coherent structures (Table 28) using the THOR data. While most of the presented analysis methods are developed for single-point measurements, THOR also has the ability to make multi-point measurements using multiple electric field probes at different locations on the spacecraft. This enables an estimate of the phase velocity of electric field waveforms in the spacecraft spin plane.

6.4.1 Waves and turbulent fields

Particle heating and acceleration happen in both quasi-monochromatic waves and in turbulent fluctuations. While the quasi-monochromatic waves have discrete frequencies and wavevectors and appear as clear peaks in the energy spectrum, the turbulent fields no longer have clear spatial or temporal structures and appear as a continuous spectrum.

Properties of the quasi-monochromatic waves can be studied by THOR using a variety of analysis methods. Using the magnetic field data, one may determine the energy spectra for different fluctuation components, the compressibility of magnetic field, the field rotation sense around the mean magnetic field, and the wavevector direction through minimum variance analysis. When combined with the electric field and plasma data, one may determine the phase speed, the Poynting flux, the helicity quantities, the wave distribution function, and the wavevectors.

For the study of turbulent fluctuations, the slope and the shape (flattening or steepening) of the energy spectrum are determined not only in the frequency domain (in the spacecraft frame) but also in the wavenumber domain using Taylor's frozen-in flow hypothesis. The spectra of the helicity quantities can also be determined. Wave-wave and wave-particle interactions can be studied, e.g., for the detection of Landau and cyclotron resonances, pitch angle scattering, and three-wave couplings (bispectrum). Statistical behaviour, in particular the non-Gaussian nature of the turbulent fluctuations can be studied using the method of phase coherence, probability density functions, and the local intermittency measure.

Table 27 shows some of the methods for analysing waves and turbulent fluctuations. All are single spacecraft methods, however most of them have been validated using multi-spacecraft Cluster data.

Table 27: Analysis methods for waves and turbulent fluctuations.

Target	Output data	Input data	References
Energy spectra	$P_{\parallel}, P_{\text{perp}}$, incompressible and compressible components	B or E	[246,247]
	P_R, P_L (Stokes I and V) circularly polarized components	B or E	[248]
	z^+, z^- (Elsasser variables)	B and U	[249]
Compressibility	C_{\parallel}	B	[250]
Ellipticity	epsilon (polarization sense)	B or E	[251]
Wavevector angle	theta_kB (minimum variance)	B	[252]
Streamwise wavenumber	k_{\parallel} (Taylor's hypothesis)	f and U	[253]
Phase speed	v_{ph} (induction equation)	B and E	[50]
Poynting flux	S	B and E	[254]
Helicity quantities	h_c (reduced cross helicity) h_m (magnetic helicity)	B and U	[255]
Wave distribution function	F(k), energy distribution in k	B or E	[256–259]
Resonance parameters	zeta_L, Landau resonance	ω, k, T	[247,250]
	zeta_c, cyclotron resonance	ω, k, T	[247,250]
Wavevector	k (from phase speed)	B and E	[260]
	k (from oscillating electric current)	j and B	[261]
	k (from multiple probes)	E	[246]
Pitch angle scattering	f_plateau(v) and apparent phase speed omega/k_para	f(v)	[72,139,262]
Wave-wave coupling	bispectrum	B and n	[263]
Phase coherence	phase coherence index	B	[264]
Non-Gaussian fluctuations	probability density function	B or U	[8]
	local intermittency measure	B	[8]

6.4.2 Structures and discontinuities

Turbulent fields are closely associated with coherent structures and discontinuities. Shock waves, for example, are a major driver of turbulence. The interplay of turbulence with the shocks serves as a very efficient particle acceleration mechanism such as diffusive shock acceleration. Also, phase coherence and fluid nonlinearity generate coherent structures in a turbulent field such as eddies, current sheets, and flux tubes.

In order to investigate 1D plasma structures such as current sheets or 2D and 3D structures such as magnetic islands and flux ropes, it is often useful to transform them into a proper, co-moving reference frame. Often, it is also necessary to establish the orientation of plasma structures.

To do this, a number of methods are available. In particular, variance analysis and residue methods have proven to be very useful for this purpose. Residue methods are typically based on simple conservation laws for example conservation of energy, mass or flux. The most commonly used method is probably minimum variance [265] of the magnetic field to establish the orientation of a 1D current sheet. A unified approach to variance analysis and residue methods, applicable to any measured quantity (both vector fields and scalars) which obeys classical conservation laws was presented in [266]. In its simplest form, the unified approach only takes the magnetic field as input. More refined variants take the electric field, density, plasma flow or higher order moments such as pressure or heat flux as inputs.

An advantage of residue methods is that they can provide error estimates both for the frame velocity and for the boundary normal of the structure. A benchmark of selected single spacecraft method versus multi-spacecraft method was also given in [267] and showed that single spacecraft methods can perform equally well as multi-spacecraft timing methods. [256,257] used generic residue analysis methods to study energy conservation at the terrestrial magnetopause and thus demonstrating the usability of the methods.

THOR with its high time resolution plasma instruments and better 3D E-field experiment will be able to study far smaller structures and with a higher accuracy than existing missions. Table 28 below lists some of the methods and the required measurements anticipated to be useful for the THOR mission.

Table 28 Analysis methods for coherent structures and discontinuities.

Target	Output data	Input data	References
Plane normal direction	n_plane	B (or E or V and n)	[246,265,265,266]
Plane velocity	v_plane	B, E (or U) and n,P,Q,W	[266,270]
Plane acceleration	a_plane, de Hoffmann-Teller frame	B, E (or U)	[271,272]
Electrostatic potential profile	Phi (Liouville mapping)	f(v) and B	[261]
Magnetostatic structure	B(x,y), n(x,y) Grad-Shafranov reconstruction	B and else	[131]
Flux tube structure	B(z)		[195]
Structure detection	partial variance of increments (PVI)	B	[121]

6.5 Wave-particle correlation capabilities

The key physical phenomenon addressed by THOR is the exchange of energy between electromagnetic field fluctuations and plasma particles on kinetic scales. This process can be analysed by directly correlating the electromagnetic field waveform with time evolution of the particle distribution on time scales of a fraction of the wave period. This analysis is particularly relevant for the study of excitation of plasma waves in unstable plasma and wave dissipation. The phase correlation technique [274] allows the resonant transfer of energy between fields and particles to be calculated as a function of energy and pitch angle. Correlation between particle counts and field oscillations also allows nonlinear effects such as particle trapping or bunching to be identified [275].

In the THOR dataset, the ion distribution functions will be available on time scales shorter than, or comparable to, the period of ion wave modes, such as kinetic Alfvén waves and ion-cyclotron waves. The THOR ion instruments will sample the 3D plasma distribution by sweeping the energy and angular space, accumulating particle counts in individual bins over intervals much shorter than typical ion wave periods. An analogous technique cannot be directly applied to study electron plasma waves at frequencies above 1 kHz using electron distributions provided by the TEA instrument, since the accumulation period of particle counts for each energy bin (approximately 150 μ s) is not sufficiently smaller than the wave period. To circumvent this issue, TEA will provide a high-resolution electron data product consisting of exact impact times of individual detected electrons, complemented by their energy and arrival direction. This superburst data product will only be available for short intervals synchronized with high resolution electromagnetic field waveform snapshots captured by FWP. Accurate time synchronization between particle and field data (1 μ s accuracy) and will allow meaningful correlations up to the electron plasma frequency.

Analysis of numerical simulation data [276] has shown that the technique works well for coherent waves, such as magnetospheric whistlers (Figure 83) or Langmuir waves. Several recent spacecraft missions implement the calculation of wave particle correlations in on-board software (ERG, JUICE) to avoid

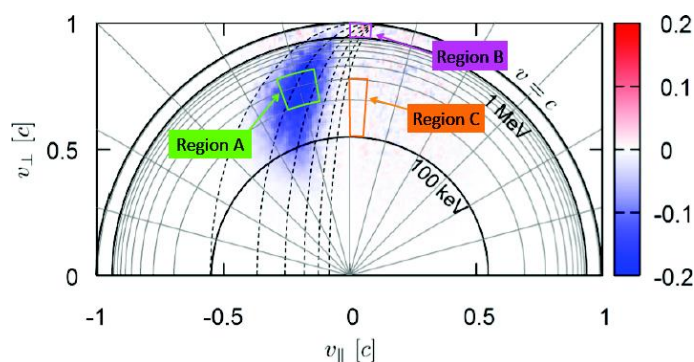


Figure 83: Example of wave-particle correlation technique applied to a numerical simulation of magnetospheric chorus waves. The colour shows the variation of the kinetic energy of electrons due to interaction with waves as a function of parallel and perpendicular electron velocity. Negative change of electron kinetic energy in Region A corresponds to wave growth and positive energy transfer in region B to particle acceleration by the wave [276].

transmitting the large telemetry volume associated with individual particle data. Considering the focus of the THOR mission on details of kinetic physics and relatively large telemetry allocation, it was decided to transmit the superburst data to the ground, which offers much wider data analysis and validation options compared to on-board calculations.

6.6 Numerical simulation support

Our knowledge about the fundamental processes responsible for turbulent plasma heating and particle acceleration at kinetic scales as of today mainly comes from numerical simulations. Different simulations, studying the kinetic dynamics of the main ion species (protons and alpha particles) and electrons, have clearly shown that kinetic physics is different for different species and is an essential ingredient for the description of plasma heating and particle acceleration in turbulent

space plasmas at kinetic scales. Therefore, the numerical modelling support for the THOR mission is crucial, both from the science and mission design point of view. The numerical simulation support is provided by the synergistic activities of the Numerical Simulation Support Team (NSST), which includes scientists developing, running and supplying results from different plasma simulation codes, and the Virtual Instrument Team (VIT), which aids the definition of the THOR instruments making use of the output of fields and particle distribution functions from numerical simulations and generating synthetic observations based on instrument characteristics.

Table 29 lists numerical tools available to NSST and VIT to support science, data analysis and mission planning. The results from most of those simulations are used in the THOR mission preparation, see Figure 84. In particular, the Eulerian low-noise algorithms provide a clean description of the particle velocity distributions and of the resonant wave-particle interaction, especially in the short-wavelength range of the turbulent cascade, where the amplitude of the fluctuations is typically low. On the other hand, the particle-in-cell (PIC) codes are well suited for studying particle interaction with large amplitude fluctuations and/or localized structures. The PIC codes have larger statistical noise but they are significantly less computationally time demanding than the Eulerian codes and can model the plasma dynamics over many decades of scales, retaining the kinetic physics of both ion and electron species. Both Eulerian (Vlasiator) and PIC (iPIC3D and vpic-H3D) codes are also available in global configuration and allow to model the global interaction of the interplanetary medium with the Earth's magnetosphere including the generation of the Earth's bow shock. Finally, magnetohydrodynamic (MHD) and two-fluid algorithms can address the physics of the large spatial scales ranges of turbulence. In summary, the numerical tools in Table 29 can fully support the science of THOR, covering a wide range of plasma processes.

Table 29: Major numerical simulation codes available to support THOR. For additional material, including simulation movies, see <http://thor.irfu.se/home/numerical-simulation>.

Simulation type	Available simulation codes
Eulerian	HVM3D3V, Vlasiator (hybrid Vlasov); AstroGK, GENE (gyrokinetic); FourierVlasov (Fourier in velocity); Gkeyll (full Vlasov)
Particle in cell	iPIC3D (implicit moment PIC); dHybrid, Camelia (hybrid PIC); P3D (explicit PIC); vpic-H3D (relativistic 3D PIC)
Semi-Lagrangian	Vlem2D3V (Vlasov-Maxwell)
Fluid	TFPC (two-fluid Pisa code); GHOST (multi-solver framework)

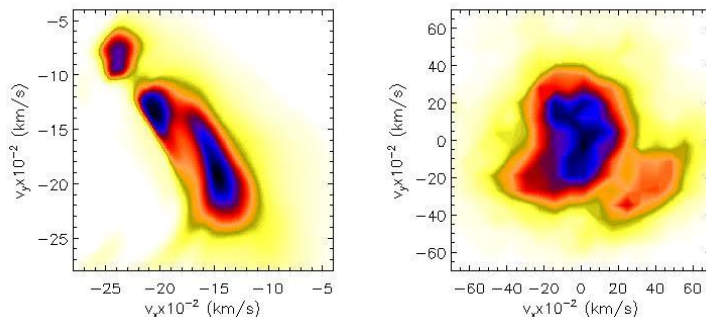


Figure 84: Examples of proton distribution functions in simulations of a turbulent shock (left, the Vlasiator code) and turbulence (right, the iPIC3D code). Such distribution functions are analysed by the virtual instrument simulators to confirm the sufficiency of the THOR instrument geometric factors.

NSST and VIT have done extensive work during Study Phase. Guided by data from previous space missions, global and local numerical simulations have been run to model the plasma dynamics in the THOR key science regions (pristine solar wind, shock, magnetosheath). A common database, accessible to all THOR team members, has been created based on the output from different runs of numerical codes. Virtual THOR spacecraft have been flown through the simulation box to collect data in the different simulation runs. In order to support the design phase of particle instruments, a virtual electrostatic analyser (top-hat) has been used to sample the velocity distribution functions from the simulations [240,241] based on the characteristics of the CSW, IMS and TEA instruments. Realistic energy and angular resolutions and geometric factors have been used: as an example, Figure 85 shows how the alpha particle and the electron velocity distributions from turbulent kinetic simulations would be detected by a sensor with a resolution and geometric factor of CSW and TEA, respectively. These results have been analysed and the characteristics of each instrument optimized correspondingly. In summary, NSST and VIT have confirmed that the final THOR payload is well suited to perform measurements required to achieve the scientific goals of the mission.

Numerical simulations have been also employed to investigate and compare the validity limits of different techniques using single and multi-point measurements to estimate the current density and to reconstruct ω - k spectra of fluctuations. For example, the validity limits of the Taylor hypothesis [277] have been investigated by launching a virtual spacecraft at different speeds and angles with respect to the ambient field across the simulation box of evolving turbulence. Spectra reconstructed from the Taylor hypothesis have been compared to the exact spectra obtained through the Fourier analysis on the numerical data. This analysis shows that for kinetic Alfvén wave turbulence the frozen-in Taylor hypothesis is fulfilled down to sub-proton scales, especially for fast flows typical of the fast solar wind (see Figure 86). Moreover, recent analysis on MMS data confirms that multi-spacecraft techniques provide evidence consistent with single-spacecraft Taylor hypothesis ones.

Fluctuation spectra in ω - k space have also been reconstructed based on multi-point measurements of virtual spacecraft applying the k -filtering technique [278]. As another example, the limits of the curlometer technique [279] for the estimation of the current density have been investigated by analysing synthetic data of virtual satellites in a tetrahedron configuration (spanning a wide range of separations among the spacecraft) launched across a static 3D turbulent field and comparing with direct measurements of the current density as the first order velocity moment of the particle distribution function. The conclusion is that a superior method to resolve

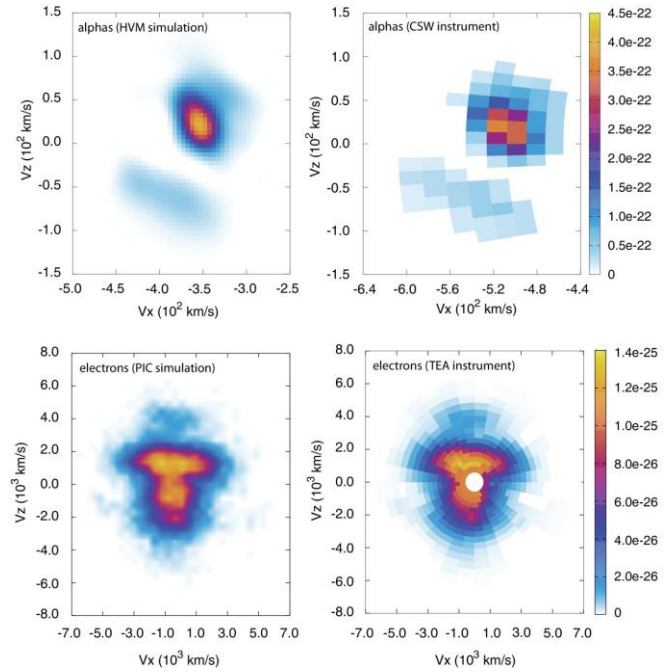


Figure 85: Top: alpha particle velocity distribution from a HVM simulation of solar-wind turbulence (left) and as sampled by the CSW instrument (right). Bottom: electron velocity distribution from a PIC simulation of solar-wind turbulence (left) and as sampled by the TEA instrument (right).

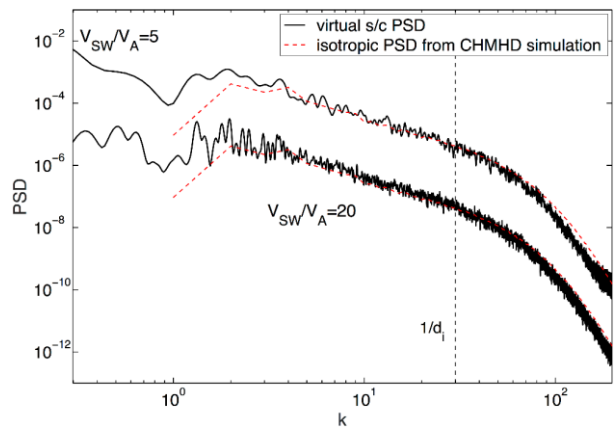


Figure 86: Power spectral density (PSD) as a function of wavenumber, measured by a single virtual spacecraft launched across the numerical box of a compressible Hall MHD simulation (black), as compared to the exact spectrum (red), for two values of the solar wind speed.

the current at electron kinetic scales, assuming the lower limit of the spacecraft separation to be about 5-10 km, is to use single spacecraft particle instrument observations.

NSST and VIT will continue their work during the next phases of the mission. The main goals will be: (1) during the pre-launch phase to support the design of instruments and mission where needed, as well as to develop new numerical algorithms and to prepare the required simulations and tools for the later support of data analysis, (2) after launch to support the science community with the necessary simulations and virtual satellite runs, as well as actively participate in the scientific planning of the mission. During both phases NSST will also work closely together with the theory and modelling teams of Solar Orbiter and Solar Probe Plus. In summary, NNST and VIT will help to ensure the maximum scientific output from the mission.

Some of important tasks for the following years are: (1) Low noise simulations of the kinetic plasma dynamics down to electron scales. (2) Improvement of techniques proposed during Study Phase to identify physical processes responsible for the plasma non-Maxwellianity. (3) Improve the identification of structures in velocity space and associated velocity scales. (4) Further development of the analysis of the particle distribution functions to characterize their deformations in velocity space, triggered by kinetic effects. (5) Simulation of the field-particle correlator used to measure the energy transfer from fields to particles associated with collisionless damping of the turbulent fluctuations. (6) Comparative analyses of different non-Maxwellian indicators, already proposed during Study Phase, will be performed to examine the possibility of implementing the calculations of these indicators on board, with the aim of identifying time intervals relevant for studying kinetic physics. (7) Design of numerical simulations based on nested algorithms, each of them modelling the plasma dynamics in a specific range of spatial scales. This would provide a description of the system over many decades of scales along the turbulent cascade, in particular, approaching the ultimate goal of modelling scales from the system size of Earth's magnetosphere interacting with solar wind down to kinetic scales.

7 Management

7.1 Procurement scheme

ESA is responsible for the spacecraft manufacturing, launch and operations, as well as the data archiving and distribution.

National agencies will provide all of the scientific instruments. Table 30 shows the institutions with a planned hardware contribution to the THOR payload and their responsibility within the instrument consortia. In addition to hardware provision, the national agencies will support instrument operations, data calibration and data processing, at least through the nominal phase of the mission.

Table 30: Institutions with a planned hardware contribution to the THOR payload.

Instrument	PI	Co-PI	Lead-CoI
MAG	R. Nakamura IWF (Austria)	J. Eastwood ICL (UK)	
SCM	F. Sahraoui LPP (France)	J.-L. Pinçon LPC2E (France)	
EFI	Y. Khotyaintsev IRF (Sweden)	S. Bale SSL (USA)	H. Rothkaehl SRC-PAS (Poland) N. Ivchenko KTH (Sweden)
FWP	J. Soucek IAP-CAS (Czech Republic)	H. Rothkaehl SRC-PAS (Poland)	M. Balikhin Univ.Sheffield (UK) A. Zaslavsky LESIA (France)
TEA	A. Fazakerley MSSL (UK)	T. Moore NASA/GSFC (USA)	Y. Saito ISAS/JAXA (Japan)
CSW	B. Lavraud IRAP (France)	J. De Keyser BIRA-ISAB (Belgium)	
IMS	A. Retinò LPP (France)	H. Kucharek UNH (USA)	Y. Saito ISAS/JAXA (Japan) M. Fraenz MPS(Germany)
PPU	M. F. Marcucci INAF-IAPS (Italy)		
FAR	Z. Nemecek CU FMF (Czech Republic)	Y. Yermolaev IKI (Russia)	
EPE	R. Wimmer- Schweiggruber IEAP (Germany)	R. Vainio Univ.Turku (Finland)	

7.2 Programme participation

The possible modes of participation in the THOR programme are:

Principal Investigator (PI), heading an instrument consortium providing an instrument.

Co-Principal Investigator (Co-PI), appointed if he/she is responsible for a major contribution to the development and building of an instrument and he/she is from a country/institution different from that of the PI.

Lead Co-Investigator (Lead-CoI), appointed if he/she is responsible for a significant development and building of an instrument and he/she is from a country/institution different from that of the PI.

Co-Investigator (Co-I), a member of a consortium providing an instrument and having a well-defined role in the instrument team, serving under the direction of the PI, and being critical for the successful completion of instrument goals by contributing unique expertise and/or capabilities.

Interdisciplinary Scientist (IDS), an expert in specific overarching science themes connected to the mission objectives who takes advantage of synergistic use of the THOR data. To ensure a top-level oversight of mission science, four IDSs will be selected through an open AO process after the start of the implementation phase. In general, IDSs should not reflect instrument specific domains, but rather cover specific science themes (e.g., shocks, turbulence, numerical simulations, etc.).

Guest Investigator (GI), a scientist responsible for dedicated data collection and analysis campaigns. GIs can support their campaigns by performing laboratory studies, theoretical or numerical investigations. Their proposals shall be submitted to ESA following an open AO process during the operational phase of the mission. Their observations will be planned via the master science plan similar to normal operations.

7.3 Science management

Science management for THOR is typical for ESA science projects (as for example JUICE):

Project Scientist (PS), nominated by ESA. The PS is the agency's interface with the PIs and will chair the Science Working Team (SWT) and coordinate its activities.

Science Working Team (SWT), consisting of the PS, PIs and IDSs. Co-PIs, Co-Is, GIs and other interested scientists will be invited to participate in SWT meetings as appropriate. The SWT will monitor and advise ESA on all aspects of the mission that will affect its scientific performance. The SWT is responsible for planning science operations and the development of the Master Science Plan (MSP).

7.4 Schedule

The Definition Phase (B1) system study is expected to start in the 3rd quarter of 2017 for a period of 15 months, with the objective of enabling the mission final adoption at the beginning of 2019. In parallel, if needed, a Technology Development Activity (TDA) for bi-propellant tank will be initiated directly after mission down-selection. The System Requirements Review will close the Definition Phase by consolidating the overall mission concept for enabling an efficient start of the Implementation Phase, should the mission be finally adopted.

After potential mission adoption early in 2019, a prime contractor for the mission will be chosen for phase B2/C/D through open competition and by taking into account geographical distribution requirements. The launch is currently planned for mid 2026. An overview of the schedule is shown below in Figure 87.

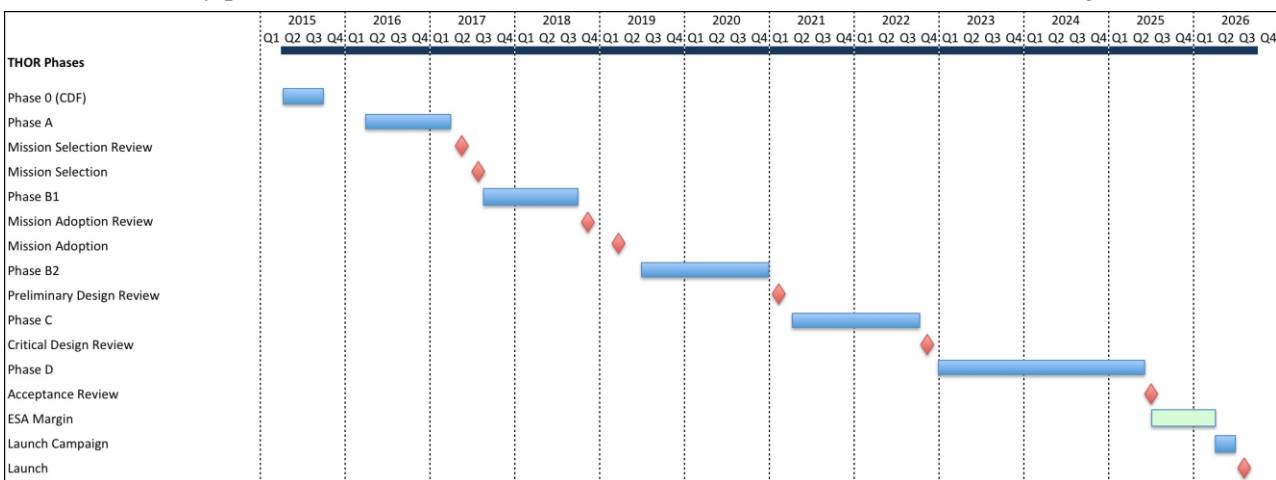


Figure 87: An estimated schedule for the THOR mission.

8 Communication and outreach

THOR is a mission to understand fundamental plasma processes, such as particle acceleration, energy dissipation and heating by turbulent fluctuations, in the plasma environment in near-Earth space. Many of these processes are shared with other scientific communities, for example, they occur in fusion plasmas, astrophysics and solar physics, and the study of these topics will lead to important progress in understanding other plasma environments in the Solar System, universe and laboratory. Turbulence is commonly observed in everyday phenomena such as ocean waves, fast flowing rivers, billowing storm clouds, or smoke from a cigarette and in stirring a cup of coffee, and most fluid flows occurring in nature and created in engineering applications are turbulent. The term "turbulence" is, therefore, often used in everyday language. This gives many opportunities to connect to everyday life outside of plasma physics and provides a wide spectrum of possibilities for communication, outreach and education opportunities.

Based on experience from recent missions, there will be many exciting new research results that can be demonstrated and presented to the general public through press releases, outreach activities and educational material. Solar wind turbulence, turbulence in stellar winds and the interstellar medium, the Earth's bow shock, shocks at coronal mass ejections, supernova shocks, and plasma fusion devices are some of the examples that will be used to show the application of the science results, and which will provide visual and tangible vehicles to convey the mission message. Space science is fun and of fundamental importance for society. THOR will be a clear demonstration of the important European role in space science.



Figure 88: Students being shown a demonstration at a stand of the Aurora Explorer exhibition at the Royal Society Summer Exhibition 2011.

The THOR project has a common integrated web presence at <http://thor.irfu.se>, where in addition to information about the mission, spacecraft, instruments and data access, different outreach-specific material will be available, such as movies that reproduce the spacecraft trajectory within a simulated plasma environment in realistic physical conditions. All of the material in the THOR website can be used on the official ESA/THOR web page. The preparation of that material will be based on the successful experience in using such material from Cluster, THEMIS, MMS and other missions, together with ground-based observatories and facilities where appropriate.

A public YouTube channel will be set up to give coverage on the mission status and on the scientific outcomes. Each important scientific discovery achieved through the THOR measurements will be presented by the lead THOR scientists and researchers in the form of TV interviews. Outstanding high-school students, as well as university and PhD students, will be given the opportunity to take part in these TV shows, interact and directly ask questions to the THOR scientific team members. Moreover, social network profiles dedicated to THOR will be set up and frequently updated with news about the progress of the mission.

A traveling exhibition entitled "Discover Space Plasmas" will be organized in different institutions by members of the THOR consortium, in order to introduce a general audience of all ages to the fascinating aspects and the myriad of applications of plasmas in everyday life. The exhibition will guide each guest in a breath-taking journey through space and astrophysical environments, laboratory experiments for nuclear fusion and industrial plasma applications. Interactive experiments, videos, presentations and THOR gadgets will help guests to discover the secrets of our Solar System as seen by the eyes of THOR.

During the exhibition, guests will meet and talk with professional scientists and ESA engineers in the field of space physics, aeronautics and plasma physics, directly involved in the THOR science and construction, and visit their displays to learn about current research in this cutting-edge field. Updates on THOR operations, measurements and orbits will be also presented during the exhibition for the interested public in the form of scientific seminars and presentations. Visitors will hopefully be captivated and surprised by this absorbing study into the importance of science in space and the future of space exploration.

Members of the THOR team have already been involved in the organization of such outreach activities. For example, the UK Cluster teams, several members of whom are now working on the THOR mission, created an exhibit stand for the Royal Society Summer Exhibition 2011 (see Figure 88). The overall exhibition had 13,700 visitors in 6 days, including schools, general public, VIPs (including government ministers), and turned out to be a successful outreach activity.

Moreover, before launch, school classes (age 6 to 16) will be given the opportunity to provide examples (photos or sound recordings) of what they consider "turbulence" and selected items will be stored on some suitable medium on-board THOR before launch. In a similar way photos of the classes can be "sent into space". At a suitable time before launch, school classes and their teachers will be invited together with the press to see the (nearly finished) flight instruments in the corresponding instrument laboratories and to visit the supercomputer facilities in Europe, where simulations are performed supporting the different phases of the mission.

Then, at the time of the launch, they will be invited to watch the live (ESA) TV coverage of the launch together with some of the scientists and engineers involved in the mission. After launch, our web page will give continue information on the position of THOR, which ground station is being used and other technical information, together with a preliminary near-real-time overview scientific data open to the general public.

9 Bibliography

1. Alfvén, H., *Phys. Today* **39**, 22–27 (1986).
2. Biskamp, D., (Cambridge, UK: Cambridge University Press, |c2003, 2003).
3. Hajivassiliou, C. A., *Nature* **355**, 232–234 (1992).
4. *Phys. Plasmas* **13**, 56501 (2006).
5. Brandenburg, A. *et al.*, *Rep. Prog. Phys.* **74**, 46901 (2011).
6. Elmegreen, B. G. *et al.*, *Annu. Rev. Astron. Astrophys.* **42**, 211–273 (2004).
7. Arzoumanian, D. *et al.*, *Astron. Astrophys.* **529**, L6 (2011).
8. Bruno, R. *et al.*, *Living Rev. Sol. Phys.* **10**, 2 (2013).
9. Galtier, S., *ArXiv E-Prints* (2012).
10. Alexandrova, O. *et al.*, *Space Sci. Rev.* **178**, 101–139 (2013).
11. Saur, J., *Astrophys. J. Lett.* **602**, L137 (2004).
12. Uritsky, V. M. *et al.*, *J. Geophys. Res. Space Phys.* **116**, 9236 (2011).
13. von Papen, M. *et al.*, *J. Geophys. Res. Space Phys.* **119**, 2797–2818 (2014).
14. Reynoso, E. M. *et al.*, *Astron. J.* **145**, 104 (2013).
15. von Alfthan, S. *et al.*, *J. Atmospheric Sol.-Terr. Phys.* **120**, 24–35 (2014).
16. Gekelman, W. *et al.*, *Rev. Sci. Instrum.* **87**, 25105 (2016).
17. Ricci, P. *et al.*, *Phys. Rev. Lett.* **104**, 145001 (2010).
18. Sorriso-Valvo, L. *et al.*, *Phys. Rev. Lett.* **99**, 115001 (2007).
19. Alexandrova, O. *et al.*, *Phys. Rev. Lett.* **103**, 165003 (2009).
20. Leamon, R. J. *et al.*, *J. Geophys. Res. Space Phys.* **103**, 4775–4787 (1998).
21. Sahraoui, F. *et al.*, *Phys. Rev. Lett.* **102**, 231102 (2009).
22. Sundkvist, D. *et al.*, *Phys. Rev. Lett.* **99**, 25004 (2007).
23. Karimabadi, H. *et al.*, *Phys. Plasmas* **20**, 12303 (2013).
24. Camporeale, E. *et al.*, *Astrophys. J.* **730**, 114 (2011).
25. Chandran, B. D. G. *et al.*, *Astrophys. J.* **720**, 503 (2010).
26. Servidio, S. *et al.*, *Phys. Rev. Lett.* **102**, 115003 (2009).
27. Servidio, S. *et al.*, *Phys. Rev. Lett.* **108**, 45001 (2012).
28. TenBarge, J. M. *et al.*, *Astrophys. J. Lett.* **771**, L27 (2013).
29. Cho, J. *et al.*, *Astrophys. J.* **701**, 236 (2009).
30. Howes, G. G. *et al.*, *Phys. Rev. Lett.* **107**, 35004 (2011).
31. Schekochihin, A. A. *et al.*, *Astrophys. J. Suppl. Ser.* **182**, 310 (2009).
32. Kis, A. *et al.*, *Astrophys. J.* **771**, 4 (2013).
33. Soucek, J. *et al.*, *Ann Geophys* **29**, 1049–1060 (2011).
34. Voitenko, Y. *et al.*, *Sol. Phys.* **209**, 37–60 (2002).
35. Malaspina, D. M. *et al.*, *J. Geophys. Res. Space Phys.* **118**, 591–599 (2013).
36. Valentini, F. *et al.*, *Phys. Rev. E* **71**, 17402 (2005).
37. Boldyrev, S. *et al.*, *Astrophys. J. Lett.* **758**, L44 (2012).
38. Cho, J. *et al.*, *Astrophys. J. Lett.* **615**, L41–L44 (2004).
39. Galtier, S. *et al.*, *Astrophys. J.* **656**, 560–566 (2007).
40. Meyrand, R. *et al.*, *Phys. Rev. Lett.* **111**, 264501 (2013).
41. Gary, S. P. *et al.*, *Astrophys. J.* **816**, 102 (2016).
42. Howes, G. G. *et al.*, *Phys. Rev. Lett.* **100**, 65004 (2008).
43. Passot, T. *et al.*, *Astrophys. J. Lett.* **812**, L37 (2015).
44. Sahraoui, F. *et al.*, *Phys. Rev. Lett.* **96**, 75002 (2006).
45. Soucek, J. *et al.*, *J. Geophys. Res. Space Phys.* **113**, A04203 (2008).
46. Russell, C. T. *et al.*, *Geophys. Res. Lett.* **36**, L05106 (2009).
47. Jian, L. K. *et al.*, *Astrophys. J. Lett.* **701**, L105–L109 (2009).
48. Verscharen, D. *et al.*, *Phys. Plasmas* **19**, 022305–022305 (2012).

49. Wicks, R. T. *et al.*, *Astrophys. J.* **819**, 6 (2016).
50. Bale, S. D. *et al.*, *Phys. Rev. Lett.* **94**, 215002 (2005).
51. Salem, C. S. *et al.*, *Astrophys. J. Lett.* **745**, L9 (2012).
52. Chen, C. H. K. *et al.*, *Phys. Rev. Lett.* **110**, 225002 (2013).
53. Boldyrev, S. *et al.*, *Astrophys. J.* **777**, 41 (2013).
54. Gary, S. P. *et al.*, *J. Geophys. Res. Space Phys.* **114**, A12105 (2009).
55. TenBarge, J. M. *et al.*, *Astrophys. J.* **753**, 107 (2012).
56. Kiyani, K. H. *et al.*, *Astrophys. J.* **763**, 10 (2013).
57. Song, P. *et al.*, *J. Geophys. Res.* **99**, 6011–6025 (1994).
58. Howes, G. G. *et al.*, *Astrophys. J. Lett.* **709**, L49–L52 (2010).
59. He, J. *et al.*, *Astrophys. J.* **731**, 85 (2011).
60. Podesta, J. J. *et al.*, *Astrophys. J.* **734**, 15 (2011).
61. Lacombe, C. *et al.*, *Astrophys. J.* **796**, 5 (2014).
62. Sahraoui, F. *et al.*, *Astrophys. J.* **777**, 15 (2013).
63. Alexandrova, O. *et al.*, *Astrophys. J.* **760**, 121 (2012).
64. Chen, C. H. K. *et al.*, *Phys. Rev. Lett.* **104**, 255002 (2010).
65. Sahraoui, F. *et al.*, *Phys. Rev. Lett.* **105**, 131101 (2010).
66. Narita, Y. *et al.*, *Geophys. Res. Lett.* **38**, L05101 (2011).
67. Mangeney, A. *et al.*, *Ann Geophys* **24**, 3507–3521 (2006).
68. Alexandrova, O. *et al.*, *Ann Geophys* **26**, 3585–3596 (2008).
69. Horbury, T. S. *et al.*, *Phys. Rev. Lett.* **101**, 175005 (2008).
70. Chen, C. H. K. *et al.*, *Astrophys. J. Lett.* **789**, L8 (2014).
71. Isenberg, P. A., *Space Sci. Rev.* **95**, 119–131 (2001).
72. Marsch, E. *et al.*, *Ann Geophys* **29**, 2089–2099 (2011).
73. Smith, C. W. *et al.*, *Astrophys. J.* **745**, 8 (2012).
74. Plunk, G. G., *Phys. Plasmas* **20**, 32304 (2013).
75. Schekochihin, A. A. *et al.*, *J. Plasma Phys.* **82**, 905820212 (2016).
76. Johnson, J. R. *et al.*, *Geophys. Res. Lett.* **28**, 4421–4424 (2001).
77. Chaston, C. C. *et al.*, *Geophys. Res. Lett.* **41**, 8185–8192 (2014).
78. Isenberg, P. A. *et al.*, *Astrophys. J.* **731**, 88 (2011).
79. Gary, S. P. *et al.*, *Geophys. Res. Lett.* **35**, L02104 (2008).
80. Li, T. C. *et al.*, *Astrophys. J. Lett.* **832**, L24 (2016).
81. Howes, G. G., *Phys. Plasmas* **15**, 055904–055904 (2008).
82. Klein, K. G. *et al.*, *Astrophys. J.* **820**, 47 (2016).
83. Fisk, L. A. *et al.*, *Space Sci. Rev.* **130**, 153–160 (2007).
84. Servidio, S. *et al.*, *Astrophys. J. Lett.* **781**, L27 (2014).
85. Valentini, F. *et al.*, *Phys. Plasmas* **21**, 82307 (2014).
86. Haynes, C. T. *et al.*, *Astrophys. J.* **783**, 38 (2014).
87. Pezzi, O. *et al.*, *Phys. Rev. Lett.* **116**, 145001 (2016).
88. Klein, K. G. *et al.*, *Astrophys. J. Lett.* **826**, L30 (2016).
89. Howes, G. G. *et al.*, *J. Plasma Phys.* **83**, (2017).
90. He, J. *et al.*, *Astrophys. J. Lett.* **813**, L30 (2015).
91. Balbus, S. A. *et al.*, *Rev. Mod. Phys.* **70**, 1–53 (1998).
92. Riquelme, M. A. *et al.*, *Astrophys. J.* **755**, 50 (2012).
93. Kunz, M. W. *et al.*, *Phys. Rev. Lett.* **117**, 235101 (2016).
94. Quataert, E. *et al.*, *Astrophys. J.* **577**, 524 (2002).
95. Sharma, P., *PhD Thesis* (2007).
96. Hoshino, M., *Phys. Rev. Lett.* **114**, 61101 (2015).
97. Hellinger, P. *et al.*, *Geophys. Res. Lett.* **33**, L09101 (2006).
98. Valentini, F. *et al.*, *New J. Phys.* **18**, 125001 (2016).
99. Narayan, R. *et al.*, 148–182 (1998).

100. Mangeney, A., *Astrophys. Space Sci.* **277**, 117–122 (2001).
101. Matthaeus, W. H. *et al.*, *Phys. Fluids* **28**, 303–307 (1985).
102. Veltri, P., *Plasma Phys. Control. Fusion* **41**, A787 (1999).
103. Kiyani, K. H. *et al.*, *Phys. Rev. Lett.* **103**, 75006 (2009).
104. Alexandrova, O. *et al.*, *Astrophys. J.* **674**, 1153 (2008).
105. Stawarz, J. E. *et al.*, *J. Geophys. Res. Space Phys.* **121**, 2016JA023458 (2016).
106. Franci, L. *et al.*, *Astrophys. J. Lett.* **804**, L39 (2015).
107. Retinò, A. *et al.*, *Nat. Phys.* **3**, 236–238 (2007).
108. Osman, K. T. *et al.*, *Astrophys. J. Lett.* **727**, L11 (2011).
109. Sorriso-Valvo, L. *et al.*, *Astrophys. J.* **807**, 86 (2015).
110. Zhdankin, V. *et al.*, *Mon. Not. R. Astron. Soc.* **457**, L69–L73 (2016).
111. Howes, G. G., *Astrophys. J.* **827**, L28 (2016).
112. Carbone, V. *et al.*, *Phys. Fluids* **2**, 1487–1496 (1990).
113. Cowley, S. C. *et al.*, *Phys. Rep.* **283**, 227–251 (1997).
114. Leamon, R. J. *et al.*, *Astrophys. J.* **537**, 1054–1062 (2000).
115. Matthaeus, W. H. *et al.*, **679**, 427–432 (2003).
116. Ambrosiano, J. *et al.*, *J. Geophys. Res. Space Phys.* **93**, 14383–14400 (1988).
117. Hoshino, M., *Phys. Rev. Lett.* **108**, 135003 (2012).
118. Lazarian, A. *et al.*, *Astrophys. J.* **703**, 8 (2009).
119. Gosling, J. T., *Space Sci. Rev.* **172**, 187–200 (2012).
120. Perri, S. *et al.*, *Phys. Rev. Lett.* **109**, 191101 (2012).
121. Osman, K. T. *et al.*, *Phys. Rev. Lett.* **112**, 215002 (2014).
122. Chian, A. C.-L. *et al.*, *Astrophys. J. Lett.* **733**, L34 (2011).
123. Egedal, J. *et al.*, *Nat. Phys.* **8**, 321–324 (2012).
124. Drake, J. F. *et al.*, *Phys. Plasmas* **21**, 72903 (2014).
125. Ergun, R. E. *et al.*, *J. Geophys. Res. Space Phys.* **120**, 1832–1844 (2015).
126. Caprioli, D. *et al.*, *Astrophys. J.* **783**, 91 (2014).
127. Schwartz, S. J. *et al.*, *Geophys. Res. Lett.* **18**, 373–376 (1991).
128. Parks, G. K. *et al.*, *Astrophys. J. Lett.* **771**, L39 (2013).
129. Treumann, R. A., *Astron. Astrophys. Rev.* **17**, 409–535 (2009).
130. Wan, M. *et al.*, *Phys. Rev. Lett.* **109**, 195001 (2012).
131. Hasegawa, H. *et al.*, *Nature* **430**, 755–758 (2004).
132. Sundkvist, D. *et al.*, *Nature* **436**, 825–828 (2005).
133. Alexandrova, O. *et al.*, *J. Geophys. Res. Space Phys.* **111**, A12208 (2006).
134. Borovsky, J. E. *et al.*, *J. Geophys. Res. Space Phys.* **119**, 2014JA019758 (2014).
135. Blasi, P., *Astrophys. J.* **525**, 603 (1999).
136. Emslie, A. G. *et al.*, *J. Geophys. Res. Space Phys.* **109**, A10104 (2004).
137. Emslie, A. G. *et al.*, *Astrophys. J.* **759**, 71 (2012).
138. Richardson, J. D. *et al.*, *Geophys. Res. Lett.* **22**, 325–328 (1995).
139. Marsch, E., *Living Rev. Sol. Phys.* **3**, 1–+ (2006).
140. Kasper, J. C. *et al.*, *Phys. Rev. Lett.* **101**, 261103 (2008).
141. Burgess, D. *et al.*, *Space Sci. Rev.* **118**, 205–222 (2005).
142. Eastwood, J. P. *et al.*, *Space Sci. Rev.* **118**, 41–94 (2005).
143. Lucek, E. A. *et al.*, *βr* **118**, 95–152 (2005).
144. Liu, Y. *et al.*, *Astrophys. J. Lett.* **659**, L65 (2007).
145. Araneda, J. A. *et al.*, *Phys. Rev. Lett.* **102**, 175001 (2009).
146. Bowers, K. J. *et al.*, *J. Phys. Conf. Ser.* **180**, 12055 (2009).
147. Markidis, S. *et al.*, *Math. Comput. Simul.* **80**, 1509–1519 (2010).
148. Sonnendrücker, E. *et al.*, *J. Comput. Phys.* **149**, 201–220 (1999).
149. Valentini, F. *et al.*, *J. Comput. Phys.* **225**, 753–770 (2007).
150. Bourouaine, S. *et al.*, *Astrophys. J. Lett.* **777**, L3 (2013).

151. Maneva, Y. G. *et al.*, *J. Geophys. Res. Space Phys.* **118**, 2842–2853 (2013).
152. Chandran, B. D. G. *et al.*, *Astrophys. J.* **776**, 45 (2013).
153. Li, X. *et al.*, *J. Geophys. Res. Space Phys.* **110**, A10109 (2005).
154. Telsoni, D. *et al.*, *Astron. Astrophys.* **476**, 1341–1346 (2007).
155. Kronberg, E. A. *et al.*, *J. Geophys. Res. Space Phys.* **116**, A02210 (2011).
156. Perrone, D. *et al.*, *Eur. Phys. J. D* **68**, 209 (2014).
157. Chasapis, A. *et al.*, *Astrophys. J. Lett.* **804**, L1 (2015).
158. Chasapis, A. *et al.*, *Astrophys. J.* **836**, 247 (2017).
159. Cairns, I. H. *et al.*, *Phys. Plasmas* **12**, 102110 (2005).
160. Afanasiev, A. *et al.*, *Astrophys. J.* **790**, 36 (2014).
161. Lario, D. *et al.*, *Astrophys. J.* **813**, 85 (2015).
162. Dmitruk, P. *et al.*, *J. Geophys. Res. Space Phys.* **111**, A12110 (2006).
163. Drake, J. F. *et al.*, *Astrophys. J. Lett.* **763**, L5 (2013).
164. Zank, G. P. *et al.*, *Astrophys. J.* **797**, 28 (2014).
165. Bell, A. R., *Mon. Not. R. Astron. Soc.* **182**, 147–156 (1978).
166. Caprioli, D. *et al.*, *Astrophys. J. Lett.* **798**, L28 (2015).
167. Furno, I. *et al.*, *J. Plasma Phys.* **81**, (2015).
168. Fasoli, A. *et al.*, *Nucl. Fusion* **53**, 63013 (2013).
169. Furno, I. *et al.*, *Plasma Phys. Control. Fusion* **58**, 14023 (2016).
170. Perrone, D. *et al.*, *Space Sci. Rev.* **178**, 233–270 (2013).
171. Zimbardo, G. *et al.*, *J. Plasma Phys.* **81**, (2015).
172. Bovet, A. *et al.*, *Phys. Rev. Lett.* **113**, 225001 (2014).
173. Van Compernelle, B. *et al.*, *Phys. Rev. Lett.* **114**, 245002 (2015).
174. Schaeffer, D. B. *et al.*, *Phys. Plasmas* **22**, 113101 (2015).
175. Dorfman, S. *et al.*, *Phys. Rev. Lett.* **116**, 195002 (2016).
176. Tripathi, S. K. P. *et al.*, *Phys. Rev. E* **91**, 13109 (2015).
177. Podesta, J. J. *et al.*, *Phys. Plasmas* **17**, 112905 (2010).
178. Wicks, R. T. *et al.*, *Phys. Rev. Lett.* **106**, 45001 (2011).
179. Chen, C. H. K. *et al.*, *Astrophys. J.* **770**, 125 (2013).
180. Maruca, B. A. *et al.*, *Phys. Rev. Lett.* **111**, 241101 (2013).
181. Pulupa, M. P. *et al.*, *J. Geophys. Res. Space Phys.* **119**, 647–657 (2014).
182. Phan, T. D. *et al.*, *Astrophys. J. Lett.* **719**, L199–L203 (2010).
183. Gosling, J. T., *Astrophys. J. Lett.* **671**, L73 (2007).
184. Armstrong, J. W. *et al.*, *Astrophys. J.* **443**, 209–221 (1995).
185. Hennebelle, P. *et al.*, *Astron. Astrophys. Rev.* **20**, 55 (2012).
186. Falceta-Gonçalves, D. *et al.*, *Nonlinear Process. Geophys.* **21**, 587–604 (2014).
187. Zhuravleva, I. *et al.*, *Nature* **515**, 85–87 (2014).
188. Herbst, E., *Annu. Rev. Phys. Chem.* **46**, 27–54 (1995).
189. Joulain, K. *et al.*, *Astron. Astrophys.* **340**, 241–256 (1998).
190. Spangler, S. R. *et al.*, *Astrophys. J. Lett.* **353**, L29–L32 (1990).
191. Foullon, C. *et al.*, *Astrophys. J. Lett.* **729**, L8 (2011).
192. Masters, A. *et al.*, *J. Geophys. Res. Space Phys.* **115**, A07225 (2010).
193. Paral, J. *et al.*, *Nat. Commun.* **4**, 1645 (2013).
194. Borovikov, S. N. *et al.*, *Astrophys. J. Lett.* **783**, L16 (2014).
195. Zaqarashvili, T. V. *et al.*, *Astrophys. J. Lett.* **783**, L19 (2014).
196. Zaqarashvili, T. V. *et al.*, *Astron. Astrophys.* **561**, A62 (2014).
197. Borovsky, J. E. *et al.*, *J. Geophys. Res. Space Phys.* **115**, A10101 (2010).
198. Hasegawa, H. *et al.*, *J. Geophys. Res. Space Phys.* **114**, A12207 (2009).
199. Ofman, L. *et al.*, *Astrophys. J. Lett.* **734**, L11 (2011).
200. Gómez, D. O. *et al.*, *Astrophys. J.* **818**, 126 (2016).
201. Burgess, D. *et al.*, *Space Sci. Rev.* **178**, 513–533 (2013).

-
202. Desai, M. *et al.*, *Living Rev. Sol. Phys.* **13**, 3 (2016).
 203. Karimabadi, H. *et al.*, *Phys. Plasmas* **21**, 62308 (2014).
 204. Bale, S. D. *et al.*, *Space Sci. Rev.* **118**, 161–203 (2005).
 205. Lucek, E. A. *et al.*, *J. Geophys. Res. Space Phys.* **113**, A07S02 (2008).
 206. Wilson, L. B. *et al.*, *Phys. Rev. Lett.* **117**, 215101 (2016).
 207. McKenzie, J. F. *et al.*, *Planet. Space Sci.* **17**, 1029–1037 (1969).
 208. Vainio, R. *et al.*, *Astron. Astrophys.* **331**, 793–799 (1998).
 209. Meziane, K. *et al.*, *J. Geophys. Res. Space Phys.* **112**, A01101 (2007).
 210. Lucek, E. A. *et al.*, *Space Sci. Rev.* **118**, 95–152 (2005).
 211. Johlander, A. *et al.*, *Phys. Rev. Lett.* **117**, 165101 (2016).
 212. Masters, A. *et al.*, *Nat. Phys.* **9**, 164–167 (2013).
 213. Tu, C.-Y. *et al.*, *J. Geophys. Res. Space Phys.* **94**, 11739–11759 (1989).
 214. Wicks, R. T. *et al.*, *Mon. Not. R. Astron. Soc. Lett.* **407**, L31–L35 (2010).
 215. Wicks, R. T., *Phys. Rev. Lett.* **110**, (2013).
 216. Wicks, R. T. *et al.*, *Astrophys. J.* **746**, 103 (2012).
 217. Bavassano, B. *et al.*, *J. Geophys. Res. Space Phys.* **97**, 19129–19137 (1992).
 218. Phan, T. D. *et al.*, *Nature* **439**, 175–178 (2006).
 219. Phan, T. D. *et al.*, *Geophys. Res. Lett.* **36**, L09108 (2009).
 220. Mistry, R. *et al.*, *Geophys. Res. Lett.* **42**, 2015GL066820 (2015).
 221. Mistry, R. *et al.*, *Phys. Rev. Lett.* **117**, 185102 (2016).
 222. Huttunen, K. E. J. *et al.*, *J. Geophys. Res. Space Phys.* **112**, A01102 (2007).
 223. Bale, S. D. *et al.*, *Geophys. Res. Lett.* **26**, 1573–1576 (1999).
 224. Pulupa, M. *et al.*, *Astrophys. J.* **676**, 1330 (2008).
 225. Lee, M. A. *et al.*, *Space Sci. Rev.* **32**, 205–228 (1982).
 226. Perri, S. *et al.*, *Astrophys. J. Lett.* **671**, L177 (2007).
 227. Perri, S. *et al.*, *J. Geophys. Res. Space Phys.* **113**, A03107 (2008).
 228. Perri, S. *et al.*, *Astron. Astrophys.* **596**, A34 (2016).
 229. Zimbardo, G. *et al.*, *Space Sci. Rev.* **156**, 89–134 (2010).
 230. Sergeev, V. *et al.*, *Geophys. Res. Lett.* **36**, L21105 (2009).
 231. Khotyaintsev, Y. V. *et al.*, *Phys. Rev. Lett.* **106**, 165001 (2011).
 232. Zieger, B. *et al.*, *Geophys. Res. Lett.* **38**, L22103 (2011).
 233. Fu, H. S. *et al.*, *Geophys. Res. Lett.* **38**, L16104 (2011).
 234. Angelopoulos, V. *et al.*, *Science* **341**, 1478–1482 (2013).
 235. Kalmoni, N. M. E. *et al.*, *J. Geophys. Res. Space Phys.* **120**, 2015JA021470 (2015).
 236. Schrijver, C. J. *et al.*, *Adv. Space Res.* **55**, 2745–2807 (2015).
 237. Graham, D. B. *et al.*, *J. Geophys. Res. Space Phys.* **122**, 2016JA023572 (2017).
 238. Greco, A. *et al.*, *Phys. Rev. E* **86**, 66405 (2012).
 239. Perrone, D. *et al.*, *J. Geophys. Res. Space Phys.* **119**, 2400–2410 (2014).
 240. Cara, A. *et al.*, *J. Geophys. Res. Space Phys.* 2016JA023269 (2017).
 241. De Marco, R. *et al.*, *J. Instrum.* **11**, C08010 (2016).
 219. THOR Science Requirement Document, ESA-THOR-EST-SCI-RS-001, Issue 1. (2017).
 243. Soucek, J. *et al.*, *2016 ESA Workshop on Aerospace EMC (Aerospace EMC)* 1–4 (2016).
 244. Leinweber, H. K. *et al.*, *Meas. Sci. Technol.* **19**, 55104 (2008).
 225. THOR Mission Requirement Document, THOR-EST-MIS-RS-001, Issue 1. (2017).
 246. Paschmann, G. *et al.*, (ESA Publications Division, Noordwijk, The Netherlands, 1998).
 247. Narita, Y., (Springer, 2012).
 248. Comișel, H. *et al.*, *Ann Geophys* **34**, 975–984 (2016).
 249. Tu, C.-Y. *et al.*, *Space Sci. Rev.* **73**, 1–210 (1995).
 250. Gary, S. P., (Cambridge University Press, 1993).
 251. Fowler, R. A. *et al.*, *J. Geophys. Res.* **72**, 2871–2883 (1967).
 252. Arthur, C. W. *et al.*, *Radio Sci.* **11**, 833–845 (1976).

-
253. Taylor, G. I., *Proc. R. Soc. Lond. Ser. A* **164A**, 476–490 (1938).
 254. Schäfer, S. *et al.*, *Ann Geophys* **25**, 1011–1024 (2007).
 255. Matthaeus, W. H. *et al.*, *J. Geophys. Res. Space Phys.* **87**, 6011–6028 (1982).
 256. Storey, L. R. O. *et al.*, *Geophys. J. Int.* **56**, 255–269 (1979).
 257. Storey, L. R. O. *et al.*, *Geophys. J. Int.* **62**, 173–194 (1980).
 258. Oscarsson, T. E. *et al.*, *J. Geophys. Res. Space Phys.* **94**, 2417–2428 (1989).
 259. Oscarsson, T. *et al.*, *Phys. Chem. Earth Part C Sol. Terr. Planet. Sci.* **26**, 229–235 (2001).
 260. Eastwood, J. P. *et al.*, *Phys. Rev. Lett.* **102**, 35001 (2009).
 261. Bellan, P. M., *J. Geophys. Res. Space Phys.* **121**, 2016JA022827 (2016).
 262. Marsch, E. *et al.*, *J. Geophys. Res. Space Phys.* **106**, 8357–8361 (2001).
 263. Kim, Y. C. *et al.*, *IEEE Trans. Plasma Sci.* **7**, 120–131 (1979).
 264. Hada, T. *et al.*, *Space Sci. Rev.* **107**, 463–466 (2003).
 265. Sonnerup, B. U. Ö. *et al.*, *ISSI Sci. Rep. Ser.* **1**, 185–220 (1998).
 266. Sonnerup, B. U. Ö. *et al.*, *J. Geophys. Res. Space Phys.* **111**, A05203 (2006).
 267. Haaland, S. E. *et al.*, *Ann Geophys* **22**, 1347–1365 (2004).
 268. Anekallu, C. R. *et al.*, *J. Geophys. Res. Space Phys.* **116**, A11204 (2011).
 269. Anekallu, C. R. *et al.*, *J. Geophys. Res. Space Phys.* **118**, 1948–1959 (2013).
 270. Khrabrov, A. V. *et al.*, *Geophys. Res. Lett.* **25**, 2373–2376 (1998).
 271. Khrabrov, A. V. *et al.*, *Analysis Methods for Multi-Spacecraft Data* (eds. Paschmann, G. *et al.*) 221 (ESA Publications Division, 1998).
 272. Paschmann, G. *et al.*, *ISSI Sci. Rep. Ser.* **8**, 65–74 (2008).
 273. Lefebvre, B. *et al.*, *J. Geophys. Res. Space Phys.* **112**, A09212 (2007).
 274. Fukuhara, H. *et al.*, *Earth Planets Space* **61**, 765 (2009).
 275. Ergun, R. E. *et al.*, *J. Geophys. Res. Space Phys.* **96**, 11371–11378 (1991).
 276. Katoh, Y. *et al.*, *Ann Geophys* **31**, 503–512 (2013).
 277. Klein, K. G. *et al.*, *Astrophys. J. Lett.* **790**, L20 (2014).
 278. Pinçon, J. L. *et al.*, *J. Geophys. Res. Space Phys.* **96**, 1789–1802 (1991).
 279. Dunlop, M. W. *et al.*, *J. Geophys. Res. Space Phys.* **107**, 1384 (2002).

10 List of acronyms

AOCS	Attitude and Orbit Control System	LGA	Low-Gain Antenna
BCR	Burst Collection Region	MAG	THOR, fluxgate magnetometer
CAA	Cluster Active Archive	MHD	MagnetoHydroDynamic
CAM	Collision Avoidance Manoeuvres	MMH	MonoMethylHydrazine
CDMU	Central Data Management Unit	MMS	Magnetospheric Multiscale mission
CFRP	Carbon Fiber Reinforced Plastics	MOC	Mission Operation Centre
CSA	Cluster Science Archive	MON	Mixed Oxides of Nitrogen
CSW	THOR, Cold Solar Wind instrument	NSP	Nominal Science Phase
DET	Direct Energy Transfer	NSST	Numerical Simulation Support Team
DCP	Decommissioning Phase	OBC	On-Board Computer
EFI	THOR, Electric Field Instrument	OBT	spacecraft On-Board Time
EMC	Electromagnetic Cleanliness	PIC	Particle-In-Cell
EPE	THOR, Energetic Particle Experiment	PMD	Propellant Management Device
EOL	End Of Life	PPU	THOR, Particle Processing Unit
ERG	Exploration of energization and Radiation in Geospace	PRM	Perigee Raising Manoeuvre
ESAC	European Space Astronomy Centre	PSF	Planning Skeleton Files
ESDC	ESAC Science Data Centre	RCS	Reaction control system
ESOC	European Space Operations Centre	SciRD	Science Requirement Document
ESP	Extended Science Phase	SCM	THOR, SearchCoil Magnetometer
FAR	THOR, Faraday Cup	SEE	Single Event Effect
FOM	Figure Of Merit	SGS	Science Ground Segment
FOV	Field-of-View	SITL	Scientist In The Loop
FWP	THOR, Fast Wave Processor	SOC	Science Operations Centre
GEO	Geosynchronous Equatorial Orbit	SPICE	Spacecraft Planet Instrument Pointing Events
GS	Ground Segment	sps	samples per second
GTO	Geostationary Transfer Orbit	SSPA	Solid State Power Amplifiers
HK	House-Keeping	SWT	Science Working Team
IMF	Interplanetary Magnetic Field	TEA	THOR, Turbulence Electron Analyser
IMS	THOR, Ion Mass Spectrometer	TM	Telemetry
ITO	Indium—Tin Oxide	TOF	Time-of-Flight
ITU	International Telecommunications Union	TPR	Top Priority Region
JSpOC	Joint Space Operations Center	TWTA	Traveling Wave Tube Amplifiers
KSR	Key Science Region	UTC	Coordinated Universal Time
LEOP	Launch and Early Orbit Phase	VDF	Velocity Distribution Function
		VIT	Virtual Instrument Team

11 Annex A: Assessment study contributors

In addition to the THOR SST, PIs, those responsible for several subsections (see page 3), Co-PIs and Lead-CoIs (see Section 7.1), major contributions to the Assessment Study Report were made by the following THOR team scientists:

Neus Agueda²³, Olga Alexandrova¹³, Mats André¹⁰, Wolfgang Baumjohann¹¹, John Bonnell²⁰, David Burgess⁸⁰, Alexandros Chasapis²⁶, Enrico Camporeale², Damiano Caprioli⁹³, Troy Carter⁹⁰, Stefan Eriksson⁹⁵, Dominique Fontaine¹⁵, Ivo Furno⁷⁷, Steve Fuselier²¹, Daniel Graham¹⁰, Melvyn L Goldstein¹⁷, Michael Hesse²⁴, Tim Horbury⁸, Masahiro Hoshino⁶⁷, Greg Howes⁹⁶, Andreas Johlander¹⁰, Johan De Keyser¹, Lynn Kistler²², Hantao Ji¹⁸, Elena Kronberg⁵¹, Homa Karimabadi, Kris Klein²², Matthew Kunz¹⁸, Milan Maksimovic¹³, Yana Maneva²⁹, Rossana De Marco⁷, Samara Marilia¹⁷, W. H. Matthaeus²⁶, Cecilia Norgren¹⁰, Hermann Opgenoorth¹⁰, Minna Palmroth²⁷, Silvia Perri²⁵, Denise Perrone⁴, Oreste Pezzi²⁵, Francesco Pucci²⁵, Vadim Roytershteyn¹¹¹, Sergio Servidio²⁵, Luca Sorriso-Valvo³, Zoltan Vörös¹¹,

and ESA members:

Fabrice Cipriani⁶, Michael Khan⁵, Andrew Walsh⁴, Alain Hilgers⁶.

THOR payload engineers

CSW: C. Amoros⁹, M. Anciaux¹, R. Baruah⁹, B. Beeckman¹, S. Berkenbosch¹, O. Bernal¹¹⁰, S. Bonnewijn¹, A. Cara⁹, A. Fedorov⁹, C. Feugeade⁹, L. Licciardi⁹, J. Maes¹, W. Marty⁹, R. Mathon⁹, E. Neefs¹, E. Penou⁹, S. Ranvier¹, H. Tap¹¹⁰, K. Wong⁹

MAG: W. Magnes¹¹, G. Laky¹¹, G. Berghofer¹¹, A. Valavanoglou¹¹, M. Delva¹¹, H. O'Brien⁸, C. M. Carr⁸, E. Cupido⁸

EFI: L. Åhlén¹⁰, T. Barcinski¹⁹, M. Berglund¹⁰, A. Bialek¹⁹, L. Bylander⁷³, V. Cripps¹⁰, G. Dalton²⁰, J. Davidsson¹⁰, M. Ludlam²⁰, J. Fredriksson¹⁰, A. Godlewski¹⁹, T. Kowalski¹⁹, D. Pankow²⁰

EPE: J. Steinhagen¹², L. Seimetz¹², S. Böttcher¹², B. Schuster¹²

FAR: I. Cermak¹⁰⁶

FWP: L. Uhler⁴⁰, R. Lan⁴⁰, I. Kolmasova⁴⁰, A. Godlewski¹⁹, T. Barcinski¹⁹, M. Morawski¹⁹, M. Winkler¹⁹, A. Bialek¹⁹, K. Yearby²⁸, M. Dekkali¹³

IMS: C. Verdeil¹⁵, J.-D. Techer¹⁵, F. Leblanc¹⁵, S. Pledel¹⁵, G. Degret¹⁵, J. Macri²², J. Gaidos²², C. Bancroft²², M. Witholm²², C. Frost²², D. Heirtzler²², S. Meyers²², D. Rau²², H. Fischer⁵¹,

PPU: D. Brienza⁷, G. Capuano¹⁰⁷, D. Titomanlio¹⁰⁷, R. Ascolese¹⁰⁷, R. Calvanese¹⁰⁷, G. Formicola¹⁰⁷, L. Amoroso¹⁰⁸, V. Fortunato¹⁰⁸

SCM: G. Jannet¹⁴, M. Mansour¹⁵, G. Chalumeau¹⁴, M. Chabassière¹⁴, T. Hachemi¹⁴, A. Jeandet¹⁵.

TEA: B. Hancock¹⁶, M. Hailey¹⁶, D. Rust¹⁶, J. Jones¹⁶, C. Brockley-Blatt¹⁶, D. Steinfeld¹⁷, Q. V. Nguyen¹⁷, T. Cameron¹⁷, U. Gliese¹⁷, T. Gehring¹⁷, P. Coronado¹⁷

Full list of THOR team members (<http://thor.irfu.se/thor-team>):

Austria: W. Baumjohann¹¹, M. Bentley¹¹, M. Khodachenko¹¹, W. Magnes¹¹, R. Nakamura¹¹, T. Nakamura¹¹, Y. Narita¹¹, F. Plaschke¹¹, D. Schmid¹¹, M. Volwerk¹¹, Z. Voros¹¹, T. Zaqarashvili¹¹

Belgium: F. Darrouzet¹, J. De Keyser¹, M. Echim¹, H. Gunell¹, H. Lamy¹, G. Lapenta²⁹, Y. Maneva²⁹, V. Pierrard¹, Y. Voitenko¹, F. Pucci²⁹

Canada: C. Cully³⁰, A. Yau³⁰, A. Hamza³¹, K. Meziane³¹, I. Mann³²

China: X. Deng³³, A. Du³⁴, X. Feng³⁵, H. Fu³⁶, J. He³⁷, Q. Lu³⁸, C. Shen³⁵, J. Shi³⁵, J. Zhong³⁹, Q. Zong³⁷

Czech Republic: B. Grison⁴⁰, P. Hellinger⁴¹, I. Kolmasova⁴⁰, V. Krupar⁴⁰, O. Kruparova⁴⁰, F. Nemecek⁴², Z. Nemecek⁴², J. Pavlu⁴², D. Pisa⁴⁰, L. Prech⁴², J. Safrankova⁴², O. Santolik⁴⁰, J. Soucek⁴⁰, J. Urbar⁴⁰

Denmark: R. Behlke⁴³

Ecuador: C. Vasconez⁴⁴

Finland: M. Battarbee⁴⁵, U. Ganse⁴⁵, R. Vainio⁴⁵, N. Ganushkina⁴⁶, S. Hoilijoki⁴⁶, Y. Kempf⁴⁶, M. Palmroth⁴⁶, S. von Alftan⁴⁶, E. Kulpa²⁷

France: N. Aunai¹⁵, G. Belmont¹⁵, M. Berthomier¹⁵, H. Breuillard¹⁵, A. Ciardi¹¹², O. Le Contel¹⁵, D. Delcourt¹⁵, D. Fontaine¹⁵, S. Galtier¹⁵, S. Huang¹⁵, K. Kiyani¹⁵, C. Krafft¹⁵, A. Retinò¹⁵, L. Rezeau¹⁵, F. Sahraoui¹⁵, A. Alexandrova¹⁵, O. Alexandrova¹³, C. Briand¹³, M. Maksimovic¹³, A. Vecchio¹³, A. Zaslavsky¹³, D. Del Sarto⁴⁷, A. Ghizzo⁴⁷, E. Gravier⁴⁷, S. Heuraux⁴⁷, T. Dudok de Wit¹⁴, V. Krasnoselskikh¹⁴, M. Kretzschmar¹⁴, J. L. Pincon¹⁴, N. Andre⁹, V. Genot⁹, B. Lavraud⁹, P. Louarn⁹, A. Marchaudon⁹, C. Mazelle⁹, R. Pinto⁹, F. Rincon⁹, A. Rouillard⁹, Y. Vernisse⁹, P. Henri¹⁴, B. Lembege⁴⁸, T. Passot⁴⁹, P. L. Sulem⁴⁹, R. Marino⁵⁰

Germany: R. Bucic⁵¹, J. Buchner⁵¹, M. Franz⁵¹, S. Haaland⁵¹, E. Kronberg⁵¹, J. Saur⁵², D. Told⁵³, F. Jenko⁵³, R. Wimmer-Schweingruber¹²

Greece: A. Anastasiadis⁵⁴

Hungary: G. Facsko⁵⁵, A. Kis⁵⁵

Israel: M. Gedalin⁵⁶

Italy: D. Grasso⁵⁷, T. Alberti²⁵, F. Califano¹⁰⁵, V. Carbone²⁵, S. Cerri¹⁰⁵, F. Catapano²⁵, G. De Vita²⁵, A. Greco²⁵, F. Lepreti²⁵, E. Leonardis²⁵, F. Malara²⁵, G. Nigro²⁵, S. Perri²⁵, O. Pezzi²⁵, L. Primavera²⁵, S. Savaglio²⁵, S. Servidio²⁵, F. Valentini²⁵, P. Veltri²⁵, G. Zimbardo²⁵, L. Franci⁵⁸, S. Landi⁵⁸, A. Verdini⁵⁸, R. Bruno⁷, D. Brienza⁷, M. Laurenza⁷, M. F. Marcucci⁷, G. Pallocchia⁷, G. Consolini⁷, R. D'Amicis⁷, R. De Marco⁷, G. De Masi⁵⁹, E. Martines⁵⁹, P. Veltri⁵⁹, N. Vianello⁵⁹, M. Zuin⁵⁹, M. Materassi⁶⁰, D. Bruno⁶¹, P. Minelli⁶¹, F. Tacconga⁶¹, M. Romè⁶², D. Telloni⁶³, P. Francia⁶⁴, M. Vellante⁶⁴, L. Sorriso-Valvo⁶⁵

Japan: H. Hasegawa⁶⁶, Y. Saito⁶⁶, I. Shinohara⁶⁶, M. Hoshino⁶⁷, N. Yokoi⁶⁷, S. Saito⁶⁸, S. Zenitani⁶⁹, S. Kasahara⁶⁶, S. Yokota⁶⁶, Y. Kasaba¹¹³

Netherlands: E. Camporeale², O. Roberts⁶

Norway: K. Oksavik²⁴, M. Hesse²⁴

Poland: J. Blecki¹⁹, W. Macek¹⁹, H. Rothkaehl¹⁹, M. Strumik¹⁹

Romania: C. Munteanu⁷⁰

Russia: E. Grigorenko⁷¹, A. Petrukovich⁷¹, M. Riazantseva⁷¹, Y. Yermolaev⁷¹

Spain: N. Agueda²³, A. Aran²³, B. Sanahuja²³, D. Perrone⁴, S. Toledo Redondo⁴

Sweden: M. André¹⁰, S. Buchert¹⁰, A. Eriksson¹⁰, E. Eriksson¹⁰, D. Graham¹⁰, Y. Khotyaintsev¹⁰, T. Leyser¹⁰, W. Li¹⁰, H. Nilsson⁷⁶, C. Norgren¹⁰, H. Opgenoorth¹⁰, A. Vaivads¹⁰, J. E. Wahlund¹⁰, E. Yordanova¹⁰, A. Brandenburg⁷², H. Dahlgren⁷³, N. Ivchenko⁷³, T. Karlsson⁷³, P. Lindqvist⁷³, S. Markidis⁷³, G. Marklund⁷³, I. B. Peng⁷³, T. Fulop⁷⁴, M. Hamrin⁷⁵, T. Pitkanen⁷⁵, G. Stenberg-Wieser⁷⁶, M. Yamauchi⁷⁶

Switzerland: I. Furno⁷⁷, P. Ricci⁷⁷, P. Wurz¹⁰⁹

United Kingdom: O. Allanson⁷⁸, M. Balikhin²⁸, Y. Bogdanova⁷⁹, D. Burgess⁸⁰, C. M. Carr⁸, S. Chapman⁸¹, C. H. K. Chen⁸, J. Davies⁷⁹, M. Dunlop⁷⁹, J. Eastwood⁸, B. Eliasson⁸², A. Fazakerley¹⁶, C. Foullon⁸³, M. Hapgood⁷⁹, T. Horbury⁸, D. Kataria¹⁶, X. Li⁸⁴, L. Matteini⁸, K. Osman⁸¹, C. J. Owen¹⁶, A. Schekochihin⁸⁵, S. Schwartz⁸, J. E. Stawarz⁸, B. Teaca⁸⁶, L. Trenchi⁸⁷, S. Walker²⁸, R. Wicks¹⁶, P. Wu⁸⁹, K. Yearby²⁸

United States of America: V. Angelopoulos⁹⁰, S. Bale²⁰, S. Boldyrev⁹¹, J. Bonnell²⁰, J. Borovsky⁹², D. Caprioli⁹³, T. Carter⁹⁰, B. Chandran²², A. Chasapis²⁶, C. Chaston²⁰, L. J. Chen¹⁷, G. A. Collinson¹⁷, G. Delzanno⁹⁴, S. Eriksson⁹⁵, S. Fuselier²¹, A. Galvin²², M. Goldstein¹⁷, H. Hietala⁹⁰, G. Howes⁹⁶, H.

Ji⁹⁷, H. Karimabadi, J. Kasper⁹⁸, L. Kistler²², K. G. Klein²², H. Kucharek²², M. Kunz¹⁸, A. Lazarian⁹¹, D. Malaspina⁹⁵, W. Matthaeus²⁶, T. E. Moore¹⁷, C. Mouikis²², K. Nykyri⁹⁹, L. Ofman¹⁷, M. Opher¹⁰⁰, C. Pollock¹⁷, M. J. Pueschel⁹¹, V. Roytershteyn¹¹¹, M. Samara¹⁷, D. Schaffner¹⁰¹, C. W. Smith²², D. Sundkvist²⁰, J. TenBarge¹⁰², K. Trattner⁹⁵, D. Turner⁹⁰, M. Velli⁹⁰, D. Verscharen²², A. Vinas¹⁷, L. B. Wilson¹⁷, B. Zieger¹⁰⁰

Ukraine: L. Kozak¹⁰³, V. Olshevsky¹⁰⁴

Affiliations

(1) BIRA, Belgium (2) CWI, Amsterdam, Netherlands (3) CNR, Italy (4) ESA/ESAC, Madrid, Spain (5) ESA/ESOC, Germany (6) ESA/ESTEC, Noordwijk, The Netherlands (7) INAF-IAPS, Italy (8) Imperial College, UK (9) IRAP, Toulouse, France (10) IRF, Uppsala (11) IWF, Graz, Austria (12) CAU, Kiel, Germany (13) LESIA, Paris Observatory, Meudon (14) LPC2E, France, (15) LPP, France (16) MSSL, UK (17) NASA/GSFC; USA (18) Princeton Univ., USA (19) SRC/PAS, Warsaw, Poland (20) SSL, UCB, USA, (21) SWRI, USA (22) UNH, USA (23) Univ. Barcelona, Barcelona, Spain (24) Univ. Bergen, Norway (25) UNICAL, Italy (26) Univ. Delaware, USA (27) Univ. Helsinki, Finland (28) Univ. Sheffield, UK (29) KU Leuven, Leuven, Belgium; (30) Univ. Calgari, Calgari, Canada; (31) Univ. New Brunswick, Canada; (32) Univ. Alberta, Canada; (33) Nachang Univ., Jiangxi, China; (34) IGG/CAS, Beijing, China; (35) NSSC/CAS, Beijing, China; (36) Beihang Univ., Beijing, China; (37) Peking Univ., Beijing, China; (38) USTC, Beijing, China; (39) Beijing Normal Univ., Beijing, China; (40) IAP/CAS, Prague, Czech Republic; (41) ASU, Prague, Czech Republic; (42) Charles University, Faculty of Mathematics and Physics, Prague, Czech Republic; (43) Technical Univ., Copenhagen, Denmark; (44) Escuela Politécnica Nacional, Quito, Ecuador; (45) Univ. Turku, Turku, Finland; (46) FMI, Helsinki, Finland; (47) Univ. Nancy, France; (48) LATMOS, Guyancourt, France; (49) Obs. Cote d'Azur, Nice, France; (50) Ecole Centrale de Lyon, Lyon, France; (51) MPS, Göttingen, Germany; (52) Univ. Cologne, Germany; (53) IPP, Garching, Germany; (54) National Observatory of Athens, Greece; (55) RCAES, Sopron, Hungary; (56) Ben-Gurion Univ., Israel; (57) CNR-ICS, Torino; (58) Univ. Firenze, Italy; (59) Consorzio RFX, Padova, Italy; (60) CNR-ISC, Sesto Fiorentino, Italy; (61) CNR-NANOTEC, Bari, Italy; (62) Univ. Milano, Italy; (63) INAF, Italy; (64) Univ. L'Aquila, Italy; (65) CNR-NANOTEC, Rende, Italy; (66) ISAS/JAXA, Japan; (67) Univ. Tokyo, Japan; (68) Nagoya Univ., Japan; (69) National Astronomical Observatory, Tokyo, Japan; (70) ISS, Romania; (71) IKI, Moscow, Russia; (72) Nordita, Stockholm, Sweden; (73) KTH, Stockholm, Sweden; (74) Chalmers Univ. Tech, Gothenburg, Sweden; (75) Univ. Umea, Sweden; (76) IRF, Kiruna, Sweden; (77) EPFL, Lausanne, Switzerland; (78) Univ. St Andrews, UK; (79) RAL, Oxfordshire, UK; (80) QMUL, London, UK; (81) Univ. Warwick, UK; (82) Strathclyde Univ., UK; (83) Univ. Exeter, UK; (84) Univ. Aberystwyth, UK; (85) Univ. Oxford, UK; (86) Coventry Univ., UK; (87) Univ. Southampton, UK; (88) UCL, London, UK; (89) Queen's Univ. Belfast, UK; (90) UCLA, Los Angeles, California, USA; (91) Univ. Wisconsin, Madison, Wisconsin, USA; (92) SSI, Boulder, Colorado, USA; (93) Univ. Chicago, Illinois, USA; (94) LANL, Los Alamos, New Mexico, USA; (95) Univ. Colorado, Boulder, Colorado, USA; (96) Univ. Iowa, Iowa City, Iowa, USA; (97) PPPL, Princeton, New Jersey, USA; (98) HSCA, Cambridge, Massachusetts, USA; (99) Embry-Riddle Aeronautical Univ., Daytona Beach, Florida, USA; (100) Boston Univ., Boston, Massachusetts, USA; (101) Bryn Mawr College, Bryn Mawr, Pennsylvania USA; (102) Univ. Maryland, College Park, Maryland, USA; (103) Kyiv Taras Shevchenko Univ., Kyiv, Ukraine; (104) Main Astron. Obs., Kyiv, Ukraine; (105) Univ. Pisa, Italy; (106) CGC Instruments, Chemnitz, Germany; (107) TSD, Pozzuoli, Italy; (108) Planetek, Bari, Italy; (109) Univ. Bern, Switzerland; (110) LAAS, France; (111) Space Science Institute, Boulder, Colorado; (112) Sorbonne Univ. and Obs. de Paris, LERMA, France; (113) Tohoku Univ., Japan

12 Annex B: L1 and L2 requirements

Table 31: Correspondence between the Level 1 and Level 2 requirements within the Assessment Study Report (“L1” and “L2”) and the corresponding Level 1 and Level 2 requirements within the Science Requirement Document (SciRD).

Requirement	L1	SciRD L1 requirements	L2	SciRD L2 requirements
EM field cadence	R1	SR-PAY-1_R (E field) SR-PAY-2_R (B field)	RP1	PR-PAY-1_R PR-PAY-2_R
EM field sensitivity	R2	SR-PAY-3_R (E field) SR-PAY-4_R (B field)	RP2	PR-PAY-3_R PR-PAY-4_R
EM field accuracy	R3	SR-PAY-5_R (E field) SR-PAY-6_R (B field) SR-PAY-7_R (B range) SR-PAY-8_R (E range) SR-PAY-9_R (s/c potential)	RP3	PR-PAY-5_R PR-PAY-6_R PR-PAY-7b_R PR-PAY-7a_R PR-PAY-8_R
Phase velocity	R4	SR-PAY-10_R	RP4	PR-PAY-9_R
Ion composition	R5	SR-PAY-11_R		PR-PAY-10_R
Particle moments	R6	SR-PAY-12_R (ions) SR-PAY-13_R (electrons)		PR-PAY-11_R PR-PAY-12_R
Particle distribution functions in thermal range	R7	SR-PAY-14_R SR-PAY-15_R SR-PAY-16_R SR-PAY-17_R	RP7	PR-PAY-13_R PR-PAY-14_R
Particle distribution functions in suprathermal range	R8	SR-PAY-16_R SR-PAY-17_R SR-PAY-18_R		PR-PAY-15_R PR-PAY-16_R
Energetic particles	R9	SR-PAY-19_R (cadence) SR-PAY-20_R (energy resol.) SR-PAY-21_R (energy range)	RP9	PR-PAY-16_R
Key Science Regions	R10	SR-PAY-22_R SR-MIS-5_G		
Characteristic scales	R11	SR-PAY-25_R		
Mission requirements				
Orbit	R13	SR-MIS-1_T		
S/c and payload operations	R14	SR-MIS-1_T (TPR definition) SR-MIS-2_R (data return) SR-MIS-3_R (on-board memory) SR-MIS-4_R (payload operation) SR-MIS-5_R (contin. operation) SR-MIS-8_R (s/c attitude) SR-MIS-9_R (s/c spin)		
Science Ground Segment	R15	SR-MIS-6_R (data policy) SR-MIS-7_R (cross-callibration)		